

March 2015

## Developing Fluorescent Sensors for the Bioimaging of Chelatable Iron(III) Ions

Ziya Aydin

Follow this and additional works at: [https://scholarworks.umass.edu/dissertations\\_2](https://scholarworks.umass.edu/dissertations_2)

 Part of the [Inorganic Chemistry Commons](#)

---

### Recommended Citation

Aydin, Ziya, "Developing Fluorescent Sensors for the Bioimaging of Chelatable Iron(III) Ions" (2015).  
*Doctoral Dissertations*. 281.  
[https://scholarworks.umass.edu/dissertations\\_2/281](https://scholarworks.umass.edu/dissertations_2/281)

This Open Access Dissertation is brought to you for free and open access by the Dissertations and Theses at ScholarWorks@UMass Amherst. It has been accepted for inclusion in Doctoral Dissertations by an authorized administrator of ScholarWorks@UMass Amherst. For more information, please contact [scholarworks@library.umass.edu](mailto:scholarworks@library.umass.edu).

**DEVELOPING FLUORESCENT SENSORS FOR THE BIOIMAGING OF CHELATABLE IRON(III) IONS**

A Dissertation Presented

by

ZIYA AYDIN

Submitted to the Graduate School of the  
University of Massachusetts Amherst in partial fulfillment  
of the requirements for the degree of

DOCTOR OF PHILOSOPHY

February 2015

Department of Chemistry

© Copyright by Ziya Aydin 2015

All Rights Reserved

# DEVELOPING FLUORESCENT SENSORS FOR THE BIOIMAGING OF CHELATABLE IRON(III) IONS

A Dissertation Presented

by

ZIYA AYDIN

Approved as to style and content by:

---

Maolin Guo, Chair

---

Michael J. Maroney, Member

---

Michael J. Knapp, Member

---

Alejandro P. Heuck, Member

---

Professor Craig T. Martin, Head

Chemistry Department

## **DEDICATION**

This thesis is dedicated to my dear parents, loving wife, and son

## ACKNOWLEDGMENTS

I would like to express great appreciation to my advisor Dr. Maolin Guo, who has been a great mentor. I have benefited a lot from his creative scientific ideas, writing corrections and fruitful discussions. Without his support and guidance, I would not have had a productive, enriching graduate school experience. Special thanks as well to Dr. Yibin Wei for his supervision and encouragement during the experimental work. Particular thanks should be given to my committee members, Dr. Michael Maroney, Dr. Michael Knapp, and Dr. Alejandro Heuck for their critical review and excellent feedback on my prospectus defense, proposal defense, data defense, and this dissertation. I appreciate Dr. Tracie Ferreira for providing zebrafish for animal studies. I also want to extend my appreciation to my fellow lab mates Yong Tong, Carlos Perez, Kruti Patel, Hasan Ilhan, Yi Zhang, Zhiwei Liu, Siddhartha Maiti, Bing Yan, Xiaofei Fu, Bayan Alhawsah for their kindness and enlightening discussions. Last but not least, I greatly appreciate my wife Elif Aydin for her support. I would also like to thank my parents Ali and Nurhayat Aydin, my brothers Efsal, Unsal, Alihan and my sisters Zuhale, Seval, and Hilal for their support. I also extend my thanks to my friend Volkan Sozen for his encouragement and support.

## ABSTRACT

DEVELOPING FLUORESCENT SENSORS FOR THE BIOIMAGING OF CHELATABLE IRON(III) IONS

FEBRUARY 2015

ZIYA AYDIN, B.A., CUKUROVA UNIVERSITY

M.S., UNIVERSITY OF MASSACHUSETTS DARTMOUTH

Ph.D., UNIVERSITY OF MASSACHUSETTS AMHERST

Directed by: Professor Maolin Guo

Iron is an essential element for the body and plays important roles in many metabolic processes. A transient labile iron pool (LIP) has been proposed to play key roles in cellular iron trafficking and metabolism. However, free iron ions ( $\text{Fe}^{3+}$  and  $\text{Fe}^{2+}$ ) in this pool are toxic and damaging to cells due to their involvement in the production of oxygen radicals. The damages may lead to aging and various diseases including stroke, cancer, and several neurological disorders like Parkinson's disease, Alzheimer's disease and atherosclerosis. Determination of free iron ions in cells may contribute to a better understanding of iron's function and transport pathways under physiological and pathological conditions. Early methods to identify a labile and transient iron pool needed to disrupt cells. Over the past two decades, fluorescent sensors have emerged to visualize metal ions in living cells without any damage. To visualize intercellular iron ions, specific fluorescent sensors are needed. Even though fluorescent sensors have been applied into cells for two decades, only a few  $\text{Fe}^{3+}$ -selective sensors are capable of cellular imaging with limited success.

Chapter 1 introduces the biological background of iron as well as recently developed fluorescent sensors for iron detection.

In chapter 2, a new rhodamine-based sensor, RPE, was synthesized and characterized by  $^1\text{H}$  NMR,  $^{13}\text{C}$  NMR, and MS. The sensor responds to  $\text{Fe}^{3+}$  via coordination induced fluorescent activation (CIFA) mechanism and gives a distinct rapid and reversible fluorescence response upon the alteration of intracellular  $\text{Fe}^{3+}$  levels with little interference from other biologically relevant metal ions. RPE can readily detect endogenous chelatable  $\text{Fe}^{3+}$  via a confocal microscope in live human SH-SY5Y cells at subcellular resolution in real time, with two labile  $\text{Fe}^{3+}$  pools being successfully located in mitochondria and endosomes/lysosomes in both untreated and  $\text{Fe}^{3+}$ -loaded human SH-SY5Y cells for the first time. RPE is thus a promising tool for probing the cell biology of  $\text{Fe}^{3+}$ .

Sensors, such as RPE, which emit lights in visible range, suffer from some significant drawbacks, including intrinsic signal caused by auto-fluorescence, high light scattering, and poor light penetration when they are applied to biological tissues. To overcome these limitations, near infrared sensors can be used because they emit at longer wavelength so they display low autofluorescence background, deeper penetration to tissues and cause less damage to biological samples. In chapter 3, a heptacyanine based sensor, IRPE, was synthesized and characterized by  $^1\text{H}$  NMR,  $^{13}\text{C}$  NMR, and MS. IRPE showed selective response to  $\text{Fe}^{3+}$  and binds it in a 1:1 stoichiometry with an apparent binding constant  $2.0 \times 10^5 \text{ M}^{-1}$  in ACN/HEPES (1/1 v/v) solution. The sensor displays a change in color and fluorescence upon the alteration of  $\text{Fe}^{3+}$  levels in solution with a reversible response and little interference with other biological relevant metal ions. IRPE is a good  $\text{Fe}^{3+}$ -selective sensor but, cell studies showed that it was not capable of detecting free iron ions in cells.



To get cell permeable and  $\text{Fe}^{3+}$ -selective near infrared sensors, it was decided to change the strategy for near-infrared sensor design. In chapter 4, a Changsha based sensor, NIRh-Ac, was developed. The sensor gives a distinct rapid and reversible fluorescence response upon the alteration of intracellular  $\text{Fe}^{3+}$  levels with little interference from other biologically relevant metal ions. Confocal experiments showed that NIRh-Ac could readily detect exogenous chelatable  $\text{Fe}^{3+}$  in live human SH-SY5Y cells and live fibroblast cell (ws1) at subcellular resolution, with the chelatable  $\text{Fe}^{3+}$  pools located in mitochondria and endosomes/lysosomes for SH-SY5Y cells and in mitochondria for ws1 cells. Kinetic experiments with the sensor provided a visual imaging of  $\text{Fe}^{3+}$  transport pathway in human fibroblast cells in real time, i.e., from endosomes to lysosomes and finally to mitochondria via a direct “Lyso-mito docking” mechanism, bypassing the cytosol. Studies using zebrafish clearly demonstrated the capability of the NIRh-Ac sensor in imaging  $\text{Fe}^{3+}$  in live animals.

In chapter 5, another Changsha-based near infrared sensor, NRPA, was developed to detect endogenous  $\text{Fe}^{3+}$  ions in cells. It is a highly sensitive, highly selective, and reversible turn-on near infrared fluorescent sensor for  $\text{Fe}^{3+}$ . The sensor gives a rapid and reversible fluorescence response upon the alteration of intracellular  $\text{Fe}^{3+}$  levels with little interference from other biologically relevant metal ions. Confocal imaging studies demonstrate that NRPA can readily detect endogenous free  $\text{Fe}^{3+}$  in live human SH-SY5Y cells and live fibroblast cell (ws1) at subcellular resolution, with the chelatable  $\text{Fe}^{3+}$  pools located in mitochondria and endosomes/lysosomes in SH-SY5Y cells while in mitochondria only in ws1 cells. It was concluded that different cell lines store/handle iron in different ways. The ability of NRPA to detect endogenous free  $\text{Fe}^{3+}$  ions in zebrafish was also demonstrated and free  $\text{Fe}^{3+}$  ions were found located in liver/gall bladder of 6-days-old zebrafish.

In chapter 6, highly sensitive, highly selective, and reversible turn-on near infrared Changsha-based fluorescent  $\text{Fe}^{3+}$ -sensors, NRPK and NRP were described. The initial goal was to synthesize Fe(II)-selective fluorescence sensor; however, NRPK turned out to be a sensor for Fe(III). Both NRP and NRPK coordinate  $\text{Fe}^{3+}$  with O/N/N binding motif with 2:1 ratio. The NRPK appears not to use the carbonyl group linked to the pyridine ring for coordination. Cell imaging experiments with NRPK showed that it could readily detect endogenous free  $\text{Fe}^{3+}$  in live bovine aortic endothelial cells (BAEC) and human SH-SY5Y cells at subcellular resolution, with free iron(III) ions located in mitochondria and endosomes/lysosomes for both BAEC and SH-SY5 cells. Finally, NRPK demonstrated the ability to detect exchangeable free iron(III) in zebrafish *in vivo*.

Finally, a novel sensor was developed to quantify the concentration of  $\text{Fe}^{3+}$  in the LIP and to confirm that the images observed by the sensors such as RPE, NIRh-Ac, NRPA and NRPK reflect the true locations of cellular chelatable  $\text{Fe}^{3+}$ , not instead the locations of the sensors themselves. A ratiometric near infrared sensor, CR-PK, was presented in chapter 7. The CR-PK sensor shows NIR and visible emission in its spirolactam ring-open and closed forms, respectively. The reaction of CR-PK with  $\text{Fe}^{3+}$  leads to the ring opening of the spirocyclic moiety of CR-PK, causing a large red shift  $\sim 222$  nm of the absorption band. Cell imaging experiments with CR-PK revealed that CR-PK is evenly distributed in the cells except the nuclei region; however, chelatable labile  $\text{Fe}^{3+}$  ions are located in certain organelles in live bovine aortic endothelial cells (BAEC), fibroblast (ws1) cells and human neuroblastoma cell (SH-SY5Y). The ratiometric sensor CR-PK enables the direct determination of endogenous labile  $\text{Fe}^{3+}$  concentration in the cells for the first time, with a value of  $\sim 0.6$   $\mu\text{M}$  determined ( $0.43 \pm 0.23$   $\mu\text{M}$  by Method 1 and  $0.8 \pm 0.28$   $\mu\text{M}$  by Method 2) for ws1 cells,  $\sim 1.78$   $\mu\text{M}$  determined ( $2.18 \pm 0.35$

$\mu\text{M}$  by Method 1 and  $1.38 \pm 0.47 \mu\text{M}$  by Method 2 ) for BAEC cells, and  $\sim 3.05 \mu\text{M}$  determined ( $3.2 \pm 0.63 \mu\text{M}$  by Method 1 and  $3.1 \pm 0.53 \mu\text{M}$  by Method 2 ) for SH-SY5Y cells.

The various highly selective  $\text{Fe}^{3+}$  sensors developed in this work offer novel tools for molecular imaging of  $\text{Fe}^{3+}$  in live cells and live animals. The sensors, covering wavelength in the visible and near infrared regions with affinity to  $\text{Fe}^{3+}$  in micro to nanomolar levels, are ideal to image  $\text{Fe}^{3+}$  at subcellular resolution in real time, with the chelatable  $\text{Fe}^{3+}$  pools identified in various cell lines and live animals for the first time. Moreover, the ratiometric sensor enabled the determination of  $\text{Fe}^{3+}$  concentration in live cells for the first time. The  $\text{Fe}^{3+}$  sensors will contribute to a better understanding of the cell biology of iron and its related pathology and medical applications.

## TABLE OF CONTENTS

	Page
ACKNOWLEDGMENTS.....	v
ABSTRACT.....	vi
LIST OF TABLES.....	xv
LIST OF FIGURES.....	xvii
LIST OF SCHEMES.....	xxix
LIST OF ABBREVIATIONS.....	xxxi
CHAPTER	
1: INTRODUCTION.....	1
1.1 Iron in biology.....	1
1.2 Cellular Iron Pools.....	2
1.3 Iron Detection in Cells.....	4
1.3.1 Visualization of Labile Iron Pools.....	5
1.4 Fluorescence Quenching by Transition Metal Ions.....	20
1.5 Requirements for Fluorescent Sensors in Bioimaging.....	23
1.6 Objective and Organization of the Thesis.....	24
1.7 References.....	25
2: A RHODAMINE BASED TURN-ON FLUORESCENT SENSOR RPE FOR IMAGING LABILE Fe <sup>3+</sup> IN CELL.....	31
2.1 Introduction.....	31
2.2 Experimental.....	33
2.2.1 Materials and Reagents.....	33
2.2.2 Instrumentation.....	33
2.2.3 Synthesis.....	34
2.2.4 Procedures for Metal Ion Sensing.....	34

2.2.5 Cell Culture and Confocal Imaging.....	35
2.3 Results and Discussion .....	36
2.3.1 Design and Synthesis of RPE .....	36
2.3.2 Spectroscopic and Selectivity Studies.....	36
2.3.3 Binding Studies .....	39
2.3.4 Biological Imaging Studies .....	42
2.4 Conclusion.....	50
2.5 References .....	50
3: HEPTAMETHINE CYANINE BASED FLUORESCENT SENSORS FOR Fe <sup>3+</sup> .....	53
3.1 Introduction .....	53
3.2 Experimental Section .....	57
3.2.1 Materials and instruments.....	57
3.2.2 Synthesis and Characterization.....	58
3.3 Results and Discussion.....	61
3.3.1 Design and synthesis.....	61
3.3.2 Spectroscopic Properties .....	62
3.3.3 Binding Studies .....	65
3.3.4 Cell Studies.....	69
3.4 Conclusion.....	70
3.5 References .....	71
4: A NEAR INFRARED TURN-ON FLUORESCENT SENSOR NIRH-AC FOR DETECTION OF EXOGENOUS Fe <sup>3+</sup> IN LIVE CELLS AND ZEBRAFISH .....	73
4.1 Introduction .....	73
4.2 Experimental Section .....	74
4.2.1 Materials and Reagents .....	74

4.2.2 Instrumentation .....	75
4.2.3 Synthesis and Characterization.....	75
4.2.4 Procedures for Metal Ion Sensing.....	77
4.2.5 Binding Studies .....	78
4.2.6 Quantum Yield .....	79
4.2.7 Cell culture .....	80
4.2.8 Zebrafish Studies.....	81
4.2.9 Confocal Fluorescence Microscopy .....	81
4.3 Results and Discussion .....	82
4.3.1 Design and Synthesis of NIRh-Ac .....	82
4.3.2 Spectroscopic Studies .....	83
4.3.3 Binding Studies .....	86
4.3.4 Biological Imaging Studies .....	88
4.3.5 Imaging Fe <sup>3+</sup> in Zebrafish .....	99
4.4 Conclusion.....	100
4.5 References .....	101
5: TURN-ON NEAR-INFRARED FLUORESCENT SENSOR NRPA FOR IMAGING ENDOGENOUS Fe <sup>3+</sup> IN LIVE ORGANISMS.....	103
5.1 Introduction .....	103
5.2 Experimental Section .....	104
5.2.1 Materials and Reagents .....	104
5.2.2 Synthesis .....	104
5.2.3 Zebrafish Experiments .....	105
5.3 Results and discussion .....	106
5.3.1 Design and synthesis.....	106

5.3.2 Spectroscopic and Selectivity Studies.....	106
5.3.3 Binding Studies .....	109
5.3.4 Cell Studies.....	111
5.3.5 Zebrafish Studies.....	118
5. 4 Conclusion.....	120
5.5 References .....	121
<b>6: TURN-ON NEAR-INFRARED FLUORESCENT SENSORS NRP AND NRPK FOR IMAGING ENDOGENOUS Fe<sup>3+</sup> IN LIVE ORGANISMS .....</b>	<b>122</b>
6.1 Introduction .....	122
6.2 Experimental Part .....	123
6.2.1 Materials and Reagents .....	123
6.2.2 Synthesis .....	124
6.2.3 Binding Studies .....	125
6.2.4 Cell and Zebrafish Studies.....	126
6.3 Results and Discussion.....	127
6.3.1 Design and Synthesis .....	127
6.3.2 Spectroscopic and Selectivity Studies.....	128
6.3.3 Binding Studies .....	132
6.3.4 Cell Studies.....	137
6.3.5 Zebrafish Studies.....	142
6.4 Conclusions .....	143
6.5 References .....	144
<b>7: DEVELOPING RATIOMETRIC SENSORS FOR DETERMINATION OF IRON(III) CONCENTRATION IN LIVING SYSTEMS.....</b>	<b>145</b>
7.1 Introduction .....	145
7.2 Experimental.....	148

7.2.1 Materials and Instruments .....	148
7.2.2 Synthesis of CR-PK .....	149
7.2.3 Procedures for Metal Ion Sensing.....	150
7.2.4 Quantum Yield .....	151
7.2 .5 Cell culture .....	152
7.3 Results and Discussion .....	152
7.3.1 Design and synthesis.....	152
7.3.2 Spectroscopic and Selectivity Studies.....	153
7.3.3 Binding Studies .....	157
7.3.4 Cell Studies.....	159
7.4 Conclusions .....	171
7.5 References .....	171
APPENDICES	
A: OTHER SYNTHETIC ATTEMPTS TO MAKE IRON SENSORS.....	173
B: TABLE SUMMARIZING THE MAJOR PROPERTIES OF THE IRON SENSORS .....	181
C: DISTINGUISHING THE OXIDATION STATE OF IRON IN CELLS WITH THE SENSOR CR-PK .....	183
D: SPECTROSCOPIC DATA.....	186
BIBLIOGRAPHY .....	214



## LIST OF TABLES

Table	Page
7.1	Confocal fluorescence ratiometric images averages (a) BAEC cells incubated with CR-PK (10 $\mu$ M) for 30 min; (b) BAEC cells were first pre-incubated with ferric citrate(10 $\mu$ M) for 30 min, then incubated with CR-PK (10 $\mu$ M) for another 30 min; (c) BAEC cells were first pre-incubated with SIH (200 $\mu$ M) for 30 min, then incubated with CR-PK (10 $\mu$ M) for another 30 min. Confocal fluorescence ratiometric images are the average ratio in regions of interest.....163
7.2	Free Fe <sup>3+</sup> concentration in the cells .....167
7.3	Free Fe <sup>3+</sup> concentration in the organelles of the cells.....170
B.1	The major properties of the sensors .....182

## LIST OF FIGURES

Figure	Page
1.1 Fenton and Haber-Weiss Reactions.....	2
1.2 Dynamics of labile iron in cells and a schematic depiction of a mammalian cell showing the interconnections between the labile iron pools in various organelles.....	3
1.3 Molecular structures of a few sensors for Mg(II), Zn(II), and Ca(II).....	5
1.4 Chemical structures of Calceine and Phen Green SK.....	6
1.5 Structures of fluorescent sensors for Fe <sup>2+</sup> .....	7
1.6 Structures of Fe <sup>2+</sup> -selective fluorescent sensors applied in cells for bioimaging .....	8
1.7 Some recently published turn-off Fe <sup>3+</sup> fluorescent sensors (numbers in the parentheses show the year when they were published). .....	11
1.8 Chemical structures of some published iron(III)-selective turn-on fluorescent sensors(numbers in the parentheses show the year when they were published). .....	14
1.9 Some recently published ratiometric Fe <sup>3+</sup> fluorescent sensors (numbers in the parentheses show the year when they were published). .....	16
1.10 Structures of Fe <sup>3+</sup> -selective fluorescent sensors applied in cell for bioimaging (numbers in the parentheses show the year when they were published).....	19
1.11 (a) A simplified Jablonski diagram (b) Possible electron transitions during absorption for d-block complexes .....	20
1.12 Orbital scheme illustrating the quenching of a photo-excited fluorophore (FI*) by a metal center (M), via an M-to-FI* electron transfer process (eT). In this case, the metal center M displays oxidizing tendencies.....	21
1.13 Orbital scheme illustrating the quenching of a photo-excited fluorophore (FI*) by a metal center (M), via an FI* to M electron transfer process (eT).....	22
1.14 Orbital scheme illustrating the quenching of a photo-excited fluorophore F1* by a nearby metal center M via an electronic energy transfer (ET) mechanism .....	22
2.1 Absorption responses of 20 μM RPE to various metal ions (20 μM for Zn <sup>2+</sup> , Cr <sup>3+</sup> , Ni <sup>2+</sup> , Hg <sup>2+</sup> , Fe <sup>3+</sup> , Mn <sup>2+</sup> , Ag <sup>+</sup> , Pb <sup>2+</sup> , Fe <sup>2+</sup> , Cu <sup>+</sup> , Cu <sup>2+</sup> , and Co <sup>2+</sup> ; 100 μM for Na <sup>+</sup> , K <sup>+</sup> , Mg <sup>2+</sup> and Ca <sup>2+</sup> ) in ACN/Tris-HCl buffer (10 mM, pH 7.3, v/v 2:1. ....	37

2.2	Fluorescence response ( $\lambda_{\text{Ex}}/\lambda_{\text{Em}}$ 510/580 nm, filter 515 nm) of 20 $\mu\text{M}$ RPE to various metal ions (20 $\mu\text{M}$ for $\text{Ni}^{2+}$ , $\text{Cu}^+$ , $\text{Cu}^{2+}$ , $\text{Zn}^{2+}$ , $\text{Pb}^{2+}$ , $\text{Fe}^{2+}$ , $\text{Fe}^{3+}$ , $\text{Cr}^{3+}$ , $\text{Hg}^{2+}$ , $\text{Mn}^{2+}$ , $\text{Ag}^+$ , and $\text{Co}^{2+}$ ; 100 $\mu\text{M}$ for $\text{K}^+$ , $\text{Na}^+$ , $\text{Ca}^{2+}$ , and $\text{Mg}^{2+}$ ) in the ACN/Tris buffer .....38	38
2.3	Variation of fluorescence intensity (585 nm) of RPE and RPE+Fe(III) (20 $\mu\text{M}$ each) at various pH values in ACN/ $\text{H}_2\text{O}$ (2/1, v/v) solution .....38	38
2.4	Fluorescence responses of 20 $\mu\text{M}$ RPE to the presence of various metal ions (gray bar) and the subsequent addition of $\text{Fe}^{3+}$ (black bar) in the ACN/Tris buffer; the bars represent the fluorescence intensity at 585 nm. ....39	39
2.5	Job plot. The total concentrations of RPE and $\text{Fe}^{3+}$ were kept constant at 20 $\mu\text{M}$ and the absorption intensity was measured at 559 nm in the ACN/Tris buffer.....40	40
2.6	Titration of 20 $\mu\text{M}$ RPE with increasing concentrations of $\text{FeCl}_3$ (0, 2, 4, 6, 10, 12, 14, 16, 18, 20, 28, 36, 44,52, 60, and 80 $\mu\text{M}$ , respectively) in ACN/Tris-HCl buffer (10 mM, pH 7.32, v/v 2:1) .....41	41
2.7	Treatment of 40 $\mu\text{M}$ RPE- $\text{Fe}^{3+}$ complex with increasing concentration of EDTA (0, 4, 8, 12, 16, 20, 24, 28, 32, and 40 $\mu\text{M}$ , from top to bottom) in ACN/Tris-HCl buffer (10 mM, pH 7.32, v/v 2:1) .....42	42
2.8	Confocal microscopy images of live Human SH-SY5Y neuroblastoma cells treated with 10 $\mu\text{M}$ RPE in 1:1 mixture of Eagles Minimal Essential medium (ATCC) and Ham's F12 medium (ATCC) for 5, 10, 15, 20, 25, and 30 min. Fluorescence intensity collected at 547-703 nm .....43	43
2.9	Confocal microscopy images of live human SH-SY5Y neuroblastoma cells treated with RPE (10 $\mu\text{M}$ , 30 min) and Hoechst 33258 (2 $\mu\text{g}/\text{mL}$ , 30 min) in a 1:1 mixture of Eagles Minimal Essential medium (ATCC) and Ham's F12 medium (ATCC) for 5, 10, 15, 20, 25, and 30 min. Fluorescence intensity collected at 547-703 nm (for RPE) and 426-535 nm (for Hoechst 33258) .....44	44
2.10	Confocal microscopy images (with DIC) of live human SH-SY5Y neuroblastoma cells treated with (a) 10 $\mu\text{M}$ RPE sensor after 30 min incubation (b) the cells were then incubated with $\text{Fe}^{3+}$ (20 $\mu\text{M}$ Fe(8-HQ)) for 30 min. The brighter and more widely distributed fluorescence signals in (b) suggest elevated $\text{Fe}^{3+}$ levels in $\text{Fe}^{3+}$ -loaded human SH-SY5Y cells. Fluorescence intensity was collected at 547-703 nm (for RPE). .....45	45
2.11	Confocal microscopy images (with DIC) of live human SH-SY5Y neuroblastoma cells treated with (A) 5 $\mu\text{M}$ RPE sensor after 40 min incubation (B) the cells were then incubated with 100 $\mu\text{M}$ $\text{Fe}^{3+}$ -chelator pyridoxalisonicotinoyl hydrazone (PIH) for 4 hrs (C) after overnight incubation with 100 $\mu\text{M}$ PIH (D) Bar chart of the mean intensity of (A), (B) and (C). Fluorescence intensity was collected at 547-703 nm (for RPE).....46	46

2.12	Confocal microscopy images (with DIC) of live human SH-SY5Y neuroblastoma cells with prior iron depletion by 200 $\mu\text{M}$ cell permeable $\text{Fe}^{3+}$ -chelator salicylaldehyde isonicotinoyl hydrazone (SIH) for overnight and then treated with RPE (10 $\mu\text{M}$ ) in 1:1 mixture of Eagles Minimal Essential medium (ATCC) and Ham's F12 medium (ATCC) for 5, 10, 15, 20, 25, and 30 min (time in seconds was shown in each panel).....	47
2.13	Representative confocal images of intracellular colocalization studies of 10 $\mu\text{M}$ RPE incubated with live human SH-SY5Y cells co-labeled with MitoTracker Green (100 nM) and LysoTracker Blue DND-22 (50 nM).....	48
2.14	Representative confocal microscopy images of intracellular colocalization studies of 10 $\mu\text{M}$ RPE incubated with $\text{Fe}^{3+}$ -loaded human SH-SY5Y cells (pre-implemented with 10 $\mu\text{M}$ $\text{Fe}^{3+}$ ) co-labeled with MitoTracker Green FM (100 nM, incubated for 30 min) and LysoTracker Blue DND-22 (50 nM, incubated for 120 min).....	49
3.1	General structure of carbocyanine dyes.....	55
3.2	General structure of heptamethine cyanine dyes substituted at the meso-position by halogen group.....	55
3.3	Suggested addition/elimination mechanism of heptamethine amino cyanine dyes.....	56
3.4	Some heptamethine cyanine based fluorescent sensors which were designed for $\text{Fe}^{3+}$ (see Appendix A for experimental details), only IRPE shows response to $\text{Fe}^{3+}$ .....	57
3.5	(a) Absorbance response of 5 $\mu\text{M}$ IRPE to increasing concentration of $\text{Fe}^{3+}$ (top to bottom, 0, 0.05, 0.1, 0.15, 0.2, 0.3, 0.5, 0.7, 0.8, 0.9, 1.0, 1.2, 1.5, and 2 equiv in ACN/HEPES buffer (10 mM, pH 7.3, v/v 1:1) (b) UV-vis spectra of 3 $\mu\text{M}$ IRPE to various metal ions (3 $\mu\text{M}$ for $\text{Zn}^{2+}$ , $\text{Cr}^{3+}$ , $\text{Ni}^{2+}$ , $\text{Hg}^{2+}$ , $\text{Fe}^{3+}$ , $\text{Mn}^{2+}$ , $\text{Ag}^+$ , $\text{Pb}^{2+}$ , $\text{Fe}^{2+}$ , $\text{Cu}^+$ , $\text{Cu}^{2+}$ and $\text{Co}^{2+}$ ; 15 $\mu\text{M}$ for $\text{Na}^+$ , $\text{K}^+$ , $\text{Mg}^{2+}$ , and $\text{Ca}^{2+}$ ) in ACN/HEPES buffer (10 mM, pH 7.0, v/v 1:1).....	62
3.6	Color changes of 3 $\mu\text{M}$ IRPE with various metal ions (3 $\mu\text{M}$ for $\text{Zn}^{2+}$ , $\text{Cr}^{3+}$ , $\text{Ni}^{2+}$ , $\text{Hg}^{2+}$ , $\text{Fe}^{3+}$ , $\text{Pb}^{2+}$ , $\text{Fe}^{2+}$ , $\text{Cu}^{2+}$ ; 20 $\mu\text{M}$ for $\text{K}^+$ ) in ACN/HEPES buffer (10 mM, pH 7.0, v/v 1:1).....	63
3.7	(a) Time course plot of fluorescent response of IRPE (5 $\mu\text{M}$ ) in ACN/HEPES buffer (10 mM, pH 7.0, v/v 1:1) (b) Time course plot of ratiometric fluorescent responses of IRPE (5 $\mu\text{M}$ ) and $\text{FeCl}_3 \cdot 6\text{H}_2\text{O}$ (5 $\mu\text{M}$ ) in ACN/HEPES buffer (10 mM, pH 7.0, v/v 1:1).....	63
3.8	(a) Fluorescence response of 5 $\mu\text{M}$ IRPE to increasing concentration of $\text{Fe}^{3+}$ (top to bottom, 0, 0.05, 0.1, 0.15, 0.2, 0.3, 0.5, 0.7, 0.8, 0.9, 1.0, 1.5, and 2.0 equiv in ACN/HEPES buffer (10 mM, pH 7.3, v/v 1:1), ( $\lambda_{\text{ex}}$ 650 nm) (b) Fluorescence response of 3 $\mu\text{M}$ IRPE to increasing concentration of $\text{Fe}^{3+}$ .....	64

3.9	Fluorescence responses $F_{580}/F_{760}$ of 3 $\mu\text{M}$ IRPE ( $\lambda_{\text{ex}}=520\text{ nm}$ ) to the presence of various metal ions (gray) and the subsequent addition of $\text{Fe}^{3+}$ (black bar) in the ACN/HEPES buffer (10 mM, pH 7.3, v/v 1:1) .....	65
3.10	(a) Job's plot of the complexation between IRPE and $\text{Fe}^{3+}$ , $[\text{IRPE}] + [\text{Fe}^{3+}] = 5\ \mu\text{M}$ in /HEPES buffer (10 mM, pH 7.0, v/v 1:1); (b) Titration of 3 $\mu\text{M}$ IRPE with increasing concentrations of $\text{FeCl}_3$ (0.5, 1,1.5, 2.0, 2.5, 3.0, 3.5, 4.0, 4.5, 5.0, 5.5, 6.0, 7.5, 10.0, 12.5, and 15 $\mu\text{M}$ , respectively) in ACN /HEPES buffer (10 mM, pH 7.0, v/v 1:1). The absorption intensities increased at 523 nm and decreased at 664 nm .....	67
3.11	ESI-MS spectrum of the solution of IRPE with $\text{FeCl}_3$ (1 $\mu\text{M}$ sensor and excess $\text{Fe}^{3+}$ in ACN/ $\text{H}_2\text{O}$ ). .....	67
3.12	(a) Ratiometric fluorescent responses of IRPE and IRPE+Fe(III) (3 $\mu\text{M}$ each) at various pH values in ACN/ $\text{H}_2\text{O}$ (1/1, v/v) solution. pH was adjusted by HCl (0.1 M) and NaOH (0.1 M) (b) Reversibility of IRPE (3 $\mu\text{M}$ ) to $\text{Fe}^{3+}$ ions by EDTA ((a) free IRPE (3 $\mu\text{M}$ ), (d) IRPE + 1equiv of $\text{Fe}^{3+}$ , (c) IRPE + 1 equiv of $\text{Fe}^{3+}$ + 1 equiv of EDTA, (b) IRPE + 1 equiv of $\text{Fe}^{3+}$ + 2 equiv of EDTA).....	68
3.13	Confocal microscopy images (with DIC) of B16-F melanoma cells treated with (a,c) 10 $\mu\text{M}$ CR-PK sensor after 30 min incubation; (b,d) the cells were incubated with $\text{Fe}^{3+}$ (10 $\mu\text{M}$ ) for 8 h then incubate with the sensor for 30 min (Excitation wavelength was 633 nm for a,b, 514 for c,d; fluorescence emission collected 520-620 nm for blue channels, 660-750 nm for red channels) .....	70
4.1	Absorption responses of 20 $\mu\text{M}$ NIRh-Ac to various metal ions (20 $\mu\text{M}$ for $\text{Zn}^{2+}$ , $\text{Cr}^{3+}$ , $\text{Ni}^{2+}$ , $\text{Hg}^{2+}$ , $\text{Fe}^{3+}$ , $\text{Mn}^{2+}$ , $\text{Ag}^+$ , $\text{Pb}^{2+}$ , $\text{Fe}^{2+}$ , $\text{Cu}^+$ , $\text{Cu}^{2+}$ , and $\text{Co}^{2+}$ ; 100 $\mu\text{M}$ for $\text{Na}^+$ , $\text{K}^+$ , $\text{Mg}^{2+}$ and $\text{Ca}^{2+}$ ) in ACN/Tris-HCl buffer (10 mM, pH 7.3, v/v 1:1).....	83
4.2	Color changes of 20 $\mu\text{M}$ NIRh-Ac with various metal ions.....	83
4.3	Fluorescence response ( $\lambda_{\text{ex}}$ 690nm,) of 20 $\mu\text{M}$ NIRh-Ac to various metal ions (20 $\mu\text{M}$ for $\text{Ni}^{2+}$ , $\text{Cu}^+$ , $\text{Cu}^{2+}$ , $\text{Zn}^{2+}$ , $\text{Pb}^{2+}$ , $\text{Fe}^{2+}$ , $\text{Fe}^{3+}$ $\text{Cr}^{3+}$ , $\text{Hg}^{2+}$ , $\text{Mn}^{2+}$ , $\text{Ag}^+$ , and $\text{Co}^{2+}$ ; 100 $\mu\text{M}$ for $\text{K}^+$ , $\text{Na}^+$ , $\text{Ca}^{2+}$ , and $\text{Mg}^{2+}$ ) in the ACN/Tris buffer(10 mM, pH 7.3, v/v 1:1 .....	84
4.4	Fluorescence responses of 20 $\mu\text{M}$ NIRh-Ac to the presence of various metal ions (gray bar) and the subsequent addition of $\text{Fe}^{3+}$ (black bar) in the ACN/Tris buffer; the bars represent the fluorescence intensity at 735 nm .....	85
4.5	Fluorescence responses of 20 $\mu\text{M}$ NIRh-Ac to the presence of various metal ions (gray bar) and the subsequent addition of $\text{Fe}^{3+}$ (black bar) in the ACN/Tris buffer; the bars represent the fluorescence intensity at 735 nm. ....	86
4.6	Titration of 20 $\mu\text{M}$ NIRh-Ac with increasing concentrations of $\text{FeCl}_3$ (2, 4, 6, 10, 12, 14, 16, 18, 20, 28, 36, 44, 52, and 60 $\mu\text{M}$ , respectively) in ACN/Tris-HCl buffer (10 mM, pH 7.3, v/v 1:1). Inset, a plot of fluorescent emissions at 713 nm versus the ratio of $[\text{Fe}^{3+}]/[\text{NIRh-Ac}]$ . .....	87

4.7	(a) Job's plot. The total concentrations of NIRh-Ac and Fe <sup>3+</sup> were kept at constant 20 μM and the absorption intensity was measured at 713 nm in the ACN/Tris buffer (10 mM, pH 7.3, v/v 1:1) (b) Treatment of 20 μM NIRh-Ac-Fe <sup>3+</sup> complex with increasing concentration of EDTA (0 to 40 μM, from top to bottom) in ACN/Tris-HCl buffer (10 mM, pH 7.3, v/v 1:1) (c) ESI-MS spectrum of the solution of NIRh-Ac with FeCl <sub>3</sub> (1 μM sensor and 1 μM Fe <sup>3+</sup> in ACN/H <sub>2</sub> O). ....	87
4.8	Confocal microscopy images (with DIC) of live human SH-SY5Y neuroblastoma cells and Fibroblast cells (WS1) treated with (a) human SH-SY5Y neuroblastoma cells were incubated 20 μM NIRh-Ac (30 min) (b) human SH-SY5Y neuroblastoma cells were pre-incubated with 20 μM Fe <sup>3+</sup> for 8 h then 20 μM NIRh-Ac sensor was added and image were taken after 30 min incubation (c) Fe <sup>3+</sup> -chelator SIH (100 μM) was then added and incubated for over night (d) Bar chart of fluorescent intensity of (a), (b) and(c), (e) human fibroblast cells (ws1) were incubated with 20 μM NIRh-Ac (30 min), (f) Fibroblast cells (ws1) were pre-incubated with 20 μM Fe <sup>3+</sup> for 8 h then the sensor was added. (g) Fe <sup>3+</sup> -chelator SIH (100 μM) was then added and incubated for overnight. (g) Bar chart of fluorescent intensity of (e), (f) and (g). (Fluorescence intensity was collected at 700-800 nm (for NIRh-Ac)). ....	89
4.9	Representative confocal microscopy images of intracellular colocalization studies of 10 μM NIRh-Ac incubated with Fe <sup>3+</sup> -loaded human SH-SY5Y cells (pre-incubated with 10 μM Fe <sup>3+</sup> ) co-labeled with MitoTracker Green FM (100 nM, incubated for 30 min) and LysoTracker Blue DND-22 (50 nM, incubated for 120 min) .....	91
4.10	Representative confocal microscopy images of intracellular colocalization studies of 20 μM NIRh-Ac incubated with Fe <sup>3+</sup> -loaded fibroblast cells (ws1) (pre-incubated with 20 μM Fe <sup>3+</sup> (FeCl <sub>3</sub> incubated for overnight) co-labeled with MitoTracker Green FM (100 nM, incubated for 30 min) and LysoTracker Blue DND-22 (50 nM, incubated for 120 min) .....	92
4.11	Subcellular kinetic experiments for NIRh-Ac-Fe <sup>3+</sup> in live fibroblast cells (ws1) .....	96
4.12	Colored areas changing at different time in Figure 4.12 (Area of the all color dots were measured and assumed that the total area is 100%, then each color area was calculated as a percentage (A <sub>x</sub> /A <sub>t</sub> )) .....	97
4.13	Hypothetical schematic of one possible cellular distribution process for free iron (III) ions in live fibroblast cells .....	98
4.14	Confocal microscopy images (with DIC) Fibroblast cells (ws1) treated with (a) NIRh-Ac (10μM), Mito tracker green (100 nM), and lyso tracker blue (50 nM) for 30 min (b) 1 min (c) 2 min (d) 3 min after Fe <sup>3+</sup> ions added (b, c, and d are the zoomed images of the area shown in a) .....	99

4.15	Confocal microscopy images of 6 day old zebrafish larvae (a) Zebrafish larva was incubated with 5 $\mu\text{M}$ NIRh-Ac for 30 min (b) Zebrafish larva incubated with 10 $\mu\text{M}$ (c) 50 $\mu\text{M}$ $\text{FeCl}_3$ then 5 $\mu\text{M}$ NIRh-Ac was added and incubated for 30 min. ....	100
5.1	Absorption responses (a) and Fluorescence responses (b) of 20 $\mu\text{M}$ NRPA to various metal ions (20 $\mu\text{M}$ for $\text{Zn}^{2+}$ , $\text{Cr}^{3+}$ , $\text{Ni}^{2+}$ , $\text{Hg}^{2+}$ , $\text{Fe}^{3+}$ , $\text{Mn}^{2+}$ , $\text{Ag}^+$ , $\text{Pb}^{2+}$ , $\text{Fe}^{2+}$ , $\text{Cu}^+$ , $\text{Cu}^{2+}$ , and $\text{Co}^{2+}$ ; 100 $\mu\text{M}$ for $\text{Na}^+$ , $\text{K}^+$ , $\text{Mg}^{2+}$ and $\text{Ca}^{2+}$ ) in ACN/Tris-HCl buffer (10 mM, pH 7.3, v/v 2:1).....	107
5.2	Fluorescence intensity versus increasing concentration of NRPA- $\text{Fe}^{3+}$ (1:1) in ACN/Tris-HCl buffer (10 mM, pH 7.3, v/v 2:1). Detection limit of 0.1 $\mu\text{M}$ was obtained from the plot .....	108
5.3	Fluorescence responses of 20 $\mu\text{M}$ NRPA to the presence of various metal ions (gray bar) and the subsequent addition of $\text{Fe}^{3+}$ (black bar) in the ACN/Tris buffer (10 mM, pH 7.3, v/v 2:1).The bars represent the fluorescence intensity at 750 nm .....	108
5.4	(a) Absorption of NRPA and NRPA + $\text{Fe}^{3+}$ (20 $\mu\text{M}$ , the absorption intensity was measured at 710 nm) at various pH values in ACN/ $\text{H}_2\text{O}$ (2/1, v/v) solution (b) Variation of fluorescence intensity (750 nm) of NRPA and NRPA+ $\text{Fe}(\text{III})$ (20 $\mu\text{M}$ each) at various pH values in ACN/ $\text{H}_2\text{O}$ (2/1, v/v) solution .....	109
5.5	Titration of 20 $\mu\text{M}$ NRPA with increasing concentrations of $\text{FeCl}_3$ (2, 4, 6, 10, 12, 14, 16, 18, 20, 28, 36, 44, 52, 60, and 80 $\mu\text{M}$ , respectively) in ACN/Tris-HCl buffer (10 mM, pH 7.3, v/v 2:1). The absorption intensities were measured at 710 nm. ....	110
5.6	(a) Job plot. The total concentrations of NRPA and $\text{Fe}^{3+}$ were kept at constant 25 $\mu\text{M}$ and the absorption intensity was measured at 710 nm in the ACN/Tris buffer (b) Treatment of 40 $\mu\text{M}$ NRPA- $\text{Fe}^{3+}$ complex with increasing concentration of EDTA (0 to 40 $\mu\text{M}$ , from top to bottom) in ACN/Tris-HCl buffer (10 mM, pH 7.3, v/v 2:1) .....	111
5.7	Confocal microscopy images (with DIC) of live human SH-SY5Y neuroblastoma cells treated with (a) 20 $\mu\text{M}$ NRPA sensor after 30 min incubation (b) the cells were then incubated with $\text{Fe}^{3+}$ (20 $\mu\text{M}$ $\text{Fe}(\text{8-HQ})$ ) for 30 min. The brighter and more widely distributed fluorescence signals in (b) suggest elevated $\text{Fe}^{3+}$ levels in $\text{Fe}^{3+}$ -loaded human SH-SY5Y cells. Fluorescence intensity was collected at 680-750 nm (for NRPA). (DIC image of cells with 10 $\mu\text{m}$ scale bar.).....	112

5.8	Confocal microscopy images (with DIC) of live human SH-SY5Y neuroblastoma cells with prior iron depletion by 100 $\mu\text{M}$ cell permeable $\text{Fe}^{3+}$ -chelator salicylaldehyde isonicotinoyl hydrazone (SIH) for overnight and then treated with NRPA (10 $\mu\text{M}$ ) in 1:1 mixture of Eagles Minimal Essential medium (ATCC) and Ham's F12 medium (ATCC). (a) DIC image of cells with 10 $\mu\text{m}$ scale bar (b) 10 $\mu\text{M}$ NRPA sensor after 30 min incubation (c) 100 $\mu\text{M}$ cell permeable $\text{Fe}^{3+}$ -chelator salicylaldehyde isonicotinoyl hydrazone (SIH) for overnight and then treated with NRPA. Fluorescence intensity was collected at 680-750 nm (for NRPA).....	113
5.9	Representative confocal images of intracellular colocalization studies of 10 $\mu\text{M}$ NRPA incubated with live human SH-SY5Y cells co-labeled with MitoTracker Green (100 nM) and LysoTracker Blue DND-22 (50 nM).....	114
5.10	Representative confocal microscopy images of intracellular colocalization studies of 10 $\mu\text{M}$ NRPA incubated with $\text{Fe}^{3+}$ -loaded human SH-SY5Y cells (pre-incubated with 10 $\mu\text{M}$ $\text{Fe}^{3+}$ ) co-labeled with MitoTracker Green FM (100 nM, incubated for 30 min) and LysoTracker Blue DND-22 (50 nM, incubated for 120 min).....	115
5.11	Confocal microscopy images (with DIC) of live human skin fibroblast cells (ws1) (a) DIC image of cells with 10 $\mu\text{m}$ scale bar (a) 10 $\mu\text{M}$ NRPA sensor after 30 min incubation (b) Fibroblast cells (ws1) were then incubated with 20 $\mu\text{M}$ $\text{Fe}^{3+}$ for 8 h then the sensor was added (c) 100 $\mu\text{M}$ SIH for overnight and then treated with NRPA (d) Bar chart of fluorescent intensity of A, B, C. (Fluorescence intensity was collected at 680-750 nm (for NRPA)).....	116
5.12	Representative confocal images of intracellular colocalization studies of 10 $\mu\text{M}$ NRPA incubated with live human ws1 cells co-labeled with MitoTracker Green (100 nM) and LysoTracker Blue DND-22 (50 nM).....	117
5.13	Representative confocal microscopy images of intracellular colocalization studies of 20 $\mu\text{M}$ NRPA incubated with $\text{Fe}^{3+}$ -loaded fibroblast cells (ws1) (pre-incubated with 20 $\mu\text{M}$ $\text{Fe}^{3+}$ ) co-labeled with MitoTracker Green FM (100 nM, incubated for 30 min).....	118
5.14	Confocal microscopy images of 3 and 6 day old zebrafish larvae (a,e) Zebrafish only (b,f) Zebrafish larva was incubated with 10 $\mu\text{M}$ NRPA for 30 min (c,g) Zebrafish larva incubated with 10 $\mu\text{M}$ and (d,h) incubated with 40 $\mu\text{M}$ $\text{FeCl}_3$ for 3 days then 10 $\mu\text{M}$ NRPA was added and incubated for 30 min. ....	120
6.1	(a) Absorption responses and (b) Fluorescence response and (c) Color changes of 25 $\mu\text{M}$ NRP with various metal ions (25 $\mu\text{M}$ for $\text{Zn}^{2+}$ , $\text{Cr}^{3+}$ , $\text{Ni}^{2+}$ , $\text{Hg}^{2+}$ , $\text{Fe}^{3+}$ , $\text{Mn}^{2+}$ , $\text{Ag}^+$ , $\text{Pb}^{2+}$ , $\text{Fe}^{2+}$ , $\text{Cu}^+$ , $\text{Cu}^{2+}$ , and $\text{Co}^{2+}$ ; 100 $\mu\text{M}$ for $\text{Na}^+$ and $\text{Ca}^{2+}$ ) in ACN/Tris-HCl buffer (10 mM, pH 7.2, v/v 3:1).....	129



6.2	Fluorescence responses of 25 $\mu\text{M}$ NRPK to the presence of various metal ions (gray bar) and the subsequent addition of $\text{Fe}^{3+}$ (black bar) in the ACN/Tris buffer (10 mM, pH=7.3, v/v 3;1). The bars represent the fluorescence intensity at 740 nm. ....	130
6.3	(a) Variation of absorption (715 nm) of NRPK and NRPK + $\text{Fe}^{3+}$ (25 $\mu\text{M}$ each) at various pH values in ACN/ $\text{H}_2\text{O}$ (3/1, v/v) solution (b) Variation of intensity (740 nm) of NRPK and NRPK + $\text{Fe}^{3+}$ (25 $\mu\text{M}$ each) at various pH values in ACN/ $\text{H}_2\text{O}$ (3/1, v/v) solution. pH's were adjusted by adding HCl or NaOH .....	131
6.4	(a) Absorption responses and (b) Fluorescence response, and (c) Color changes of 25 $\mu\text{M}$ NRP with various metal ions (25 $\mu\text{M}$ for $\text{Zn}^{2+}$ , $\text{Cr}^{3+}$ , $\text{Ni}^{2+}$ , $\text{Hg}^{2+}$ , $\text{Fe}^{3+}$ , $\text{Mn}^{2+}$ , $\text{Ag}^+$ , $\text{Pb}^{2+}$ , $\text{Fe}^{2+}$ , $\text{Cu}^+$ , $\text{Cu}^{2+}$ , and $\text{Co}^{2+}$ ; 100 $\mu\text{M}$ for $\text{Na}^+$ and $\text{Ca}^{2+}$ ) in ACN/Tris buffer (10 mM, pH 7.3, v/v 3;1) .....	132
6.5	Titration of 25 $\mu\text{M}$ NRPK with increasing concentrations of $\text{FeCl}_3$ (2.5, 5, 7.5, 10, 12.5, 15, 20, 25, 31.25, 37.5, and 50 $\mu\text{M}$ , respectively) in ACN/Tris-HCl buffer (10 mM, pH 7.2, v/v 3:1). Inset, a plot of fluorescent emissions at 715 nm versus the ratio of $[\text{Fe}^{3+}]/[\text{sensor}]$ .....	133
6.6	(a) Job's plot. The total concentrations of NRPK and $\text{Fe}^{3+}$ were kept at constant 50 $\mu\text{M}$ and the absorption intensity was measured at 715 nm in ACN/Tris-HCl buffer (10 mM, pH 7.2, v/v 3:1) (b) Treatment of 25 $\mu\text{M}$ NRPK- $\text{Fe}^{3+}$ complex with increasing concentration of EDTA (0 to 50 $\mu\text{M}$ , from top to bottom) in ACN/Tris-HCl buffer (10 mM, pH 7.2, v/v 3:1).....	134
6.7	Titration of 25 $\mu\text{M}$ NRP with increasing concentrations of $\text{FeCl}_3$ (2.5, 5, 7.5, 10, 12.5, 15, 20, 25, 31.25, 37.5, and 50 $\mu\text{M}$ respectively) in ACN/Tris-HCl buffer (10 mM, pH 7.2, v/v 3:1). ....	135
6.8	(a) Job's plot. The total concentrations of NRP and $\text{Fe}^{3+}$ were kept at constant 50 $\mu\text{M}$ and the absorption intensity was measured at 714 nm in ACN/Tris-HCl buffer (10 mM, pH 7.2, v/v 3:1) (b) Treatment of 25 $\mu\text{M}$ NRP-35 $\mu\text{M}$ $\text{Fe}^{3+}$ complex with increasing concentration of EDTA (0 to 50 $\mu\text{M}$ , from top to bottom) in ACN/Tris-HCl buffer (10 mM, pH 7.2, v/v 3:1).....	136
6.9	Confocal microscopy images (with DIC) of BAEC treated with (a) cell only (b) the sensor after 30 min incubation (c) the cells were then incubated with 10 $\mu\text{M}$ $\text{Fe}^{3+}$ for 30 min then the sensor was added. (d) the cells were then incubated with 10 $\mu\text{M}$ $\text{Fe}^{3+}$ for 30 min then the sensor was added the SIH for overnight (e) the cells were incubated with SIH ( $\text{Fe}^{3+}$ -chelator) (100 $\mu\text{M}$ ) overnight then sensor was added. (f) Bar chart of the mean intensity of (a), (b), (c), (d) and (e). Fluorescence intensity was collected at 680-750 nm (Excited at 633 nm). ....	138
6.10	Representative confocal images of intracellular colocalization studies of 10 $\mu\text{M}$ NRPK incubated with live BAEC cells co-labeled with MitoTracker Green (100 nM) and LysoTracker Blue DND-22 (50 nM) .....	139

6.11	Representative confocal microscopy images of intracellular colocalization studies of 10 $\mu\text{M}$ NRPK incubated with $\text{Fe}^{3+}$ -loaded BAEC cells (pre-incubated with 10 $\mu\text{M}$ $\text{Fe}^{3+}$ ) co-labeled with MitoTracker Green FM (100 nM, incubated for 30 min) and LysoTracker Blue DND-22 (50 nM, incubated for 120 min).....	140
6.12	Representative confocal microscopy images of intracellular colocalization studies of 10 $\mu\text{M}$ NRPK incubated with $\text{Fe}^{3+}$ -loaded human SH-SY5Y cells (pre-incubated with 10 $\mu\text{M}$ $\text{Fe}^{3+}$ ) co-labeled with MitoTracker Green FM (100 nM, incubated for 30 min) and LysoTracker Blue DND-22 (50 nM, incubated for 120 min).....	141
6.13	Confocal microscopy images of 3 and 6 day old zebrafish larvae (a,e) Zebrafish only (b,f) Zebrafish larva was incubated with 10 $\mu\text{M}$ NRPK for 30 min (c,g) Zebrafish larva incubated with 10 $\mu\text{M}$ and (d,h) incubated with 40 $\mu\text{M}$ $\text{FeCl}_3$ for 3 days then 10 $\mu\text{M}$ NRPK was added and incubated for 30 min. ....	143
7.1	Structure of the ratiometric CR-based fluorescent sensors (1) cysteine and homocysteine-selective and (2) $\text{Hg}^{2+}$ -selective sensors.....	147
7.2	(a) Absorbance response of 10 $\mu\text{M}$ CR-PK to increasing concentration of $\text{Fe}^{3+}$ (top to bottom, 0, 0.05, 0.1, 0.15, 0.2, 0.3, 0.5, 0.7, 0.8, 0.9, 1.0, 1.2, 1.5, and 2 equiv in EtOH/HEPES buffer (10 mM, pH 7.4, v/v 1:4) (b) UV-vis spectra of 20 $\mu\text{M}$ CR-PK to various metal ions (10 $\mu\text{M}$ for $\text{Zn}^{2+}$ , $\text{Cr}^{3+}$ , $\text{Ni}^{2+}$ , $\text{Hg}^{2+}$ , $\text{Fe}^{3+}$ , $\text{Mn}^{2+}$ , $\text{Ag}^+$ , $\text{Pb}^{2+}$ , $\text{Fe}^{2+}$ , $\text{Cu}^+$ , $\text{Cu}^{2+}$ , and $\text{Co}^{2+}$ ; 15 $\mu\text{M}$ for $\text{Na}^+$ , $\text{K}^+$ , $\text{Mg}^{2+}$ , and $\text{Ca}^{2+}$ ) in EtOH/HEPES buffer (10 mM, pH 7.4, v/v 4:1). ....	154
7.3	(a) Fluorescence response of 10 $\mu\text{M}$ CR-PK to increasing concentration of $\text{Fe}^{3+}$ ( $\lambda_{\text{Ex}}$ 650 nm) (b) Fluorescence response of 10 $\mu\text{M}$ CR-PK to increasing concentration of $\text{Fe}^{3+}$ ( $\lambda_{\text{Ex}}$ 450 nm) (top to bottom, 0, 0.125, 0.250, 0.375, 0.50, 0.625, 0.750, 0.875, 1.0, 1.25, eqv. in EtOH/HEPES buffer (10 mM, pH 7.4, v/v 1:4).....	155
7.4	Fluorescence responses $F_{704}/F_{470}$ of 10 $\mu\text{M}$ CR-PK ( $\lambda_{\text{ex}} = 450 \text{ nm}$ ) to the presence of various metal ions (gray bars) and the subsequent addition of $\text{Fe}^{3+}$ (black bar) in the EtOH/HEPES buffer (10 mM, pH 7.4, v/v 1:4).....	156
7.5	(a) Variation of absorption and (b) fluorescent intensity of CR-PK in response to different pH.....	157
7.6	(a) Job's plot of the complexation between CR-PK and $\text{Fe}^{3+}$ [ $\text{CR-PK}$ ] + [ $\text{Fe}^{3+}$ ] = 20 $\mu\text{M}$ in EtOH/HEPES buffer (10 mM, pH 7.4, v/v 1:4) (b) Titration of 10 $\mu\text{M}$ CR with increasing concentrations of $\text{FeCl}_3$ (1.0, 2.0, 3.0, 4.0, 5.0, 6.0, 7.0, 8.0, 9.0, 10.0, 11.0, 15.0, and 20 $\mu\text{M}$ respectively) in EtOH/HEPES buffer (10 mM, pH 7.4, v/v 1:4). The absorption intensities increased at 647 nm and decreased at 425 nm. ....	158
7.7	Reversibility of CR-PK (10 $\mu\text{M}$ ) to $\text{Fe}^{3+}$ ions by EDTA (a) CR-PK + 1equiv of $\text{Fe}^{3+}$ (b) CR-PK + 1 equiv of $\text{Fe}^{3+}$ + 2 equiv of EDTA (c) free CR-PK (10 $\mu\text{M}$ ) .....	158

7.8	Confocal microscopy images of live aortic endothelial cells (BAEC) cells treated with different concentration of Fe <sup>3+</sup> (ferric citrate) for 30 min, and then incubated with NRPA (20 μM) in 1:1 mixture of Eagles Minimal Essential medium (ATCC) and Ham's F12 medium (ATCC). Fluorescence intensity collected at 680-750 nm (NRPA was excited at 633 nm).....	161
7.9	Confocal microscopy images (with DIC) of BAEC treated with (a,d) 10 μM CR-PK sensor after 30 min incubation (b,e) the cells were incubated with Fe <sup>3+</sup> (20 μM) for 8 h then incubate with the sensor for 30 min (c,f) the cells were incubated with SIH (100 μM) for 8 h then incubated with the sensor for 30 min (Excitation wavelength was 458 nm for a,b,c and 633 nm for d,e,f), (g,h,i) ratio images of a,d; b,e; c,f. The ratio images were obtained for the regions where Fe <sup>3+</sup> ions are located. Confocal fluorescence ratiometric images are the average ratio in regions of interest.....	162
7.10	<i>In vitro</i> calibration of CR-PK with [Fe <sup>3+</sup> ] .....	164
7.11	Confocal microscopy images (with DIC) of ws1 treated with (b,c) 10 μM CR-PK sensor after 30 min incubation (f,g) the cells were incubated with Fe <sup>3+</sup> (20 μM) for 1 h then incubated with the sensor for 30 min (j,k) the cells were incubated with SIH (100 μM) for 8 h then incubate with the sensor for 30 min (Excitation wavelength was 458 nm for b,f,j and 633 nm for (c,g,k); (d,h,l) ratio images of b,c; f,g; j,k. Confocal fluorescence ratiometric images are the average ratio in regions of interest.....	165
7.12	Confocal microscopy images (with DIC) of SH-SY5H treated with (b,c) 10 μM CR-PK sensor after 30 min incubation (f,g) the cells were incubated with Fe <sup>3+</sup> (20 μM) for 1 h then incubate with the sensor for 30 min (j,k) the cells were incubated with SIH (100 μM) for 8 h then incubate with the sensor for 30 min (Excitation wavelength was 458 nm for (b,f,j) and 633 nm for (c,g,k), (d,h,l) ratio images of b,c; f,g; j,k. Confocal fluorescence ratiometric images are the average ratio in regions of interest.. .....	166
7.13	Representative confocal microscopy images of intracellular colocalization studies of 10 μM CR-PK incubated with live BAEC cells co-labeled with MitoTracker Green FM (100 nM, incubated for 30 min) and LysoTracker Blue DND-99 (50 nM, incubated for 30 min) .....	168
7.14	Representative confocal microscopy images of intracellular colocalization studies of 10 μM CR-PK incubated with live ws1 cells co-labeled with MitoTracker Green FM (100 nM, incubated for 30 min) and LysoTracker Blue DND-99 (50 nM, incubated for 30 min) .....	169
7.15	Representative confocal microscopy images of intracellular colocalization studies of 10 μM CR-PK incubated with live SH-SY5H cells co-labeled with MitoTracker Green FM (100 nM, incubated for 30 min) and LysoTracker Blue DND-99 (50 nM, incubated for 30 min) .....	170

B.1	Molecular structures of the Fe <sup>3+</sup> -selective fluorescent sensors presented in this thesis .....	181
C.1	Confocal microscopy images (with DIC) of live bovine aortic endothelial cells (BAEC) treated with (a) incubated 20 μM CR-PK (30 min) (b) were pre-incubated with 20 μM Fe <sup>2+</sup> (ferrous ammonium sulfate) for overnight then 20 μM CR-PK sensor was added and image were taken after 30 min incubation (c) were pre-incubated with 20 μM Fe <sup>3+</sup> for overnight then 20 μM CR-PK sensor was added and the images were taken after 30 min incubation (d) Bar chart of fluorescent intensities of (a), (b) and (c).....	184
C.2	Confocal microscopy images (with DIC) of live human fibroblast cells (ws1) treated with (a) incubated 20 μM CR-PK (30 min) (b) pre-incubated with 20 μM Fe <sup>2+</sup> for overnight then 20 μM CR-PK sensor was added and image were taken after 30 min incubation (c) pre-incubated with 20 μM Fe <sup>3+</sup> for overnight then 20 μM CR-PK sensor was added and the images were taken after 30 min incubation (d) Bar chart of fluorescent intensities of (a), (b) and(c) .....	185
D.1	ESI-Mass spectrum of the sensor RPE .....	187
D.2	<sup>1</sup> H NMR spectrum of the sensor RPE in CDCl <sub>3</sub> .....	188
D.3	<sup>13</sup> C NMR spectrum of the sensor RPE in CDCl <sub>3</sub> .....	189
D.4	ESI-Mass spectrum of IR-780 in CDCl <sub>3</sub> .....	190
D.5	<sup>1</sup> H NMR spectrum of IR-780 in CDCl <sub>3</sub> .....	191
D.6	ESI-Mass spectrum of the sensor IRPE .....	192
D.7	<sup>1</sup> H NMR spectrum of the sensor IRPE in CDCl <sub>3</sub> .....	193
D.8	ESI-Mass spectrum of NIRh.....	194
D.9	<sup>1</sup> H NMR spectrum of NIRh in CDCl <sub>3</sub> .....	195
D.10	<sup>13</sup> C NMR spectrum of NIRh in CDCl <sub>3</sub> .....	196
D.11	ESI-Mass spectrum of the sensor NIRh-Ac.....	197
D.12	<sup>13</sup> C NMR spectrum of the sensor NIRh-Ac in CDCl <sub>3</sub> .....	198
D.13	<sup>1</sup> H NMR spectrum of the sensor NIRh-Ac in CDCl <sub>3</sub> .....	199
D.14	ESI-Mass spectrum of the sensor NRPA.....	200
D.15	<sup>13</sup> C NMR spectrum of the sensor NRPA in CDCl <sub>3</sub> .....	201
D.16	<sup>1</sup> H NMR spectrum of the sensor NRPA in CDCl <sub>3</sub> .....	202

D.17	ESI-Mass spectrum of the sensor NRPK.....	203
D.18	$^{13}\text{C}$ NMR spectrum of the sensor NRPK in $\text{CDCl}_3$ .....	204
D.19	$^1\text{H}$ NMR spectrum of the sensor NRPK in $\text{CDCl}_3$ .....	205
D.20	ESI-Mass spectrum of the sensor NRP .....	206
D.21	$^{13}\text{C}$ NMR spectrum of the sensor NRP in $\text{CDCl}_3$ .....	207
D.22	$^1\text{H}$ NMR spectrum of the sensor NRP in $\text{CDCl}_3$ .....	208
D.23	ESI-Mass spectrum of CR .....	209
D.24	$^1\text{H}$ NMR spectrum of CR in $\text{DMSO}/\text{CDCl}_3$ (v/v, 1:1) .....	210
D.25	ESI-Mass spectrum of $\text{CR-NH}_2$ .....	211
D.26	$^1\text{H}$ NMR spectrum of $\text{CR-NH}_2$ in $\text{CDCl}_3$ .....	212
D.27	$^{13}\text{C}$ NMR spectrum of $\text{CR-NH}_2$ in $\text{CDCl}_3$ .....	213

## LIST OF SCHEMES

Scheme	Page
2.1 Mechanism of fluorescence “turn-on” metal sensors based on “coordination-induced fluorescent enhancement (or activation) (CIFE or CIFA) process .....	32
2.2 Synthesis route for RPE.....	36
2.3 Proposed 1:1 binding mode of RPE with Fe <sup>3+</sup> in ACN/Tris-HCl buffer (10 mM, pH 7.32, v/v 2:1) .....	42
3.1 Synthetic scheme of the IRPE sensor.....	61
3.2 Proposed reversible 1:1 binding mode between IRPE and Fe <sup>3+</sup> .....	69
4.1 Equilibrium between the open form and spirocyclic form of rhodamine (a) and one of Changsha (CS) near infrared fluorophores .....	74
4.2 Synthesis route for NIRh-Ac.....	82
4.3 Proposed 1:1 binding mode of NIRh-Ac with Fe <sup>3+</sup> in ACN/Tris-HCl buffer (10 mM, pH 7.3, v/v 1:1).....	88
5.1 Synthesis route for NRPA.....	106
5.2 Proposed 1:1 binding mode of NRPA with Fe <sup>3+</sup> in ACN/Tris-HCl buffer (10 mM, pH 7.3, v/v 2:1).....	111
6.1 Synthesis of the sensors, NRPK ad NRP .....	128
6.2 Proposed 2:1 binding mode of NRP with Fe <sup>3+</sup> in ACN/Tris-HCl buffer (10 mM, pH 7.3, v/v 3:1) .....	136
6.3 Proposed 2:1 binding mode of NRPK with Fe <sup>3+</sup> in ACN/Tris-HCl buffer (10 mM, pH 7.3, v/v 3:1).....	137
7.1 Equilibrium between the open form and spirocyclic form of rhodamine (a) and dye CR (b).....	147
7.2 Synthesis route for CR-PK .....	153
7.3 Proposed reversible 1:1 binding mode between CR-PK and Fe <sup>3+</sup> .....	159
A1.1 Synthesis route for IR-Sal.....	174
A1.2 Synthesis route for IRPhen .....	175

A1.3	Synthesis route for IR-PEA .....	176
A1.4	Synthesis route for IR-EtG.....	177
A1.5	Synthesis route for IR-AMA .....	178
A1.6	Synthesis route for Rh-2S and Rh-3S .....	180

## LIST OF ABBREVIATIONS

$\mu\text{L}$	micro liter
ACN	acetonitrile
BAEC	Bovine Aortic Endothelial Cells
BOP	(Benzotriazol-1-yloxy)tris(dimethylamino)phosphonium hexafluorophosphate
$\text{CDCl}_3$	deuterated chloroform
DCM	dichloromethane
DMF	N,N-dimethylformamide
DMSO	dimethyl sulfoxide
equiv	equivalent
ESI	electron spray ionization
eT	electron transfer
ET	energy transfer
EtOH	ethanol
Fl	fluorophore
Fl*	excited fluorophore
FRET	fluorescence resonance energy transfer
FTIR	Fourier transform infrared spectroscopy
g	gram
h	hour(s)
HEPES	2-[4-(2-hydroxyethyl)piperazin-1-yl]ethanesulfonic acid
HOMO	highest occupied molecular orbital
Hz	hertz
j	coupling constant
LIP	labile iron pool



LUMO	lowest unoccupied molecular orbital
M	molar
mg	milligram
MHz	mega hertz
min	minute(s)
mL	milliliter
MOP	3-(N-morpholino)propanesulfonic acid
NIR	near-infrared
nm	nanometer
NMR	nucleic magnetic resonance
∅	quantum yield
PET	photoinduced electron transfer
ROS	reactive oxygen species
rt	room temperature
SH-SY5Y	live human neuroblastoma cells
TEA	triethanolamine
TRIS	tris(hydroxymethyl)aminomethane)
UV-Vis	Ultraviolet-visible
ws1	live human fibroblast cells
δ	chemical shift
ε	molar absorptivity

## CHAPTER 1

### INTRODUCTION

#### 1.1 Iron in biology

Metal ions, though scarcely present in the human body, play essential roles in many biological processes.<sup>[1]</sup> Among them, iron is the most abundant transition metal in the body.<sup>[2]</sup> It is an essential component of proteins containing iron-sulphur clusters, heme, mono or diiron-oxo centers and other iron-containing metal clusters that are involved in many important cellular processes such as oxygen transport, mitochondrial respiration and DNA synthesis and repair.<sup>[2,3]</sup> The biological functions of iron are based on its chemical properties. Because iron is a transition metal, it can serve as an electron acceptor or donor. In living cells, iron can be found in ferrous ( $\text{Fe}^{2+}$ ) or ferric ( $\text{Fe}^{3+}$ ) forms. Iron has favorable redox potential to switch between Fe(II) and Fe(III) ( $(\text{Fe}(\text{OH})_2)^{2+/3+}$ , +0.772 V (vs. NHE) at pH 7).<sup>[4]</sup> Iron can also coordinate to various organic ligands in dynamic and flexible modes.<sup>[4-5]</sup>

Although iron is an essential element for the body, free iron ions ( $\text{Fe}^{2+}$  and  $\text{Fe}^{3+}$ ) are toxic even at concentration below  $10^{-18}$  M. Iron's toxicity is generally believed that it promotes the production of hydroxyl radicals ( $\text{OH}\cdot$ ) from superoxide ( $\text{O}_2^{\cdot-}$ ) (the Haber-Weiss reaction) or hydrogen peroxide ( $\text{H}_2\text{O}_2$ ) (the Fenton reaction (Fig. 1)).<sup>[6]</sup> Hydroxyl radicals are highly reactive oxygen species (ROS) that damage DNA, proteins, lipids, and cell membranes. The damages may lead to aging and several diseases such as stroke, cancer, and neurological diseases like Parkinson's disease, Alzheimer's disease and atherosclerosis.<sup>[6-7]</sup>

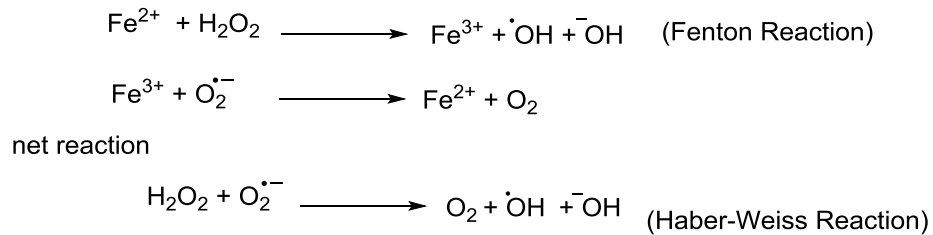


**Figure 1.1** Fenton and Haber-Weiss Reaction[6]

## 1.2 Cellular Iron Pools

The total amount of iron in an adult body is maintained at an average of 3-5 grams.<sup>[8]</sup> The majority of total body iron, about 60-70 % is present in hemoglobin in circulating erythrocytes. Another 10 % of essential body iron is present in the forms of myoglobin, cytochromes, and iron-containing enzymes amounting to no more than 4-8 mg of iron. Even though most of the remaining iron in the body, around 20-30 %, is found in hepatocytes and reticubendothelial macrophages which serve as storage depots,<sup>[8-10]</sup> the presence of “free iron pools” in certain cells may still be possible (in quiescent conditions represents only a minor fraction (<5%) of the total cell iron (50 -100 μM)).<sup>[11, 12]</sup> Figure 1.3 shows how these labile iron pools can exist.

Iron is taken up by cells from circulating transferrin via transferrin receptors TfR1 and TfR2.<sup>[13]</sup> After binding and internalization of the Tf-Fe complex, ferric ions are released from transferrin in an acidic endosomal compartment. It has been proposed that  $\text{Fe}^{3+}$  can be reduced to  $\text{Fe}^{2+}$  by Dcyb and then to cytosol by divalent cation transport (DMT1).<sup>[13-15]</sup> Iron may also enter this iron pool via DMT on cell surface.<sup>[16]</sup> Iron enters the pool not only from outside of the cell, but may also from several sources inside the cell.<sup>[16]</sup> Iron can be exported from the lysosomes and proteosomes after degradation of the iron-storage protein ferritin (Ft).<sup>[16]</sup> Moreover, iron

may be exported from degradation of heme-containing proteins in the lysosomes and proteasomes.<sup>[17]</sup> The exported iron from different organelles can reach several targets again. Iron in these pools are primarily used by mitochondria for the synthesis of heme and iron-sulfur clusters.<sup>[18]</sup> There are three mechanisms proposed to explain the delivery of iron to mitochondria.<sup>[18]</sup> The first mechanism is direct uptake from the cytosolic labile iron pool (LIP).<sup>[13-16]</sup> The second mechanism involves a complex with chaperone-like moieties to reach the mitochondria in a chelator-inaccessible form.<sup>[19]</sup> The third mechanism, so-called “kiss and run”, is the direct transfer of iron from endosomes to mitochondria.<sup>[20]</sup> Even though the transported iron is used in mitochondria, LIP was observed.<sup>[18]</sup> Although there are not sources and function of nuclear LIP, LIP was observed in nuclei.<sup>[21]</sup>

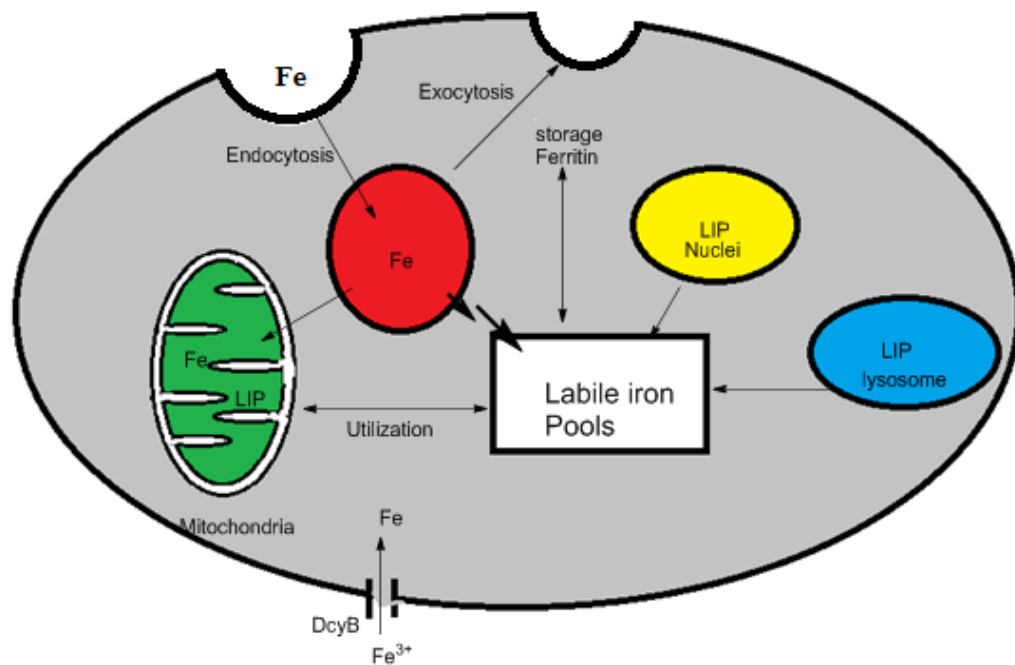


**Figure 1.2** Dynamics of labile iron in cells and a schematic depiction of a mammalian cell showing the interconnections between the labile iron pools in various organelles

Any excess iron in LIP is stored in ferritin. However, around 3-5% of this iron is “free” iron that is responsible for oxygen-mediated iron toxicity.<sup>[11]</sup> This chelatable "free iron" is poorly characterized. There are several studies on the determination of LIP. Based on the experimental approach, methods for the determination of LIP can be divided into two main groups: the methods that require disruption of cell integrity and fractionation of cellular components and the methods that enable measurements in intact cells.<sup>[22-25]</sup>

### 1.3 Iron Detection in Cells

Traditional magnetic resonance imaging (MRI) technology can provide the overall iron distribution in the body but cannot deliver the cellular/subcellular resolution necessary for an understanding at the cellular or molecular level.<sup>[26]</sup> Histochemical staining with Perl's method or the Turnbull method are the traditional methods to study labile iron ( $\text{Fe}^{2+}$  and  $\text{Fe}^{3+}$ ) qualitatively in tissue samples.<sup>[27]</sup> However, their insensitivity, toxicity, and the need to use fixed samples limit their usage in living cells. Radioactive  $^{59}\text{Fe}$  has been used to provide important information on iron trafficking but it lacks the ability to distinguish the oxidation states of iron in cells.<sup>[28-29]</sup> Moreover, the ionizing radiation from  $^{59}\text{Fe}$  is highly deleterious to the subject. Another method is using chelators such as DFO to detect LIP in living cells. It cannot distinguish the oxidation states of iron and needs for cell disruption.<sup>[30]</sup>

In contrast, membrane permeable fluorescent sensors have been demonstrated to be powerful tools for the non-invasive visualization of intracellular distribution of metal cations in live cells.<sup>[31]</sup> Dynamic changes of metal concentration in cells can be monitored by confocal microscopy. Currently, a few fluorescent sensors are available for wide range of biologically relevant cations such as magnesium, calcium, potassium, and zinc. For example, Mag-fura is a commercially available magnesium selective sensor.<sup>[32]</sup> Zinquin is also commercially available as

a zinc-selective probe.<sup>[33]</sup> Fura-2 has provided information of calcium neurophysiology.<sup>[34]</sup> The molecular structures of a few such sensors are shown in Figure 1.3.

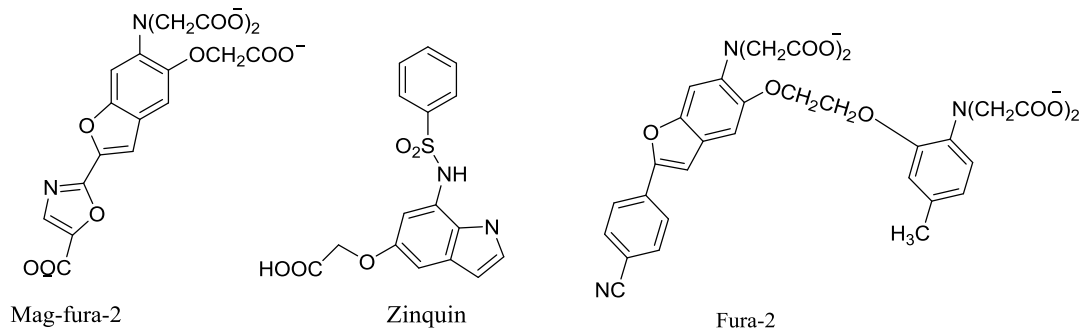


**Figure 1.3** Molecular structures of a few sensors for Mg(II), Zn(II), and Ca(II)

### 1.3.1 Visualization of Labile Iron Pools

Currently, there are only two fluorescent sensors commercially available for iron detection in cells. Calcein (structure shown in Figure 1.4) has been reported by Cabantchik *et al.* as a Fe(II)-selective sensor to trace iron in cells.<sup>[35]</sup> Calcein's structure consists of a fluorescein fluorophore with an EDTA-like binding moiety. It is a turn-off (quenching) sensor and is more selective for Fe(II) over Fe(III) but also gives response to other metals, including Ni<sup>2+</sup>, Co<sup>2+</sup>, and Cu<sup>2+</sup>. Moreover, the calcein-iron complex has been shown to generate radical species that can degrade the free form of the sensor, resulting in fluorescent decrease.<sup>[36]</sup> Phen Green SK (structure shown in Figure 1.4) is another sensor that responds to both major oxidation states of iron, providing a 93% turn-off response to Fe<sup>2+</sup> and a 51% turn-off response to Fe<sup>3+</sup>.<sup>[37]</sup> It is also a fluorescein-based sensor linked to Phenanthroline as the iron-binding moiety. Once again, it gives response to other metal ions as well.<sup>[37]</sup>

Because of their limitations, several research groups have been trying to develop better iron-selective fluorescent sensors over the past two decades.

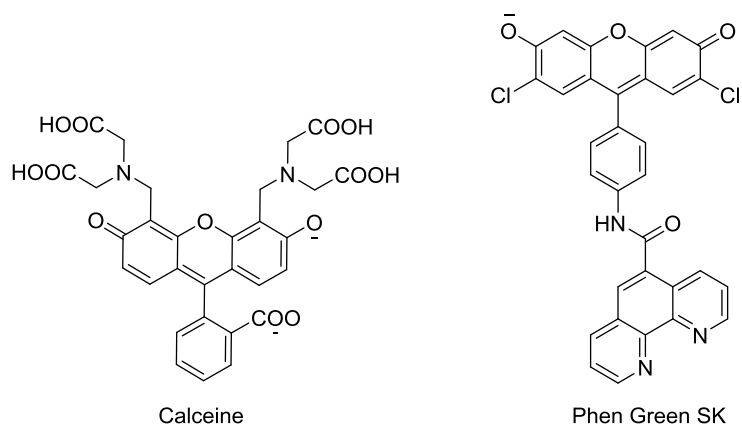


**Figure 1.4** Chemical structures of Calcein and Phen Green SK

### 1.3.1.1 Fluorescent Sensors for $\text{Fe}^{2+}$

Over the past few years, there have been only a few  $\text{Fe}^{2+}$ -selective sensors published (Figure 1.5 and 1.6). Pyrene-TEMPO is a reaction-based fluorescent sensor. When the spin radical TEMPO links to the fluorophore pyrene, its fluorescence is quenched; however,  $\text{Fe}^{2+}$  can reduce the TEMPO radical to a non-radical form and pyrene's fluorescence is thus restored.<sup>[38]</sup> However, it has two limitations preventing its application in cell imaging: the reaction is pH-dependent (favored at low pHs) and other radicals and other biological relevant reductants can reduce TEMPO radical. DansSQ is another  $\text{Fe}^{2+}$ -selective sensor that consists of a dansyl group-linked styrylquinoline. Binding of  $\text{Fe}^{2+}$  results in blocking ICT (intermolecular charge transfer) between two fragments and it shows a 15-fold fluorescence increase at 460 nm.<sup>[39]</sup> This sensor has also drawbacks that limit its biological use. It is only soluble in organic solvents and it is not entirely selective for  $\text{Fe}^{2+}$ .

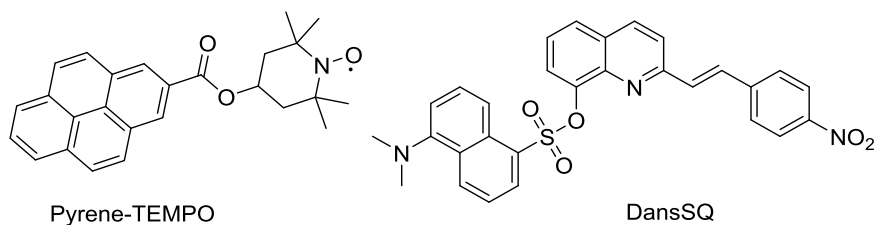


**Figure 1.5** Structures of fluorescent sensors for  $\text{Fe}^{2+}$

In the past few years, several new  $\text{Fe}^{2+}$ -selective sensors have been reported for free  $\text{Fe}^{2+}$  imaging in live cells (Figure 1.6). AGD is a coumarin-based  $\text{Fe}^{2+}$  selective turn-off fluorescent sensor. The coumarin fluorophore linked to two-amino-two-(hydroxymethyl)propane-1,3-diol as a  $\text{Fe}^{2+}$  binding moiety that has a decreased fluorescence response to  $\text{Fe}^{2+}$  binding. The sensor localizes to the cell membrane, where it can detect change in  $\text{Fe}^{2+}$  concentration.<sup>[40]</sup> The first  $\text{Fe}^{2+}$ -selective turn-on sensor, developed by Hirayama *et al.* in 2013, was a rhodamine based fluorescent sensor, RhoNox-1.<sup>[41]</sup> RhoNox-1 has an N-oxide group on the tertiary amine of the sensor. In the presence of  $\text{Fe}^{2+}$ , the N-oxide group is reduced and the sensor shows an increased fluorescence. It was reported that RhoNox-1 was able to trace endogenous  $\text{Fe}^{2+}$ , which was concluded to be located in the Golgi apparatus by colocalization experiments. Although the sensor is capable for cell images, it has two limitations: the mechanism of sensing is not known, and it is not reversible. Another reaction-based  $\text{Fe}^{2+}$  selective sensor IP1, which was reported by Au-Yeung, is a fluorescein based turn-on fluorescent sensor.<sup>[42]</sup> It is selective for  $\text{Fe}^{2+}$  over other metal ions at their biological concentrations and can detect endogenous levels of labile  $\text{Fe}^{2+}$  in liver cells. However, like RhoNox-1, it is a reaction-based sensor and it does not show reversible response to  $\text{Fe}^{2+}$ .



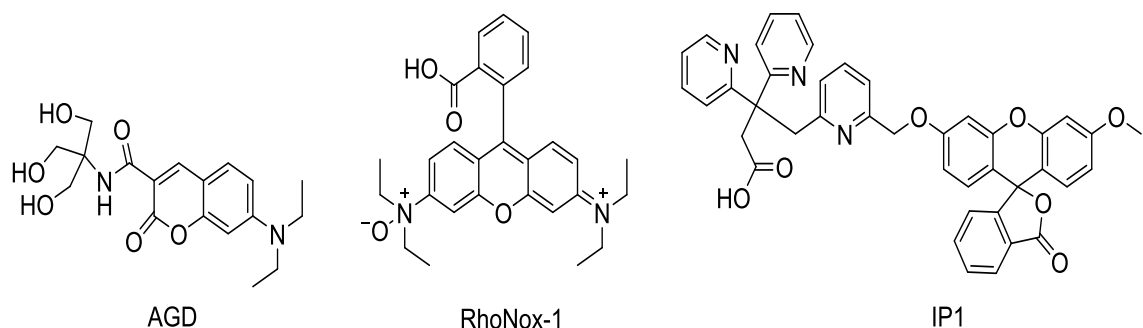


**Figure 1.6** Structures of Fe<sup>2+</sup>-selective fluorescent sensors applied in cells for bio imaging

### 1.3.1.2 Fluorescent Sensors for Fe<sup>3+</sup>

In contrast to the small number of Fe<sup>2+</sup>-selective sensors reported, there is more Fe<sup>3+</sup>-selective fluorescent sensors reported. Most of them are turn-off sensors; however, some turn-on and ratiometric sensors have been developed in the past 5 years.

The first turn-off Fe<sup>3+</sup> sensor, Sensor 1 (Figure 1.7), is a calixarene-based sensor. The calixarene moiety is linked to the 3-alkoxy-2-naphthoic acid moiety that can coordinate with Fe<sup>3+</sup> or Cu<sup>2+</sup>. This sensor is pH dependent. The binding ratio and coordination number are changeable at different pH because naphthoic acid and -COOH groups on calixarene are protonated at low pH's, but at intermediate pH the naphthoic acid is deprotonated and increases the affinity to the metal ions.<sup>[43]</sup> Wolf *et al.* reported a 1,8-diacridylnaphthalene-derived fluorosensor, Sensor 2.<sup>[44]</sup> Fluorescent studies showed highly Fe(III)-selective quenching in water/acetonitrile (1:1, v/v) even in the presence of excess other metal ions. However, Sensor 2 also gives response to Cr<sup>2+</sup>. Sensor 3 and Sensor 4 were developed by Costa *et al.* in 2003<sup>[45]</sup>, consisting of naphthalene and linked hydroxamic acid. The sensors interact with Fe<sup>3+</sup> at low pH (pH<4). They are also not entirely Fe<sup>3+</sup>-selective, also giving responses to Cu<sup>2+</sup> and Zn<sup>2+</sup>. Peng *et al.* reported a quinoline based sensor for Fe<sup>3+</sup> (Sensor 5).<sup>[46]</sup> The sensor also responded to Cr<sup>3+</sup>,

with a 93% turn-off response to  $\text{Fe}^{3+}$  and a 54% turn-off response to  $\text{Cr}^{3+}$ . The sensor, MD1 was synthesized from diethoxycarbonyl glycoluril cyclic ether and 1, 2-dihydroindazol-3-one.<sup>[47]</sup> MD1 binds  $\text{Fe}^{3+}$  with the polarized carbonyl groups and the nitrogen atoms. The  $\text{Fe}^{3+}$ -binding results in a quenched fluorescence in 425 nm. Sensor 6 shares similar properties as those of Sensor 3 and 4. However, Sensor 6 is more selective towards  $\text{Fe}^{3+}$  with a two step 1:1 and 1:2 (L:M) quenching mechanism at pH 3 in methanol/water (1:1) system.<sup>[48]</sup> Yao *et al.* designed a new coumarin derivative sensor for  $\text{Fe}^{3+}$  (L in Figure 1.7). The sensor gave a turn-off response to  $\text{Fe}^{3+}$  in water/methanol system.<sup>[49]</sup> Naphthalene-based sensors, Sensor 7 and Sensor 8, were developed by Singh *et al.* in 2009. These sensors were designed according to the fluorophore spacer-receptor format associated with photoinduced electron transfer (PET) mechanism. For Sensor 7, naphthalene was linked to aminobisulfonate via methylene spacer for a binding group for  $\text{Fe}^{3+}$ . Sensor 7 and Sensor 8 were both pH dependent sensors. At low pH's, the amine nitrogen of the sensors is protonated and its oxidation potential raised. The PET process is thus canceled and the sensors' fluorescence restored.<sup>[50]</sup> The same group also developed Sensor 9. The design of Sensor 9 involved the incorporation of Fe(III) binding sites observed in naturally occurring siderophores into a synthetic sensing assembly.<sup>[51]</sup> Even though the selectivity of the sensor on  $\text{Fe}^{3+}$  is high, the sensor still shows 30% emission quenching with  $\text{Cu}^{2+}$  and has minimal aqueous solubility. Another design of  $\text{Fe}^{3+}$  turn-off sensor includes anthracene-L- aspartic acid and anthracene-L- glutamic acid sensors.<sup>[52]</sup> The fluorophore anthracene was linked to amino acids aspartic acid and glutamic acid for the detection of  $\text{Fe}^{3+}$  ions. Although both the sensors are soluble in aqueous solvents, the  $\text{Fe}^{3+}$ -selectivity of the sensors is pH-dependent, and their affinities to  $\text{Fe}^{3+}$  are maximum at pH 5. Sensor 10 and Sensor 11 are similar to the sensor anthracene-L-aspartic acid. Here, naphthalene and dansyl chloride were conjugated with aspartic acid as a receptor for the detection of  $\text{Fe}^{3+}$  ions. The both sensors show emission

quenching fluorescence; however, Sensor 10's excitation wavelength ( $\lambda_{\text{ex}} = 278 \text{ nm}$ ) is little shorter than that of Sensor 11 ( $\lambda_{\text{ex}} = 330 \text{ nm}$ ), and their reversibility results with EDTA are 60% (Sensor 10) and 90% (Sensor 11).<sup>[53]</sup> Sensor 12 was developed by Callan and his co-worker for the detection of  $\text{Fe}^{3+}$  in THF/HEPES (9:1) solution at pH 7.<sup>[54]</sup> The sensor contains two Schiff base type receptors directly connected to naphthalene fluorophores. Although the sensor shows selective fluorescence quenching to  $\text{Fe}^{3+}$  up to 90%, it also shows 50% quenching emission for Cu(II). DMADC is a chalcone based  $\text{Fe}^{3+}$ -selective sensor.<sup>[55]</sup> Despite this thoughtful design, the sensor shows only 40% emission quenching with  $\text{Fe}^{3+}$ . Sensor 13 is very similar to Sensor 12. The difference is that a naphthalene fluorophore was linked to other two naphthalene fluorophores. The sensor binds to  $\text{Fe}^{3+}$  in 1:1 ratio and shows a decreased fluorescence. However, the sensor's detection limit is in the milli-molar range ( $\sim 0.14 \text{ mM}$ ).<sup>[56]</sup>

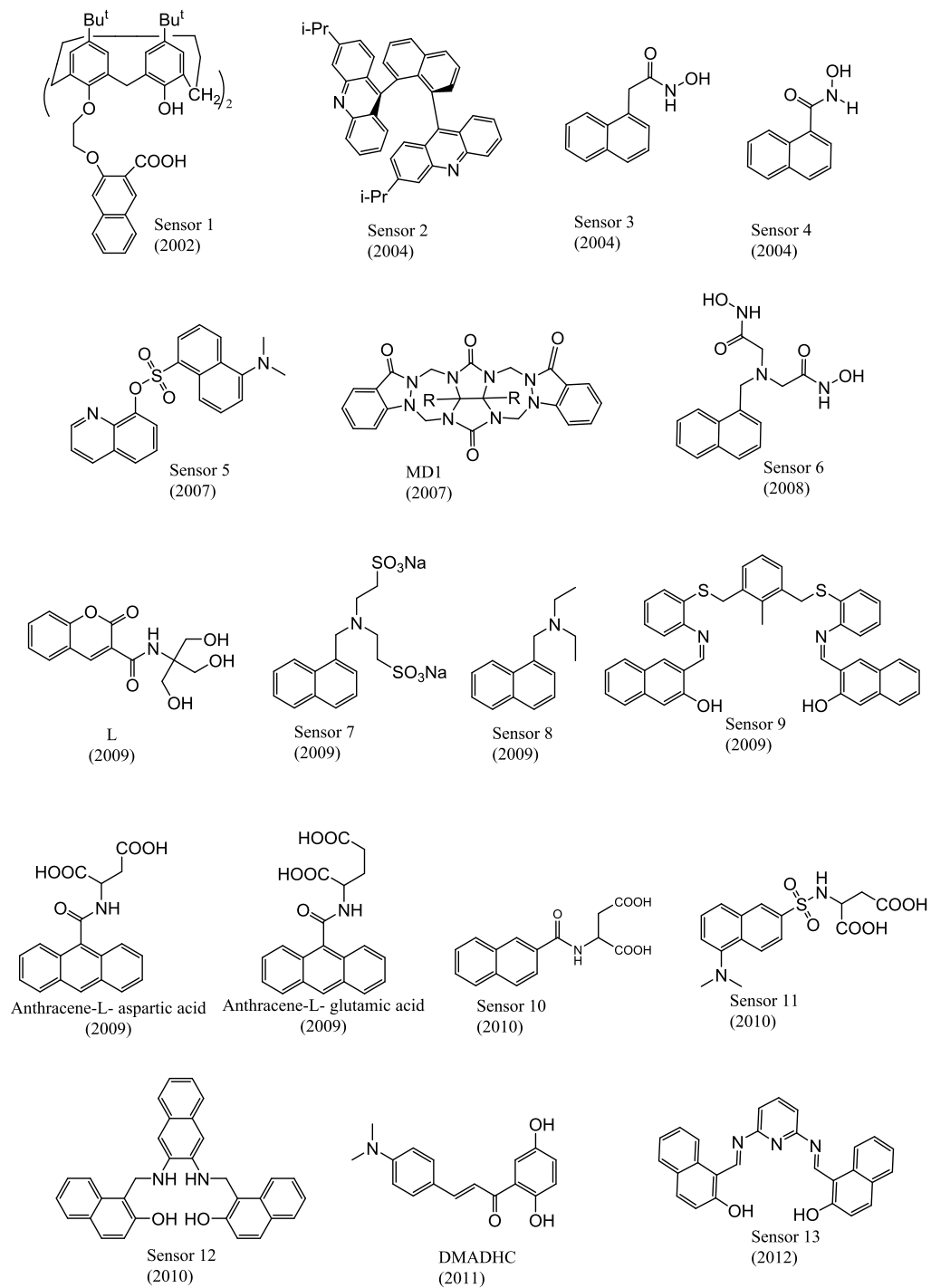


**Figure 1.7** Some recently published turn-off Fe<sup>3+</sup> fluorescent sensors (numbers in the parentheses show the year when they were published)

There are also several sensors exhibiting fluorescence emission enhancement upon binding to  $\text{Fe}^{3+}$  ions. Due to the paramagnetic effect of  $\text{Fe}^{3+}$  ions, developing turn-on sensors is more challenging. Rhodamine derivatives are mostly used to develop turn-on sensors for  $\text{Fe}^{3+}$  and summarized in literature.<sup>[57, 58]</sup> Here, some rhodamine based and other turn-on sensors were discussed. Sensor H1, shown in Figure 1.8, is the first turn-on sensor for the detection of  $\text{Fe}^{3+}$  ions.<sup>[59]</sup> It uses a new electronic push-pull fluorophore, 4-amino-1, 8-dicyanonaphthalene, for metal ions. It shows a considerable fluorescence enhancement upon  $\text{Fe}^{3+}$ -binding. However, H1 has two limitations for cell imaging applications: it is very pH sensitive and gives response to other metal ions such as  $\text{Cr}^{3+}$ . Sensor 14 is another turn-on  $\text{Fe}^{3+}$ -selective sensor containing two aza-18-crown-6 as iron binding moieties linked to a coumarin.<sup>[60]</sup> This sensor shows an increased fluorescence with  $\text{Fe}^{3+}$  under biologically relevant conditions; however, its affinity to  $\text{Fe}^{3+}$  is a moderate ( $K_d \sim 6.7 \mu\text{M}$ ), and it also exhibits fluorescence enhancement for  $\text{Cu}^{2+}$ . Sensor 15 is an anthracene-based fluorescent PET sensor.<sup>[61]</sup> The sensor contains a tridentate ionophore of amide/ $\beta$ -amino alcohol being very good selectivity and sensitivity for  $\text{Fe}^{3+}$ . Even though it has a considerable affinity for  $\text{Fe}^{3+}$  ( $K_d \sim 0.03 \mu\text{M}$ ), it is also selective for  $\text{Hg}^{2+}$ . FerriBRIGHT-Q (8-(3,4-dihydroxyphenyl)-2,6-bis(ethoxycarbonyl)-1,3,5,7-tetramethyl-4,4-difluoro-4-bora-3a,4a-diaza-s-indacene), a BODIPY-based sensor, was rationally designed with the aid of computational methods. The binding of FerriBRIGHT-Q with  $\text{Fe}^{3+}$  results in an oxidation of the sensor, exhibiting a stronger fluorescence. This sensor also has limitations: the oxidation occurs with 10 equiv of  $\text{Fe}^{3+}$  in methanol, also the sensor gives response to some other oxidizing species.<sup>[62]</sup> PDI-2 is a perylene tetracarboxylic diimide-based turn on sensor containing two di-(2-picoyl)-amine (DPA) groups as  $\text{Fe}^{3+}$  binding receptors. When DPAs bind the fluorophore, they can act as electron donor and cause PET on the sensor. The  $\text{Fe}^{3+}$ -binding results in blocking on PET and the sensor exhibits fluorescence enhancement. However, PDI-2 is a very large molecule and it is only

soluble in polar organic solvents.<sup>[63]</sup> A squaramide hydraxamate based fluorescent sensor which gave  $\text{Fe}^{3+}$ -selective fluorescence intensity increase was reported by Lim *et al.* (Sensor 16).<sup>[64]</sup>

FS1, Rh-OH-Rh, Y3, and RD1 are all rhodamine-based turn-on sensors. When  $\text{Fe}^{3+}$  binds these sensors, the spirolactam of rhodamine opens then the sensors increase in fluorescence emission.<sup>[65-67]</sup> FS1 was synthesized from rhodamine 6G ethylenediamine and 2-hydroxy-5-nitrobenzaldehyde.<sup>[65]</sup> This is a reaction based sensor. When the sensor coordinates with  $\text{Fe}^{3+}$ , it hydrolyzes 2-hydroxy-5-nitrobenzaldehyde part then, the sensor exhibits fluorescence enhancement. Our group developed Rh-OH-Rh.<sup>[66]</sup> It used three oxygen atoms to coordinate with  $\text{Fe}^{3+}$ . Even though it has perfect selectivity to  $\text{Fe}^{3+}$  over a large range of tested metal ions, it is not cell permeable. Y3 is another interesting rhodamine-based sensor. Although the carbonyl group on the rhodamine is not related to the binding, the ring-open process is still observed.<sup>[67]</sup> The limitation of the sensor is low affinity to  $\text{Fe}^{3+}$  (5  $\mu\text{M}$ ). RD1 is another rhodamine-based sensor published very recently. When it binds  $\text{Fe}^{3+}$ , it shows turn-on fluorescent and colorimetric responses in aqueous solution.<sup>[68]</sup>

Sensor 17 is a fluoranthene-based PET sensor. There is only one  $-\text{NH}_2$  group on the sensor and it causes PET because it acts as an electron donor.<sup>[69]</sup> When Sensor 17 coordinates with  $\text{Fe}^{3+}$  (2:1, sensor: $\text{Fe}^{3+}$ ), PET is blocked and it shows increase in fluorescence emission. Sensor 18 is a very small Schiff-based sensor. The sensor exhibits a blue shift emission band upon binding with  $\text{Fe}^{3+}$ .<sup>[70]</sup> The sensor also shows response to  $\text{Al}^{3+}$  and  $\text{Cu}^{2+}$  without any shifting in emission.

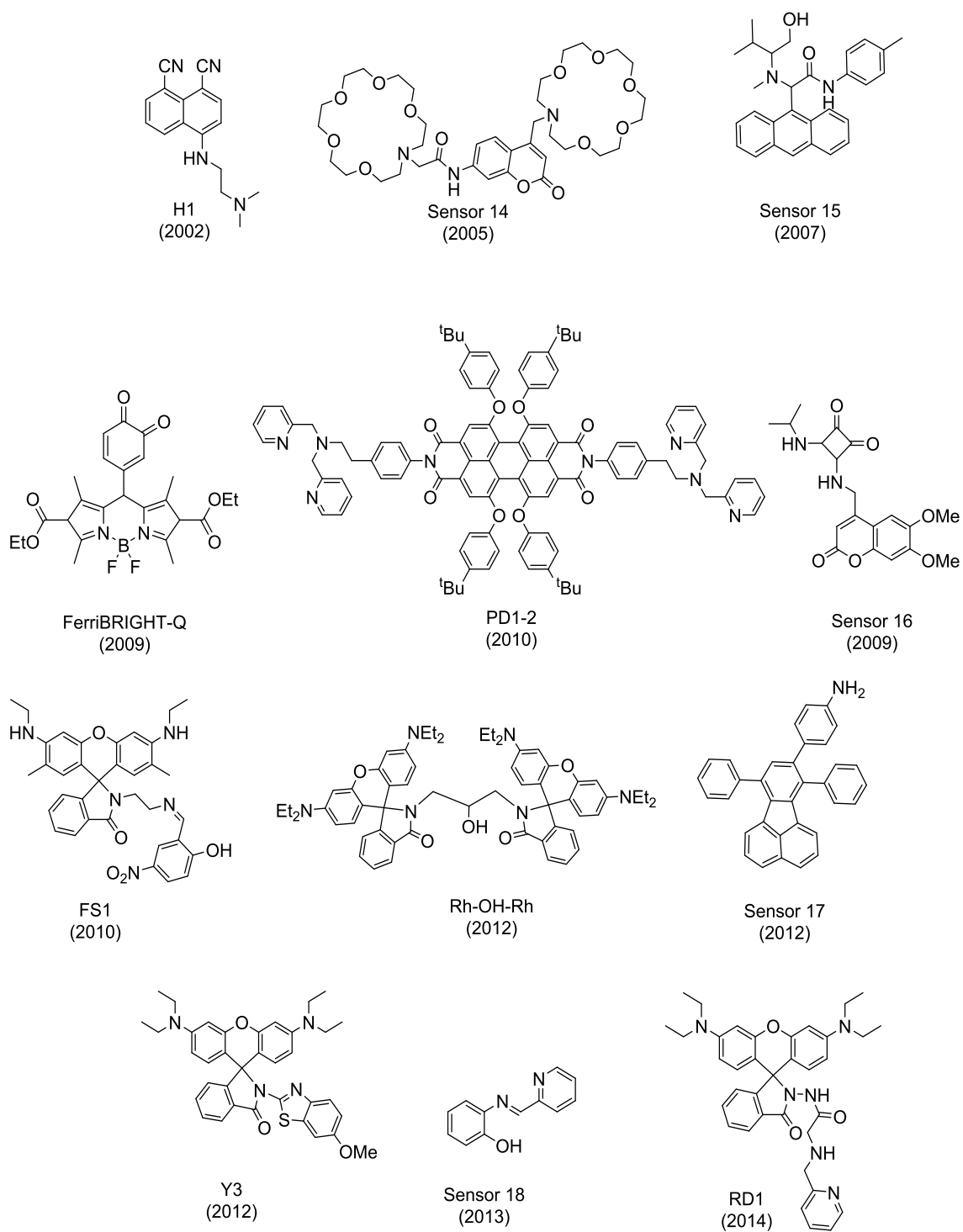


**Figure 1.8** Chemical structures of some published iron(III)-selective turn-on fluorescent sensors (numbers in the parentheses show the year when they were published)

There are also several sensors that show a ratiometric change in emission upon the binding of  $\text{Fe}^{3+}$  (Figure 1.9). Rurack and his co-workers developed the first ratiometric Fe(III) sensor.<sup>[71]</sup> Sensor 19 consists of a BODIPY fluorophore and a crowned binding group. Even though the binding group contains two soft S bases, it still binds hard acid  $\text{Fe}^{3+}$ .  $\text{Fe}^{3+}$  binding induces an increase in emission at 511 nm and a decrease at 634 nm in aqueous solutions. Sensor 20 is a benzimidazole-based sensor. The sensor exhibits a shift in emission (an increase at 475 nm and a decrease at 412 nm) upon binding with  $\text{Fe}^{3+}$  in  $\text{CH}_3\text{CN}/\text{H}_2\text{O}$  (95: 5, v/v).<sup>[72]</sup> Sensor 21 consists of a phenanthroimidazole dye and a bipyridyl binding receptor for  $\text{Fe}^{3+}$ .  $\text{Fe}^{3+}$  binding induces a decrease in emission at 500 nm and new intense emission band at 440 nm. The sensor is useful for the detection of  $\text{Fe}^{3+}$  in the pH range of 5.0-10.0 in 50% aqueous methanol solution.<sup>[73]</sup> Hao *et al.* synthesized a triazole-containing 8-hydroxyquinoline (8-HQ) ether, Sensor 22. It shows a strong fluorescence in non-protic solvents and a weak fluorescence in protic solvents. The sensor is capable of detection not only  $\text{Fe}^{3+}$  but also other metal ions such as  $\text{Zn}^{2+}$  due to its dramatic water-induced fluorescence change. When Sensor 22 coordinates with  $\text{Fe}^{3+}$ , it shows 81 nm blue-shifted emission, but on the other hand, with  $\text{Zn}^{2+}$ , it exhibits 62 nm blue-shifted fluorescence.<sup>[74]</sup> NT is a naphthalene-based sensor. The binding moiety of the sensor includes N/S/O atoms. NT itself shows weak fluorescence at 425 nm and 485 nm. However, the addition of  $\text{Fe}^{3+}$  resulted in a significant increase of both bands with a 104% increase for the 425 nm band and a 194% increase for the 485 nm band in THF/water solution.<sup>[75]</sup> Sensor 23 was synthesized from 2,6-diacetyl pyridine and 4-(diethylamino) benzaldehyde. This sensor shows different properties in UV-vis and fluorescence spectroscopy. In UV-vis spectroscopy, it gives a peak at 430 nm.  $\text{Fe}^{3+}$ -binding causes a decrease at 430 nm and increases at 724 nm and 960 nm. However, in fluorescence spectroscopy, its properties are highly dependent on the choice of solvents. In polar protic solvents the fluorescence of Sensor 23 is almost fully quenched, but in



non-polar solvents the sensor is highly fluorescent.<sup>[76]</sup> The sensor itself shows fluorescence at 538 nm; the addition of  $\text{Fe}^{3+}$  quenches the fluorescence and shifts by 17 nm to 555 nm, and a new peak at 460 nm appears. This sensor also gives response to  $\text{Cu}^{2+}$  as well, but the binding ratio of the metals with the sensor is different (1:1 for  $\text{Fe}^{3+}$  and 1:2 for  $\text{Cu}^{2+}$  (metal: sensor)).

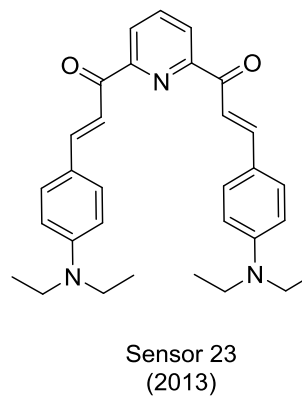
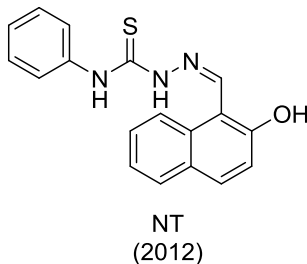
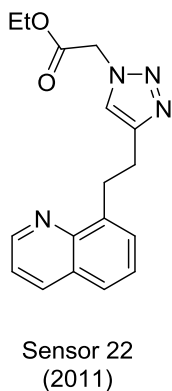
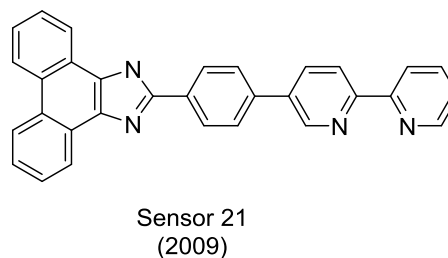
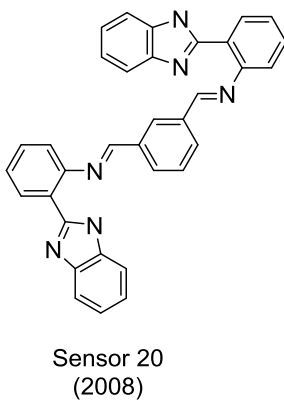
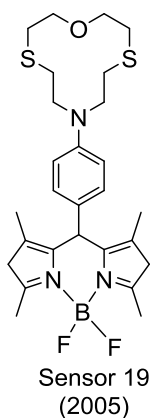


**Figure 1.9** Some recently published ratiometric  $\text{Fe}^{3+}$  fluorescent sensors (numbers in the parentheses show the year when they were published)

Although the number of Fe<sup>3+</sup>-selective sensors is vast, there are only a limited numbers of the sensors that are applied (or were suitable) in cell imaging for visualization of cellular labile iron pools. Some of them are discussed here (Figure 1.10). FD1 is the first rhodamine-based turn-on sensor that was used for Fe<sup>3+</sup> imaging in cells. Pig intestinal endothelial (PIEC) cells were pre-incubated with 50 μM exogenous Fe<sup>3+</sup>. Then FD1 was added and incubated for another 15 min to observe an increase in the fluorescence emission, but showed no signal before addition of Fe<sup>3+</sup>.<sup>[77]</sup> Fakhri *et al.* developed a fluorescein-based turn-off sensor, SF 34.<sup>[78]</sup> SF 34 shows 77.4% fluorescence quenching upon binding Fe<sup>3+</sup>, and is selective for Fe<sup>3+</sup> over other biological metals. SF 34 was applied in mouse bone marrow macrophage (BMMØ) cells and was traced Fe<sup>3+</sup> in endosomes/lysosomes of the cells.<sup>[78]</sup> RQ6 is a rhodamine-based FRET sensor. The rhodamine part was conjugated with a quinoline fluorescent group. In the closed form, RQ6 emits fluorescence at 482 nm. With the addition of Fe<sup>3+</sup>, an emission at 584 nm appeared and the emission at 482 nm decreased.<sup>[79]</sup> When HeLa cells were incubated with RQ6, no intercellular fluorescence was observed, but with exogenous added Fe<sup>3+</sup>, a considerable fluorescence signal was observed. Sensor 24 is a simple rhodamine based turn-on sensor. Rhodamine B was reacted with ethylenediamine to obtain Sensor 24. It is stable at biological pH, but it also gives response to Fe<sup>2+</sup> and Cr<sup>3+</sup>. Sensor 34 was used to detect intracellular Fe<sup>3+</sup>, but it is capable of detecting exogenous Fe<sup>3+</sup>.<sup>[80]</sup> DNSCH is a dansyl-based turn-off sensor. It is selective for Fe<sup>3+</sup> over other biological metal ions, but 2.5 μM of DNSCH was significantly quenched with 15 M of Fe<sup>3+</sup>. Because the binding constant between Fe<sup>3+</sup> and DNSCH is low, a high concentration of Fe<sup>3+</sup> (100 μM) is needed to observe fluorescence signals in African green monkey kidney (Vero) cells.<sup>[81]</sup> Sen *et al.* developed the sensor, HL1 (6-thiophen-2-yl-5,6-dihydrobenzo[4,5]imidazo-[1,2-c]quinazoline).<sup>[82]</sup> It is possible to distinguish Fe<sup>2+</sup> and Fe<sup>3+</sup> with the sensor at different pH's. At lower pH's, it is selective for Fe<sup>2+</sup>, but at biological pH, it is selective for Fe<sup>3+</sup>. The sensor has

ability to detect  $\text{Fe}^{3+}$  ions in fixed HeLa cells. RPE was developed in our laboratory. RPE can readily detect endogenous chelatable  $\text{Fe}^{3+}$  in live human neuroblastoma (SH-SY5Y) cells at subcellular resolution in real time, with two labile  $\text{Fe}^{3+}$  pools being successfully located in mitochondria and endosomes/lysosomes in both untreated and  $\text{Fe}^{3+}$ -loaded SH-SY5Y cells.<sup>[83]</sup> RPE will be discussed in detail in Chapter 2 of this thesis. Sensor 25 was synthesized by the condensation of rhodamine B hydrazine and 2-(N-methylpiperazinylimino) acetaldehyde.<sup>[84]</sup> It is selective for  $\text{Fe}^{3+}$  but  $\text{Cu}^{2+}$  also shows weak fluorescence enhancement. The sensor is capable of detection of exogenous  $\text{Fe}^{3+}$  ions in HeLa cells. Sensor 26 is a pyrene-based excimer sensor. The binding of  $\text{Fe}^{3+}$  to the sensor shows an emission at 507 nm due to the formation of a  $\pi$ - $\pi^*$  excimer that is induced by  $\text{Fe}^{3+}$ -binding. It is selective for  $\text{Fe}^{3+}$  over other biological metal ions, and it can capture exogenous  $\text{Fe}^{3+}$  ions in live HeLa cells.<sup>[85]</sup> RNP1 is also a rhodamine-based FRET sensor.<sup>[86]</sup> The sensor was synthesized by linking a conjugated naphthalene fluorophore to rhodamine dye. The sensor is selective for  $\text{Fe}^{3+}$  and  $\text{Cr}^{3+}$ . RNP1, linked to a lipophilic triphenylphosphonium (TPP) cation, is a mitochondria targeted sensor.<sup>[86]</sup> It is capable for the detection of exogenous  $\text{Fe}^{3+}$  ions in the mitochondria of live HeLa cells. Sensor 27 is another rhodamine-based turn-on sensor. The sensor produces fluorescence with the addition of  $\text{Fe}^{3+}$  in aqueous methanol, but in acetonitrile it shows no fluorescence with  $\text{Fe}^{3+}$ .<sup>[87]</sup> The sensor was applied to live murine fibroblast (L-929) and live baby hamster kidney fibroblasts (BHK-21) cells and was able to detect exogenous  $\text{Fe}^{3+}$  ions in both the cell lines. DAT-1 is a coumarin-based turn-off sensor that is highly selective and sensitive towards  $\text{Fe}^{3+}$  over other common metal ions. This sensor is very similar to the  $\text{Fe}^{2+}$ -selective sensor AGD (Figure 1.6) but there is an -OH group on the coumarin moiety instead of - $\text{NH}_2$  group. The sensor can be used for exogenous  $\text{Fe}^{3+}$  imaging in living breast cancer (MCF-7: Michigan Cancer Foundation-7) cells.<sup>[88]</sup> Recently published  $\text{L}_1$  is a quinoline based turn-on sensor.<sup>[89]</sup> The sensor contains a benzimidazole moiety

which is responsible for  $\text{Fe}^{3+}$ -binding. The sensor exhibits high selectivity towards  $\text{Fe}^{3+}$  in the presence of a large excess of other competing metal ions. The sensor was used to detect  $\text{Fe}^{3+}$  ions in fetal blood serum, banana pith, and living Hela cells. Cell studies show that it can detect exogenous  $\text{Fe}^{3+}$  ions in living cells.

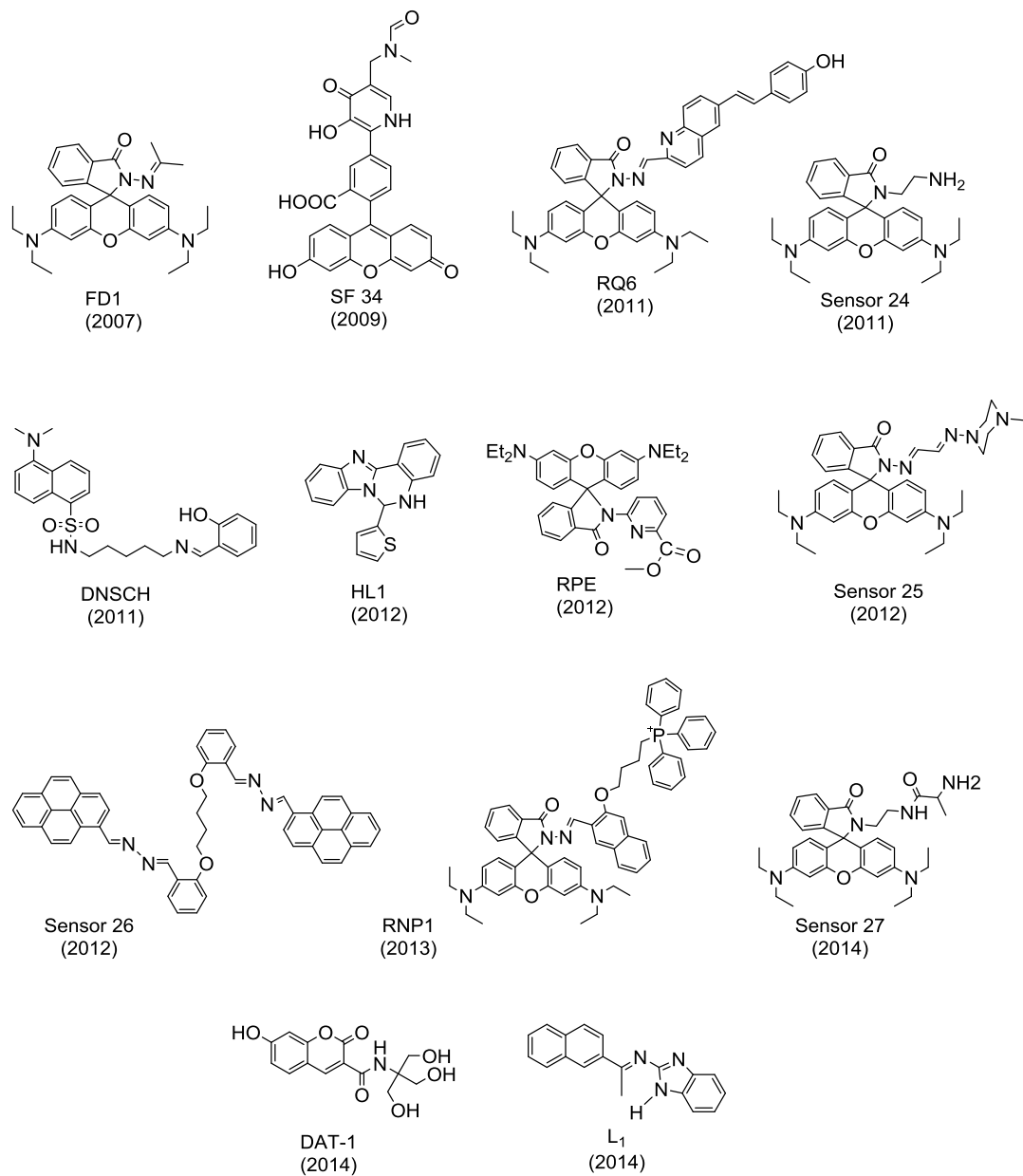
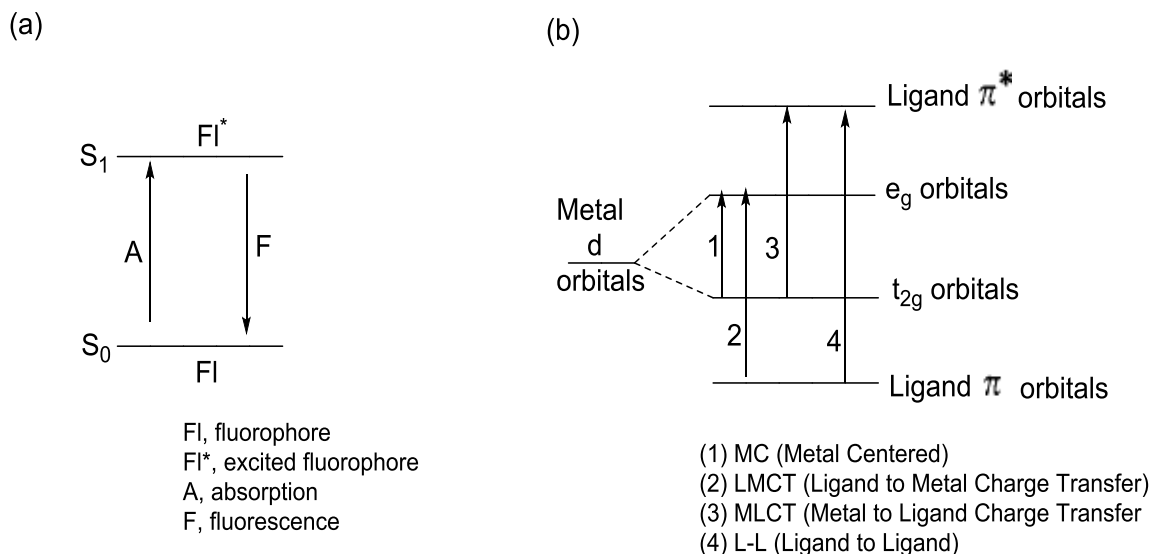


**Figure 1.10** Structures of  $\text{Fe}^{3+}$ -selective fluorescent sensors applied in cell for bioimaging (numbers in the parentheses show the year when they were published)

## 1.4 Fluorescence Quenching by Transition Metal Ions

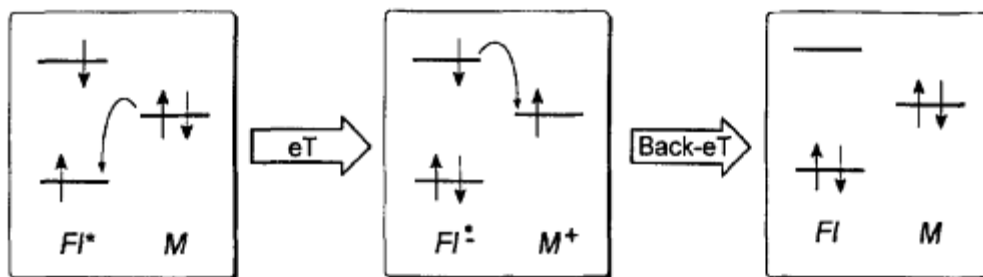
Figure 1.11a, a simplified Jablonski diagram, shows that upon absorption of photons, a fluorophore (FI) is excited to singlet excited electronic state ( $S_1$ ) and form an excited fluorophore (FI\*). The fluorescence is generated when FI\* relaxes to ground singlet electronic state ( $S_0$ ) via photon emission.<sup>[90,91]</sup> However, FI\* could return to  $S_0$  by various competing pathways such as non-radiative relaxation and phosphorescence.<sup>[90,91]</sup>

In a fluorophore formed by organic conjugates, fluorescence results from a  $\pi^*-\pi$  transition. When metal ions, specifically d-block metals, bind to the fluorophore, there are three additional transitions possible<sup>[92, 93]</sup> (Figure 1.11b). A d-d transition, when an electron is excited from a metal d orbital to an unoccupied metal d orbital. These can also involve either an electron excited from the ligand to the metal, called Ligand to Metal Charge Transfer (LMCT), or from the metal to the ligand (MLCT).



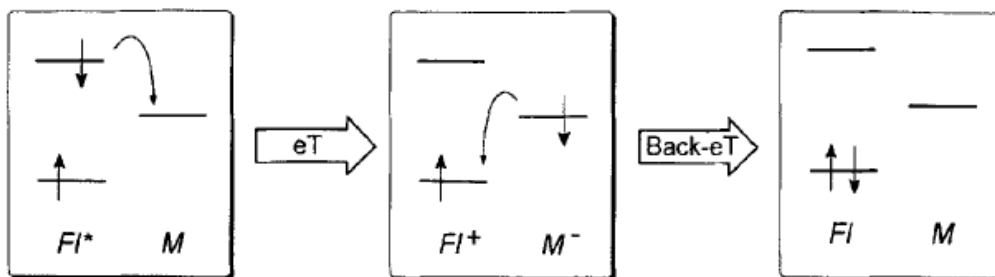
**Figure 1.11** (a) A simplified Jablonski diagram (b) Possible electron transitions during absorption for d-block complexes

To explain the quenching effects of metal ions on the fluorescence of fluorophores, the metal centered transition will be considered. As seen Figure 1.12, an electron is transferred from a filled (or half-filled) d level to the half-filled  $\pi$  level of the excited fluorophore, resulting in the formation of the transition species ( $Fl^-$ ,  $M^+$ ). Then, a back-electron transfer (eT) occurs from the  $\pi^*$  of  $Fl^-$  to the half-filled orbital of  $M^+$ , a process that regenerates the original partners in their ground state. Thus, in presence of the reducing metal  $M$ , the photonic energy assumed by the fluorophore is no longer restored through the  $\pi^*$  to  $\pi$  radiative transition, but is released via a non-radiative pathway which involves the metal. As a consequence, the natural fluorescence of  $Fl$  is quenched.<sup>[94-96]</sup>



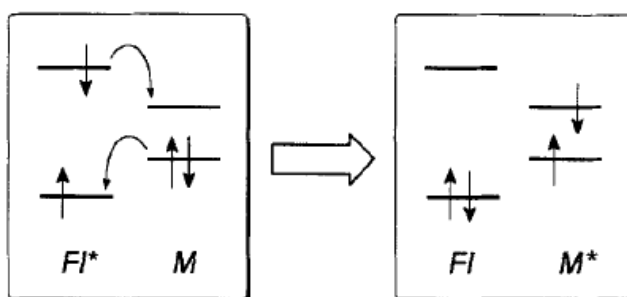
**Figure 1.12** Orbital scheme illustrating the quenching of a photo-excited fluorophore ( $Fl^*$ ) by a metal centre ( $M$ ), via an  $M$ -to- $Fl^*$  electron transfer process (eT). In this case, the metal centre  $M$  displays oxidizing tendencies[94].

Figure 1.13 shows the other possible fluorescence quenching mechanism caused by an eT process. In this case,  $M$  offers an empty orbital of adequate energy to which an electron is transferred from the  $\pi^*$  level of the proximate photo-excited fluorophore  $Fl^*$ . The photonic energy is deactivated through a non-radiative pathway, which involves the formation of the transient state ( $Fl^+$ ,  $M^-$ ) and the subsequent back-electron transfer process. At the end, the partners are restored to their ground state and fluorescence has been quenched.<sup>[94-96]</sup>



**Figure 1.13** Orbital scheme illustrating the quenching of a photo-excited fluorophore (FI\*) by a metal center (M), via an FI\* to M electron transfer process (eT)[94]

Energy transfer (ET) is the other mechanism that may be responsible for the fluorescence quenching by a transition metal center. This mechanism is for cations having a  $d^1$ - $d^9$  electronic configuration. As seen in Figure 1.14, M has some empty or half-filled energy levels, which are located between  $\pi^*$  and  $\pi$ . In this case, a simultaneous exchange of two electrons takes place (from the  $\pi^*$  orbital to the empty level of the metal and from the filled level of the metal to  $\pi$ ). The circular double-electron exchange restores FI in its ground state and produces the metal-centered excited state  $M^*$ . Metal-centered (d-d) excited states in most cases give rise to a non-radiative decay, thus fluorescence is quenched.<sup>[94,96]</sup>



**Figure 1.14** Orbital scheme illustrating the quenching of a photo-excited fluorophore FI\* by a nearby metal center M via an electronic energy transfer (ET) mechanism[94]

Some metal ions have the emission suppressing effect that results in strong quenching of fluorescence. Moreover, quenching metal ions such as  $Hg^{2+}$ ,  $Cu^{2+}$ ,  $Co^{2+}$ ,  $Ni^{2+}$ , and  $Fe^{3+}$  can

interfere with the fluorescent signal of the sensors in detecting other metals.<sup>[97-102]</sup> Because of these quenching tendencies, it is difficult to design a sensor that yields a positive (turn-on) signal. Several strategies have been used to develop turn-on fluorescent sensors for quenching metals, such as separating the ligand moiety from the chromophore via rigid linker<sup>[103, 104]</sup>; the use of PET,<sup>[105, 106]</sup> FRET<sup>[107, 108]</sup> or excimer formation<sup>[109, 110]</sup>; or exploiting the specific reactivity of a given metal ion.<sup>[111, 112]</sup> In this work, separating the ligand moiety from the chromophore which undergoes a spiro lactam close-open process upon iron(III)-binding will be used to develop turn-on fluorescent sensors for iron(III) (see chapter 2 for further information).

### **1.5 Requirements for Fluorescent Sensors in Bioimaging**

Fe<sup>3+</sup>-selective sensors are vast, but there are only a few limited number of the sensors being applied (or were suitable) in cells for visualization of labile iron pools because a reliable fluorescent sensor for imaging in living cells should meet several strict requirements. In this section, these requirements are discussed.

For using in cell studies, sensors should be cell permeable with balanced water/lipid solubility, binding analyte rapidly and ideally reversibly. Sensors should show an increased emission signal (turn-on), and their excitation wavelengths are preferred in the visible range ( $\geq 400$  nm) or near infrared range (650-900 nm). For bioimaging applications, UV excitation can damage cells and causes also interfering background with fluorophores such as NADH, and nucleic acids.<sup>[113]</sup> If a fluorophore exhibits a peak emission of 480 nm or higher, interfering background autofluorescence can be readily removed. Sensors also must be photochemically stable and must not be subject to excessive photobleaching under long time exposure. For animal imaging, both excitation and emission wavelengths should be at the near infrared (NIR) region (650-900 nm) to avoid auto fluorescence from the background.<sup>[114]</sup>



In addition, the sensors should be specific for  $\text{Fe}^{3+}$  in cells. Hard-soft acid base theory (HSAB), Irving-Williams rules, and ligand field geometry are the general inorganic principles for the design of  $\text{Fe}^{3+}$  sensors.<sup>[115]</sup> Moreover, the binding part should possess a binding constant matching the concentration of  $\text{Fe}^{3+}$  in cells. If the binding affinity is too strong, it could remove  $\text{Fe}^{3+}$  ions from storage proteins or essential iron-containing enzymes. On the other hand, if the binding is too weak, it may not bind  $\text{Fe}^{3+}$  in the labile iron pool (LIP) because  $\text{Fe}^{3+}$  coordinates small anions (*e.g.*,  $\text{PO}_4^{3-}$ ,  $\text{CO}_3^{2-}$ , acetate, citrate, nucleotides, and amino acids) in LIP. Sensors also should be insensitive towards Ca (II), Na, Mg (II), and K, all of which are found in micro- to millimolar concentrations in cells.<sup>[116]</sup>

## 1.6 Objective and Organization of the Thesis

None of the sensors reported so far (except our RPE sensor reported in 2012 and described in chapter 2 of the thesis) fulfills all of the criteria that are required for bioimaging of iron ions. This is a challenging task. The overall research goal of this thesis is to develop selective and sensitive "turn-on" and "ratiometric" fluorescent sensors for  $\text{Fe}^{3+}$  imaging in living systems, including live cells and live animals. To fulfill the goals, four different dyes were used as the fluorophores and the binding sites on the fluorophores were created to coordinate with  $\text{Fe}^{3+}$ . Rhodamine B was the first dye used to develop sensors for the detection of  $\text{Fe}^{3+}$  in single cells and they were successfully applied to the cells to determine the subcellular localizations of  $\text{Fe}^{3+}$  in cells, *i.e.*, organelles in cells. Changsha (modified rhodamine) dye was used to synthesize near-infrared sensors to be applied in zebrafish. Cyanine dyes and a modified dye (rhodamine/coumarin hybrid) were used to obtain ratiometric sensors that were used to determine the concentration of  $\text{Fe}^{3+}$  in cells. The sensors were used for visualization of the subcellular distribution and localization of labile  $\text{Fe}^{3+}$  pools in a few cell lines (live human SH-

SY5Y neuroblastoma cells, live human fibroblast cells (ws1), and live bovine aortic endothelial cells (BAEC)). The NIR sensors were also applied to animal models (zebrafish) to detect free Fe<sup>3+</sup> and to specify which organs the Fe<sup>3+</sup> ions are located. With the ratiometric sensors, the concentrations of free Fe<sup>3+</sup> ions in the cells were also determined. Moreover, using the sensors, Fe<sup>3+</sup> transport in fibroblast cells was successfully monitored in real time.

## 1.7 References

1. Bertini I., Gray H. B., Stiefel E. I., Valentine J. S., Biological Inorganic Chemistry; Structure and Reactivity, Sausalite, California, **2007**
2. Roat-Malone, M. Bioinorganic chemistry; a short course, John Wiley and Sons, New Jersey, **2002**, pp.1-3
3. Altamura S., Muckenthaler M. U., J. Alzheimer Dis., **2009**, 16, 879-895
4. Papanikolaou G., Pantopoulos K., Toxicol. Appl. Pharmacol., **2002**, 202, 199-211
5. Arredondo M., Nunez M. T., Mol. Aspects Med., **2005**, 26, 313-327
6. Imlay J. A., Chin S. M., S. Linn, Science, **1988**, 240, 640-642
7. Braun V., Killmann H., Trends Biochem. Sci., **1999**, 24, 104-109
8. Ponka P., Blood, **1997**, 89, 1-25
9. Andrew N. C., N. Engl. J. Med., **1999**, 341, 1986-1995
10. Crichton R., Inorganic Biochemistry of Iron Metabolism; From Molecular Mechanisms to Clinical Consequences, John Wiley and Sons, Baffins Lane, Chichester, **2001**, pp.167-174
11. Shaw G. C., Cope J. J., Li L, Corson K., Hersey C., Ackermann G. E., Gwynn B., Lambert A. J., Wingert R. A., Traver D., Trede N. S., Barut B. A., Zhou Y., Minet E., Donovan A., Brownlie A., Balzan R., Weiss M. J., Peters L. L., Kaplan J., Zon L. I., Paw B. H., Nature, **2006**, 440, 96-100
12. Epsztejn, S.; Glickstein, H.; Picard, V.; Slotki, I. N.; Breuer, W.; Beaumont, C.; Cabantchik, Z. I. Blood, **1999**, 94, 1-12
13. Cabantchik Z. I., Front. Pharmacol., **2014**, 5, 45-56
14. Rouault A. T., Nat. Rev. Neurosci., **2013**, 14, 551-564
15. Andrews N. C., Nat. Rev. Genet., **2000**, 1, 208-217

16. De Domenico I., M. Vaughn B., Li L., Bagley D., Musci G., Ward D. M., Kaplan J., EMBO J., **2006**, 25, 5396-5404
17. Wallander M. L., Leibold E. A., Eisenstein R. S., Biochim. Biophys. Acta, **2006**, 1763, 668-689
18. Breuer W., Shvertsman M., Cabantchik Z. I., Int. J. Biochem. Cell B., **2008**, 40, 350-354
19. Shvartsman M., Kikkeri R., Shanzer A., Cabantchik Z. I., Am. J. Physiol., **2007**, 293, 1383-1394
20. Richardson D. R., Lanea D. J. R., Beckera E. M., Huang M. L.-H., Whitnalla M., Rahmantoa Y. S., Sheftel A. D., Ponkac P., Proc. Natl. Acad. Sci. USA, **2010**, 107, 10775-10785
21. Glickstein H., Ben-El R. B., Link G., Breuer W., Konijn A. M., Hershko C., Nick H. Cabantchik Z. I., Blood, **2006**, 108, 3195-3203
22. Kruszewski M., Mutat. Res., **2003**, 53181-53192
23. Kakhlon O., Cabantchik Z.I., Free Radic. Biol. Med., **2002**, 33, 1037-1046
24. Petrat F., De Groot H., Sustmann R., Rauen U., Biol. Chem., **2002**, 383 489-502
25. Ma Y., Groot H. , Liu Z., Hider R. C., Petrat F., Biochem. J., **2006**, 395, 49-55
26. Bartzokis G., Tishler T. A., Cell. Mol. Biol., **2000**, 46, 821-833
27. Que E. L., Domaille D. W., Chang C. L., Chem. Rev. **2008**, 108, 1517-1549
28. Bradbury M. W. B., J. Neurochem, **1997**, 69, 443-454
29. Smith M. A., Harris P. L. R., Sayre L. M. Perry G., Proc. Natl. Acad. Sci. USA, **1997**, 94, 9866-9868
30. A. V. Kozlov, D. Y. Yegorov, Y. A. Vladimirov, Azizova O. A., Free Radic. Biol. Med., **1992**, 13, 9-16
31. Que E. L., Domaille D. W., Chang C. J., Chem. Rev., **2008**, 108, 1517-1549
32. London R. E., Annu. Rev. Physiol., **1991**, 53, 241-258
33. Zalewski P. D., Forbes T. J. and Betts W. H., Biochem. J., **1993**, 296, 403-408
34. Gryniewicz G., Poenie M., and Tsien R. Y., J. Biol. Chem., **1985**, 260, 3440-3450
35. Epsztejn S., Kakhlon O., Glickslein H., Breuer W., Cabantchik Z. I., Anal. Bio. Chem., **1997**, 248, 31-40
36. Hasinoff B. B., J. Inorg. Biochem., **2003**, 95, 157-164
37. Petrat F., Rauen U., de Groot H., Hepatology, **1999**, 29, 1171-1179
38. Chen J. L., Zhuo S. J., Wu Y. Q., Fang F., Li L., Zhu C. Q., Spectrochim. Acta, Part A, **2006**, 63, 438-443

39. Praveen L., Reddy M. L. P., Varma R. L., Tetrahedron Lett., **2010**, 51, 6626-6629
40. Garcia-Beltran O., Mena N., Yanez O., Caballero J., Vargas V., Nunez M. T., Cassels B. K., Eur. J. Med. Chem., **2013**, 67, 60-63
41. Hirayama T., Okuda K., Nagasawa H., Chem. Sci., **2013**, 4, 1250-1256
42. Au-Yeung H. Y., Chan J., Chantarojsiri T., Chang C. J., J. Am. Chem. Soc., **2013**, 135, 15165-15173
43. Liu J. M., Zheng Q. Y., Yang J. L., Chen C. F., Huang Z. T., Tetrahedron Lett., **2002**, 43, 9209-9212
44. Wolf C., Mei X., Rokadia H. K., Tetrahedron Lett., **2004**, 45, 7867-7871
45. De Costa M. D. P., Jayasinghe W. A. P. A., J. Photochem. Photobiol.A, **2004**, 162, 591-598
46. Peng R., Wang F., Sha Y., Molecules, **2007**, 12, 1191-1201
47. Hu S. L., She N. F., Yin G. D., Guo H. Z., Wu A. X., Yang C. L., Tetrahedron Lett., **2007**, 48, 1591-1594
48. Senthilnithy R., De Costa M. D. P., Gunawardhana H. D., Luminescence, **2009**, 24, 203-208
49. Yao J., Dou W., Qin W., Liu W., Inorg. Chem. Commun., **2009**, 12, 116-118
50. Singh N., Kaur N., Dunn J., MacKay M., Callan J. F., Tetrahedron Lett., **2009**, 50, 953-956
51. Singh N., Kaur N., Callan J. F., J. Fluoresc., **2009**, 19, 649-654
52. Lohani C. R., Kim J. M., Lee K. H., Bioorg. Med. Chem.Lett., **2009**, 19, 6069-6073
53. Lohani C. R., Lee K. H., Sens. Actuators, B, **2010**, 143, 649-654
54. Jung H. J., Singh N., Lee D. Y., Jang D. O., Tetrahedron Lett., **2010**, 51, 3962-3965
55. Wei Y., Qin G., Wang W., Bian W., Shuang S., Dong C., J. Lumin., **2011**, 131, 1672-1676
56. Marenco M. J. C., Fowley C., Hyland B. W., Galindo-Riano D., Sahoo S. K., Callan J. F., J. Fluoresc., **2012**, 22, 795-798
57. Sahoo S. K., Sharma D., Bera R. K., Crisponi G., Callan J. F., Chem. Soc. Rev., **2012**, 41, 7195-7227
58. Chen X., Pradhan T., Wang F., Kim J. S., Yoon J., Chem. Rev., **2012**, 112, 1910-1956
59. Qian X. and Xiao Y., Tetrahedron Lett., **2002**, 43, 2991-2994
60. Hua J., Wang Y. G., Chem. Lett., **2005**, 98-99

61. Sung K., Fu H. K., Hong S. H., *J. Fluoresc.*, **2007**, 17, 383-389
62. Kennedy D. P., Kormos D. M., Burdette S. C., *J. Am. Chem. Soc.*, **2009**, 131, 8578-8586
63. Wang H., Wang D., Wang Q., Li X., C. A. Schalley, *Org. Biomol. Chem.*, **2010**, 8, 1017-1026
64. Lim N. C., Pavlova S. V., Brückner C., *Inorg. Chem.*, **2009**, 48, 1173-1182
65. Lee M. H., Giap T. V., Kim S. H., Lee Y. H., Kang C., Kim J. S., *Chem. Commun.*, **2010**, 46, 1407-1409
66. Aydin Z., Wei Y., Guo M., *Inorg. Chem. Commun.*, **2012**, 20, 93-96
67. Yang Z., She M., Yin B., Cui J., Zhang Y., Sun W., Li J., Shi Z., *J. Org. Chem.*, **2012**, 77, 1143-1147
68. Ji S., Meng X., Ye W., Feng Y., Sheng H., Cai Y., Liu J., Zhu X. Guo Q., *Dalton Trans.*, **2014**, 43, 1583-1588
69. Li Z., Zhang L., Li X., Guo Y., Ni Z., Chen J., Wei L., Yu M., *Dyes Pigm.*, **2012**, 94, 60-65
70. Chen C. H., Hung P. J., Wan C. F., Wu A. W., *Inorg. Chem. Commun.*, **2013**, 38, 74-77
71. Bricks J. L., Kovalchuk A., Trieflinger C., Nofz M., Buschel M., Tolmachev A. I., Daub J., Rurack K., *J. Am. Chem. Soc.*, **2005**, 127, 13522-13529
72. Jung H. J., Singh N., Jang D. O., *Tetrahedron Lett.*, **2008**, 49, 2960-2964
73. Lin W., Long L., Yuan L., Cao Z., Feng J., *Anal. Chim. Acta*, **2009**, 634, 262-266
74. Hao E., Meng T., Zhang M., Pang W., Hou Y. Z., Jiao L., *J. Phys. Chem., A*, **2011**, 115, 8234-8241
75. Marenco M. J. C., Fowley C., Hyland B. W., Hamilton G. R. C., Galindo-Riano D., Callan J. F., *Tetrahedron Lett.*, **2012**, 53, 670-673
76. Diwan U., Kumar A., Kumar V., Upanhyay K. K., *Dalton Trans.*, **2013**, 42, 13889-13896
77. Zhang M., Gao Y., Li M., Yu M., Li F., Li L., Zhu M., Zhang J., Yi T., Huang C., *Tetrahedron Lett.*, **2007**, 48, 3709-3712
78. Fakhri S., Podinovskaia M., Kong X., Schaible U. E., Collins H. L., Hider R. C., *J. Pharm. Sci.*, **2009**, 98, 2212-2226
79. Wang S., Meng X., Zhu M., *Tetrahedron Lett.*, **2011**, 52, 2840-2843
80. Zhang L., Wang J., Fan J., Guo K., Peng X., *Bioorg. Med. Chem. Lett.*, **2011**, 21, 5413-5416
81. Smanmoo S., Nasomphan W., Tangboriboonrat, *Inorg. Chem. Commun.*, **2011**, 14, 351-354
82. Sen S., Sarkar S., Chattopadhyay B., Moirangtham A., Basu A., Dhara K., Chattopadhyay P., *Analyst*, **2012**, 137, 3335-3342

83. Wei Y., Aydin Z., Yi Z., Liu Z., Guo M., ChemBioChem, **2012**, 13, 1569-1573
84. Liu S. R., Wu S. P., Sensor Actuat. B-Chem., **2012**, 171-172, 1110-1116
85. Chung P. K., Liu S. R., Wang H. F., Wu S. P., J. Fluoresc., **2013**, 23, 1139-1145
86. Chen W. D., Gong W. T., Ye Z. Q., Lin Y., Ning G. L., Dalton Trans., **2013**, 42, 10093-10096
87. Saleem M., Abdullah R., Ali A., Park B. J., Choi E. H, Hong I. S., Lee K. H., Bioorg. Med. Chem., **2014**, 22, 2045-2051
88. En D., Guo Y., Chen B. T., Dong B., Peng M. J., RSC Adv., **2014**, 4, 248-253
89. Kar C., Samanta S., Mukherjee S., Datta B. K., Ramesh A., Das G., New J. Chem., **2014**, 38, 2660-2669
90. Berezin M. Y., Achilefu S., Chem. Rev., **2010**, 110, 2641-2684
91. Valeur B., Molecular Fluorescence-Principles and Applications; Wiley-VCH, Weinheim, **2002**
92. Smith N. A., Sadler P. J., Phil. Trans. R. Soc. A, **2013**, 371, 20120519
93. Farrer N. J., Salassa L., Sadler P. J., Dalton Trans., **2009**, 48, 10690-10701
94. Sauvage J. P., Transition Metals in Supramolecular Chemistry; Perspectives in supramolecular Chemistry Volume 5, Wiley-VCH, **1999**, pp. 93-100
95. Bergonzi R., Fabbri L., Licchelli M., Mangano C., Coord. Chem. Rev., **1998**, 170, 31-46
96. Kim J. S., Quang T., Chem. Rev., **2007**, 107, 3780-3799
97. Nolan E. M., Lippard S. J., Chem. Rev., **2008**, 108, 3443-3480
98. Fabbri L., Licchelli M., Pallavicini P., Sacchi D., Taglietti A., Analyst, **1996**, 121, 1763-1768
99. Fabbri L., Licchelli M., Mancin F., Pizzeghello M., Rabaioli G., Taglietti A., Tecilla P., Tonellato U., Chem. Eur. J., **2002**, 8, 94-101
100. Czarnik A. W., Acc. Chem. Res., **1994**, 27, 302-308
101. Chae M. Y., Czarnik A. W., J. Am Chem. Soc., **1992**, 114, 9704-9705
102. Tan S. S., Kim S. J., Kool E. T., J. Am. Chem. Soc., **2011**, 133, 2664-2671
103. Tumambac G. E., Rosencrance C. M., Wolf C., Tetrahedron, **2004**, 60, 11293-11297
104. Grabchev I., Chovelon J. M., Quian X., New J. Chem., **2003**, 27, 337-340
105. Dodani S. C., He Q., Chang C. J., J. Am. Chem. Soc., **2009**, 131, 18020-18021
106. Ghosh P., Bharadwaj P. K., Roy J., Ghosh S., J. Am. Chem. Soc., **1997**, 119, 11903-11909
107. Coskun A., Akkaya E. U., J. Am. Chem. Soc., **2006**, 128, 14474-14475

- 108.** Mokhir A., Kiel A., Herten D. P., Kraemer R., *Inorg. Chem.*, **2005**, 44, 5661-5666
- 109.** Yang R. H., Chan W. H., Lee A. W. M., Xia P. F., Zhang H. K., Li K., *J. Am. Chem. Soc.*, **2003**, 125, 2884-2885
- 110.** Sankaran N. B., Banthia S., Das A., Samanta A., *New J. Chem.*, **2002**, 26, 1529-1531
- 111.** Song F., Watanabe S., Floreancig P. E., Koide K., *J. Am. Chem. Soc.*, **2008**, 130, 16460-16461
- 112.** Zhao Y., Lin Z., He C., Wu H., Duan C., *Inorg. Chem.*, **2006**, 45, 10013-10015
- 113.** Sugasawa K., Masutani C., Hanaoka F., *J. Biological Chem.*, **1993**, 268, 9098-9104
- 114.** Miwa M., *Open Surg. Oncol. J.*, **2010**, 2, 26-28
- 115.** Liu Z., He W., Guo Z., *Chem. Soc. Rev.*, **2013**, 42, 1568-1600
- 116.** Bertini I., Gray H. B., Stiefel E. I., Valentine J. S., *Biological Inorganic Chemistry; Structure and Reactivity*, Sausalite, California, **2007**, pp. 60-61

## CHAPTER 2

### A RHODAMINE BASED TURN-ON FLUORESCENT SENSOR RPE FOR IMAGING LABILE $\text{Fe}^{3+}$ IN CELLS

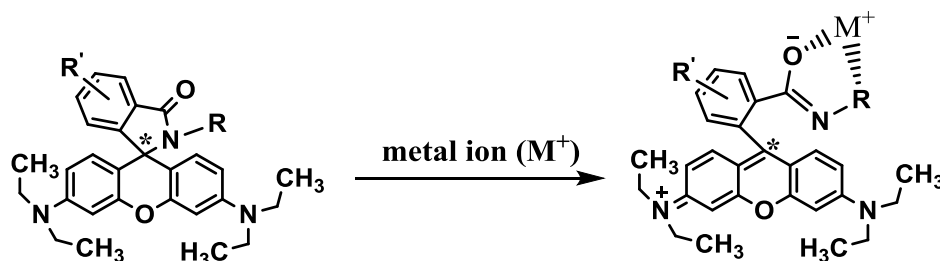
#### 2.1 Introduction

Fluorescence sensors are one of most powerful tools for detecting metal ions in biological systems and has already proven useful for imaging metal ions such as  $\text{Ca}^{2+}$ ,  $\text{Zn}^{2+}$ , and  $\text{Mg}^{2+}$ .<sup>[1-5]</sup> Traditional fluorescence chemosensors utilize photophysical changes produced by the following mechanisms: photo-induced electron transfer (PET),<sup>[6]</sup> photo-induced charge transfer (PCT),<sup>[7]</sup> excimer formation,<sup>[8]</sup> and fluorescence resonance energy transfer (FRET).<sup>[9]</sup> The demand for selective fluorescent sensors for iron ions in cellular system is high but the available fluorescent sensors are very limited and suffer from various drawbacks for cellular imaging. Fluorescent probes that exhibit a turn-on emission increase or a shift in excitation/emission profiles response to iron ions are preferred over a turn-off emission-quenching response due to their better spatial resolution under a light microscope. However, it has been difficult to obtain these probes owing to the paramagnetic quenching nature of iron ions (both  $\text{Fe}^{2+}$  and  $\text{Fe}^{3+}$ ) in aqueous solution.<sup>[10]</sup> Recently, rhodamine derivatives have been used as turn-on sensors for metal ions.<sup>[11-16]</sup>

The mechanism of action of the recently reported rhodamine-based “turn-on” metal sensors has been proposed to be based on producing the ring-opened form of rhodamine.<sup>[17-19]</sup> A deeper understanding of the fluorescent turn-on mechanism is proposed here (Scheme 2.1): the ring-closed spirolactam form of rhodamine is non-fluorescent due to the fact that the carbon atom at the 9-position of the molecule (indicated by \* in Scheme 2.1) has  $\text{sp}^3$



hybridization, which breaks the conjugation in the xanthene fluorophore moiety; upon metal coordination (via the carbonyl and “R” group) the spirolatam ring is broken, and the carbon at 9-position changes to  $sp^2$  hybridization that restores the conjugation in the xanthene fluorophore moiety and consequently the molecule becomes fluorescent, *i.e.* “turn-on”. Because the metal (*e.g.*, Fe) center is at a distance from the xanthene fluorophore moiety, the paramagnetic quenching effect is insignificant compared to the fluorescent enhancement induced by restoring the conjugation in the 3-ring xanthene fluorophore moiety, thus a net fluorescent “turn-on” is observed. This interesting mechanism may be called as “coordination-induced fluorescent enhancement (or activation) (CIFE or CIFA)”.<sup>[14-18]</sup>



**Scheme 2.1** Mechanism of fluorescence “turn-on” metal sensors based on “coordination-induced fluorescent enhancement (or activation) (CIFE or CIFA) process

Here we describe the properties of a highly selective, sensitive, and reversible off-on fluorescent  $Fe^{3+}$  sensor RPE<sup>1</sup> (Scheme 2.2) which can be used to visualize native  $Fe^{3+}$  in live cells. The unique reversible turn-on property and high sensitivity of RPE allows observation of the endogenous exchangeable  $Fe^{3+}$  pools at subcellular resolution for the first time in live human neuroblastoma SH-SY5Y cells. This cell line has been generally used as a cellular model to study

<sup>1</sup>This chapter is based on the published work (ChemBioChem, **2012**, 13, 1569-1573)

Parkinson's disease (PD) and Alzheimer's disease (AD) where abnormal iron accumulation in the brain has been implicated in their pathogenesis.<sup>[20]</sup>

## **2.2 Experimental**

### **2.2.1 Materials and Reagents**

All the reagents and solvents were of the highest commercial quality and were used without further purification. Acetonitrile anhydrous (99.8 % Sigma-Aldrich), DMF anhydrous (99.8 % Sigma-Aldrich), 1,2-dichloro ethane anhydrous (99.8 % Sigma-Aldrich), and double-distilled water were used as solvents. Rhodamine B base was purchased from Sigma-Aldrich. Methyl 6-aminopicolinate (98 %) was purchased from Combi-blocks. MitoTracker Green FM, LysoTracker Blue DND-22, and the nuclear stain Hoechst 33258 were purchased from Life Technologies and used in accordance with the manufacturer's protocols.

### **2.2.2 Instrumentation**

<sup>1</sup>H and <sup>13</sup>C NMR spectra were recorded on a Bruker DRX-300 spectrometer. Chemical shifts are reported in delta ( $\delta$ ) unit per million (ppm) downfield tetramethylsilane. Splitting patterns are abbreviated as follows: s, singlet; d, doublet; t, triplet; q, quartet; m, multiplet; br, broad.

ESI-MS analyses were performed on a PerkinElmer API 150EX mass spectrometer. UV/Vis spectra were recorded on a Perkin-Elmer Lambda 25 spectrometer at 298 K. Fluorescence spectra were recorded on a Perkin-Elmer LS55 luminescence spectrometer at 293 K. The excitation wavelengths and filters used were indicated in the figures. The pH measurements were carried out on a Corning pH meter equipped with a Sigma-Aldrich micro combination electrode calibrated with standard buffer solution.

### 2.2.3 Synthesis

#### 2.2.3.1 Synthesis of RPE: Methyl 6-(3',6'-bis(diethylamino)-3-oxospiro-[isoindoline-1,9'-

**xanthen]-2-yl)picolinate.** To a solution of rhodamine B base (1.0 g, 2.3 mmol) in 10 mL of 1,2-dichloroethane, phosphorus chloride (1.1 g, 6.9 mmol) was added drop wise over a period of 10 min. The solution was stirred and refluxed for 5 h, and then cooled to room temperature. The solvent was removed by vacuum evaporation, yielding the rhodamine acid chloride, which was dissolved into 30 mL dry acetonitrile and directly used in the next step. This solution was added drop wise over one h into a solution of methyl 6-aminopicolinate (0.35 g, 2.3 mmol), and then stirred overnight to obtain a pink precipitate. The crude product was further purified using silica gel chromatography (hexane/ethyl acetate, 3:1 v/v), affording the pure RPE as a pale yellow solid (0.45 g, yield 34%). <sup>1</sup>H NMR (CDCl<sub>3</sub>, 300 MHz): δ=8.72 (d, J=8.1 Hz, 1 H), 8.00 (d, J=6.5 Hz, 1 H), 7.68-7.57 (m, 2 H), 7.52-7.43 (m, 2H), 7.13 (d, J=6.8 Hz, 1 H), 6.44-6.36 (m, 4H), 6.11 (d, J=8.7 Hz, 2 H), 3.91 (s, 3H), 3.29 (m, 8 H), 1.12 ppm (t, J=7.0 Hz, 12H); <sup>13</sup>C NMR (CDCl<sub>3</sub>, 75 MHz): δ=168.8, 154.3, 153.3, 150.1, 148.3, 145.7, 137.7, 133.8, 129.6, 128.1, 127.4, 124.5, 123.2, 119.9, 118.9, 108.1, 107.097.7, 66.5, 51.7, 44.3, 12.7 ppm; ESI-MS (positive mode) m/z 577.3 [M+H]<sup>+</sup>.

#### 2.2.4 Procedures for Metal Ion Sensing

Solutions of metal ions of Ni<sup>2+</sup>, Cu<sup>2+</sup>, Zn<sup>2+</sup>, Pb<sup>2+</sup>, Fe<sup>2+</sup>, Fe<sup>3+</sup>, Cr<sup>3+</sup>, Hg<sup>2+</sup>, Mn<sup>2+</sup>, Ag<sup>+</sup>, Co<sup>2+</sup>, K<sup>+</sup>, Na<sup>+</sup>, Ca<sup>2+</sup>, and Mg<sup>2+</sup> (10 mM) were prepared by dissolving their chloride or nitrate salts into double-distilled water (freshly for Fe(II) and Fe(III) with 100 mM HCl). Solution of Cu<sup>+</sup> (10 mM) was prepared freshly by dissolving tetrakis(acetonitrile)copper(I) (Sigma-Aldrich) into double-distilled water. The sensor is stable in acetonitrile (ACN) solution and a stock solution of RPE (500 μM) was prepared in acetonitrile and diluted to 20 μM with ACN/Tris-HCl buffer (10 mM,

pH 7.32, v/v 2:1) before use. In selectivity experiments, the test samples were prepared by appropriate amount of metal ion stocks into 1 ml solution of sensors.

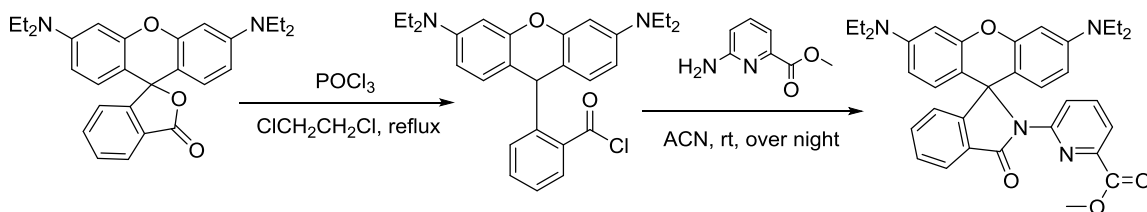
### **2.2.5 Cell Culture and Confocal Imaging**

Human SH-SY5Y neuroblastoma cells were obtained from ATCC (American Type Culture Collection). Cells were maintained in a 1:1 mixture of Eagle's Minimal Essential medium (ATCC) and Ham's F12 medium (ATCC) supplemented with 10% fetal bovine serum (FBS, ATCC) without antibiotics and incubated at 37 °C in a humidified 5% CO<sub>2</sub> atmosphere. The cells were routinely subcultured using 0.05% trypsin-EDTA solution (ATCC). The cells were seeded onto 2-chamber slides for 48 h at 5x10<sup>4</sup> cells/chamber and grown until each chamber was 20-30% confluent. A stock solution of RPE (1 mM in acetonitrile) was diluted to a concentration of 10 μM in culture medium without FBS. Cell culture medium was removed from the chambers and replaced with fresh medium containing RPE (5-10 μM). The fluorescence responses of the sensor in living cells were measured under a Zeiss LSM 710 laser scanning confocal microscope. For images with the RPE sensor, the excitation wavelength of the laser was 543 nm and emission was integrated over the range 547-703 nm. For images with MitoTracker Green FM, LysoTracker Blue DND-22 and Hoechst 33258, the excitation wavelengths recommended by the manufacturer were used (483 nm for MitoTracker, 405nm for LysoTracker and 405 nm for Hoechst 33258). Emissions were integrated at 492-548 nm (MitoTracker), 409-484 nm (LysoTracker) and 426-535 nm (Hoechst 33258), respectively. The REUSE function controlled by Zeiss software was applied to guarantee that all spectra were recorded under the same instrumental conditions.

## 2.3 Results and Discussion

### 2.3.1 Design and Synthesis of RPE

The initial goal of the synthesis of RPE was to develop a rhodamine-based sensor for  $\text{Fe}^{3+}$  by adding a coordination site for  $\text{Fe}^{3+}$  ions. The design of RPE was carefully developed with a coordination site of a nitrogen atom and two oxygen atoms (O/N/O receptor moiety). RPE was synthesized via a two-step procedure as outlined in Scheme 2.2 with an overall yield of 34 %. It was characterized by  $^1\text{H}$  NMR,  $^{13}\text{C}$  NMR, and ESI-MS.



**Scheme 2.2** Synthesis route for RPE

### 2.3.2 Spectroscopic and Selectivity Studies

Selectivity is a very important parameter to evaluate the performance of a fluorescence sensor. In this section, the selectivity and spectroscopic properties of the sensor were investigated. The colorless compound RPE displays almost no absorption peak in the visible range ( $>400$  nm). The changes in UV-vis spectra after the addition of various metal ions are shown in Figure 2.1. Only the addition of  $\text{Fe}^{3+}$  to the solution of RPE showed an obvious pink color with an absorption peak at 559 nm in  $\text{ACN}/\text{Tris-HCl}$  buffer (10 mM, pH 7.32, v/v 2:1). The color change for  $\text{Fe}^{3+}$  is readily detected visually. Compared with that of  $\text{Fe}^{3+}$ , other metal ions did not induce any changes in UV-vis absorption. Only  $\text{Fe}^{2+}$  showed minor response to RPE. This may be due to the presence of residue  $\text{Fe}^{3+}$  in the  $\text{Fe}^{2+}$  solution resulted from partially oxidation of  $\text{Fe}^{2+}$  in the aerobic environment.

The changes in fluorescence spectra of RPE with the addition of different metal ions in ACN/Tris-HCl buffer (10 mM, pH 7.32, v/v 2:1) are shown in Figure 2.2. RPE shows very weak fluorescence in the 400-600 nm range in the absence of metal ions. When  $\text{Fe}^{3+}$  was added into the solution of RPE, a large fluorescence enhancement at 585 nm was observed, which attributed to the spirolactam ring opening, induced by the complexation of  $\text{Fe}^{3+}$ . The emission intensity enhancement at 585 nm is greater than 10-fold with 1.0 equiv of  $\text{Fe}^{3+}$ , suggesting that RPE is a great turn-on fluorescent sensor for  $\text{Fe}^{3+}$ . In contrast to  $\text{Fe}^{3+}$ , other metal ions such as  $\text{Zn}^{2+}$ ,  $\text{Cr}^{3+}$ ,  $\text{Ni}^{2+}$ ,  $\text{Hg}^{2+}$ ,  $\text{Fe}^{2+}$ ,  $\text{Mn}^{2+}$ ,  $\text{Ag}^+$ ,  $\text{Pb}^{2+}$ ,  $\text{Cu}^+$ ,  $\text{Cu}^{2+}$ ,  $\text{Co}^{2+}$ ,  $\text{Na}^+$ ,  $\text{K}^+$ ,  $\text{Mg}^{2+}$ , and  $\text{Ca}^{2+}$  did not induce any spectral response under identical conditions. Similar as that observed by UV-vis, only  $\text{Fe}^{2+}$  showed a minor enhancement in fluorescence under these conditions.

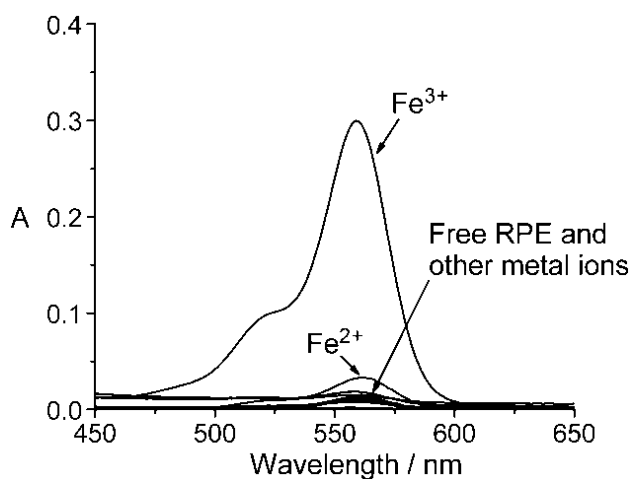


**Figure 2.1** Absorption responses of 20  $\mu\text{M}$  RPE to various metal ions (20  $\mu\text{M}$  for  $\text{Zn}^{2+}$ ,  $\text{Cr}^{3+}$ ,  $\text{Ni}^{2+}$ ,  $\text{Hg}^{2+}$ ,  $\text{Fe}^{3+}$ ,  $\text{Mn}^{2+}$ ,  $\text{Ag}^+$ ,  $\text{Pb}^{2+}$ ,  $\text{Fe}^{2+}$ ,  $\text{Cu}^+$ ,  $\text{Cu}^{2+}$ , and  $\text{Co}^{2+}$ ; 100  $\mu\text{M}$  for  $\text{Na}^+$ ,  $\text{K}^+$ ,  $\text{Mg}^{2+}$ , and  $\text{Ca}^{2+}$ ) in ACN/Tris-HCl buffer (10 mM, pH 7.3, v/v 2:1)

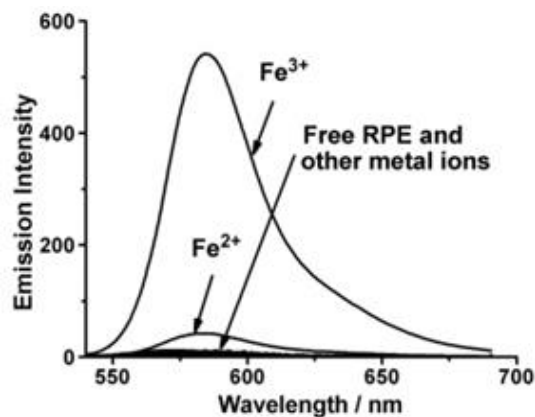


**Figure 2.2** Fluorescence response ( $\lambda_{Ex}/\lambda_{Em}$  510/580 nm, filter 515 nm) of 20  $\mu\text{M}$  RPE to various metal ions (20  $\mu\text{M}$  for  $\text{Zn}^{2+}$ ,  $\text{Cr}^{3+}$ ,  $\text{Ni}^{2+}$ ,  $\text{Hg}^{2+}$ ,  $\text{Fe}^{3+}$ ,  $\text{Mn}^{2+}$ ,  $\text{Ag}^+$ ,  $\text{Pb}^{2+}$ ,  $\text{Fe}^{2+}$ ,  $\text{Cu}^+$ ,  $\text{Cu}^{2+}$ , and  $\text{Co}^{2+}$ ; 100  $\mu\text{M}$  for  $\text{Na}^+$ ,  $\text{K}^+$ ,  $\text{Mg}^{2+}$ , and  $\text{Ca}^{2+}$ ) in ACN/Tris-HCl buffer (10 mM, pH 7.3, v/v 2:1)

Rhodamine-based sensors also give response to hydrogen ions. A good sensor for bioimaging should be stable in biological pH range.<sup>[5]</sup> The effect of pH on the stability of the sensors were investigated at different pHs and monitored by absorption and fluorescence spectra. The pH of the solutions was adjusted by adding HCl into the solutions. The fluorescence of RPE at different pH values was plotted in Figure 2.3 which shows that the sensor is stable over the biological pH range down to pH 5.5 while the Fe(III)-complex is even stable at pH < 4.0. Thus, RPE may be applied in bioimaging.

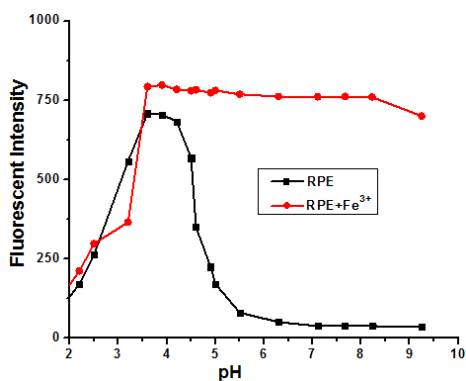


**Figure 2.3** Variation of fluorescence intensity (585 nm) of RPE and RPE+Fe(III) (20  $\mu\text{M}$  each) at various pH values in ACN/ $\text{H}_2\text{O}$  (2/1, v/v) solution

The interferences from a few other metal ions were examined for the ability of RPE in detecting  $\text{Fe}^{3+}$ . Upon the addition of 1 equiv of  $\text{Fe}^{3+}$  into solutions containing one of the other metal ions tested. The fluorescence (gray bars in Figure 2.4) was activated and the intensity increased to a level similar to that observed in the presence of  $\text{Fe}^{3+}$  only (the black bars in Figure 2.4). This demonstrated that these metal ions did not interfere with the response of  $\text{Fe}^{3+}$  to RPE.

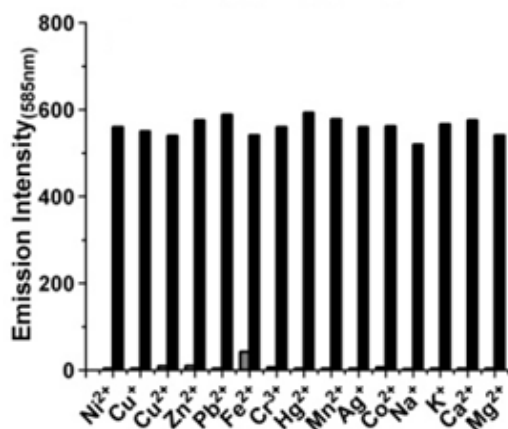


**Figure 2.4** Fluorescence responses of 20  $\mu\text{M}$  RPE to the presence of various metal ions (gray bar) and the subsequent addition of  $\text{Fe}^{3+}$  (black bar) in the ACN/Tris buffer; the bars represent the fluorescence intensity at 585 nm.

### 2.3.3 Binding Studies

Besides metal-selectivity, the affinity between the sensor and the metal ion is also an important factor to be considered in bioimaging. The binding constant, which describes the strength of binding between the sensor and metal cations, is also important for biological application of the fluorescent sensors. The sensor should have an appropriate binding constant with the metal ions in study in biological system.<sup>[21-23]</sup> Before determining the binding constants, the stoichiometry between the probes (sensors) and the metal cations should be examined first. Researchers use several methods to determine the stoichiometry between sensors, metal cations.<sup>[24-27]</sup> RPE was designed to coordinate with metal ions via two oxygen atoms and one



nitrogen atom as donors with the formation of one five-membered, and one six-membered chelate rings. The stoichiometry of binding between RPE and  $\text{Fe}^{3+}$  was investigated with Job's method<sup>[24-27]</sup> and absorption titration. EDTA titration experiments were carried out to determine the reversibility of RPE-  $\text{Fe}^{3+}$  binding.

Job's method was applied to study the binding stoichiometry between RPE and  $\text{Fe}^{3+}$  and monitored by the absorbance at 559 nm. The Job's plot (Figure 2.5) using a total concentration of 20  $\mu\text{M}$  RPE and  $\text{Fe}^{3+}$  in ACN/Tris-HCl buffer (10 mM, pH 7.32, v/v 2:1) solution exhibited a maximum absorbance when the molecular fractions of  $\text{Fe}^{3+}$  and RPE were close to 50 % , suggesting a 1:1 stoichiometry for the binding of RPE and  $\text{Fe}^{3+}$ .

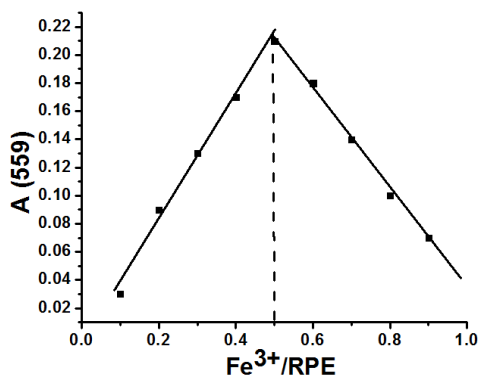


**Figure 2.5** Job plot. The total concentrations of RPE and  $\text{Fe}^{3+}$  were kept constant at 20  $\mu\text{M}$  and the absorption intensity was measured at 559 nm in the ACN/Tris buffer.

Typical UV-vis titration spectra for RPE with  $\text{Fe}^{3+}$  in ACN/Tris-HCl buffer (10 mM, pH 7.32, v/v 2:1) were shown in Figure 2.6. With the addition of  $\text{Fe}^{3+}$ , the solution became red and an absorption band appeared at 559 nm and increased in intensity. The absorbance titration curve showed a typical sigmoidal curve; inflecting at 1 equiv of  $\text{Fe}^{3+}$  and saturation of the absorbance was at >1.0 equiv of  $\text{Fe}^{3+}$ . The titration experiments indicated that a 1:1 complex was formed

between RPE and  $\text{Fe}^{3+}$ . The binding constant for the formation of this complex was determined to be  $1.9 \times 10^7 \text{ M}^{-1}$  ( $\log K = 7.3$ ) using a procedure described previously.<sup>[28]</sup>

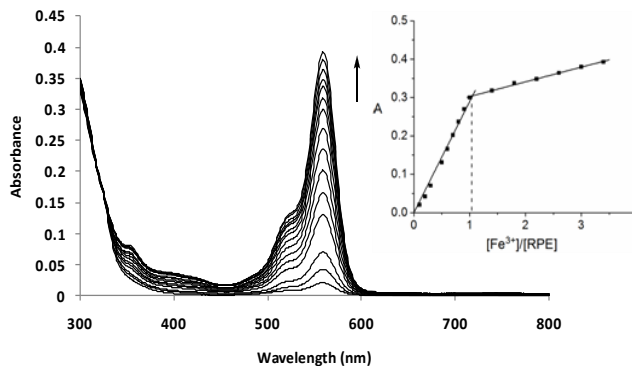


**Figure 2.6** Titration of 20  $\mu\text{M}$  RPE with increasing concentrations of  $\text{FeCl}_3$  (0, 2, 4, 6, 10, 12, 14, 16, 18, 20, 28, 36, 44, 52, 60, and 80  $\mu\text{M}$ , respectively) in ACN/Tris-HCl buffer (10 mM, pH 7.32, v/v 2:1)

Reversibility experiments were carried out by adding EDTA to the PRE- $\text{Fe}^{3+}$  complex in ACN/Tris-HCl buffer (10 mM, pH 7.32, v/v 2:1. In the absence of EDTA, the complex was red and fluorescent. After adding EDTA, the absorption of the complex decreased in intensity and finally, disappeared (Figure 2.7), suggesting a reversible binding between RPE and  $\text{Fe}^{3+}$ . A possible mechanism for the reaction and the binding mode are shown in Scheme 2.3.

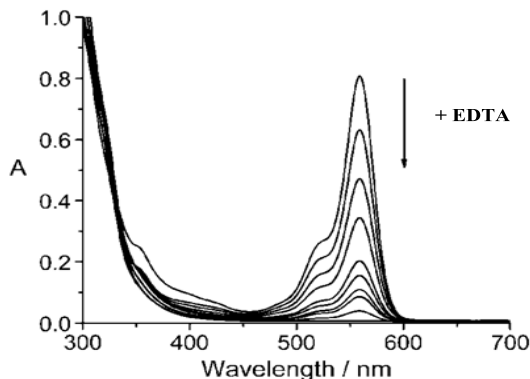
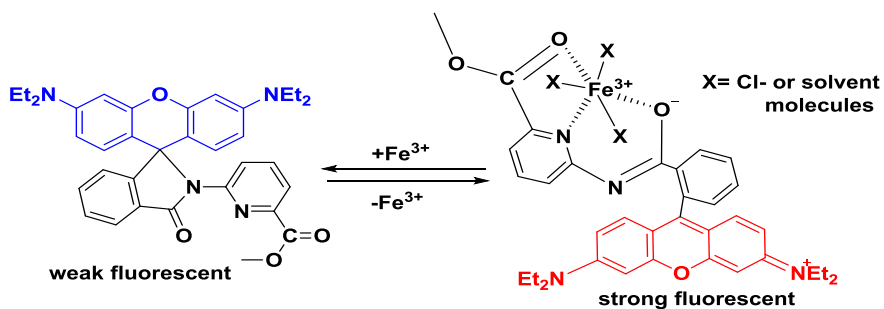


**Figure 2.7** Treatment of 40  $\mu\text{M}$  RPE- $\text{Fe}^{3+}$  complex with increasing concentration of EDTA (0, 4, 8, 12, 16, 20, 24, 28, 32, and 40  $\mu\text{M}$ , from top to bottom) in ACN/Tris-HCl buffer (10 mM, pH 7.32, v/v 2:1)



**Scheme 2.3** Proposed 1:1 binding mode of RPE with  $\text{Fe}^{3+}$  in ACN/Tris-HCl buffer (10 mM, pH 7.32, v/v 2:1)

### 2.3.4 Biological Imaging Studies

*In vitro* studies showed that the ability of RPE to detect  $\text{Fe}^{3+}$  with excellent selectivity. To examine this ability in live cells, human SH-SY5Y neuroblastoma cells were used for  $\text{Fe}^{3+}$  detection in cells (The cell imaging work was performed in collaboration with Dr. Y. Wei and Mr. Y. Zhang in the lab). The cell permeability of RPE was examined first. 10  $\mu\text{M}$  RPE was added into the culture medium containing the cells and an immediate time series scanning were performed. Initially, no intracellular fluorescence was detected, and a fluorescence turn-on triggered by endogenous  $\text{Fe}^{3+}$  was observed in cells after 10 min incubation and fluorescence intensity reached to maxima after  $\sim 30$  min incubation (Figure 2.8).

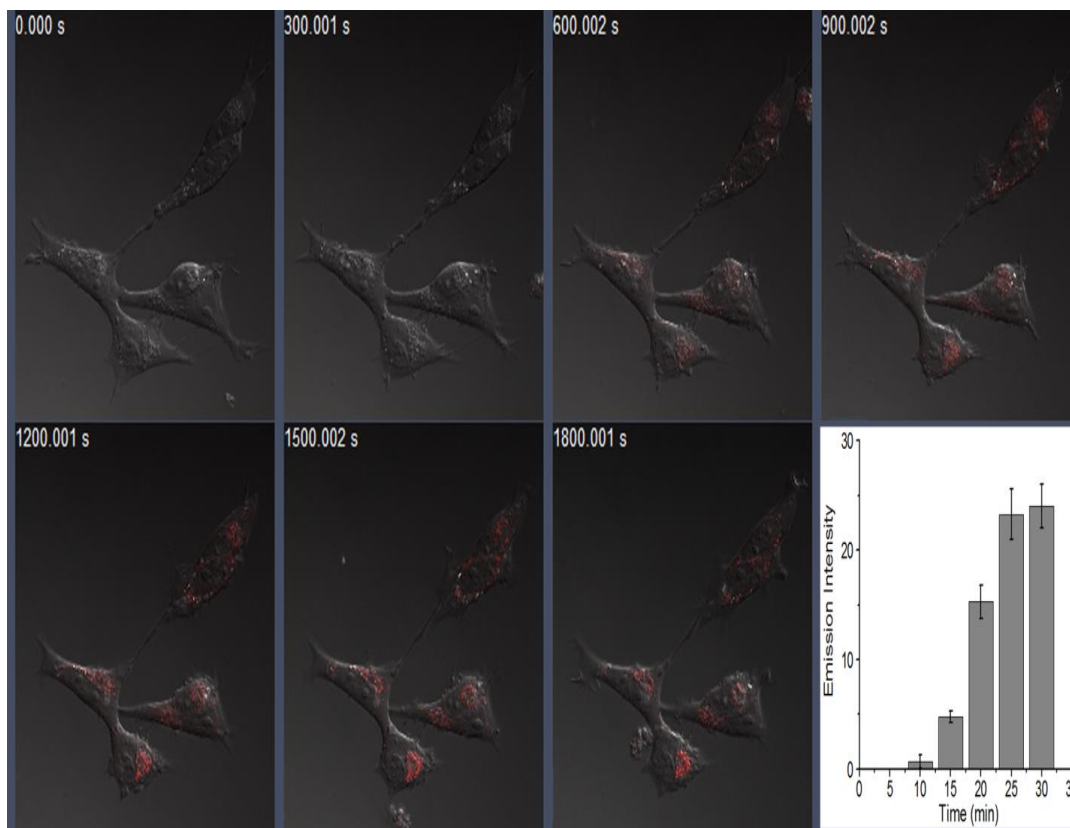


**Figure 2.8** Confocal microscopy images of live Human SH-SY5Y neuroblastoma cells treated with 10  $\mu$ M RPE in 1:1 mixture of Eagles Minimal Essential medium (ATCC) and Ham's F12 medium (ATCC) for 5, 10, 15, 20, 25, and 30 min. Fluorescence intensity collected at 547-703 nm.

A second experiment was carried out to determine whether the cells were viable throughout the imaging experiments. DIC images plus co-staining with Hoechst 33258 confirmed that the cells were viable throughout the imaging experiments with RPE (Figure 2.9). Hoechst 33258 is also used to visualize nuclei in cells.<sup>[29]</sup>

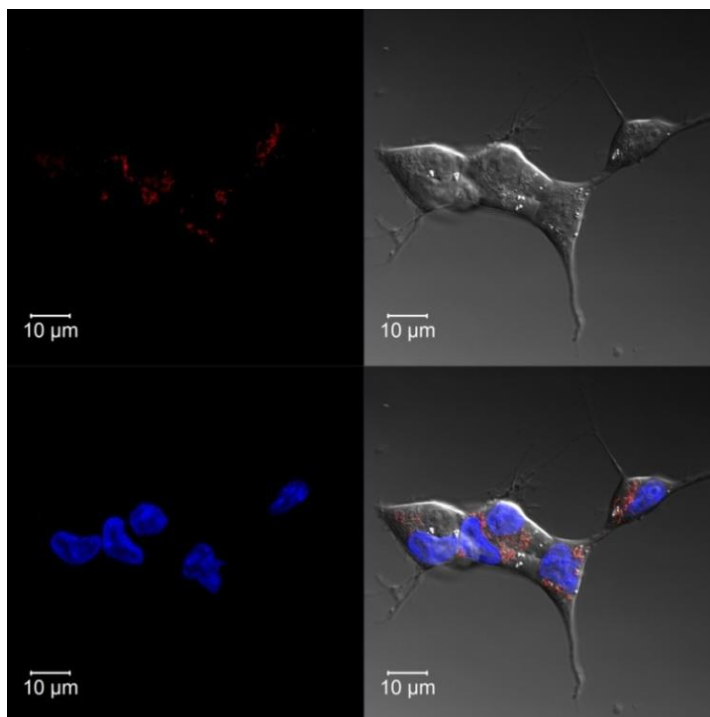


**Figure 2.9** Confocal microscopy images of live human SH-SY5Y neuroblastoma cells treated with RPE (10  $\mu$ M, 30 min) and Hoechst 33258 (2  $\mu$ g/mL, 30 min) in a 1:1 mixture of Eagles Minimal Essential medium (ATCC) and Ham's F12 medium (ATCC) for 5, 10, 15, 20, 25, and 30 minutes. Fluorescence intensities were collected at 547-703 nm (for RPE) and 426-535 nm (for Hoechst 33258).

In the first cell imaging experiment, the turn-on fluorescence is likely triggered by endogenous labile  $\text{Fe}^{3+}$ . Another possibility might be the acidic environment of certain intracellular organelles (*e.g.*, lysosomes/endosomes), as low pH can also trigger the turn-on response of rhodamine-based sensors.<sup>[30,31]</sup> To look into these possibilities carefully, we used two approaches: first, loading the cells with  $\text{Fe}^{3+}$  and second, depletion of  $\text{Fe}^{3+}$  by cell-permeable  $\text{Fe}^{3+}$ -specific chelators. The fluorescence changes under both conditions were carefully monitored. Figure 2.10 compares the confocal fluorescence images of RPE in human SH-SY5Y cells before and after being loaded with 20  $\mu$ M  $\text{Fe}^{3+}$ . Iron(III)-8-hydroxyquinoline complex (Fe(8-HQ)) was used to enhance membrane permeability of the metal ion.<sup>[32]</sup> The  $\text{Fe}^{3+}$ -loaded human SHSY5Y cells clearly showed brighter and more widely distributed fluorescence

signals in localized areas within the cytosol (Figure 2.10), suggesting a positive response of RPE to elevated labile  $\text{Fe}^{3+}$  levels in the  $\text{Fe}^{3+}$ -loaded cells.

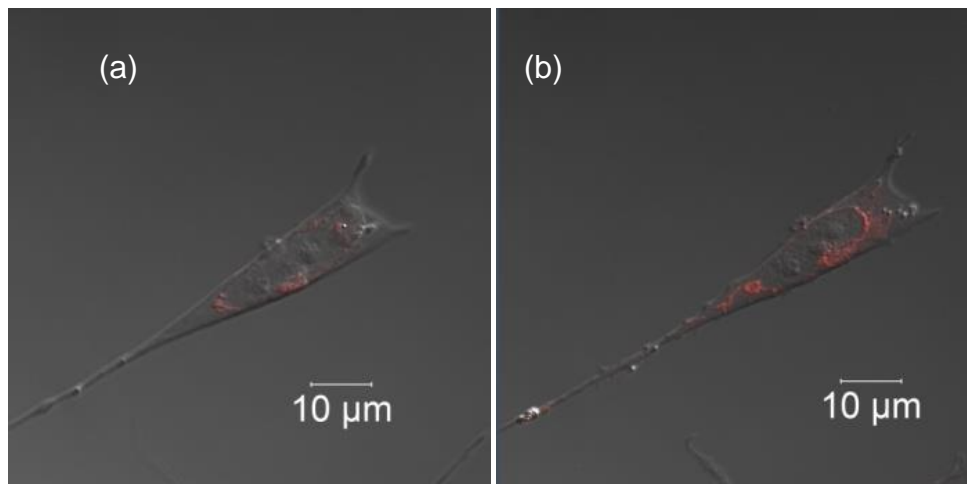


**Figure 2.10** Confocal microscopy images (with DIC) of live human SH-SY5Y neuroblastoma cells treated with (a) 10  $\mu\text{M}$  RPE sensor after 30 min incubation (b) the cells were then incubated with  $\text{Fe}^{3+}$  (20  $\mu\text{M}$  Fe(8-HQ)) for 30 min. The brighter and more widely distributed fluorescence signals in (b) suggest elevated  $\text{Fe}^{3+}$  levels in  $\text{Fe}^{3+}$ -loaded human SH-SY5Y cells. Fluorescence intensity was collected at 547-703 nm (for RPE).

To deplete labile  $\text{Fe}^{3+}$  from cells, the SH-SY5Y cells that had been dyed with RPE were treated with a cell-permeable  $\text{Fe}^{3+}$ -chelator pyridoxal isonicotinoyl hydrazone (PIH) which depletes endogenous labile iron in cells.<sup>[33]</sup> The observed fluorescence was reversed in a time-dependent manner (Figure 2.11). If the cellular labile  $\text{Fe}^{3+}$  were pre-depleted (by overnight incubation with another cell-permeable  $\text{Fe}^{3+}$ -chelator salicylaldehyde isonicotinoyl hydrazone (SIH)<sup>[34]</sup>), treating the cells with RPE revealed no fluorescence response (Figure 2.12). These data, together with those from  $\text{Fe}^{3+}$ -loaded cells (Figure 2.10) demonstrate that the fluorescence response of RPE in cells is triggered by cellular chelatable  $\text{Fe}^{3+}$ , not by acidic pH, thus confirming that RPE can detect not only endogenous labile  $\text{Fe}^{3+}$  in the cells but also the dynamic changes of  $\text{Fe}^{3+}$  in the cells.

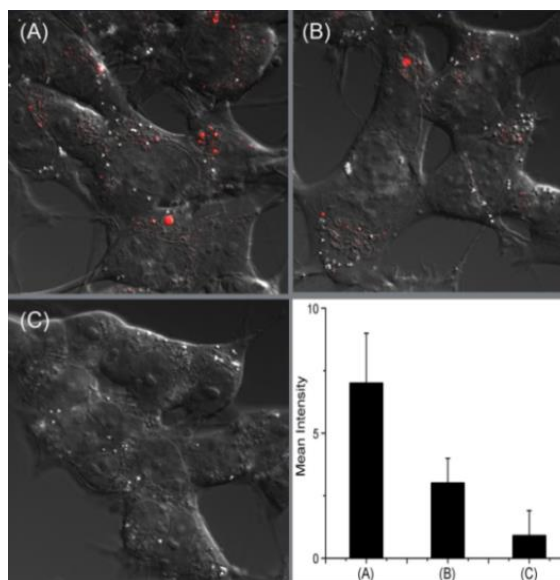


**Figure 2.11** Confocal microscopy images (with DIC) of live human SH-SY5Y neuroblastoma cells treated with (A) 5  $\mu\text{M}$  RPE sensor after 40 min incubation (B) the cells were then incubated with 100  $\mu\text{M}$   $\text{Fe}^{3+}$ -chelator pyridoxalisonicotinoyl hydrazone (PIH) for 4 h. (C) after overnight incubation with 100  $\mu\text{M}$  PIH (D) Bar chart of the mean intensity of (A), (B) and (C). Fluorescence intensity was collected at 547-703 nm (for RPE).



**Figure 2.12** Confocal microscopy images (with DIC) of live human SH-SY5Y neuroblastoma cells with prior iron depletion by 200  $\mu\text{M}$  cell permeable  $\text{Fe}^{3+}$ -chelator salicylaldehyde isonicotinoyl hydrazone (SIH) for overnight and then treated with RPE (10  $\mu\text{M}$ ) in 1:1 mixture of Eagles Minimal Essential medium (ATCC) and Ham's F12 medium (ATCC) for 5, 10, 15, 20, 25, and 30 min (time in seconds was shown in each panel). Fluorescence intensity was collected at 547-703 nm (for RPE).

The discrete confocal fluorescence images revealed by RPE in both the untreated and the Fe<sup>3+</sup>-loaded SH-SY5Y cells imply that the labile Fe<sup>3+</sup> in SH-SY5Y cells may be localized in certain subcellular compartments (organelles) and that RPE may be capable of imaging Fe<sup>3+</sup> at subcellular resolution. To explore this, the distribution of exchangeable Fe<sup>3+</sup> pools in live SH-SY5Y cells were further investigated using RPE, together with colocalization experiments using other dyes—MitoTracker Green FM (a green fluorescent dye which localizes to mitochondria in live cells regardless of mitochondrial membrane potential) and LysoTracker Blue DND-22 (a blue fluorescent dye that stains acidic compartments such as endosomes and lysosomes<sup>[35]</sup> in live cells). Human SH-SY5Y cells (without Fe<sup>3+</sup> treatment) were treated with RPE, MitoTracker Green FM, and LysoTracker Blue DND-22. As illustrated in Figure 2.13, partial colocalization between RPE-Fe<sup>3+</sup> and the MitoTracker (Figure 2.13e) as well as between RPE-Fe<sup>3+</sup> and the LysoTracker (Figure 2.13f) occurred whereas complete colocalization of RPE-Fe<sup>3+</sup>, MitoTracker, and LysoTracker (Figure 2.13g) was observed. These data suggest that the exchangeable Fe<sup>3+</sup> pools in SH-SY5Y cells detectable by RPE are localized in mitochondria and endosomes/lysosomes, not in the cytosol. Additional experiments with RPE and the organelle probes under Fe<sup>3+</sup>-supplemented conditions revealed again elevated levels of cellular chelatable Fe<sup>3+</sup> and that the labile Fe<sup>3+</sup> pools are localized in mitochondria and endosomes/ lysosomes under these conditions (Figure 2.14). This finding is consistent with recent observations that cellular Fe<sup>3+</sup> is directly transported from endosomes to mitochondria by a “kiss and run” pathway, bypassing the cytosol.<sup>[36]</sup>



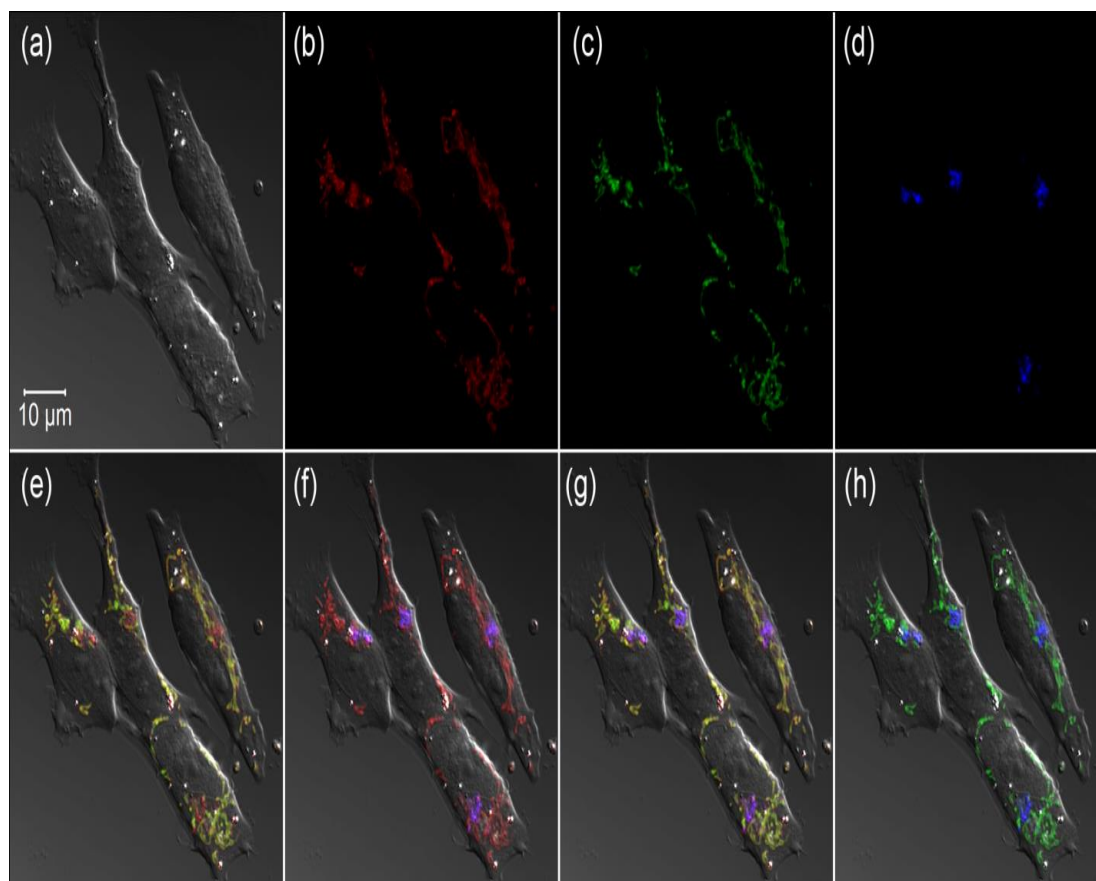


**Figure 2.13** Representative confocal images of intracellular colocalization studies of 10  $\mu\text{M}$  RPE incubated with live human SH-SY5Y cells co-labeled with MitoTracker Green (100 nM) and LysoTracker Blue DND-22 (50 nM). (a) DIC image of cells with 10  $\mu\text{m}$  scale bar. (b) RPE-Fe<sup>3+</sup> fluorescence collected at 547-703 nm (red). (c) MitoTracker fluorescence collected at 492-548 nm (green). (d) LysoTracker fluorescence collected at 409-484 nm (blue). (e) DIC image of (a) and fluorescence images of (b) and (c) were merged together. Colocalization regions are in yellow and non-overlapping regions remain in red. (f) DIC image of (a) and fluorescence images of (b) and (d) were merged together. Overlapping regions are in purple and non-overlapping regions remain in red. (g) Images of (a), (b), (c) and (d) were merged together, revealing that the RPE-Fe<sup>3+</sup> images are 100% colocalized with the sum of those of MitoTracker and LysoTracker. (h), Images of (a), (c) and (d) were merged together, showing no overlapping region between lysosomes and mitochondria.

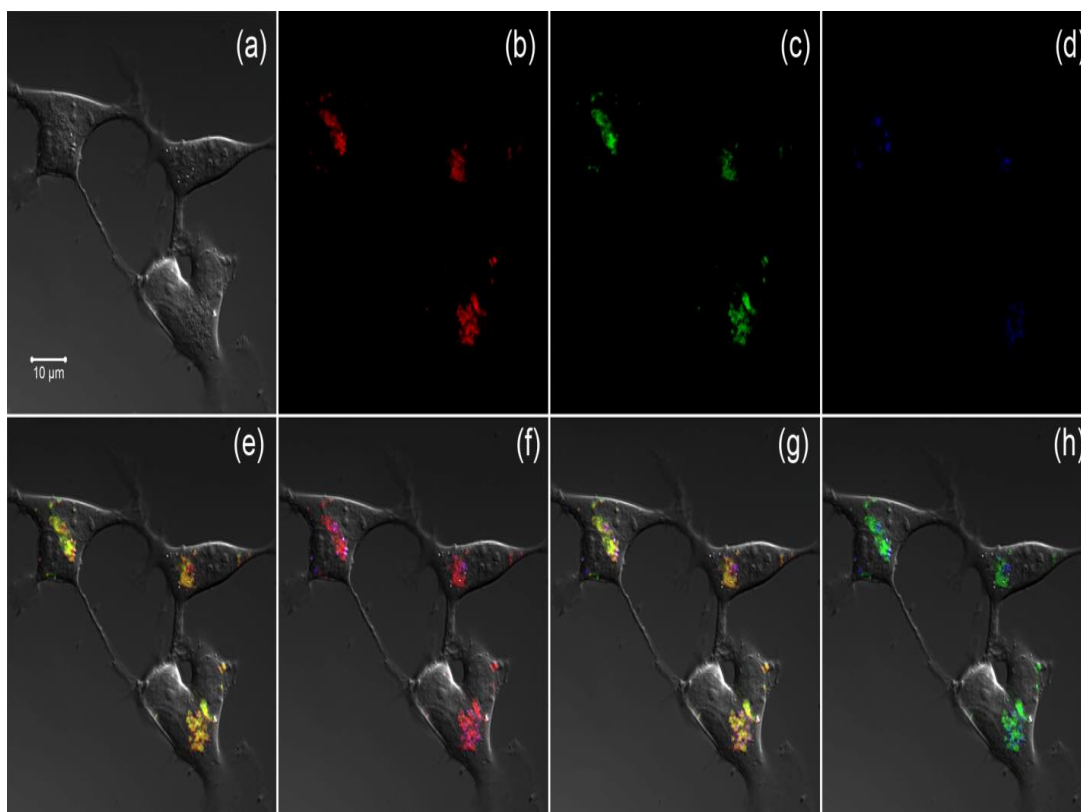


**Figure 2.14** Representative confocal microscopy images of intracellular colocalization studies of 10  $\mu\text{M}$  RPE incubated with  $\text{Fe}^{3+}$ -loaded human SH-SY5Y cells (pre-incubated with 10  $\mu\text{M}$   $\text{Fe}^{3+}$ ) co-labeled with MitoTracker Green FM (100 nM, incubated for 30 min) and LysoTracker Blue DND-22 (50 nM, incubated for 120 min). (a) DIC image of cells with 10  $\mu\text{m}$  scale bar. (b) RPE- $\text{Fe}^{3+}$  fluorescence intensity collected at 547-703 nm (red). Stronger fluorescence suggests elevated  $\text{Fe}^{3+}$  levels in  $\text{Fe}^{3+}$ -loaded human SH-SY5Y cells. (c) MitoTracker fluorescence intensity collected at 492-548 nm (green). (d) LysoTracker fluorescence intensity collected at 409-484 nm (blue). (e) DIC image of (a) and fluorescence images of (b) and (c) were merged together. Colocalization regions are in yellow and non-overlapping regions remain in red, revealing that RPE- $\text{Fe}^{3+}$  is partially colocalized with mitochondria. (f) DIC image of (a) and fluorescence images of (b) and (d) were merged together. Colocalization regions are in purple and non-overlapping regions remain in red, revealing that RPE- $\text{Fe}^{3+}$  is partially colocalized with lysosomes; (g) Images of (a), (b), (c) and (d) were merged together. Colocalization regions are in yellow or purple exclusively; no non-overlapping regions were found, suggesting that chelatable  $\text{Fe}^{3+}$  is still localized in mitochondria and lysosomes under the conditions. (h), Images of (a), (c) and (d) were merged together showing no overlapping region between lysosome and mitochondria.

## 2.4 Conclusion

In summary, a highly sensitive, highly selective, and reversible turn-on fluorescent Fe<sup>3+</sup>-sensor, RPE, has been developed. The sensor gives a distinct rapid and reversible fluorescence response upon the alteration of intracellular Fe<sup>3+</sup> levels with little interference from other biologically relevant metal ions. Confocal experiments show that RPE can readily detect endogenous chelatable Fe<sup>3+</sup> in live human SH-SY5Y cells at subcellular resolution in real time, with two labile Fe<sup>3+</sup> pools being successfully located in mitochondria and endosomes/lysosomes in both untreated and Fe<sup>3+</sup>-loaded SH-SY5Y cells for the first time. RPE is thus a promising tool for probing the cell biology of Fe<sup>3+</sup>.

## 2.5 References

1. London R. E., Annual Review of Physiology, **1991**, 53, 241-258
2. Zalewski P. D., Forbes T. J. and Betts W. H., Biochem. J., **1993**, 296, 403-408
3. Grynkiewicz G., Poenie M., and Tsien R. Y., J. Biol. Chem., **1985**, 260, 3440-3450
4. Que E. L., Domaille D. W., Chang C. J., Chem. Rev., **2008**, 108, 1517-1549
5. Domaille D. W., Qu E.L., Chang C. J., Nat. Chem. Biol., **2008**, 4,168-175
6. Jin T., Ichikawa K., and Koyama T. J., Chem. Soc., Chem. Commun., **1992**, 499-519
7. Leray I., Lefevre J. P., Delouij. F. S., Delaire J., Valeur B., Chem. Eur. J., **2001**, 7, 4590-4598
8. Lee S. H., Kim S. H., Jung S. K., and Kim J. S., J. Org. Chem., **2005**, 70, 9288-9295
9. Hecht S., Vladimirov N., and Frechet J. M. J., J. Am. Chem. Soc., **2001**, 123, 18-25
10. Inorganic Biochemistry of Iron Metabolism, 2nd ed. (Ed.: R. Crichton), Wiley, Chichester, **2001**, pp. 1- 10
11. Yong Y. K., Yook K. J., Tae J. , J. Am. Chem. Soc., **2005**, 127, 16760-16761
12. Weerasinghe A. J., Schmiesing C., Sinn E., Tetrahedron lett., **2009**, 50, 6407-6410
13. Yu M., Shi M., Chen Z., Li F., Li X., Gao Y., Xu J., Yang H., Zhuo Z., Yi T., Huang C., Chem. Eur. J., **2008**, 14, 6892-6900

14. Xi P., Dou J., Huang L., Xu M., Chen F., Wu Y., Bai D., Li W., Zeng Z., Sens. Actuators, B, **2010**, 148, 337-341
15. Wei Y., Zhang Y., Liu Z., Guo M., Chem. Comm., **2010**, 46, 4722-4726
16. Aydin Z., Wei Y., Guo M., Inorg. Chem. Commun., **2012**, 20, 93-96
17. Chen X., Jia J., Ma H., Wang S., Wang X., Anal. Chim. Acta, **2009**, 632, 9-14
18. Zhang X., Shiraishi Y., Hirai T., Org. Lett., **2007**, 9, 5039-5042
19. Tang L., Li F., Liu M., Nandhakumar R., Bull. Korean Chem.Soc., **2010**, 31, 3212-3216
20. Inorganic Biochemistry of Iron Metabolism, 2nd ed. (Ed.: R. Crichton), Wiley, Chichester, **2001**, pp. 17- 48
21. Rossotti F. J. C., Rossotti H., (Series in Advanced Chemistry), McGraw-Hill Book Company, Inc., New York, Toronto, London, **1961**, pp. 97 -98
22. Johnson I., Histochem. J., **1998**, 30, 123-140
23. Cooper M.A., Anal. Bioanal. Chem., **2003**, 377, 834-842
24. Kwon Y., Jang Y. J., Lee Y. J., Kim K. M., Seo M. S., Nam W., J. Yoon, J. Am. Chem. Soc., **2005**, 127, 10107-10111
25. Zhang X., Shiraishi Y., Hirai T., Tetrahedron Lett., **2007**, 48, 5455-5459
26. Zhang M., Gao Y., Li M., Yu M., Li Fuyou, Li L., Zhu M., Zhang J., Yi T., Huang C., Tetrahedron Lett., **2007**, 48, 3709-3712
27. Xiang Y., Tong A., Org. Lett., **2006**, 8, 1549-1552
28. Perez C. A., Guo M., Wei Y., J. Inorg. Biochem., **2009**, 103, 326-332
29. Sterzel W., Bedford P., Eisenbrand G., Anal. Biochem., **1985**, 147, 462-467
30. Chartres J. Busby D., M., Riley M. L., Davis J. J., Bernhardt P. V., Inorg.Chem., **2011**, 50, 9178-9183
31. Leite A., Silva A.M.G., Cunha-Silva L., Castro de B., Gameiro P., Rangel M., Dalton Trans., **2013**, 42, 6110-6118
32. Berchner-Pfannschmidt U., Petra F.T., Doege K., Trinidad B., Freitag P., Metzen E. , de Groot H., Fandrey J., J. Biol. Chem., **2004**, 279, 44976- 44986
33. Buss J. L., Arduini E., Shephard K.C., Ponka P., Biochem. Pharmacol., **2003**, 65, 349-360
34. Wei Y., Guo M., Angew. Chem. Int. Ed., **2007**, 46, 4722-4725

**35.** Zhang Y. Z., Olwu Z., Mao F., Haugland W. L., Mol. Biol. Cell, **1994**, 5, 113a (abstract 653)

**36.** Richardson D. R., Lanea D. J. R., Beckera E. M., Huang M. L. H., Whitnalla M., Rahmantoa Y. S., Sheftel A. D., Ponkac P., Proc. Natl. Acad. Sci. USA, **2010**, 107, 10775-10785

## CHAPTER 3

### HEPTAMETHINE CYANINE BASED FLUORESCENT SENSORS FOR Fe<sup>3+</sup>

#### 3.1 Introduction

As the most abundant transition metal in biological systems, iron plays crucial roles in many fundamental physiological processes.<sup>[1-3]</sup> Iron dyshomeostasis, either deficiency or overload, is linked to various disease conditions.<sup>[1-3]</sup> Therefore, the development of iron-selective fluorescent sensors is of great interest and could prove indispensable for monitoring the dynamic changes of iron in cells and elucidating the mechanisms of iron trafficking.<sup>[4-6]</sup> Highly sensitive, selective and reversible turn-on or ratiometric fluorescent sensors capable of subcellular iron imaging are in high demand, but are still lacking due to the challenge of overcoming cell permeability, specificity, solubility and paramagnetic quenching issues of iron ions.<sup>[4-6]</sup> The currently known fluorescent sensors that are capable of cellular iron imaging are largely limited to “turn-off” type,<sup>[7-10]</sup> providing useful information but suffering from poor sensitivity, or interference from other metal ions. Recently, a few interesting “turn-on” iron sensors have been reported,<sup>[11-15]</sup> however, they emit light in visible range. When they are applied to biological samples, they suffer from some significant drawbacks, including intrinsic signal caused by auto-fluorescence, high light scattering, and poor tissue penetration. To overcome these limitations, near infrared sensors can be used because they emit at longer wavelengths, therefore they display low autofluorescence background, deeper penetration to tissue and cause less damage to biological samples.<sup>[16-18]</sup> In human tissue, the major optical absorbers are hemoglobin and water. The visible light below 650 nm wavelength will be absorbed by hemoglobin strongly. Above 900 nm, infrared light will be also absorbed by water.

The near infrared wavelength between 650 nm and 900 nm, so called the optical window, are relatively “transparent” due to the low optical absorption of the hemoglobin and water.<sup>[19-20]</sup>

Dyes that emit in this range are of high demand.

For this purpose, tricarbocyanine dyes were selected as chromophore/fluorophore because they normally absorb light with a large extinction coefficient in the near-infrared region (650-900 nm).<sup>[21-23]</sup> Cyanine dyes are cationic molecules in which two terminal nitrogen heterocyclic units are linked by a polymethine bridge (shown in Fig. 3.1). Cyanine dyes' common names depend on the number of methine groups in the polyene chain. For example,  $n = 0$ ,  $n = 1$ ,  $n = 2$ , and  $n = 3$  are referred to as mono-, tri-, penta-, and heptamethine cyanines, respectively. Cyanine dyes have two heterocyclic moieties, acting as both electron donors and acceptors, and are joined by a single or odd number of methine groups in which  $(n+1)$  pi-electrons are distributed over  $n$  atoms<sup>[24]</sup>, producing a delocalized cation across the methine chain. Synthetic cyanines<sup>[25-27]</sup> are known to absorb between the visible and infrared regions of the electromagnetic spectrum. In addition, cyanines exhibit narrow absorption bands and high extinction coefficients. Due to these properties, cyanine dyes have been extensively employed in various applications including bioimaging. Cyanine dyes have additional advantage in bioimaging as they absorb and emit in the infrared region. As visible light can be easily absorbed by biomolecules such as hemoglobin (causing autofluorescence) and is easily scattered and cannot penetrate deeply into tissue, while light in the near-infrared region (650-900 nm) is relatively poorly absorbed by biomolecules and can penetrate deeply into tissue.<sup>[28]</sup> Near-infrared sensors are better than visible sensors for tissue or *in vivo* imaging.

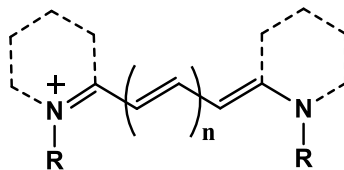


**Figure 3.1** General structure of carbocyanine dyes

Many different polymethine cyanine derivatives have been synthesized during the last decade.<sup>[29-33]</sup> Cyanine dyes have traditionally been synthesized by a condensation reaction between a heterocyclic base containing an activated methyl group and an unsaturated bisaldehyde or its equivalent, usually as Schiff base in the presence of a catalyst.<sup>[29]</sup> Cyanine dyes can be modified in various ways that lead to alterations in their spectroscopic characteristics. Modifications include altering the functional groups on the indolenine moieties with charging group, resulting in dyes with improved water solubility<sup>[29-30]</sup>, or substitutions at the meso-position by alkyl or halogen groups.<sup>[31-33]</sup> For heptamethine cyanine dyes (shown in Figure 3.2), the vinyl chlorine on the cyclohexane bridgehead of heptamethine cyanines is reactive and can be replaced by a binding group with a very strong nucleophile such as alcoholates<sup>[31]</sup>, amines<sup>[32]</sup>, and thiols<sup>[33]</sup>.

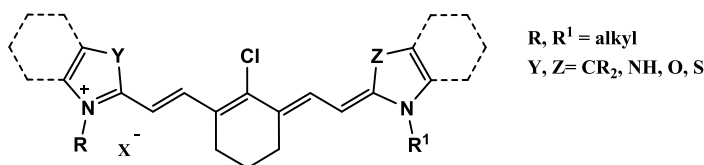


**Figure 3.2** General structure of heptamethine cyanine dyes substituted at the meso-position by halogen group

In this chapter, heptamethine cyanines were modified by amines and alcoholates (the Z group) to design iron sensors. The vinyl chlorine on the cyclohexane bridgehead of



heptamethine cyanines can react with nucleophiles via a direct addition of the nucleophile to the cationic  $\pi$ -system followed by elimination of the chlorine ion.<sup>[34]</sup> The heptamethine cyanine reaction with amines can be explained with this mechanistic pathway (Figure 3.3). The binding of amine functional groups causes a shift in the absorption maximum.<sup>[25]</sup> A Fe-chelation functionality (iron receptor) may be designed in the Z group so that when the iron receptor binding with iron, it may signal a fluorescent change (*e.g.*, a shift in the spectrum) so that an iron sensor (*e.g.*, a ratiometric sensor) may be observed. In addition, this mechanism can be used for the synthesis of heptamethine dyes with alcoholates.<sup>[31]</sup> NaH is used to make the receptor group (Z group) a negative ion that is then linked with cyanine dyes for alcoholates ( $-\text{C}_6\text{H}_4\text{-OH}$ ).

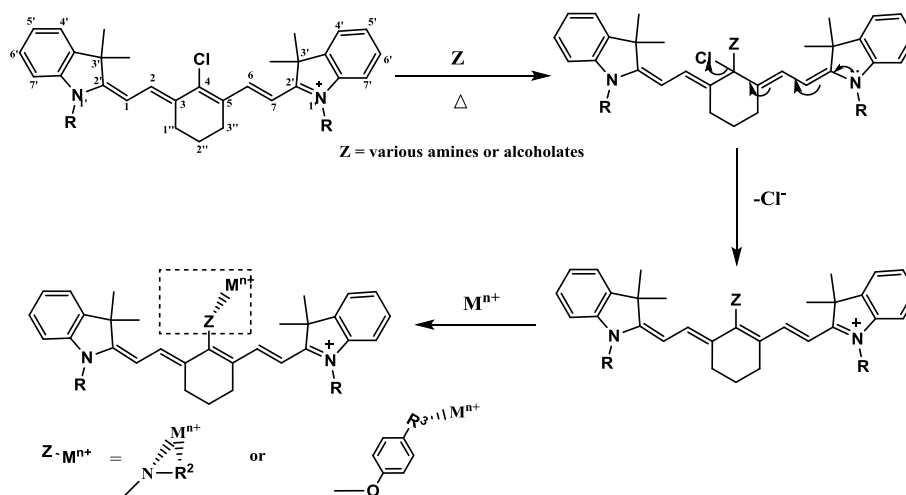


**Figure 3.3** Suggested addition/elimination mechanism of heptamethine amino cyanine dyes<sup>[24]</sup>

I synthesized several heptamethine cyanine based fluorescent sensors (structures shown in Figure 3.4) that were designed to be selective for  $\text{Fe}^{3+}$ ; however, only one of them is a  $\text{Fe}^{3+}$ -selective sensor, IRPE. Here, the properties of this highly selective, sensitive, and reversible ratiometric fluorescent  $\text{Fe}^{3+}$  sensor were described.

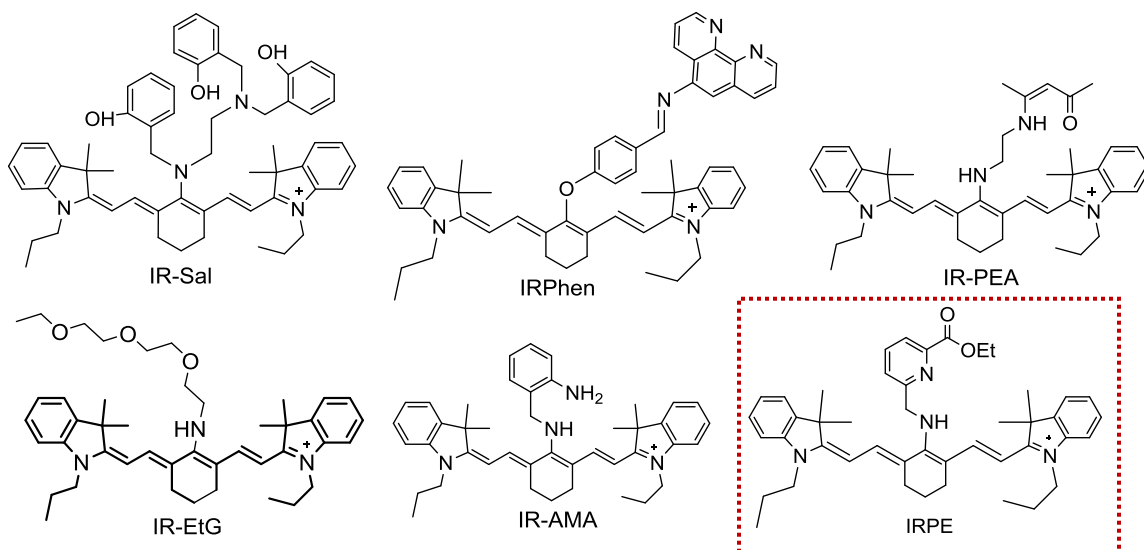


**Figure 3.4** Some heptamethine cyanine based fluorescent sensors that were designed for  $\text{Fe}^{3+}$  (see Appendix A for experimental details), only IRPE shows response to  $\text{Fe}^{3+}$

## 3.2 Experimental Section

### 3.2.1 Materials and instruments

2,6-Pyridine dicarboxylic acid diethyl ester was purchased from TCI America. The other chemicals and the solvents used in the experiments were purchased commercially. The solution of metal ions were prepared from chloride salts of  $\text{Ni}^{2+}$ ,  $\text{Fe}^{3+}$ ,  $\text{Cu}^{2+}$ ,  $\text{Mn}^{2+}$ ,  $\text{Hg}^{2+}$ ,  $\text{Na}^+$ ,  $\text{Ca}^{2+}$ ,  $\text{Zn}^{2+}$ ,  $\text{Ag}^+$ , and nitrate salts of  $\text{Mg}^{2+}$ ,  $\text{Pb}^{2+}$ ,  $\text{K}^+$ ,  $\text{Co}^{2+}$ . Stock solutions of metal ions (10 mM) were prepared in deionized water, except for  $\text{Fe}^{3+}$  and  $\text{Fe}^{2+}$  which were dissolved in 0.1 M HCl. Solution of  $\text{Cu}^+$  was freshly prepared by dissolving tetrakis(acetonitrile)copper(I) (Sigma-Aldrich) into double-distilled water. A stock solution of IRPE (500  $\mu\text{M}$ ) was prepared in ACN. The solution of IRPE was diluted to 3 or 5  $\mu\text{M}$  with ACN/HEPES buffer (1:1 v/v). In selectivity experiments, the test samples were prepared by appropriate amount of metal ion stocks into 1 ml solution of IRPE (3 or 5  $\mu\text{M}$ ).

$^1\text{H}$  and  $^{13}\text{C}$  NMR spectra were recorded on a Bruker DRX-300 NMR spectrometer. ESI-MS analyses were performed using a Perkin Elmer API 150EX mass spectrometer. UV/Vis spectra were recorded on a Perkin Elmer Lambda 25 spectrometer at 293 K. Fluorescence spectra were recorded on a Perkin-Elmer LS55 luminescence spectrometer at 293 K. The pH measurements were carried out on a Corning pH meter equipped with a Sigma-Aldrich micro combination electrode calibrated with standard buffer solutions.

### 3.2.2 Synthesis and Characterization

IR-780 and 6-(Aminomethyl)pyridine-2-carboxylic acid ethyl ester (PE) were prepared according to the published processes,<sup>[35-36]</sup> and described briefly below.

#### 3.2.2.1 Synthesis of IR-780

**Synthesis of 3H-Indolium, 2,3,3-trimethyl-1-propyl, iodide (C1).** To a solution of 2,3,3-trimethyl-3H-indole (2.0 g, 12.5 mmol, 1 equiv) in ACN, 1-iodopropane (10.6 mL, 62 mmol, 5 equiv) was added, and refluxed with continuous stirring for 15 h. The mixture was dried under high vacuum and washed with  $\text{Et}_2\text{O}$ . The resulting solid was re-crystallized in acetone to obtain 1b as a white solid (3.9 g, yield 95%).  $^1\text{H}$  NMR (300 MHz,  $\text{DMSO-d}_6$ ): 1.04 (t, 3H,  $J = 7.2$  Hz), 1.34 (m, 2H), 1.64 (s, 6H), 2.67 (s, 3H), 4.17 (t, 2H,  $J = 7.8$  Hz), 7.63 (d, 2H,  $J = 7.4$  Hz), 7.82 (m, 2H). ESI  $m/z$  ( $\text{C}_{14}\text{H}_{20}\text{N}^+$ ) calc: 202.4; found: 202.3.

**Synthesis of 2-Chloro-1-formyl-3-hydroxymethylenecyclo hexen (C2).** To a chilled solution of DMF (20 mL, 273 mmol, 5.4 equiv) in 20 mL  $\text{CH}_2\text{Cl}_2$  under  $\text{N}_2$  atmosphere, 20 mL of  $\text{POCl}_3$  (17.5 mL, 115 mmol, 2.3 equiv) in DCM were added drop wise under an ice bath. After 30 min, cyclohexanone was added (5 g, 50 mmol, 1 equiv), and the resulting mixture was refluxed with vigorous stirring for 6 h at  $80^\circ\text{C}$ , poured into ice cold water, and kept it overnight to obtain C2

as a yellow solid (8.0 g, yield 92%).  $^1\text{H}$  NMR (300 MHz,  $\text{CDCl}_3$ ): 1.57 (m, 2H), 2.35 (t, 4H,  $J = 6.3$  Hz), 2.5 (s, 1H), 10.10 (s, 1H). ESI  $m/z$  ( $\text{C}_8\text{H}_{10}\text{ClO}_2$ ): calc: 172.0; found: 173.3 [M+H].

**Synthesis of IR-780:** Under nitrogen atmosphere, C2 (1.0 g, 6 mmol, 1 equiv) and C1 (4.6 g, 12 mmol, 2 equiv) were dissolved in 50 mL of butanol/benzene (7:3) and refluxed for 16h at 160 °C in a Dean-Stark condenser. The solvent was then evaporated and the resulting green solid mixture was washed with  $\text{Et}_2\text{O}$  and purified by normal phase chromatography (elution with DCM-MeOH, 95:5) to obtain IR-780 iodide as a green solid (3.0 g, yield 80%).

### 3.2.2.2 Synthesis of 6-(Aminomethyl)pyridine-2-carboxylic acid ethyl ester

**Synthesis of 6-chloromethyl pyridine-2-carboxylic acid ethyl ester.** The diethyl ester (3 g, 22.4 mmol) was refluxed with  $\text{NaBH}_4$  (0.306 g, 13.4 mmol (0.6 equiv) in 50 mL of ethanol for 2 h. After being cooled, the solution was concentrated to a volume of 10 mL and, then 10 mL of water was added. The solution was further concentrated to 10 mL and extracted with several 20 mL portions of  $\text{CHCl}_3$ . The combined  $\text{CHCl}_3$  were dried with  $\text{Na}_2\text{SO}_3$  and was removed by rotary evaporator to yield 6-hydroxymethylpyridine-2-carboxylic acid ethyl ester (1.57 g yield 50 %). 6-hydroxymethylpyridine-2-carboxylic acid ethyl ester (1.57 g) was dissolved in  $\text{SOCl}_2$  (3 mL) at 0 °C with stirring. After 1 h, the solution was allowed to reach room temperature and the excess of  $\text{SOCl}_2$  removed under reduced pressure without heating. Toluene was added to the oily residue, the solution was extracted (2x10 mL) with a cold  $\text{NaHCO}_3$  (1 M) solution and dried with  $\text{Na}_2\text{SO}_3$ . Evaporation of the solvent afforded the oily product (1.19 g).  $^1\text{H}$  NMR (300 MHz,  $\text{CDCl}_3$ ):  $\delta$  8.18 - 7.97 (m, 1H), 7.91 (d, 2H), 7.75 (t, 1H), 4.96 - 4.69 (m, 2H), 4.65 - 4.26 (m, 2H), 1.48 (t, 3H). ESI  $m/z$  ( $\text{C}_9\text{H}_{10}\text{ClNO}_2$ ): calc: 199.04; found: 200.1 [M+H] $^+$ .

**Synthesis of 6-(Aminomethyl)pyridine-2-carboxylic acid ethyl ester (PE).** 6-chloromethylpyridine-2-carboxylic acid ethyl ester (1.19 g, 5.92 mmol) was dissolved in

anhydrous DMF (10 mL) and it was slowly added to a DMF solution of sodium phthalimide (1.10 g, 6.1 mmol). After stirring for 2h at room temperature, the reaction mixture was centrifuged. The solvent removed under pressure, and the residue was dissolved in CHCl<sub>3</sub>. The resulting solution was washed with 0.2 M NaOH solution (2x100 mL) then with water. The solvent was dried and evaporated to yield a solid residue that was dissolved in warm ethanol (60 mL). Hydrazine (NH<sub>2</sub>NH<sub>2</sub>·H<sub>2</sub>O) (1.35 g, 0.315 mL, 10 mmol) was added and the mixture was refluxed until disappearance of the starting material. The mixture was then filtered and the solvent evaporated to a small volume. Addition of ethyl ether gave a precipitate that was filtered off, evaporated, and then dissolved in acetonitrile. It was filtered off, evaporation of the solvent yielded the product as an oil (0.43 g, yield 40%). <sup>1</sup>H NMR (300 MHz, CDCl<sub>3</sub>): δ: 8.18 - 7.97 (m, 1H), 7.91 (d, 2H), 7.75 (t, 1H), 4.96 - 4.69 (m, 2H), 4.65 - 4.26 (m, 2H), 3.02(s, 2H), 1.48 (t, 3H). ESI m/z (C<sub>9</sub>H<sub>12</sub>N<sub>2</sub>O<sub>2</sub>): calc: 180.09; found: 181.3 [M+H]<sup>+</sup>.

### 3.2.2.3 Synthesis of IRPE

PE and IR-780 iodide were prepared according to the literature methods.<sup>[12]</sup> IR-780 iodide (200 mg, 0.3 mmol) and PE (110 mg, 0.6 mmol) were dissolved in dry ACN (15 mL), and N,N-disopropylethylamine (DIEA) (77 μL, 0.6mmol, 2 equiv) was added. The reaction was stirred at 70 °C for 4 h under nitrogen atmosphere. The resulting blue color crude mixture was neutralized with 0.1 M HCl, and concentrated under vacuum. The crude product was purified by column chromatography on alumina gel (DCM/MeOH; 100/0 to 95/5) to yield IRPE (58 mg, yield 24%). <sup>1</sup>H NMR (300 MHz, CDCl<sub>3</sub>): δ: 8.21 (s, 1H), 7.74 (d, *J* = 13.1 Hz, 1H), 7.33 (dd, *J* = 30.6, 18.3 Hz, 5H), 7.09 (t, *J* = 7.5 Hz, 1H), 6.92 (d, *J* = 7.9 Hz, 1H), 6.39 (dd, *J* = 60.2, 22.4 Hz, 2H), 5.74 (d, *J* = 13.1 Hz, 1H), 4.91 (s, 1H), 4.46 (d, *J* = 5.7 Hz, 2H), 3.84 (t, *J* = 7.1 Hz, 3H), 2.50 (t, *J* = 6.3 Hz, 2H), 1.99 - 1.71 (m, 4H), 1.62 (d, *J* = 23.3 Hz, 7H), 1.04 (t, *J* = 7.4 Hz, 6H). <sup>13</sup>C NMR (75 MHz, CDCl<sub>3</sub>): δ: 176.2, 166.5, 166.1, 156, 52, 143, 128.7, 128.3, 125.7, 125.3, 124.9, 124.6, 122.6, 122.3, 114.1,

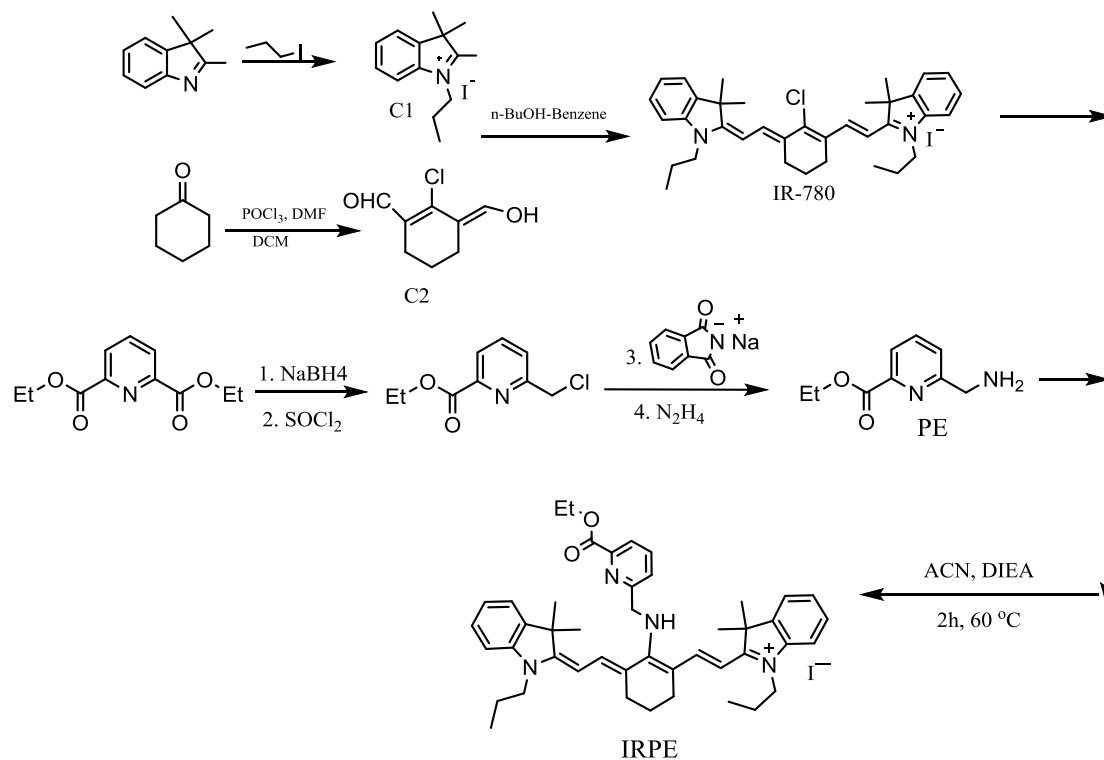
111.3, 111.1, 104.5, 97.3, 61.1, 52.6, 52.3, 49.2, 45.3, 28.7, 28.3, 28.1, 27, 26.2, 23.4, 21.9, 14.2,

12.1, 11.9. ESI m/z ( $C_{45}H_{55}O_2N_4^+$ ), calc: 683.4; found: 683.3 (without  $I^-$ ).

### 3.3 Results and Discussion

#### 3.3.1 Design and synthesis

Cyanine dyes can be modified in various ways that lead to alterations in spectroscopic characteristics. An iron-binding receptor was designed and linked on the heptamethine cyanine via the vinyl chloride on the cyclohexane bridgehead. The compound was synthesized as outlined in scheme 3. Briefly, the indolenine moiety was first modified with propyl iodide and a heptamethine cyanine with a meso-substituted with chloride was obtained. A  $Fe^{3+}$ -selective binding group was designed and synthesized next (PE). Then the binding group and the heptamethine cyanine (commercially available called IR-780) were linked together to produce IRPE with an overall yield of 25% (see Scheme 3.1).



**Scheme 3.1** Synthetic scheme of the IRPE sensor

### 3.3.2 Spectroscopic Properties

The absorption spectra of IRPE upon coordination with  $\text{Fe}^{3+}$  in ACN/HEPES at pH 7.0 (1/1, v/v) were monitored first. As shown in Figure 3.5a, the solution of IRPE alone (5.0  $\mu\text{M}$ ) exhibits an absorption maximum at 664 nm, which is responsible for the blue color of the solution. With increasing  $\text{Fe}^{3+}$  concentration, the absorbance at 664 nm ( $\epsilon = 1.8 \times 10^5 \text{ M}^{-1} \text{ cm}^{-1}$ , only IRPE) decreased, while the absorbance at 523 nm ( $\epsilon = 6.56 \times 10^4 \text{ M}^{-1} \text{ cm}^{-1}$ , IRPE and  $\text{Fe}^{3+}$  1: 1 ratio) increased concomitantly. This pronounced hypsochromic shift of the maximum absorption wavelength could be ascribed to the coordination of  $\text{Fe}^{3+}$ . Meanwhile, an isosbestic point was clearly observed around 551 nm, indicating the conversion of the free dye into the Fe(III)-complex is a clean reaction. In contrast, other metal ions such as  $\text{Ni}^{2+}$ ,  $\text{Cu}^{2+}$ ,  $\text{Mn}^{2+}$ ,  $\text{Hg}^{2+}$ ,  $\text{Na}^+$ ,  $\text{Ca}^{2+}$ ,  $\text{Zn}^{2+}$ ,  $\text{Ag}^+$ ,  $\text{Mg}^{2+}$ ,  $\text{Pb}^{2+}$ ,  $\text{K}^+$ ,  $\text{Fe}^{2+}$ ,  $\text{Co}^{2+}$ , and  $\text{Cr}^{3+}$  give little response to IRPE (Figure 3.5b). In addition, such a large blue shift of 141 nm in the absorption behavior changes the color of the resultant solution from blue to pink, allowing “naked eye” detection (Figure 3.6).

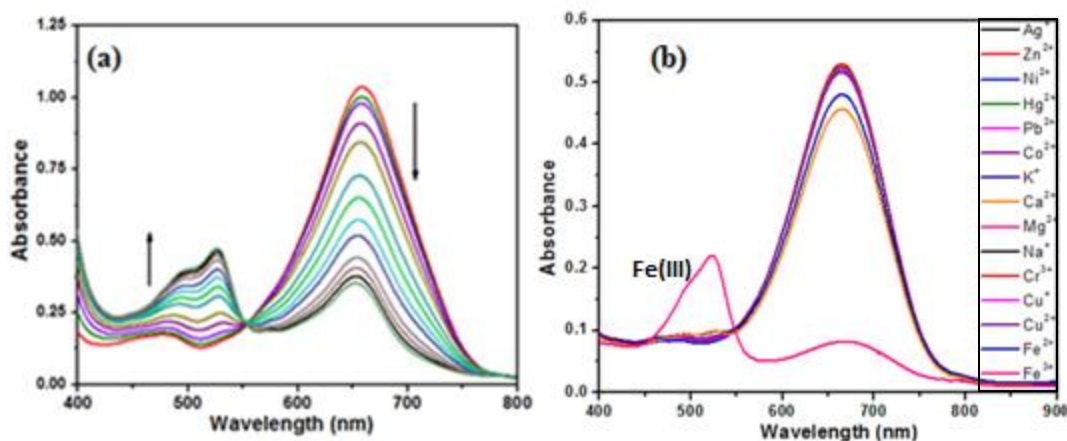


**Figure 3.5** (a) Absorbance response of 5  $\mu\text{M}$  IRPE to increasing concentration of  $\text{Fe}^{3+}$  (top to bottom, 0, 0.05, 0.1, 0.15, 0.2, 0.3, 0.5, 0.7, 0.8, 0.9, 1.0, 1.2, 1.5 and 2 equiv in ACN/HEPES buffer (10 mM, pH 7.3, v/v 1:1) (b) UV-vis spectra of 3  $\mu\text{M}$  IRPE to various metal ions (3  $\mu\text{M}$  for  $\text{Zn}^{2+}$ ,  $\text{Cr}^{3+}$ ,  $\text{Ni}^{2+}$ ,  $\text{Hg}^{2+}$ ,  $\text{Fe}^{3+}$ ,  $\text{Mn}^{2+}$ ,  $\text{Ag}^+$ ,  $\text{Pb}^{2+}$ ,  $\text{Fe}^{2+}$ ,  $\text{Cu}^+$ ,  $\text{Cu}^{2+}$ , and  $\text{Co}^{2+}$ ; 15  $\mu\text{M}$  for  $\text{Na}^+$ ,  $\text{K}^+$ ,  $\text{Mg}^{2+}$ , and  $\text{Ca}^{2+}$ ) in ACN/HEPES buffer (10 mM, pH 7.0, v/v 1:1).

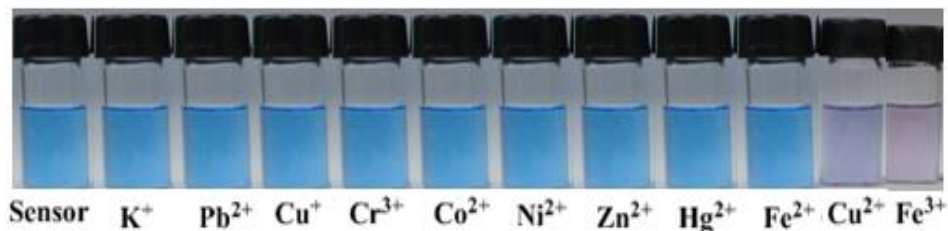


**Figure 3.6** Color changes of 3  $\mu\text{M}$  IRPE with various metal ions (3  $\mu\text{M}$  for  $\text{Zn}^{2+}$ ,  $\text{Cr}^{3+}$ ,  $\text{Ni}^{2+}$ ,  $\text{Hg}^{2+}$ ,  $\text{Fe}^{3+}$ ,  $\text{Pb}^{2+}$ ,  $\text{Fe}^{2+}$ ,  $\text{Cu}^{2+}$ ; 20  $\mu\text{M}$  for  $\text{K}^{+}$ ) in ACN/HEPES buffer (10 mM, pH 7.0, v/v 1:1)

Before performing fluorescent experiments for IRPE, I investigated the time evolution of IRPE (Figure 3.7a) and the response of the IRPE to 1 equiv of  $\text{Fe}^{3+}$  (Figure 3.7b) in ACN/HEPES at pH 7.0 (1/1, v/v). I found that the interaction of IRPE with  $\text{Fe}^{3+}$  was completed in less than 5 min, and it was stable for 15 h. IRPE itself was stable in aqueous solution for 8 h (emission at 760 nm). The results showed that the coordination of  $\text{Fe}^{3+}$  to IRPE also increased the stability of the sensor.

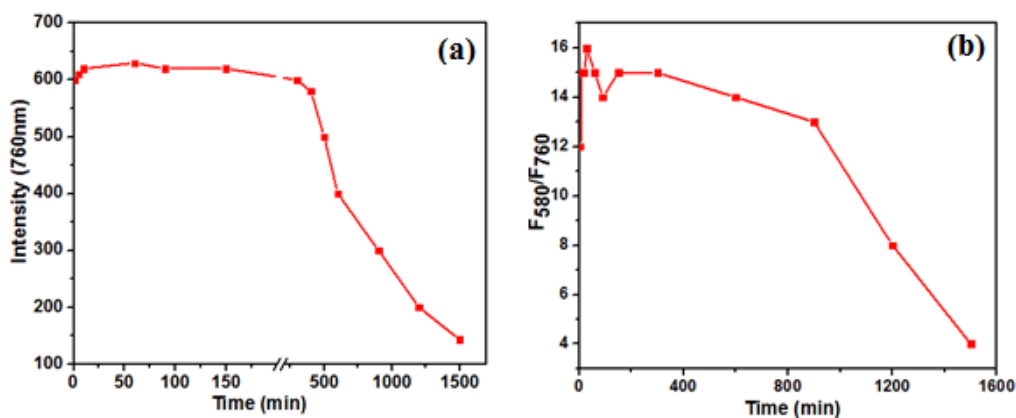


**Figure 3.7** (a) Time course plot of fluorescent response of IRPE (5  $\mu\text{M}$ ) in ACN/HEPES buffer (10 mM, pH 7.0, v/v 1:1) (b) Time course plot of ratiometric fluorescent responses of IRPE (5  $\mu\text{M}$ ) and  $\text{FeCl}_3 \cdot 6\text{H}_2\text{O}$  (5  $\mu\text{M}$ ) in ACN/HEPES buffer (10 mM, pH 7.0, v/v 1:1).



To examine the fluorescent response to  $\text{Fe}^{3+}$ , a solution of IRPE in ACN/HEPES buffer (10 mM, pH 7.0, v/v 1:1) was titrated with various concentrations of  $\text{Fe}^{3+}$ , and then they were excited at both 520 and 650 nm, individually. When excited at 650 nm, IRPE displayed two strong emission peaks at  $\sim 700$  nm and 760 nm. When  $\text{Fe}^{3+}$  was added to the IRPE solution, a decrease in the 760 nm was observed (Figure 3.8a). When it was excited at 520 nm, IRPE solution displayed three strong emission peaks, one at 760 nm and two peaks at  $\sim 700$  nm and 580 nm. When  $\text{Fe}^{3+}$  was added to IRPE solution, a decrease in intensity of the 760 nm emission and an increase in intensity of the fluorescence at 580 nm were observed. The  $\sim 700$  nm peak was less affected in the titration process.

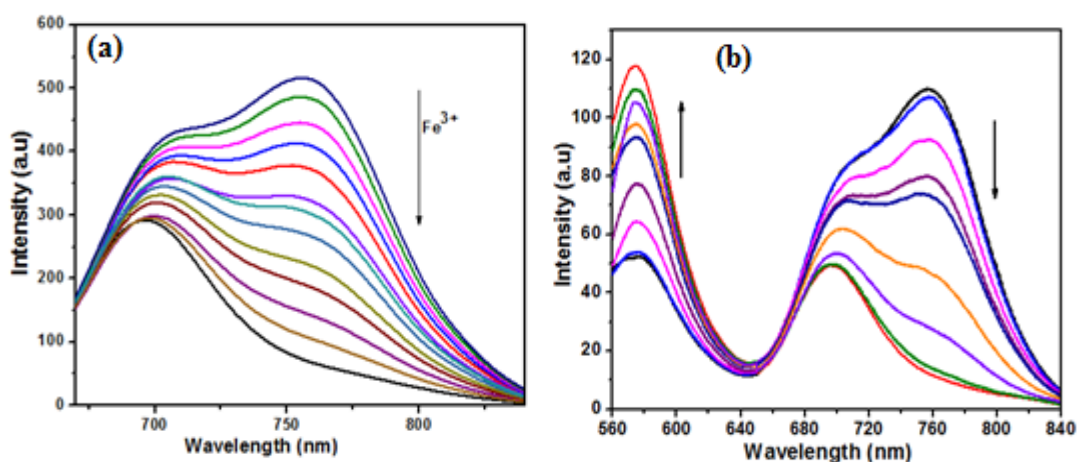


**Figure 3.8** (a) Fluorescence response of 5  $\mu\text{M}$  IRPE to increasing concentration of  $\text{Fe}^{3+}$  (top to bottom, 0, 0.05, 0.1, 0.15, 0.2, 0.3, 0.5, 0.7, 0.8, 0.9, 1.0, 1.5, and 2.0 equiv in ACN/HEPES buffer (10 mM, pH 7.3, v/v 1:1) ( $\lambda_{\text{Ex}}$  650 nm) (b) Fluorescence response of 3  $\mu\text{M}$  IRPE to increasing concentration of  $\text{Fe}^{3+}$  (top to bottom of the 760 nm peak, 0, 0.05, 0.1, 0.2, 0.3, 0.5, 0.7, 0.9, and 1.0 equiv in ACN/HEPES buffer (10 mM, pH 7.3, v/v 1:1) ( $\lambda_{\text{Ex}}$  520 nm).

Then, the ratiometric fluorescence response ( $F_{580}/F_{760}$ ) of IRPE was analyzed to determine its selectivity to different metal ions. As shown in Figure 3.9 (gray bars), the fluorescent intensity of IRPE solution exhibits a very small ratiometric value ( $F_{580}/F_{760}$ ), but upon the addition of 1 equiv of  $\text{Fe}^{3+}$ , there is a strong enhancement of this ratiometric value. The

addition of the other metal ions resulted in very little increases in this value. We also examined the interferences from the other metal ions with IRPE in its response to  $\text{Fe}^{3+}$ . Each of the metal ions was pre-incubated with IRPE before 1 equiv  $\text{Fe}^{3+}$  was added, the fluorescence response was then measured. As shown in Figure 3.9 (black bars), the fluorescence intensity ratiometric value of IRPE with  $\text{Fe}^{3+}$  was not affected significantly in the presence of any of the other metal ions tested, demonstrating little interferences from other metal ions.

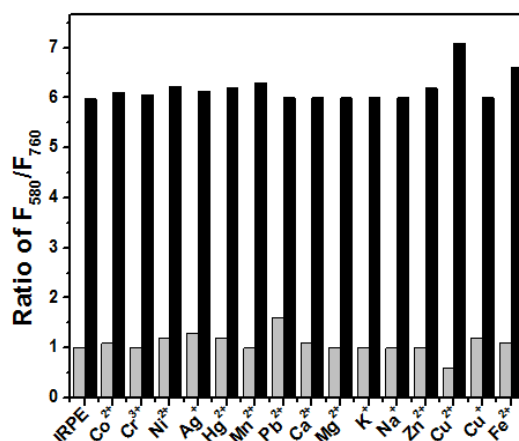


**Figure 3.9** Fluorescence responses  $F_{580}/F_{760}$  of 3  $\mu\text{M}$  IRPE ( $\lambda_{\text{Ex}}=520$  nm) to the presence of various metal ions (gray bars) and the subsequent addition of  $\text{Fe}^{3+}$  (black bar) in the ACN/HEPES buffer (10 mM, pH 7.3, v/v 1:1).

### 3.3.3 Binding Studies

In absorbance spectra of IRPE, we observed a huge blue shift with  $\text{Fe(III)}$  addition. Recently Hong Zheng *et al.* reported cyanine based fluorescent sensors for  $\text{Ag(I)}$  and  $\text{Hg(II)}$  ions. These sensors showed a huge blue shift when they coordinated with the metal ions. They explained this hypsochromic shift of the maximum absorption with H-aggregation state of the cyanine dye.<sup>[25,37]</sup> Most recently Zhigian Guo *et al.* reported a cyanine based sensor which showed a blue shift when coordinating with  $\text{Zn(II)}$ . They observed a reversible binding and explained the blue shift with N-H deprotonation resulting in shortening of the conjugated  $\pi$ -

electron system in cyanine dye.<sup>[38]</sup> To understand this huge blue shift and the mechanism of the binding between IRPE and  $\text{Fe}^{3+}$ , several control experiments were carried out .

First, the stoichiometry of IRPE and  $\text{Fe}^{3+}$  was determined. The binding stoichiometry of IRPE and  $\text{Fe}^{3+}$  was determined by Job's method and UV-titration. Job's plot (Figure 3.10a) using continuous variation with a total concentration of 3  $\mu\text{M}$  of IRPE and  $\text{Fe}^{3+}$  exhibited two maximum absorbances (at 523 and 664 nm). The results showed that the ratiometric values of the absorbance ( $A_{523}/A_{664}$ ) of the system (IRPE +  $\text{Fe}^{3+}$ ) reached a maximum value when the molecular fraction of  $\text{Fe}^{3+}$  was close to 0.5, indicating a 1:1 stoichiometry. The titration curves (a plot of absorption versus the ratio of IRPE/ $\text{Fe}^{3+}$ ) increased at 523 nm and decreased at 664 nm (Figure 3.1 and Figure 3.10b) linearly and plateaued at 1:1 ratio of the sensor and  $\text{Fe}^{3+}$ , suggesting the formation of a 1:1 of IRPE- $\text{Fe}^{3+}$  complex also. The binding constant of this complex was calculated following the method explained in chapter 2, using absorption values at 523 nm, and was determined to be  $2.0 \times 10^5 \text{ M}^{-1}$ . The species formed between IRPE and  $\text{Fe}^{3+}$  was more accurately determined by ESI-MS. Upon the mixing of  $\text{Fe}^{3+}$  and the sensor (1  $\mu\text{M}$  sensor and excess of  $\text{Fe}^{3+}$  in ACN/ $\text{H}_2\text{O}$ ), one major species were detected by ESI-MS (Figure 3.11), corresponding to IRPE+  $\text{Fe}^{3+}$  with three chloride ions and one water molecule ( $m/z=863.8$ , assignable to a 1:1 complex). This implies that  $\text{Fe}^{3+}$  is in 7-coordination with the sensor with three chloride ions and one  $\text{H}_2\text{O}$  molecule under the ESI-MS conditions.

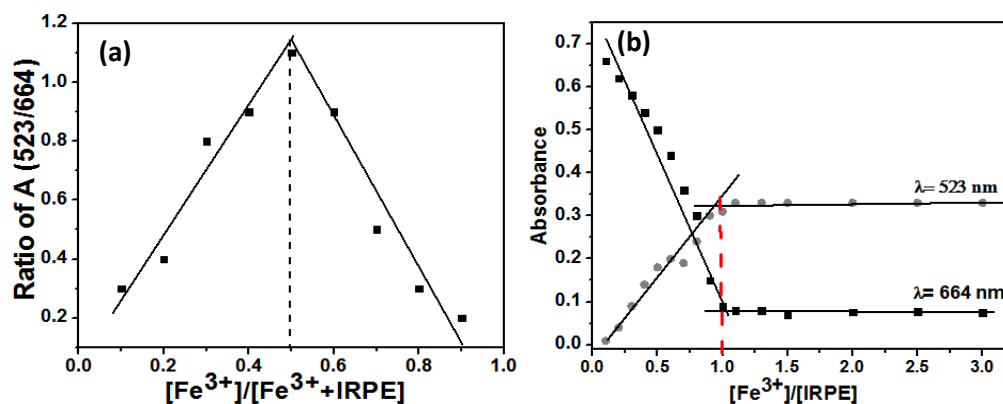


**Figure 3.10** (a) Job's plot of the complexation between IRPE and  $\text{Fe}^{3+}$  [ $\text{IRPE}] + [\text{Fe}^{3+}] = 5 \mu\text{M}$  in ACN/HEPES buffer (10 mM, pH 7.0, v/v 1:1) (b) Titration of  $3 \mu\text{M}$  IRPE with increasing concentrations of  $\text{FeCl}_3$  (0.5, 1, 1.5, 2.0, 2.5, 3.0, 3.5, 4.0, 4.5, 5.0, 5.5, 6.0, 7.5, 10.0, 12.5, and 15  $\mu\text{M}$ , respectively) in ACN/HEPES buffer (10 mM, pH 7.0, v/v 1:1). The absorption intensities increased at 523 nm and decreased at 664 nm.

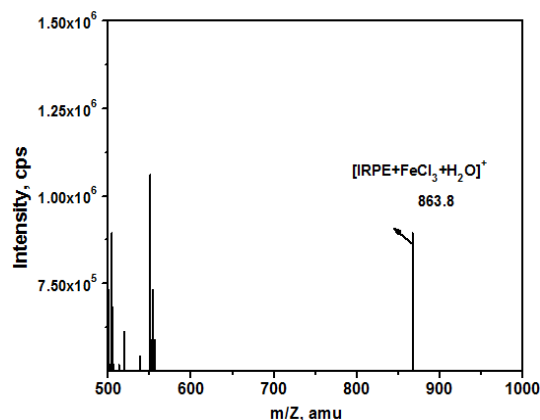


**Figure 3.11** ESI-MS spectrum of the solution of IRPE with  $\text{FeCl}_3$  ( $1 \mu\text{M}$  sensor and excess  $\text{Fe}^{3+}$  in ACN/ $\text{H}_2\text{O}$ )

To gain a better understanding of the binding between IRPE and  $\text{Fe}^{3+}$ , the effect of pH on IRPE and IRPE- $\text{Fe}^{3+}$  complex at pH range over 1 to 10 (pH was adjusted by adding HCl, NaOH and acetate buffer and measured by a pH meter) was also investigated and the response was monitored by absorption spectra. As seen in Figure 3.12a the ratiometric fluorescence response of IRPE has no response to hydrogen ions at pH between 3-8 but it does have a ratiometric fluorescence response after pH 8 (6-fold fluorescent enhancement). On the other hand, the

ratiometric fluorescence response of IRPE+Fe<sup>3+</sup> solutions was stable in pH from 3 to 10. It can be explained by deprotonation of the NH group<sup>[38]</sup> in IRPE. When IRPE coordinates with Fe<sup>3+</sup>, N-H already deprotonated and pH does not affect the complex. In contrast to the complex, IRPE itself has an N-H group and at high pH (pKa of this N-H is around 9<sup>[38]</sup>), the N-H is deprotonated and gives ratiometric fluorescence response (increase in fluorescence at 580 and decrease at 760 nm). To sum up, these remarkable hypsochromic shifts are attributed to disruption of the pull-push  $\pi$ -conjugation system of the tricarbocyanine that is induced by deprotonation of the NH group<sup>[38]</sup> in IRPE.

In addition, reversibility experiments were carried out by adding EDTA to the IRPE-Fe<sup>3+</sup> complex in the ACN/HEPES buffer (10 mM, pH 7.3, v/v 1:1). In the absence of EDTA, the complex was reddish-color and non-fluorescent at 760 nm. After adding EDTA, fluorescent intensity increased (Figure 3.12 b), suggesting a reversible binding between IRPE and Fe<sup>3+</sup>.

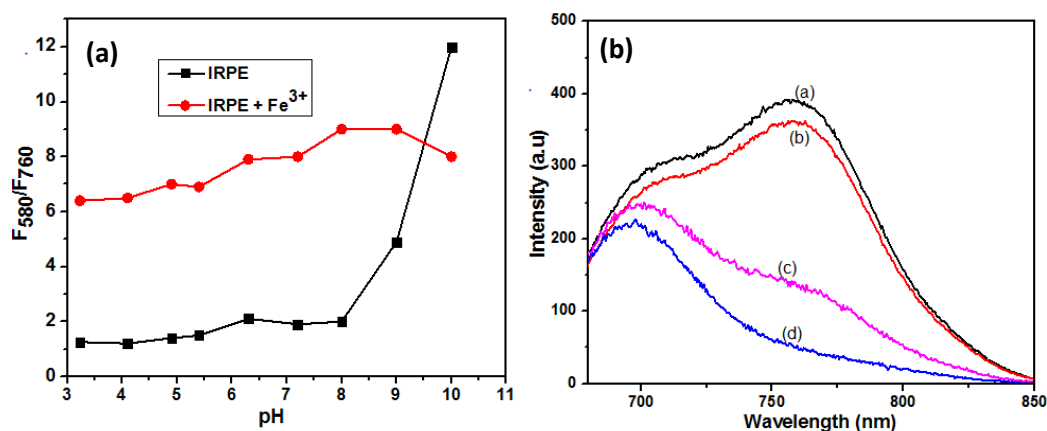
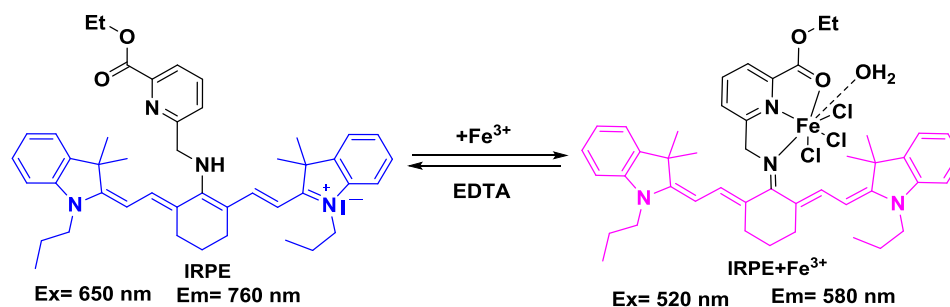


**Figure 3.12** (a) Ratiometric fluorescent responses of IRPE and IRPE+Fe(III) (3  $\mu$ M each) at various pH values in ACN/H<sub>2</sub>O (1/1, v/v) solution. pH was adjusted by HCl (0.1 M) and NaOH (0.1 M) (b) Reversibility of IRPE (3  $\mu$ M) to Fe<sup>3+</sup> ions by EDTA ((a) free IRPE (3  $\mu$ M), (d) IRPE + 1equiv of Fe<sup>3+</sup>, (c) IRPE + 1 equiv of Fe<sup>3+</sup> + 1 equiv of EDTA, (b) IRPE + 1 equiv of Fe<sup>3+</sup> + 2 equiv of EDTA)

These control experiments showed that this hypsochromic shift (141 nm) of the maximum absorption wavelength could be ascribed to shortening of the conjugated  $\pi$ -electron system in cyanine dye. A possible mechanism for the reaction and the binding mode is shown in Scheme 3.2.



**Scheme 3.2** Proposed reversible 1:1 binding mode between IRPE and Fe<sup>3+</sup>

### 3.3.4 Cell Studies

To test the ability of IRPE to capture Fe<sup>3+</sup> ions in cells, B16F-10 melanoma cells were incubated with IRPE (2  $\mu$ M) for 30 min. IRPE was cell permeable, and it exhibited fluorescence in red channel, but almost no fluorescence in blue channel. The cells were pre-incubated with FeCl<sub>3</sub> (10  $\mu$ M) for overnight and incubated with IRPE (2  $\mu$ M) for 30 min. As seen in Figure 3.13, it was not observed any significant fluorescence change. This is probably due to the weak binding between IRPE and Fe<sup>3+</sup>.

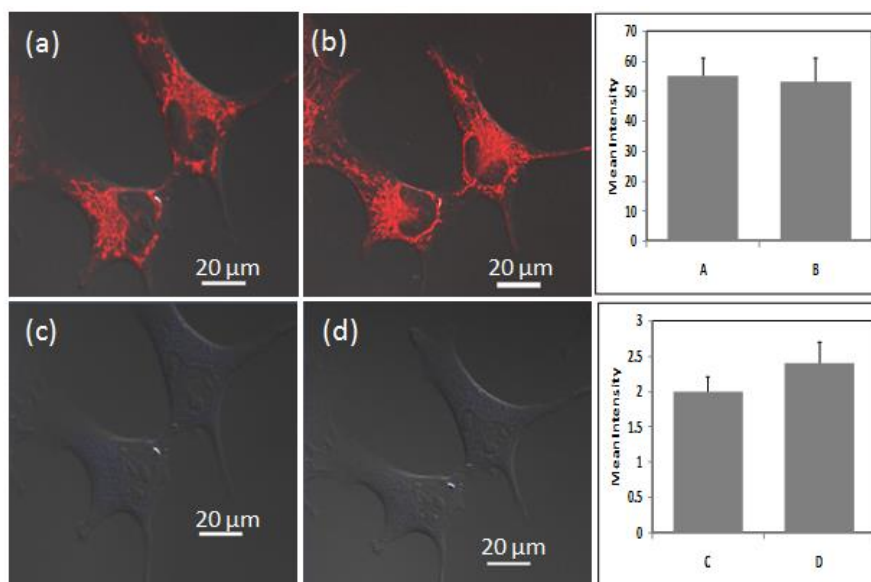


**Figure 3.13** Confocal microscopy images (with DIC) of B16-F melanoma cells treated with (a, c) 10 μM CR-PK sensor after 30 min incubation (b, d) the cells were incubated with Fe<sup>3+</sup> (10 μM) for 8 h then incubate with the sensor for 30 min (Excitation wavelength was 633 nm for a, b, 514 nm for c, d; fluorescence emission collected 520-620 nm for blue channels, 660-750 nm for red channels)

### 3.4 Conclusion

In summary, several heptamethine based near infrared fluorescent dyes were synthesized. Only IRPE showed response to Fe<sup>3+</sup>. It binds to Fe<sup>3+</sup> in a 1:1 stoichiometry with an apparent binding constant  $2.0 \times 10^5 \text{ M}^{-1}$  in ACN/HEPES (1/1 v/v) solution. The sensor displays a change in color and fluorescence upon the alteration of Fe<sup>3+</sup> levels in solution with a reversible response and little interference with other biological relevant metal ions. IRPE is a good Fe<sup>3+</sup>-selective sensor but, cell studies showed that it is not capable of detecting free iron ions in cells.

### 3.5 References

1. Crichton R., Ed. Inorganic biochemistry of iron metabolism, 2nd ed.; John Wiley & Sons Ltd.: U.K., **2001**, pp. 17-48
2. Rouault T., Nat. Chem. Biol., **2006**, 2, 406-414
3. Kell D. B., BMC Medical Genomics, **2009**, 2, 2
4. Espósito B. P., Epsztejn S., Breuer W., Cabantchik Z. I., Anal. Biochem., **2002**, 304, 1-18
5. Que E. L., Domaille D. W., Chang C. J., Chem. Rev., **2008**, 108, 1517-1549
6. Domaille D. W., Que E. L., Chang C. J., Nat. Chem. Biol., **2008**, 4, 168-175
7. Lohani C. R., Lee K.H., Sens. Actuators B, **2010**, 143, 649-654
8. Wolf C., Mei X., Rokadia H. K., Tetrahedron Lett., **2004**, 45, 7867-7871
9. Liu J. M., Zheng Q., Yang J., Chen C., Huang Z., Tetrahedron Lett., **2002**, 43, 9209-9212
10. Singh N., Kaur N., Dunn J., MacKay M., Callan J. F., Tetrahedron Lett., **2009**, 50, 953-956
11. Yang Z., She M., Yin B., Cui J., Zhang Y., Sun W., Li J., Shi Z., J. Org. Chem., **2012**, 77, 1143-1147
12. Wei Y., Aydin Z., Zhang Y., Liu Z., Guo M., ChemBioChem, **2012**, 13, 1569-1573
13. Lee M. H., Giap T. V., Kim S. H., Lee Y. H., Kang C., Kim J. S., Chem. Commun., **2010**, 46, 1047-1049
14. Wang B., Hai J., Liu Z., Wang Q., Yang Z., Sun S., Angew. Chem. Int. Ed., **2010**, 49, 4576-4579
15. Lim N. C., Pavlova S. V., Bruckner C., Inorg. Chem., **2009**, 48, 1173-1182
16. Marenco M. J. C., Fowley C., Hyland B. W., Hamilton G. R. C., Galindo-Riano D., Callan J. F., Tetrahedron Lett., **2012**, 53, 670-673
17. Jung H. J., Singh N., Jang D. O., Tetrahedron Lett., **2008**, 49, 2960-2964
18. Lee D. Y., Singh N., Jang D. O., Tetrahedron Lett., **2011**, 52, 3886-3890
19. Miwa M., Open Surg. Oncol. J., **2010**, 2, 26-28
20. Conway J.M., Norris K.M., Bodwell E.C., Am. J. Clin. Nutr., **1984**, 40, 1123-1130
21. Peng X., Song F., Lu E., Wang Y., Zhou W., Fan J., Gao Y., J. Am. Chem. Soc., **2005**, 127, 4170-4171
22. Kiyose K., Aizawa S., Sasaki E., Kojima H., Hanaoka K., Terai T., Urano Y., Nagano T., Chem. Eur. J., **2009**, 15, 9191-9200
23. Descalzo A.B., Rurack K., Chem. Eur. J., **2009**, 15, 3173-3185



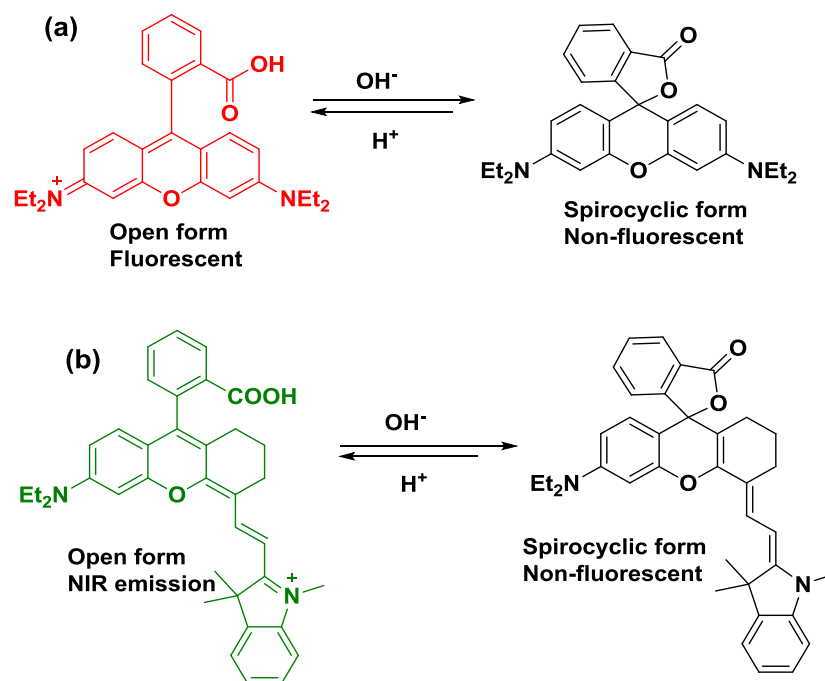
24. Mojzych M., Henary M., *Top. Heterocycl. Chem.*, **2008**, 14, 1-9
25. Zheng H., Yan M., Fan X., Sun D., Yang S., Yang L., Li J., Jiang Y., *Chem. Commun.*, **2012**, 48, 2243-2245
26. Tang B., Yu F., Li P., Tong L., Duan X., Xie T., Wang X., *J. Am. Chem. Soc.*, **2009**, 131, 3016-3023
27. Cooper M.E., Gregory S., Adie E., Kalinka S., *J. Fluoresc.*, **2002**, 12, 425-429
28. Kiyose K., Kojima H., Nagano T., *Chem. Asian J.*, **2008**, 3, 506-515
29. Amiot C. L., Xu S., Liang S., Pan L., Zhao J. X., *Sensors*, **2008**, 8, 3082-3105
30. Bouteiller C., Clave G., Bernardin A., Chipon B., Massonneau M., Renard P., Romieu A., *Bioconjugate Chem.*, **2007**, 18, 1303-1317
31. Flanagan J. H., Khan S. H., Menchen S., Soper S. A., Hammer R.P., *Bioconjugate Chem.*, **1997**, 8, 751-756
32. Song F., Peng X., Lu E., Zhang R., Chen X., Song B., *J. Photochem Photobiol A: Chem*, **2004**, 168, 53-57
33. Song F., Peng X, Lu E., Wang Y., Zhou W., Fan J., *Tetrahedron Lett.*, **2005**, 46, 4817-4820
34. Strekowski L., Lipowska M., Patonay G., *J. Org. Chem.*, **1992**, 57, 4578-4580
35. Fornasier R., Milani D., Scrimin P. Tonellato U., *J. Chem. Soc. Perkin. Trans II*, **1986**, 233-237
36. Samanta A., Vendrell M., Das R., Chang Y.T., *Chem. Comm.*, **2010**, 46, 7406-7408
37. Zheng H., X. Zhang J., Cai X., Bian Q. N., Yan M., Wu G. H., Lai X. W., Jiang Y. B., *Org. Lett.*, **2012**, 14, 1986-1989
38. Guo Z., Kim G.H., Shin I., Yoon J., *Biomaterials*, **2012**, 33, 7818-7827

## CHAPTER 4

### A NEAR INFRARED TURN-ON FLUORESCENT SENSOR NIRh-Ac FOR DETECTION OF EXOGENOUS $\text{Fe}^{3+}$ IN LIVE CELLS AND ZEBRAFISH

#### 4.1 Introduction

Because the cyanine-based sensors were not successful in *in vivo* application (chapter 3), we decided to change the design of the near-infrared sensor. Rhodamine based sensors have been successfully used in detecting  $\text{Fe}^{3+}$  ions in cells.<sup>[1-3]</sup> The spirocyclic form of rhodamine is colorless and nonfluorescent due to separating the  $\pi$ -conjugation of the original fluorophore, whereas the ring-opened form shows strong spectroscopic signals in the absorption and fluorescence spectra by retrieving the large  $\pi$ -conjugated system (Scheme 4.1a). Therefore, precise modulation of the equilibrium between the spirocyclic form and the ring-opened form of rhodamines provides an ideal strategy for constructing fluorescent probes for various analytes.<sup>[4-6]</sup> Recently, this spirocyclization-based fluorescence mechanism has been extended to some near-infrared dyes.<sup>[7-8]</sup> Most recently, Yuang *et al.* developed Changsha (CS) near infrared fluorophores.<sup>[9]</sup> CS-NIR dyes bear the same robust fluorescence ON-OFF switching mechanism as the traditional rhodamine dyes (Scheme 4.1 b for CS2). It was then decided to harness these CS near infrared dyes and the  $\text{Fe}^{3+}$ -binding group of RPE to design NIR sensors for  $\text{Fe}^{3+}$  ions detection in living systems.



**Scheme 4.1** Equilibrium between the open form and spirocyclic form of rhodamine (a) and one of Changsha (CS) near infrared fluorophores

In this chapter, the properties of a highly selective and highly sensitive reversible off-on near infrared fluorescent Fe<sup>3+</sup> sensor NIRh-Ac (Scheme 4.2) is described. The unique reversible “turn-on” property and high sensitivity of NIRh-Ac allow it to locate the exogenous exchangeable Fe<sup>3+</sup> pools at subcellular resolution in live human neuroblastoma SH-SY5Y cells. Moreover, the NIRh-Ac sensor has also been demonstrated to visualize chelatable Fe<sup>3+</sup> ions in zebrafish.

## 4.2 Experimental Section

### 4.2.1 Materials and Reagents

All the reagents and solvents were of the highest commercial quality and were used without further purification. Acetonitrile anhydrous (99.8 % Sigma-Aldrich), H<sub>2</sub>SO<sub>4</sub> (98 % Fisher), Ethanol, dichloromethane (99.8% TCI America) and double-distilled water were used as solvents.

2-(1,3,3-Trimethylindolin-2-ylidene) acetaldehyde was purchased from OChem Incorporation. 2-(4-Diethylamino-2-hydroxybenzoyl) benzoic acid and benzotriazol-1-yloxytris(dimethylamino)-phosphoniumhexafluorophosphate (BOP) were purchased from TCI America. Thin-layer chromatography was performed on silica gel 60F-254 glass plates. Reaction products were purified by flash chromatography using silica gel or alumina gel.

#### 4.2.2 Instrumentation

$^1\text{H}$  and  $^{13}\text{C}$  NMR spectra were recorded on a Bruker DRX-300 spectrometer or a Bruker AVANCE III HD w400 at ambient temperature (298K). Chemical shifts are reported in delta ( $\delta$ ) parts per million (ppm) downfield tetramethylsilane. Splitting patterns are abbreviated as follows: s, singlet; d, doublet; t, triplet; q, quartet; m, multiplet; br, broad. LC-MS analyses were performed on a Perkin Elmer API 150EX mass spectrometer. UV/Vis spectra were recorded on a Perkin Elmer Lambda 25 spectrometer at 298 K. Fluorescence spectra were recorded on a Perkin Elmer LS55 luminescence spectrometer at 298 K. Excitation and emission slits were 10 nm and emission spectra were collected 710 nm-850 nm after excited at 690 nm. The pH measurements were carried out on a Corning pH meter equipped with a Sigma-Aldrich micro combination electrode calibrated with standard buffer solution.

#### 4.2.3 Synthesis and Characterization

##### **6-(N,N Diethylamino)-9-(2-Carboxypheyl)-1,2,3,4-tetra-Hydroxantylum Perchlorate (1) :**

Freshly distilled cyclohexanone (3.3 mL, 31.9 mmol) was added drop wise to concentrated  $\text{H}_2\text{SO}_4$  (35 mL) and cooled down to 0 °C. Then, 2-(4-Diethylamino-2-hydroxybenzoyl)benzoic acid (5 g, 16 mmol) was added in portions with vigorous stirring. The reaction mixture was heated at 90 °C for 1.5 h, then cooled down, and poured onto ice (150 g). Perchloric acid (70%, 4 mL) was then

added, and the resulting precipitate was filtered off and washed with cold water (100 mL) to obtain a red solid. **1** was used for the next step without further purification.

**3H-Indolium,2-[2-[9-(2-carboxyphenyl)-6-(diethylamino)-2,3-dihydro-1H-xanthen-4-**

**yl]ethenyl]-1,3,3-trimethyl-, perchlorate (**2**):** **1** (1 g, 2.1 mmol) and 2-(1,3,3-Trimethylindolin-2-ylidene) acetaldehyde (0.44 g, 2.2 mmol) were dissolved in acetic anhydride (12 mL), and the reaction mixture was heated to 50 °C and further stirred at 50 °C for 75 min. Then, water (12 mL) was added to the reaction mixture to quench the reaction. The solvent was removed under reduced pressure to give the crude product, which was purified by alumina gel flash chromatography using CH<sub>2</sub>Cl<sub>2</sub> to CH<sub>2</sub>Cl<sub>2</sub>/methanol (200:1 to 20:1) as eluent to afford the compound **2** (0.45 g, yield 33%). <sup>1</sup>H NMR (CDCl<sub>3</sub>, 300 MHz δ(ppm)): 8.68 (d, 1H), 8.15 (d, 1H), 7.80 - 7.11 (m, 8H), 6.92 - 6.60 (m, 3H), 5.50 (s, 1H), 3.62 (d, 3H), 2.71 (t, 2H), 2.46 - 2.30 (m, 4H), 1.82 (s, 8H), 1.28 (t, 6H). ESI-MS: found: *m/z* = 559.6 [M]<sup>+</sup>, calcd for C<sub>37</sub>H<sub>39</sub>N<sub>2</sub>O<sub>3</sub><sup>+</sup> = 559.3.

**Spiro[1H-isoindole-1,9'-[9H]xanthen]-3(2H)-one,2-amino-6'-(diethylamino)-4'-[2-(1,3-dihydro-1,3,3-trimethyl-2H-indol-2-ylidene)ethylidene]-1',2',3',4'-tetrahydro (NIRh)** : To a solution of **2** (0.76 mmol, 500.1 mg) in dry CH<sub>2</sub>Cl<sub>2</sub> was successively added NH<sub>2</sub>NH<sub>2</sub>·H<sub>2</sub>O (7.6 mmol, 380.2 mg) and BOP (0.80 mmol, 360.9 mg). The mixture was stirred at room temperature for 2 h, and the solvent was evaporated under reduced pressure. The residue was purified by an alumina gel column using CH<sub>2</sub>Cl<sub>2</sub>/ methanol (V/V, 20:0 to 20: 1) to afford compound NIRh as a yellow solid (212 mg, 38 %).

**NIRh-Ac:** NIRh (0.21 g, 0.36 mmol) and acetylacetone (0.7 ml) were dissolved in ethanol (25 ml). The reaction mixture was then stirred and refluxed for overnight to obtain a pale green precipitate. The precipitate was collected by filtration, washed with ethanol, and dried in vacuum to give the 85 mg of NIRh-Ac (yield; 35 %). <sup>1</sup>H NMR (CDCl<sub>3</sub>, 300 MHz δ(ppm)): 7.91 (d,

1H), 7.58 - 7.36 (m, 4H), 7.18 (d, 4H), 6.83 (t, 1H), 6.61 (d, 1H), 6.42 (s, 2H), 6.32 (s, 3H), 5.36 (d, 1H), 5.03 (s, 1H), 3.35 (d, , 4H), 3.14 (s, 4H), 2.69 (d, 2H), 2.40 (s, 1H), 1.99 (s, 4H), 1.69 (s, 6H), 1.17 (t, 6H). <sup>13</sup>C NMR (CDCl<sub>3</sub>, 75 MHz δ(ppm)): 196.44, 167.19, 164.21, 157.85, 153.61, 149.99, 149.73, 149.17, 145.64, 139.13, 133.41, 130.06, 129.08, 128.72, 127.92, 124.31, 123.74, 121.75, 120.62, 120.10, 119.44, 108.38, 105.91, 104.51, 101.42, 98.26, 97.37, 92.52, 77.70, 77.28, 76.86, 69.13, 58.73, 45.65, 44.61, 29.38, 29.24, 28.72, 28.48, 25.60, 23.82, 22.40, 18.71, 18.44, 12.79: ESI-MS: found: m/z = 655.6 [M+H]<sup>+</sup>, calcd for C<sub>41</sub>H<sub>45</sub>N<sub>4</sub>O<sub>3</sub> = 654.4.

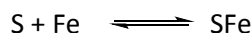
#### 4.2.4 Procedures for Metal Ion Sensing

The solution of metal ions were prepared from chloride salts of Ni<sup>2+</sup>, Fe<sup>3+</sup>, Cu<sup>2+</sup>, Mn<sup>2+</sup>, Hg<sup>2+</sup>, Na<sup>+</sup>, Ca<sup>2+</sup>, Zn<sup>2+</sup>, Ag<sup>+</sup>, and nitrate salts of Mg<sup>2+</sup>, Pb<sup>2+</sup>, K<sup>+</sup>, Co<sup>2+</sup> and ammoniumsulphate salt of Fe<sup>2+</sup>. Stock solutions of metal ions (10 mM) were prepared in deionized water, except for Fe<sup>3+</sup> and Fe<sup>2+</sup> in 0.1 M HCl. Solution of Cu<sup>+</sup> was freshly prepared by dissolving tetrakis(acetonitrile) copper(I) (Sigma-Aldrich) into double-distilled water.

A stock solution of NIRh-Ac (1 mM) was prepared in ACN. The solution of NIRh-Ac was diluted to 20 μM with ACN/Tris buffer (10 mM, pH 7.3, v/v, 1:1). Before spectroscopic measurements, solutions were freshly prepared by diluting the corresponding high-concentration stock solution. For each spectrum, 1 mL of a probe solution was added to a 1-cm quartz cell, to which different stock solutions of cations were gradually added. All spectroscopic measurements were done under simulated physiological pH, and measurements were performed at least triplicate and resulting averages are reported.

#### 4.2.5 Binding Studies

Fe<sup>3+</sup>-binding titration and Job's plots were obtained for NIRh-Ac to determine the stoichiometry between Fe<sup>3+</sup> and NIRh-Ac. For Job's plot, the total molar concentrations of the NIRh-Ac and iron(III) were held constant, but their mole fractions were varied. Then, absorption spectra or fluorescent emissions of these fractions were collected. In addition, absorption values at maximum were plotted against the mole fractions of NIRh-Ac and iron(III). Typical UV-vis titration experiments for NIRh-Ac were performed by the following process. A solution of NIRh-Ac (1 mM, prepared in ACN) was first diluted to 20 μM with ACN/Tris-HCl buffer (10 mM, pH 7.3, v/v 1:1) and the absorption spectrum were recorded in a quartz cell. Then Fe<sup>3+</sup> solution (10 mM, prepared in acetonitrile) was introduced in portions 2, 4, 6, 10, 12, 14, 16, 18, 20, 28, 36, 44, 52, and 60 μM, respectively (20 μL corresponds to 1 equiv) to each of the NIRh-Ac solutions (20 μM, 1 ml). The spectra were recorded 5 minutes after each addition. The binding constants were estimated by using the absorption titration results. The equation below was used to calculate the binding constants.<sup>[10]</sup>



Where S = Sensor, Fe = Fe<sup>3+</sup> and SFe = Sensor-Fe<sup>3+</sup> complex the equilibrium constant (apparent binding constant) is given by:

$$K = \frac{[SFe]_e}{[S]_e [Fe]_e}$$

The subscript e designates equilibrium concentrations. The ratios of the equilibrium SFe complex concentration, [SFe]<sub>e</sub>, and the initial S concentration, [S]<sub>o</sub>, can be derived from the absorbance of the solutions at a chosen wavelength both at equilibrium and far from equilibrium. The result of the derivation is as follows:

$$F_c = \frac{Au - Am}{Au - Ac} = \frac{[SFe]_e}{[S]_o}$$

Where  $F_c$  is the fraction of  $S$  that formed a complex, the subscripts  $e$  and  $o$  stand for equilibrium and initial concentrations, respectively.  $A_u$ ,  $A_m$ , and  $A_c$  are the absorbance (at a chosen wavelength) of solutions of  $S$  only (before  $Fe^{3+}$  was added);  $S$  and  $SFe$  mixture (somewhere in the middle of titration); and  $SFe$  only (at the end of titration) respectively. The concentration of free  $Fe^{3+}$  at equilibrium  $[Fe]_e$  is derived from:

$$[Fe]_e = [Fe]_o - [SFe]_e = [Fe]_o - F_c[S]_o$$

The apparent binding constant  $K$  can then be calculated from the equations above:

$$K = \frac{F_c}{1 - F_c} \times \frac{1}{[Fe]_e}$$

#### 4.2.6 Quantum Yield

Stock solutions of 40  $\mu$ M NIRh-Ac, 40  $\mu$ M Rhodamine B (standard), and 40  $\mu$ M NIRh-Ac + Fe(III) were prepared. Dilutions of NIRh-Ac, Rhodamine B, NIRh-Ac + Fe(III) were prepared in EtOH at concentrations such that their absorbance at 713 nm equaled 0.1, 0.2, 0.3, 0.4, and 0.5  $\mu$ M. Excitation was performed at 690 nm and collected emissions were normalized to the EtOH blank and then integrated from 720-850 nm. A plot of the integrated fluorescence intensity vs. the absorbance at 713 nm for each concentration was prepared and the positive slope of the linear fit was calculated. The data were compared to the rhodamine standard using the following equation, where  $\Phi_R$  is the quantum yield of the standard (0.97),  $Grad$  is the slope of the absorbance vs. emission line found for each compound,  $Grad_R$  is the slope found for the



Rhodamine standard,  $\eta$  is the refractive index of the sample solutions (1.33) and  $\eta_R$  is the refractive index of the rhodamine solution (1.33):

$$\Phi = \Phi_R (\text{Grad}/\text{Grad}_R) (\eta^2/\eta_R^2)$$

$$\Phi_{\text{NIRh-Ac}} = 0.0194$$

$$\Phi_{\text{NIRh-Ac} + \text{Fe(III)}} = 0.236$$

#### 4.2 .7 Cell culture

Two different cell lines, human SHSY5Y and fibroblast cells (ws1) both obtained from ATCC (American Type Culture Collection), were used in the study. SHSY5Y cells were maintained in a 1:1 mixture of Eagle's Minimal Essential medium (ATCC) and Ham's F12 medium (ATCC) supplemented with 10% fetal bovine serum (FBS, ATCC) without antibiotics and incubated at 37 °C in a humidified 5% CO<sub>2</sub> atmosphere. The cells were routinely subcultured using 0.05% trypsin-EDTA solution (ATCC). The cells were seeded onto 2-chamber slides for 48 h at 5x10<sup>4</sup> cells/chamber and grown until each chamber was 20-30% confluent. Fibroblast cells (WS1, primary cultured fibroblast cells) were passaged in the Eagle's Minimum Essential Medium containing 10% fetal bovine serum (complete growth medium). The cells were routinely subcultured using 0.25% trypsin-EDTA solution, neutralized by adding the complete growth medium and seeded on the 25-cm<sup>2</sup> flask without centrifuge. Medium change every two or three days until a 70% confluency before transferring into patri dish for further experiments.

A stock solution of NIRh-Ac (10 mM in DMSO) was diluted to a concentration of 20 μM in culture medium without FBS. Cell culture medium was removed from the chambers and replaced with fresh medium containing NIRh-Ac (10-20 μM). These cells were then subjected to fluorescence imaging using a LSM 710 confocal microscope. Similar imaging experiments were

performed after the cells had been incubated with  $\text{Fe}^{3+}$  ( $\text{FeCl}_3 \cdot 6\text{H}_2\text{O}$ ) for 8h first, then cells were incubated with NIRh-Ac for 30 min.

MitoTracker Green FM (M-7514) (Invitrogen, CA) and LysoTracker blue DND 22 (Invitrogen, CA) were employed for colocalization studies. In a typical experiment, SH-SY5Y neuroblastoma cells were incubated with iron(III) for overnight, then NIRh-Ac was added into cells then incubated for 30 min, followed by adding the trackers and incubating for additional 30 min.

#### **4.2.8 Zebrafish Studies**

Zebrafish was maintained under standard conditions<sup>[11]</sup> in collaborator Prof. T.Ferreira's lab (UMD, Bioengineering). Embryos were collected from natural spawning and raised up in embryo medium. Zebrafish strain nacre was utilized because it lacks pigment, allowing better visualization. Three-day-old nacre zebrafish were maintained in E3 embryo media (15mM NaCl, 0.5mM KCl, 1 mM  $\text{MgSO}_4$ , 1 mM  $\text{CaCl}_2$ , 15 mM  $\text{KH}_2\text{PO}_4$ , 0.05 mM  $\text{Na}_2\text{HPO}_4$ , 0.7 mM  $\text{NaHCO}_3$ ,  $10^{-5}$  % Methylene blue; pH 7.5). Then the zebrafish were incubated with various concentrations of  $\text{Fe}^{3+}$  ions (0, 5, 10, 50  $\mu\text{M}$ ) for 3 days in E3 media at 28 °C. Then zebrafish were washed with PBS and put in fresh E3 media and then incubated with 5  $\mu\text{M}$  of NIRh-Ac for 30 min at 28°C. The remaining probe was removed by washing with PBS and the fish were imaged by confocal microscopy.

#### **4.2.9 Confocal Fluorescence Microscopy**

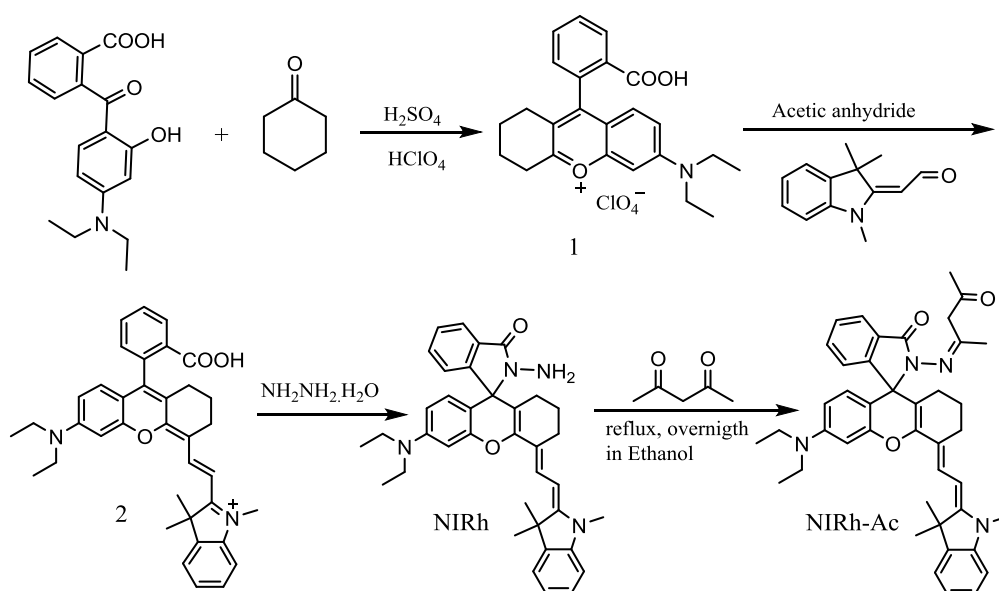
The fluorescence responses of the sensor in living cells were measured under a Zeiss LSM 710 laser scanning confocal microscope. For images with the NIRh-Ac sensor, the excitation wavelength of the laser was 633 nm and emission was integrated over the range 680-750 nm.

For images with MitoTracker Green FM, LysoTracker Blue DND-22 and Hoechst 33258, the excitation wavelengths recommended by the manufacturer were used (490 nm for MitoTracker, 405 nm for LysoTracker and 405 nm for Hoechst 33258). Emissions were integrated at 492-548 nm (MitoTracker), 409-484 nm (Lyso-Tracker) and 426-535 nm (Hoechst 33258), respectively. The REUSE function controlled by Zeiss software was applied to guarantee that all spectra were recorded under the same instrumental conditions.

### 4.3 Results and Discussion

#### 4.3.1 Design and Synthesis of NIRh-Ac

The sensor NIRh-Ac, combining a modified NIR rhodamine reporter (fluorophore) and a  $\text{Fe}^{3+}$  receptor moiety formed by a mixed O/N/O motif similar to that of the RPE sensor, was designed for a near IR sensor for  $\text{Fe}^{3+}$ . It is expected that the coordination site would consist of 2O (one from the lactone, one from the acetylacetonate) and 1N (from the hydrazine). The sensor NIRh-Ac was synthesized in a 4-step procedure (Scheme 4.2) with overall yield of ~35%.



**Scheme 4.2** Synthesis route for NIRh-Ac

### 4.3.2 Spectroscopic Studies

The spectroscopic properties of NIRh-Ac and its interactions with various metal ions were evaluated in acetonitrile (ACN)/Tris-HCl buffer (10 mM, pH 7.3, v/v, 1:1). The yellowish compound NIRh-Ac displays almost no absorption peak in the red and near IR region (>550 nm). The changes in UV-vis spectra after the addition of various ions are shown in Figure 4.1. Only the addition of Fe<sup>3+</sup> to the solution of NIRh-Ac showed an obvious green color with an absorption peak at 713 nm ( $\epsilon = 1.16 \times 10^5 \text{ M}^{-1} \text{ cm}^{-1}$ ) in ACN/Tris-HCl buffer (10 mM, pH 7.32, v/v 1:1) (Figure 4.2). Compared with that of Fe<sup>3+</sup>, other metal ions did not induce any significant changes in the absorption at wavelength greater than 500 nm. Only Cu<sup>2+</sup> showed minor response to NIRh-Ac (Figure 4.1).

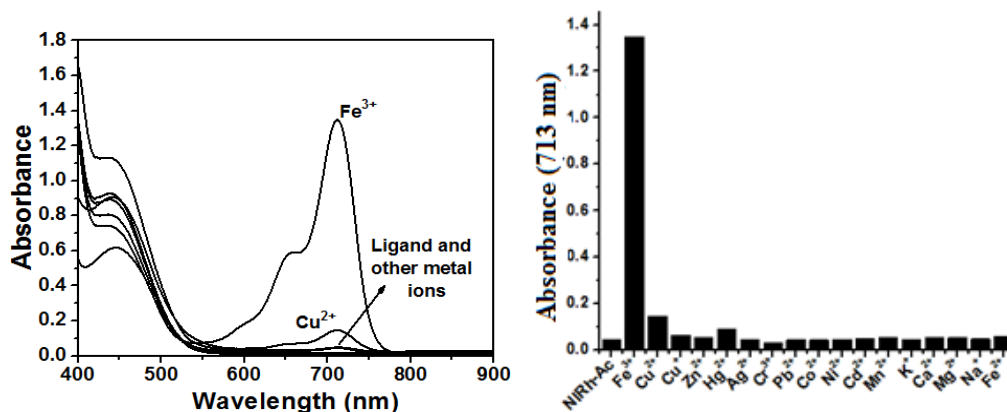


**Figure 4.1** Absorption responses of 20  $\mu\text{M}$  NIRh-Ac to various metal ions (20  $\mu\text{M}$  for Zn<sup>2+</sup>, Cr<sup>3+</sup>, Ni<sup>2+</sup>, Hg<sup>2+</sup>, Fe<sup>3+</sup>, Mn<sup>2+</sup>, Ag<sup>+</sup>, Pb<sup>2+</sup>, Fe<sup>2+</sup>, Cu<sup>+</sup>, Cu<sup>2+</sup>, and Co<sup>2+</sup>; 100  $\mu\text{M}$  for Na<sup>+</sup>, K<sup>+</sup>, Mg<sup>2+</sup>, and Ca<sup>2+</sup>) in ACN/Tris-HCl buffer (10 mM, pH 7.3, v/v 1:1)

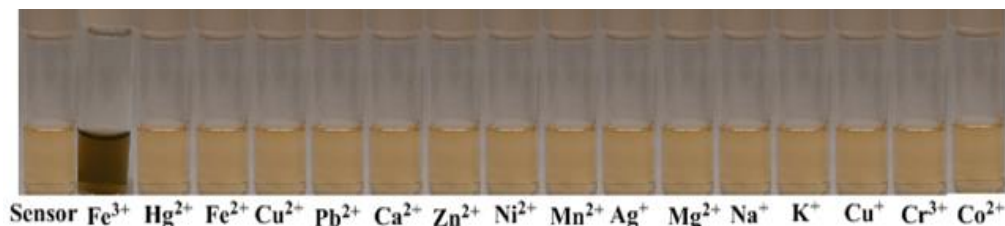


**Figure 4.2** Colour changes of 20  $\mu\text{M}$  NIRh-Ac with various metal ions (50  $\mu\text{M}$  for Zn<sup>2+</sup>, Cr<sup>3+</sup>, Ni<sup>2+</sup>, Hg<sup>2+</sup>, Fe<sup>3+</sup>, Mn<sup>2+</sup>, Ag<sup>+</sup>, Pb<sup>2+</sup>, Fe<sup>2+</sup>, Cu<sup>+</sup>, Cu<sup>2+</sup>, and Co<sup>2+</sup>; 100  $\mu\text{M}$  for Na<sup>+</sup>, K<sup>+</sup>, Mg<sup>2+</sup>, and Ca<sup>2+</sup>) in ACN/Tris Buffer (10 mM, pH 7.3, v/v 1:1)

Then the changes in fluorescence spectra of NIRh with the addition of different metal ions in ACN/Tris-HCl buffer (10 mM, pH 7.32, v/v 2:1) were investigated. NIRh-Ac shows very weak fluorescence in the 650-750 nm range in the absence of metal ions (Figure 4.3). When  $\text{Fe}^{3+}$  was added into the solution of NIRh-Ac, a large fluorescence enhancement at 735 nm was observed, which attributed to the ring opening product (Scheme 4.3), induced by the complexation of  $\text{Fe}^{3+}$ . The emission intensity enhancement at 735 nm ( $\Phi=0.236$ ) is greater than 13-fold with 1.0 equiv of  $\text{Fe}^{3+}$ , suggesting that NIRh-Ac is an excellent turn-on fluorescent sensor for  $\text{Fe}^{3+}$ . In contrast to  $\text{Fe}^{3+}$ , other metal ions such as  $\text{Zn}^{2+}$ ,  $\text{Cr}^{3+}$ ,  $\text{Ni}^{2+}$ ,  $\text{Hg}^{2+}$ ,  $\text{Fe}^{3+}$ ,  $\text{Mn}^{2+}$ ,  $\text{Ag}^+$ ,  $\text{Pb}^{2+}$ ,  $\text{Cu}^+$ ,  $\text{Co}^{2+}$ ,  $\text{Na}^+$ ,  $\text{K}^+$ ,  $\text{Mg}^{2+}$ , and  $\text{Ca}^{2+}$  did not induce any significant spectral response under identical conditions (Figure 4.3). Similar as that observed by UV-vis, only  $\text{Cu}^{2+}$  showed a minor enhancement in fluorescence under these conditions.

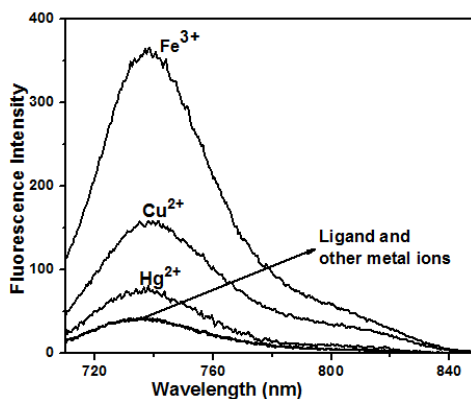


**Figure 4.3** Fluorescence response ( $\lambda_{\text{Ex}} 690\text{nm}$ ) of  $20 \mu\text{M}$  NIRh-Ac to various metal ions ( $20 \mu\text{M}$   $\text{Zn}^{2+}$ ,  $\text{Cr}^{3+}$ ,  $\text{Ni}^{2+}$ ,  $\text{Hg}^{2+}$ ,  $\text{Fe}^{3+}$ ,  $\text{Mn}^{2+}$ ,  $\text{Ag}^+$ ,  $\text{Pb}^{2+}$ ,  $\text{Fe}^{2+}$ ,  $\text{Cu}^+$ ,  $\text{Cu}^{2+}$ , and  $\text{Co}^{2+}$ ;  $100 \mu\text{M}$  for  $\text{Na}^+$ ,  $\text{K}^+$ ,  $\text{Mg}^{2+}$ , and  $\text{Ca}^{2+}$ ) in the ACN/Tris buffer (10 mM, pH 7.3, v/v 1:1)

Moreover, upon the addition of 1 equiv of  $\text{Fe}^{3+}$  into the solutions containing one of the other metal ions tested, the fluorescence was activated and the intensity increased to a level similar to that of in the presence of  $\text{Fe}^{3+}$  only demonstrating that these metal ions do not interfere with the  $\text{Fe}^{3+}$  response (Figure 4.4).

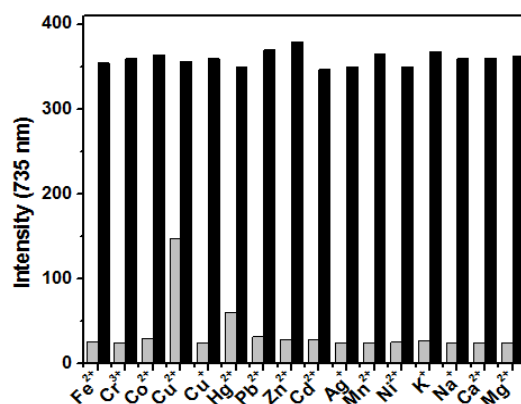


**Figure 4.4** Fluorescence responses of 20  $\mu\text{M}$  NIRh-Ac to the presence of various metal ions (gray bar) and the subsequent addition of  $\text{Fe}^{3+}$  (black bar) in the ACN/Tris buffer; the bars represent the fluorescence intensity at 735 nm

The effect of pH on the stability of the sensor was investigated at different pHs and monitored by both absorption and fluorescent spectra. The pH of the solutions was adjusted by adding HCl or NaOH into the solutions. The fluorescence and absorption of NIRh-Ac at different pH values were plotted in Figure 4.5, demonstrating that the sensor is stable at biological pH range (pH 5-8).

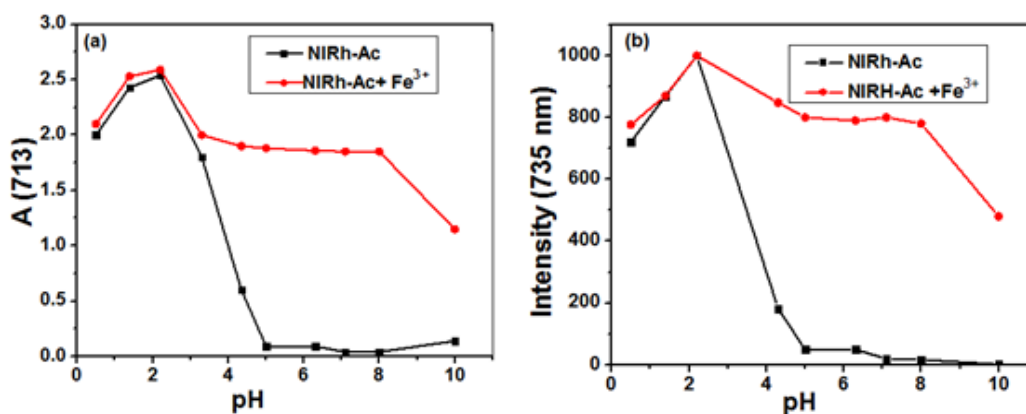


**Figure 4.5** (a) Variation of absorption (713 nm) of NIRh-Ac and NIRh-Ac +  $\text{Fe}^{3+}$  (20  $\mu\text{M}$  each) at various pH values in ACN/ $\text{H}_2\text{O}$  (1/1, v/v) solution (b) Variation of fluorescent intensity (735 nm) of NIRh-Ac and NIRh-Ac +  $\text{Fe}^{3+}$  (10  $\mu\text{M}$  each) at various pH values in ACN/ $\text{H}_2\text{O}$  (1/1, v/v) solution

### 4.3.3 Binding Studies

Job's method and UV-vis titration spectra were applied to study the binding stoichiometry between NIRh-Ac and  $\text{Fe}^{3+}$  and monitored by the absorbance at 713 nm. The titration curve (a plot of NIRh-Ac versus  $\text{Fe}^{3+}$  concentration) increased linearly and plateaued at 1:1 ratio of the sensor and  $\text{Fe}^{3+}$  (Figure 4.6), suggesting the formation of a 1:1  $\text{Fe}^{3+}$ -NIRh-Ac complex. The binding constant of this complex was calculated following a method reported previously<sup>[11]</sup>, using absorption values at 713 nm by the equations described in the experimental section, and was determined to be  $5.02 \times 10^6 \text{ M}^{-1}$ .

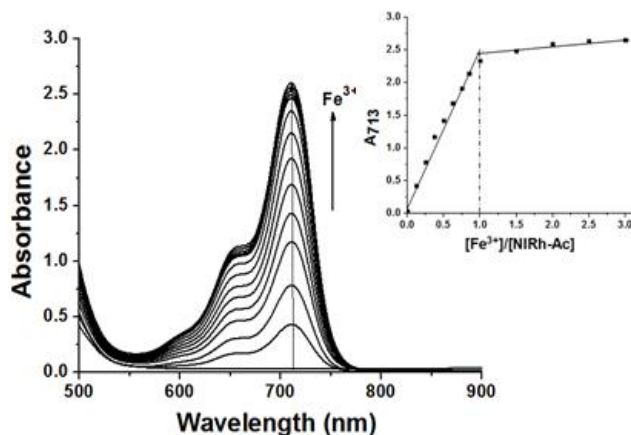


**Figure 4.6** Titration of 20  $\mu\text{M}$  NIRh-Ac with increasing concentrations of  $\text{FeCl}_3$  (2, 4, 6, 10, 12, 14, 16, 18, 20, 28, 36, 44, 52, and 60  $\mu\text{M}$ , respectively) in ACN/Tris-HCl buffer (10 mM, pH 7.3, v/v 1:1). Inset, a plot of fluorescent emissions at 713 nm versus the ratio of  $[\text{Fe}^{3+}]/[\text{NIRh-Ac}]$

The Job's plot (Figure 4.7a) using a total concentration of 20  $\mu\text{M}$  NIRh-Ac and  $\text{Fe}^{3+}$  in ACN/Tris-HCl buffer (10 mM, pH 7.32, v/v 1:1) solution exhibited a maximum absorbance when the molecular fractions of  $\text{Fe}^{3+}$  and NIRh-Ac were close to 50%, suggesting a 1:1 stoichiometry for the binding of NIRh-Ac and  $\text{Fe}^{3+}$ . The species formed between NIRh-Ac and  $\text{Fe}^{3+}$  was more accurately determined by ESI-MS. Upon the mixing of  $\text{Fe}^{3+}$  and the sensor (1  $\mu\text{M}$  each in ACN/ $\text{H}_2\text{O}$  1:1), two major species were detected by ESI-MS (Figure 4.7b): one corresponding to

the free sensor NIRh-Ac with H<sub>2</sub>O ( $m/z=671.4$ ,  $[\text{NIRh-Ac-H}_2\text{O}]^+$ ), and the other, detected at  $m/z=780.1$ , assignable to a 1:1 complex with chloride as co-ligands with a charge of 1+ ( $[\text{NIRh-Ac-Fe(III)-Cl}_2]^+$ ). This implies that Fe<sup>3+</sup> is in 5-coordination with the sensor and two chloride ions under the ESI-MS conditions (Scheme 4.3).

Reversibility experiments were carried out by adding EDTA to the sensor-Fe(III) complex in ACN/Tris-HCl buffer (10 mM, pH 7.32, v/v 1:1. In the absence of EDTA, the complex was green and fluorescent. After adding EDTA, the absorption of the complex decreased in intensity and finally, disappeared (Figure 4.7c), suggesting a reversible binding between NIRh-Ac and Fe<sup>3+</sup>. A possible mechanism for the reaction and the binding mode are shown in Scheme 4.3.

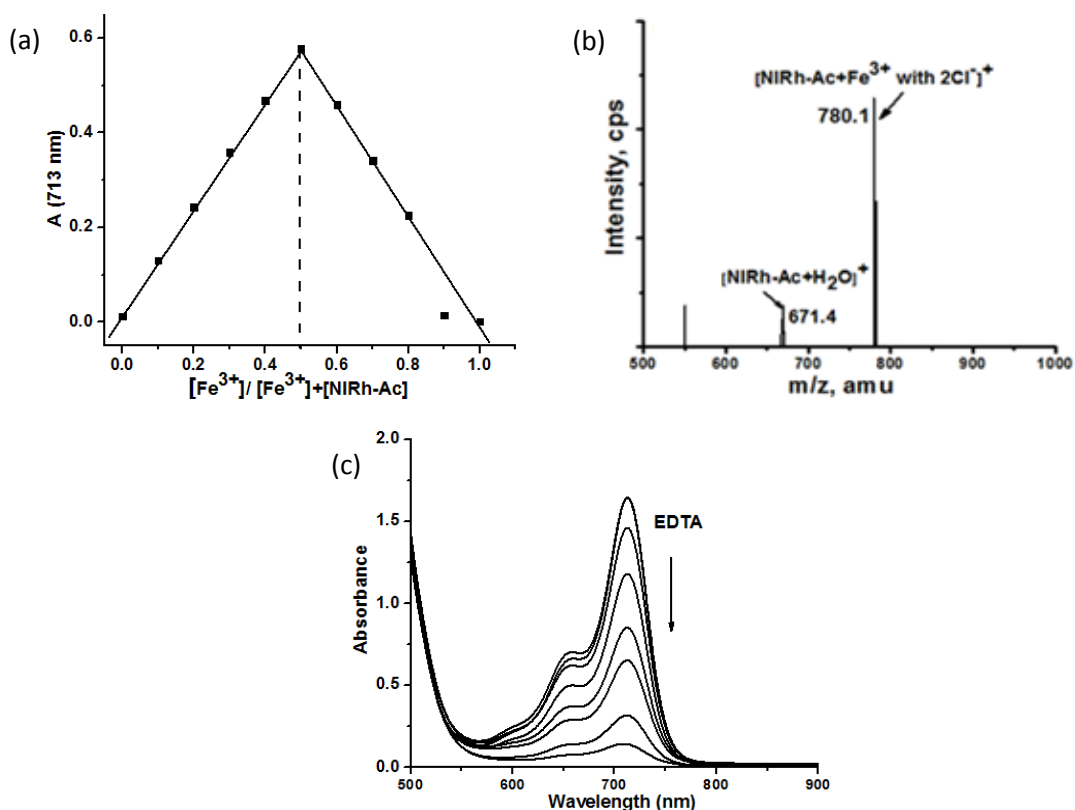
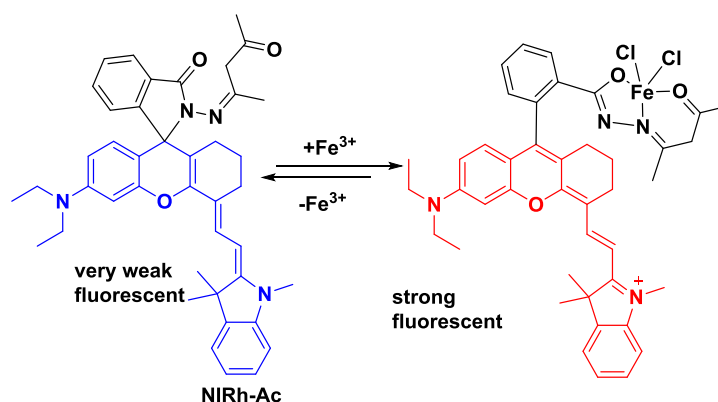


**Figure 4.7** (a) Job's plot: the total concentrations of NIRh-Ac and Fe<sup>3+</sup> were kept at constant 20  $\mu\text{M}$  and the absorption intensity was measured at 713 nm in the ACN/Tris buffer (10 mM, pH 7.3, v/v 1:1) (b) ESI-MS spectrum of the solution of NIRh-Ac with FeCl<sub>3</sub> (1  $\mu\text{M}$  sensor and 1  $\mu\text{M}$  Fe<sup>3+</sup> in ACN/H<sub>2</sub>O) (c) Treatment of 20  $\mu\text{M}$  NIRh-Ac-Fe<sup>3+</sup> complex with increasing concentration of EDTA (0 to 40  $\mu\text{M}$ , from top to bottom) in ACN/Tris-HCl buffer (10 mM, pH 7.3, v/v 1:1)





**Scheme 4.3** Proposed 1:1 binding mode of NIRh-Ac with  $\text{Fe}^{3+}$  in ACN/Tris-HCl buffer (10 mM, pH 7.3, v/v 1:1)

#### 4.3.4 Biological Imaging Studies

*In vitro* studies showed that the ability of NIRh-Ac to detect  $\text{Fe}^{3+}$  with excellent selectivity. To examine whether it can detect  $\text{Fe}^{3+}$  in living systems, human SH-SY5Y neuroblastoma cells and fibroblast cells (ws1) were used to detect exogenous  $\text{Fe}^{3+}$  ions in live cells. The cells treated with 20  $\mu\text{M}$  NIRh-Ac exhibited very weak fluorescence (Figure 4.8a and 4.8e). However, after the cells were preloaded with 20  $\mu\text{M}$   $\text{Fe}^{3+}$  for 8 h, the NIRh-Ac sensor was able to detect strong fluorescent signals in the cells (intensity increased by 14 folds for SH-SY5Y, Figure 4.8b; and 4.3 fold for ws1 cells, Figure 4.8f). These turn-on responses in fluorescence are likely being triggered by the increased cellular  $\text{Fe}^{3+}$  levels due to uptaking of the exogenous  $\text{Fe}^{3+}$ . When the cells were further treated with a cell permeable  $\text{Fe}^{3+}$ -chelator SIH (salicyl aldehydeisonicotinoyl hydrazone) that can decrease the intracellular level of  $\text{Fe}^{3+}$ , significantly decreased fluorescent signals were observed in both cell lines (Figure 4.8c & 4.8g). These experiments demonstrate that NIRh-Ac can detect  $\text{Fe}^{3+}$  in cells as well as the dynamic change of  $\text{Fe}^{3+}$  in both the cell lines.

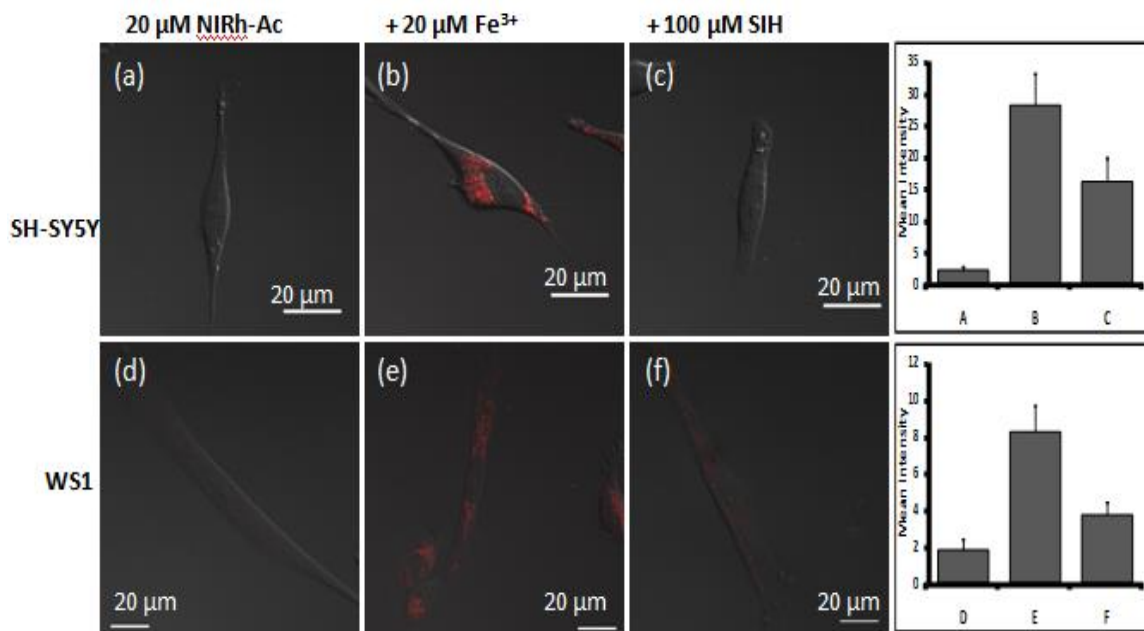


**Figure 4.8** Confocal microscopy images (with DIC) of live human SH-SY5Y neuroblastoma cells and Fibroblast cells (ws1) treated with (a) human SH-SY5Y neuroblastoma cells were incubated 20  $\mu\text{M}$  NIRh-Ac (30 min). (b) human SH-SY5Y neuroblastoma cells were pre-incubated with 20  $\mu\text{M}$   $\text{Fe}^{3+}$  for 8 h then 20  $\mu\text{M}$  NIRh-Ac sensor was added and image were taken after 30 min incubation. (c)  $\text{Fe}^{3+}$ -chelator SIH (100  $\mu\text{M}$ ) was then added and incubated for overnight. (d) Bar chart of fluorescent intensities of (a), (b) and (c). (e) Human fibroblast cells (ws1) were incubated with 20  $\mu\text{M}$  NIRh-Ac (30 min). (f) Fibroblast cells (ws1) were pre-incubated with 20  $\mu\text{M}$   $\text{Fe}^{3+}$  for 8 h then the sensor was added (g)  $\text{Fe}^{3+}$ -chelator SIH (100  $\mu\text{M}$ ) was then added and incubated for overnight (g) Bar chart of fluorescent intensity of (e), (f) and (g) (Fluorescence intensity was collected at 680-750 nm (for NIRh-Ac)).

The subcellular distribution of exchangeable  $\text{Fe}^{3+}$  pools in live cells after incubation with exogenous  $\text{Fe}^{3+}$  was then investigated using NIRh-Ac along with a few cellular trackers. Colocalization experiments were conducted by cell staining with the sensor NIRh-Ac, MitoTracker Green FM, and LysoTracker blue DND-22 concomitantly. MitoTracker Green FM (M-7514) stains mitochondria with a bright green fluorescence.<sup>[12]</sup> The LysoTracker probes are fluorescent acid tropic probes for labeling and tracking acidic organelles in live cells thus, it can be used to visualize the endosomes/lysosomes in cells.<sup>[13]</sup> Again SH-SY5Y neuroblastoma and

fibroblast cells (ws1) were used for the colocalization experiments. Figure 4.9 shows the colocalization experiments for SH-SY5Y neuroblastoma cells after staining with NIRh-Ac, MitoTracker Green FM, and LysoTracker blue DND-22. The NIRh-Ac-Fe(III) complex gives red fluorescent images (Fig. 4.9b); the MitoTracker channel is shown in green color (Fig. 4.9c); and the image given by LysoTracker blue DND 22 is shown in Fig. 4.9d as blue-colored. As shown in Figure 4.9 e&f, there are partial colocalization between NIRh-Ac-Fe(III) and MitoTracker (red + green = yellow) (Fig. 4.9e) as well as between NIRh-Ac-Fe(III) and LysoTracker (red + blue = purple) (Fig. 4.9f); however, a complete colocalization was observed among NIRh-Ac-Fe(III), MitoTracker and LysoTracker (Fig. 4.9g). It is notable that all the MitoTracker signals overlap with the NIRh-Ac-Fe(III) signals (giving rise to yellow signals) but only part of the LysoTracker signals overlap with the NIRh-Fe(III) signals (giving rise to purple signals). Part of the LysoTracker signals do not overlap with the NIRh-Ac-Fe(III) signals and kept blue (Fig. 4.9g). These findings suggest that the locations of exchangeable  $Fe^{3+}$  pools detectable via sensor NIRh-Ac separately exist in all mitochondria and part of the endosomes/lysosomes in human SH-SY5Y neuroblastoma cells, not in the cytosol. The partial lysosomal colocalization is a bit surprising to us and will be investigated further.

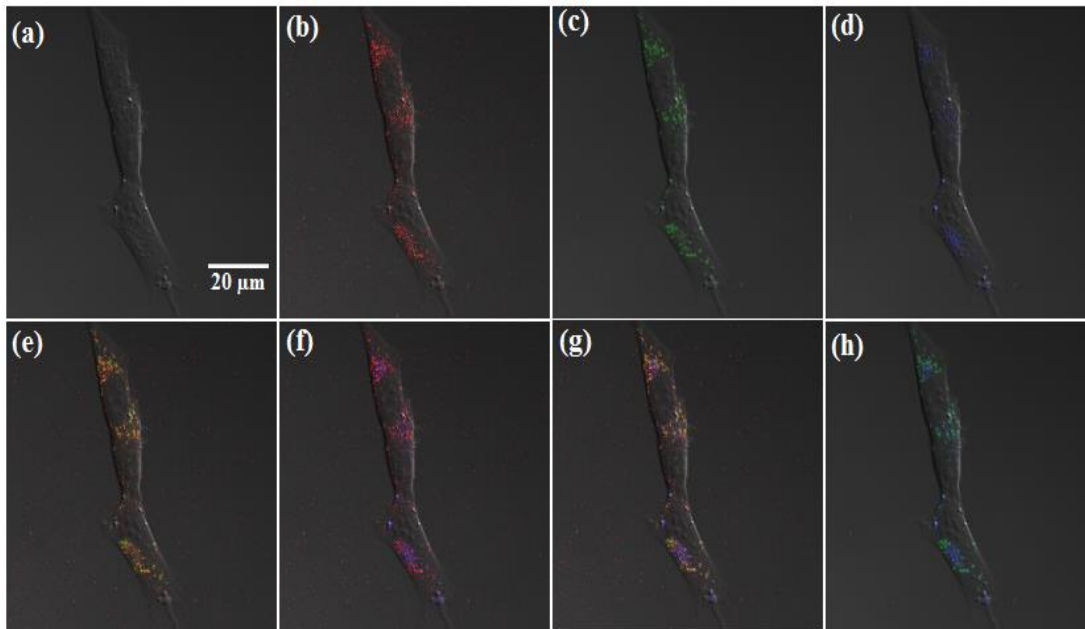


**Figure 4.9** Representative confocal microscopy images of intracellular colocalization studies of 10  $\mu\text{M}$  NIRh-Ac incubated with  $\text{Fe}^{3+}$ -loaded human SH-SY5Y cells (pre-incubated with 10  $\mu\text{M}$   $\text{Fe}^{3+}$ ) co-labeled with MitoTracker Green FM (100 nM, incubated for 30 min) and LysoTracker Blue DND-22 (50 nM, incubated for 120 min) (a) DIC image of cells with 20  $\mu\text{m}$  scale bar (b) NIRh-Ac- $\text{Fe}^{3+}$  fluorescence collected at 680-750 nm (red) (c) MitoTracker fluorescence collected at 492-548 nm (green) (d) LysoTracker fluorescence collected at 409-484 nm (blue) (e) DIC image of (a) and fluorescence images of (b) and (c) were merged together. Colocalization regions are in yellow and non-overlapping regions remain in red. (f) DIC image of (a) and fluorescence images of (b) and (d) were merged together. Overlapping regions are in purple and non-overlapping regions remain in red; (g) Images of (a), (b), (c) and (d) were merged together, revealing that the NIRh-Ac- $\text{Fe}^{3+}$  images are 100% colocalized with the sum of those of MitoTracker and LysoTracker (h) Images of (a), (c) and (d) were merged together, showing no overlapping region between lysosomes and mitochondria.

Figures 4.10 shows the subcellular distribution of exchangeable  $\text{Fe}^{3+}$  pools in live fibroblast cells (ws1) after incubation with exogenous  $\text{Fe}^{3+}$ . Again, the NIRh-Ac- $\text{Fe}(\text{III})$  complex gives red fluorescent images (Fig. 4.10a), the MitoTracker dyed mitochondria give green images (Fig. 4.10b), and LysoTracker dyed lysosomes give blue signals (Figure 4.10c) in live fibroblast cells (ws1). As shown in Figure 4.10 (e and g) there is a complete colocalization between NIRh-

Fe(III) and MitoTracker (red + green = yellowish-green). However, there is no co-localization observed between NIRh-Fe(III) complex (red) and the lysosomes (blue) (Figure 4.10 f&g). These data indicate that Fe<sup>3+</sup> detectable by NIRh-Ac in human fibroblast ws1 cells is localized in mitochondria but not in lysosomes. The mitochondria distribution is the same as that in SH-SY5Y neuroblastoma cells; however, the lysosomes distribution is different in the two cell types, which is a surprise to us.

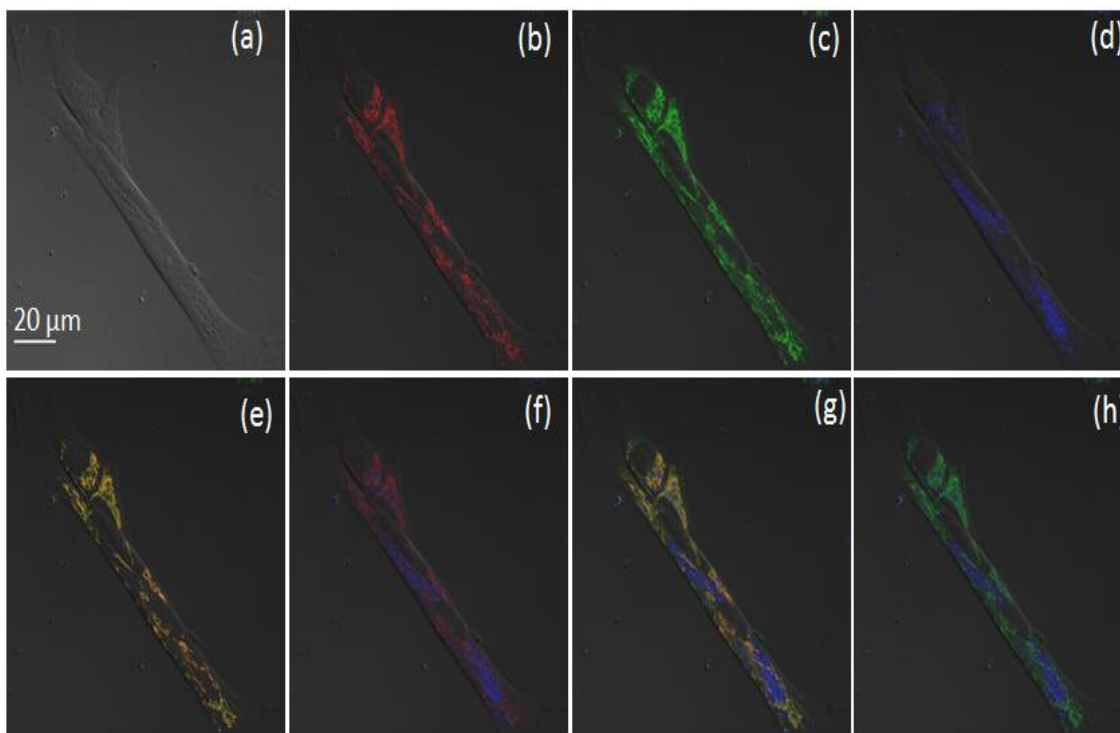


**Figure 4.10** Representative confocal microscopy images of intracellular colocalization studies of 20 μM NIRh-Ac incubated with Fe<sup>3+</sup>-loaded fibroblast cells (ws1) (pre-incubated with 20 μM Fe<sup>3+</sup> (FeCl<sub>3</sub> incubated for overnight) co-labeled with MitoTracker Green FM (100 nM, incubated for 30 min) and LysoTracker Blue DND-22 (50 nM, incubated for 120 min) DIC image of cells with 20 μm scale bar (b) NIRh-Ac-Fe<sup>3+</sup> fluorescence collected at 680-750 nm (red) (c) MitoTracker fluorescence collected at 492-548 nm (green). (d) LysoTracker fluorescence collected at 409-484 nm (blue) (e) DIC image of (a)(b) and fluorescence images of (c) were merged together. Overlapping regions are in yellowish-green and non-overlapping regions remain in red. (f) DIC image of (a), (b) and fluorescence images of (d) were merged together (g) DIC image of (a), (b) (c) and fluorescence images of (d) were merged together. NIRh-Ac-Fe<sup>3+</sup> images are 100% colocalized with MitoTracker and no overlapping of the signals were found for LysoTracker (h) Images of (a), (c) and (d) were merged together, showing no overlapping region between lysosomes and mitochondria.

Results from the cell imaging studies (Fig. 4.8 (d and h), Figs.4.9-10) show that the  $\text{Fe}^{3+}$  uptake is different in the two cell lines studied as well as the subcellular distributions. After incubation exogenous  $\text{Fe}^{3+}$ , SH-SY5Y neuroblastoma cells appeared to have higher  $\text{Fe}^{3+}$  levels and  $\text{Fe}^{3+}$  detected in both mitochondria and lysosomes while fibroblast cells (ws1) showed lower  $\text{Fe}^{3+}$  levels and  $\text{Fe}^{3+}$  detected only in mitochondria. SH-SY5Y neuroblastoma cells are cancerous neuronal cells while the fibroblast ws1 cells are primary healthy cells. It is known that neuronal cells need more iron for their unique metabolic activities and cancer cells need more iron than normal cells to keep their abnormal rapid growth<sup>[14-15]</sup>, so it is reasonable that SH-SY5Y cells uptake more iron and keep it in two organelles. However it is still surprise that only partial of the lysosomes in SH-SY5Y cells contains detectable  $\text{Fe}^{3+}$  by the NIR-Ac sensor while lysosomes in ws1 cells contains no detectable  $\text{Fe}^{3+}$  in lysosomes. One explanation is that the exogenous  $\text{Fe}^{3+}$  was uptaken into the cells into endosomes first by endocytosis, and then the endosomes fused with lysosomes. Only these lysosomes will contain elevated levels of  $\text{Fe}^{3+}$  that can be detected by the NIR-Ac sensor (purple color in Fig 4.9 f&g). The other cellular lysosomes that were not fused with the  $\text{Fe}^{3+}$ -containing endosomes will not contain extra  $\text{Fe}^{3+}$  thus is not detectable by the NIR-Ac sensor (blue color in Fig 4.9 f&g). If this explanation is correct, the NIR-Ac sensor should be able to trace the  $\text{Fe}^{3+}$  transport process in real time in cells.

To explore this possibility, the iron transport process in ws1 cells was further investigated by doing some kinetic experiments.  $\text{FeCl}_3$  was used as the iron source for these experiments. Ws1 cells were incubated with  $\text{FeCl}_3$  (20  $\mu\text{M}$ ) at different incubation time (2 h, 4 h, 6 h and 8 h) and NIRh-Ac (10  $\mu\text{M}$ ), MitoTracker Green FM (100 nM) and LysoTracker Blue DND-22 (50 nM,) were used to detect the subcellular locations of  $\text{Fe}^{3+}$ . Briefly, in a typical experiment (for example, for 2 h); ws1 cells were incubated with 20  $\mu\text{M}$   $\text{FeCl}_3$  for 1.5 h and then  $\text{FeCl}_3$  was removed by changing to fresh cell medium containing no  $\text{FeCl}_3$ , and cells were further incubated

with NIRh-Ac, MitoTracker, and LysoTracker for another 30 min. After that, extracellular dyes were removed by changing cell medium to fresh ones. Cell images were collected by a confocal microscopy immediately.

Figure 4.11 shows the results from these imaging experiments. The multichannel confocal capability allowed us to monitor several colors simultaneously in cells and the color changing at different time was shown in Figure 4.12. Red colored dots are the regions where free  $\text{Fe}^{3+}$  ions are located. Green colors belong to MitoTracker and yellow (red+green) indicates that free  $\text{Fe}^{3+}$  ions are in mitochondria. Images given by LysoTracker are shown in blue and purple indicates that free  $\text{Fe}^{3+}$  ions are in lysosomes. There are 5 columns in Figure 4.11: signals from the  $\text{Fe}^{3+}$  sensor (1st), sensor and LysoTracker (2nd), sensor and MitoTracker (3rd), sensor and both trackers (4th), Mito- and Lyso-trackers (5th). At 2 hours incubation with  $\text{Fe}^{3+}$ , when images from all channels were merged (the 4th column), it can be seen that the majority but not all  $\text{Fe}^{3+}$  were in lysosomes (purple) or mitochondria (yellow) because there are still isolated red-colored dots observed. These red-colored dots are likely being  $\text{Fe}^{3+}$ -containing early endosomes that have not yet been merged with lysosomes or their pH has not reached low enough to be dyed by the LysoTracker. Furthermore, at 2 h,  $\text{Fe}^{3+}$  did not reach all the mitochondria in cells, as significant amount of green colored mitochondria were still observable. In addition, both  $\text{Fe}^{3+}$ -loaded lysosomes (purple) and the non- $\text{Fe}^{3+}$ -loaded ones (blue) were observed. Iron is taken into cells by the transferrin-mediated endocytosis process.<sup>[16-18]</sup> The red colored dots in Figure 4.11 are likely to be the freshly formed early endosomes after the internalization of  $\text{Fe}^{3+}$  in the fibroblast cells. With the ATP-dependent proton pumps on endosomes membrane lowering the lumen pH of the endosomes,<sup>[19-22]</sup> endosomes gradually, maturation into lysosomes and the LysoTracker dye stains them blue. If free iron(III) ions are in lysosomes, purple color should be observed.

At 4 h, the number of red-colored dots ( $\text{Fe}^{3+}$ -containing early endosomes) decreased (4<sup>th</sup> column in Fig 4.11 and the red line in Fig 4.12), and purple-colored regions significantly increased (2<sup>nd</sup> column in Fig 4.11 and the purple line in Fig 4.12) as well as yellow-colored regions (3<sup>rd</sup> column in Fig 4.11 and the yellow line in Fig 4.12), indicating  $\text{Fe}^{3+}$  transfer into lysosomes and mitochondria. However, there were still green mitochondria and blue lysosomes observed. But, at 6 h, there were very little red-colored dots ( $\text{Fe}^{3+}$ -containing early endosomes, the red line in Fig 4.12) and green colored mitochondria observed (3<sup>rd</sup> and 4<sup>th</sup> columns in Fig 4.11 and the green line in Fig 4.12); purple-colored lysosomes ( $\text{Fe}^{3+}$ -loaded) (2<sup>nd</sup> column in Fig 4.11 and the purple line in Fig 4.12), also decreased in intensity while yellow colored mitochondria dominate the images (3<sup>rd</sup> and 4<sup>th</sup> columns in Fig 4.11 and the yellow line in Fig 4.12), indicating  $\text{Fe}^{3+}$  transfer into mitochondria. At 8 h post  $\text{FeCl}_3$  incubation, purple-colored lysosomes ( $\text{Fe}^{3+}$ -loaded) (2<sup>nd</sup> column) had disappeared and yellow mitochondria and blue lysosomes dominate the images (4<sup>th</sup> column), indicating that all the uptaken free iron(III) ions reached mitochondria of fibroblast cells (ws1) in 8 h. This experiment explains why the prior colocalization experiments observed free iron(III) ions only in mitochondria in ws1 cells (Fig. 4.10). The kinetics data suggest a  $\text{Fe}^{3+}$  transport pathway in human fibroblast cells, i.e., from endosomes to lysosomes and finally to mitochondria, as shown in a cartoon in Figure 4.13.



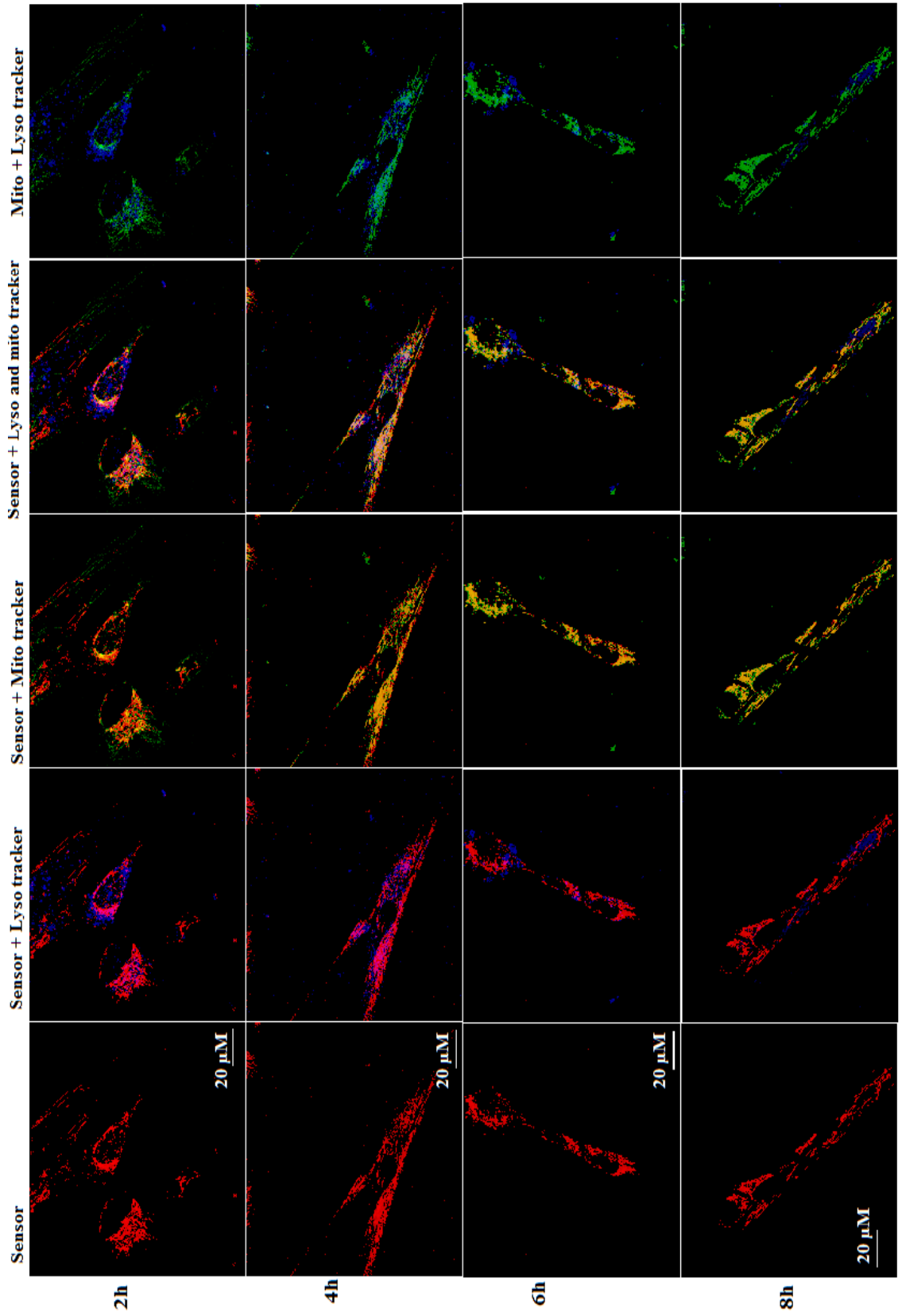


**Figure 4.11** Subcellular kinetic experiments for NIRh-Ac-Fe<sup>3+</sup> in live fibroblast cells (ws1)

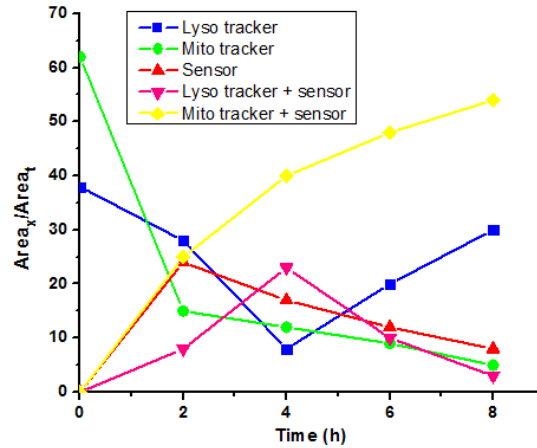


**Figure 4.12** Colored areas changing at different time in Figure 4.11. (Area of the all color dots were measured and assumed that the total area is 100%, then each color area was calculated as a percentage ( $A_x/A_t$ ))

It was believed that in the acidic media in lysosomes of cells,  $Fe^{3+}$  is released from the carriers and get into the cytoplasm of cells as a loosely bound “labile iron pool”.<sup>[23-24]</sup> However, the above kinetic and colocalization experiments did not detect such a “labile iron pool” in cytosol, instead, showing that  $Fe^{3+}$  in lysosomes appears to pass through mitochondria directly, bypassing the cytosol. It is interesting to note at the 5th column in Figure 4.11 that during the active  $Fe^{3+}$  transfer process, turquoise colored (green+blue) regions were observed at 4 h and at a less extent, at 6 h, and these regions colocalize with  $Fe^{3+}$  sensor signals (4th column), suggesting that the  $Fe^{3+}$ -loaded lysosomes are in close contact with mitochondria during the active  $Fe^{3+}$  transfer process. When the  $Fe^{3+}$  transfer, process is complete at 8 h; lysosomes (blue) are well separated from the  $Fe^{3+}$ -loaded mitochondria (4th & 5th columns at 8 h). Unfortunately, the images in Fig 4.11 cannot distinguish precisely the relative locations of the lysosomes and mitochondria during the active  $Fe^{3+}$  transfer process, giving a mixed turquoise color in the regions. This could be interpreted as fusion of the two organelles or a docking between the two.<sup>[24]</sup>

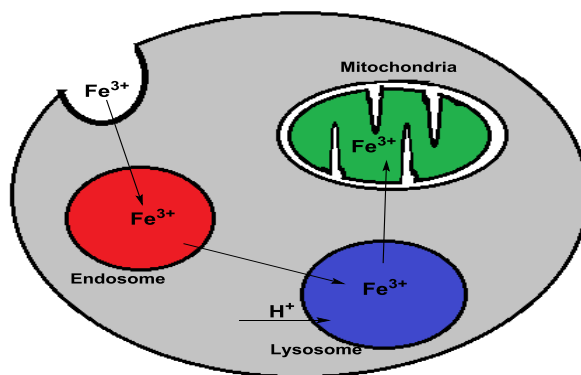


**Figure 4.13** Hypothetical schematic of one possible cellular distribution process free iron(III) ions in live fibroblast cells

To look into this issue more precisely, a more precise kinetics was followed by confocal in fibroblast cells (ws1) and with iron(III) citrate as the exogenous  $\text{Fe}^{3+}$  source as it denotes  $\text{Fe}^{3+}$  to transferrin much faster and more efficiently than that ferric chloride does. Briefly, human fibroblast cells (ws1) were pre-incubated with NIRh-Ac (10  $\mu\text{M}$ ), MitoTracker green (100 nM), and LysoTracker blue (50 nM) for 30 min. The dyes were removed by changing to fresh media without the dyes.  $\text{Fe}^{3+}$  ions (40  $\mu\text{M}$ , iron(III) citrate) were then added to the media and confocal images were collected for every 1 minute. As shown Figure 4.14, before  $\text{Fe}^{3+}$  ions were added (0 min.), green mitochondria, and blue lysosomes were observed but no red color was observed. After  $\text{Fe}^{3+}$  ions were added, red, purple, and yellow colors were observed in addition to the green and blue colors, suggesting  $\text{Fe}^{3+}$  are getting into endosomes, lysosomes, and mitochondria. At one of the particular regions shown with an arrow, in 1 min, an elongated purple dot was observed in direct contact with a green branch-shaped green mitochondrion, with their contact region in turquoise color. At this moment,  $\text{Fe}^{3+}$  ions were located in the lysosomes as seen from the purple color. At 2 min, this green mitochondrion had changed to orangish-yellow color while the lysosomes had left the region, suggesting iron(III) ions had been transferred from the lysosomes in the

mitochondrion. At 3 min, the orangish-yellow color stayed in the mitochondrion. Similar processes can also be seen in other regions. These results confirm that  $\text{Fe}^{3+}$  ions directly pass to mitochondria from lysosomes via a direct docking mechanism. This finding is consistent with recent observations that cellular  $\text{Fe}^{3+}$  is directly transported from endosomes/lysosomes to mitochondria by a 'kiss and run' pathway, bypassing the cytosol.<sup>[25]</sup>

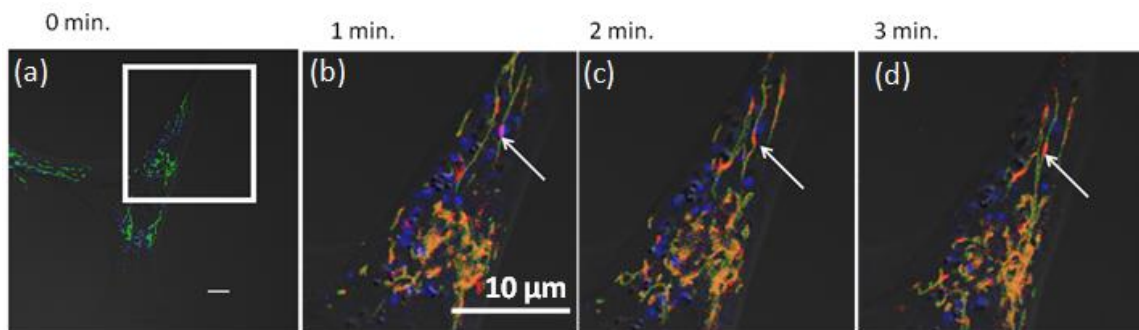


**Figure 4.14** Confocal microscopy images (with DIC) Fibroblast cells (ws1) treated with (a) NIRh-Ac (10 $\mu\text{M}$ ), MitoTracker green (100 nM), and LysoTracker blue (50 nM) for 30 min (b) 1 min (c) 2 min (d) 3 min after  $\text{Fe}^{3+}$  ions added (b, c) and (d) are the zoomed images of the area shown in (a)

#### 4.3.5 Imaging $\text{Fe}^{3+}$ in Zebrafish

As NIRh-Ac is a near IR sensor, it is interesting to test its ability in detection of  $\text{Fe}^{3+}$  in live organisms like animal models. Zebrafish are a good vertebrate model for monitoring metal ions by fluorescence microscopy owing to the permeability of ions and sensors in fish. Recently, zebrafish have been used to detect various ions and biomolecules.<sup>[26-29]</sup> So zebrafish were used to test whether NIRh-Ac can detect  $\text{Fe}^{3+}$  *in vivo*. Initial *in vivo*  $\text{Fe}^{3+}$  imaging experiments were performed with intact 3-day old zebrafish larva (without iron supplement) with NIRh-Ac staining and monitored using a confocal microscopy. However, the zebrafish larva did not show any evidence of fluorescence (Figure 4.15a). Then zebrafish larva were pre-incubated with  $\text{FeCl}_3$  (5,

10, 50  $\mu\text{M}$ ) for 3 days, and then stained with NIRh-Ac for 30 min. Red-colored spots in zebrafish were immediately seen under a confocal microscope (Figure 4.15). Only one red spot located in the liver region of zebrafish<sup>[30]</sup> was observed (Figure 4.15b) when iron concentrations were at 5 and 10  $\mu\text{M}$ . In the presence of high iron concentration (50  $\mu\text{M}$ ) of  $\text{Fe}^{3+}$ , two red spots were exhibited (Figure 4.15c), one located in the liver region, and the other in the head, likely to be located in preopticneuromast of zebrafish.<sup>[31-32]</sup> Detailed investigations of the locations of  $\text{Fe}^{3+}$  in zebrafish is beyond the scope of this work but the zebrafish clearly demonstrated the capability of the NIR-Ac sensor in imaging  $\text{Fe}^{3+}$  in live animals.

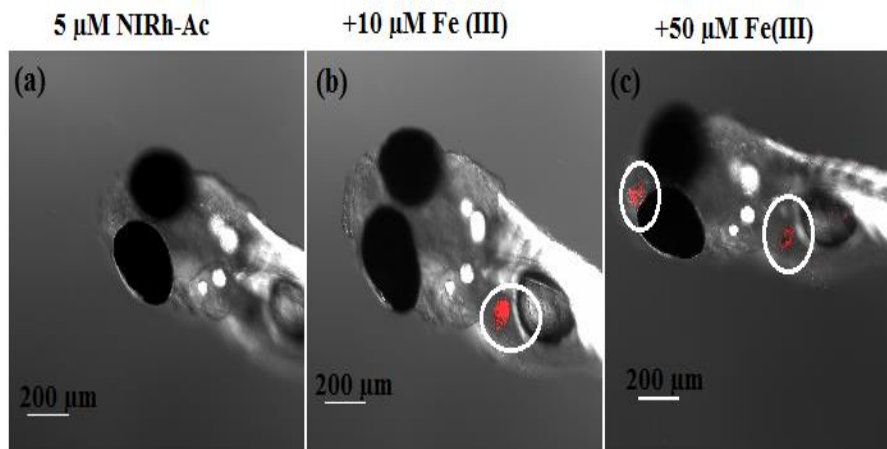


**Figure 4.15** Confocal microscopy images of 6 day old zebrafish larvae (a) Zebrafish larva was incubated with 5  $\mu\text{M}$  NIRh-Ac for 30 min (b) Zebrafish larva incubated with 10  $\mu\text{M}$  (c) 50  $\mu\text{M}$   $\text{FeCl}_3$  then 5  $\mu\text{M}$  NIRh-Ac was added and incubated for 30 min.

#### 4.4 Conclusion

In summary, I have developed a highly sensitive, highly selective, and reversible turn-on near infrared fluorescent  $\text{Fe}^{3+}$ -sensor, NIRh-Ac. The sensor gives a distinct rapid and reversible fluorescence response upon the alteration of intracellular  $\text{Fe}^{3+}$  levels with little interference from other biologically relevant metal ions. Confocal experiments show that NIRh-Ac can readily

detect exogenous chelatable  $\text{Fe}^{3+}$  in live human SH-SY5Y cells and live fibroblast cell (ws1) at subcellular resolution, with the chelatable  $\text{Fe}^{3+}$  pools located in mitochondria and endosomes/lysosomes for SH-SY5Y cells and in mitochondria for ws1 cells. The kinetic experiments provided a visual imaging of  $\text{Fe}^{3+}$  transport pathway in human fibroblast cells in real time, i.e., from endosomes to lysosomes and finally to mitochondria via a direct “Lyso-mito docking” mechanism, bypassing the cytosol. Zebrafish studies clearly demonstrated the capability of the NIR-Ac sensor in imaging  $\text{Fe}^{3+}$  in live animals.

#### 4.5 References

1. Zhang L., Wang J., Fan J., Guo K., Peng X., *Bioorg. Med. Chem. Lett.*, **2011**, 21, 5413-5416
2. Wei Y., Aydin Z., Zhang Y., Liu Z., Guo M., *ChemBioChem*, **2012**, 13, 1569-1573
3. Zhang M., Gao Y., Li M., Yu M., Li F., Li L., Zhu M., Zhang J., Yi T., Huang C., *Tetrahedron Lett.*, **2007**, 48, 3709-3712
4. Dujols V., Ford F., Czarnik A. W., *J. Am. Chem. Soc.*, **1997**, 119, 7386-87
5. Yang H., Zhou Z., Huang K., Yu M., Li F., Yi T., Huang C., *Org. Lett.*, **2007**, 9, 4729-4732
6. Zhang X., Shiraishi Y., Hirai T., *Tetrahedron Lett.*, **2008**, 49, 4178-4181
7. Koide Y., Urano Y., Hanaoka K., Terai T., Nagano T., *J. Am. Chem. Soc.*, **2011**, 133, 5680-5682
8. Wang T., Zhao Q. J., Hu H. G., Yu S. C., Liu X., Liu L., Wu Q. Y., *Chem. Commun.*, **2012**, 48, 8781-8783
9. Yuan L., Lin W., Yang Y., Chen H., *J. Am. Chem. Soc.*, **2012**, 134, 1200-1211
10. Perez C. A., Guo M., Wei Y., *J. Inorg. Biochem.*, **2009**, 103, 326-332
11. Bryson-Richardson R. J., Currie P. D., *Nat. Rev. Genet.*, **2008**, 9, 632-646
12. Chen L. B., *Methods Cell Biol.*, **1988**, 29, 103-123
13. Zhang Y. Z., Olwu Z., Mao F., Haugland W. L., *Mol. Biol. Cell*, **1994**, 5, 113a (abstract 653)
14. Kiessling M. K., Klemke C. D., Kaminski M. M., Galani I. E., Krammer P. H., Gulow K., *Cancer Res.*, **2009**, 69, 2365-2374
15. Whitnall M., Rahmanto Y. S., Sutak R., Xu X., Becker E. M., Michael M. R., Ponka P., Richardson D. R., *Proc. Nat. Acad. Sci.*, **2008**, 105, 9757-9762
16. Karin M. Mintz B., *J. Biol. Chem.*, **1981**, 256, 3245-3252

17. Klausner R. D., van Renswoude J., Ashwell G., Kempf C., Schechter A. M., Dean A., Bridges K. R., J. Biol. Chem., **1983**, 258, 4715-4724
18. Iacopetta B. J., Morgan E. H., J. Biol. Chem., **1983**, 258, 9108-9115
19. Van Renswoude J., Bridges K. R., Harford J. B., Klausner R. D., Proc. Natl. Acad. Sci. (USA), **1982**, 79, 6186-6190
20. Dautry-Varsat A., Ciechanover A., Lodish H. F., Proc. Natl. Acad. Sci. (USA), **1983**, 80, 2258-2262
21. Paterson S., Armstrong N. J., Iacopetta B. J., McArdle H. J., Morgan E. H., J. Cell. Physiol., **1984**, 120, 225-232
22. Yamashiro D. J., Tycko B., Fluss S. R., Maxfield F. R., Cell, **1984**, 37, 789-800
23. Richard D.R., Lane D. J. R., Becker E. M., Huang M. L. H., Whitnall M., Rahmanto Y. S., Sheftel A.D., Ponka P., Proc. Natl. Acad. Sci. (USA), **2010**, 107, 10775-10782
24. Andrews N. C., Nat. Rev. Genet., **2000**, 1, 208-217
25. Sheftel A. D., Zhang A. S., Brown C., Shirihai O. S., Ponka P., Blood, **2007**, 110, 125 - 132
26. Qian F., Zhang C. Zang Y., He W., Gao X., Hu P., Guo Z., J. Am. Chem. Soc., **2009**, 131, 1460-1468
27. Basu S., Sachidanandan C., Chem. Rev., **2013**, 113, 7952-7980
28. Ko S.K., Yang Y.K., Tae J., Shin I., J. Am. Chem. Soc., **2006**, 128, 14150-14155
29. Yang Y.K., Ko S.K, Shin I., Tae J., Nat. Protoc., **2007**, 2, 1740-1745
30. Ko S.K., Chen X., Yoon J., Shin I., Chem. Soc. Rev., **2011**, 40, 2120-2130
31. Trump W. J. V., McHenry M.J., J. Exp. Biol., **2011**, 2105-2115
32. Guo Z., Kim G. H. Shin., Yoon. I J., Biomaterials, **2012**, 33, 7818-7827

## Chapter 5

### TURN-ON NEAR-INFRARED FLUORESCENT SENSOR NRPA FOR IMAGING ENDOGENOUS $\text{Fe}^{3+}$ IN LIVE ORGANISMS

#### 5.1 Introduction

The *in vitro* and *in vivo* studies of the modified rhodamine based sensor, NIRh-Ac in chapter 4, have provided detailed information about the subcellular location of exogenous iron(III) pools and the iron(III) transport pathway in cells. Moreover, the sensor was able to locate the iron(III) ions in zebrafish after incubation with exogenous iron(III). However, in cells, iron enters labile iron pools not only from outside the cells, but also as a result of endogenous heme breakdown and the mobilization of ferritin iron ions.<sup>[1-4]</sup> These cellular free iron pools represent only (< 5%) of the total cell iron (50-100  $\mu\text{M}$ ).<sup>[5]</sup> In this chapter, a sensor was developed to detect the endogenous intracellular labile iron(III) pools. The properties of highly selective and highly sensitive reversible off-on near infrared fluorescent  $\text{Fe}^{3+}$  sensor NRPA (Scheme 5.1) were described. This sensor can selectively detect endogenous  $\text{Fe}^{3+}$  in live cells and organisms. The unique reversible “turn-on” property and high sensitivity of NRPA allow it to locate the endogenous exchangeable  $\text{Fe}^{3+}$  pools at subcellular resolution in live human neuroblastoma SH-SY5Y cell and human skin fibroblast (ws1). It has been also demonstrated that NRPA can be used to visualize endogenous free  $\text{Fe}^{3+}$  ions in zebrafish.



## 5.2 Experimental Section

Most of the procedures are similar as those explained in Chapter 4. In this section, only the procedures that were not provided in Chapter 4 are given.

### 5.2.1 Materials and Reagents

2,6-bis(hydroxymethyl)pyridine was purchased from Aldrich. 2-(1,3,3-Trimethylindolin-2-ylidene) acetaldehyde was purchased from OChem Incorporation. 2-(4-Diethylamino-2-hydroxybenzoyl) benzoic acid and benzotriazol-1-yloxytris (dimethylamino)-phosphonium hexafluorophosphate (BOP) were purchased from TCI America. 2,6-dihydroxypyridine was purchased from Aldrich. The other chemicals and the solvents used in the experiments were purchased commercially. The solution of metal ions were prepared from chloride salts of  $\text{Ni}^{2+}$ ,  $\text{Fe}^{3+}$ ,  $\text{Cu}^{2+}$ ,  $\text{Mn}^{2+}$ ,  $\text{Hg}^{2+}$ ,  $\text{Na}^+$ ,  $\text{Ca}^{2+}$ ,  $\text{Zn}^{2+}$ ,  $\text{Ag}^+$ , and nitrate salts of  $\text{Mg}^{2+}$ ,  $\text{Pb}^{2+}$ ,  $\text{K}^+$ ,  $\text{Co}^{2+}$ . Stock solutions of metal ions (10 mM) were prepared in deionized water, except for  $\text{Fe}^{3+}$  and  $\text{Fe}^{2+}$  that were dissolved in 0.1 M HCl solution. Solution of  $\text{Cu}^+$  was freshly prepared by dissolving tetrakis (acetonitrile) copper(I) (Sigma-Aldrich) into double-distilled water.

### 5.2.2 Synthesis

NIRh was synthesized as described in Chapter 4.

**Synthesis of 6-(hydroxymethyl) pyridine-2-carbaldehyde:**  $\text{MnO}_2$  (1.594 g, 18.3 mmol) was added slowly to a stirring solution of 2,6-bis(hydroxymethyl)pyridine (1.12 g, 7.27 mmol) in  $\text{CHCl}_3$  (20 mL). The mixture was stirred and refluxed for 3 h, at which point more  $\text{MnO}_2$  (1.71 g, 14.6 mmol) was added, and the reflux resumed for a further 3 h. After cooling, the mixture was filtered through Celite, and the black inorganic salts were washed with  $\text{CH}_3\text{OH}$ . The combined filtrate and washings were concentrated by rotary evaporation and the resulting oily residue

subjected to column chromatography with an ethyl acetate/petroleum ether gradient (30 to 70%), giving the product as a white solid (0.5 g, 50%) (Second fraction from the column). <sup>1</sup>H NMR (CDCl<sub>3</sub>, 300 MHz δ(ppm)): 9.58 (s, 1H), 8.31 (t, 1H), 8.16 (m, 1H), 8.01 (t, 1H), 4.98 (s, 2H).

**Synthesis of NRPA:** NIRh (0.150 g, 0.26 mmol) and 6-hydroxymethylpyridine-2-carbaldehyde (0.05 g, 0.36mmol) were dissolved in Ethanol (20 mL). The reaction mixture was then stirred and refluxed for overnight to obtain a pale green precipitate. The precipitate was collected by filtration, washed with cold ethanol, and dried in vacuum to give the 30 mg of NRPA (yield; 17 %). <sup>1</sup>H NMR (CDCl<sub>3</sub>, 300 MHz δ(ppm)): δ 8.93 (s, 1H), 7.96 (s, 1H), 7.56(t, , 3H), 7.26 - 7.11 (m, 3H), 7.24 (d, 2H), 6.96 (s, 1H), 6.77 (s, 1H), 6.64 (s, 1H), 6.34 (d, , 2H), 6.13 (s, 1H), 5.11 (s, 1H), 5.02 - 4.97 (m, 2H), 3.56 - 3.44 (m, 3H), 3.44 - 3.34 (m, 2H), 3.21 - 3.16 (m, 3H), 2.29 - 2.24 (m, 2H), 2.08 - 2.03 (m, 2H), 1.60 - 1.53 (m, 8H), 1.13 - 0.96 (m, 6H). <sup>13</sup>C NMR (CDCl<sub>3</sub>, 75 MHz δ(ppm)): 165.4, 157.8, 154.2, 150.4, 148.4, 147.68, 145.5, 130.6, 133.4, 129.6, 128.4, 127.7, 127.6, 123.5, 121.6, 120.7, 119.4, 119.2, 106.2, 105.9, 104.4, 98.1, 66.2, 58.9, 45.5, 44.3, 29.2, 28.4, 25.3, 22.9, 22.3, 16.5, 12.7, 12.5; ESI-MS: found: *m/z* = 692.2 [M+H]<sup>+</sup> and *m/z* = 714.5 [M+Na]<sup>+</sup>, calcd for C<sub>44</sub>H<sub>45</sub>N<sub>5</sub>O<sub>3</sub> = 691.1.

### 5.2.3 Zebrafish Experiments

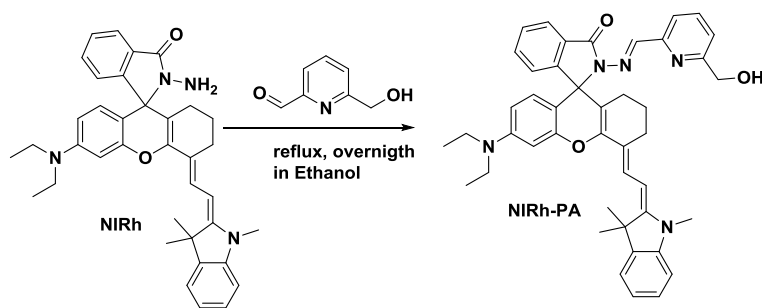
Zebrafish was maintained under standard conditions in collaborator Prof. T. Ferreira's lab (UMD, Biology). Embryos were collected from natural spawning and raised up in embryo medium.<sup>[6]</sup> Zebrafish strain nacre was utilized because it lacks pigment, allowing better visualization.<sup>[7]</sup> Zebrafish embryos at 2, 3, and 6 dpf were incubated with 10 μM NRPA in E3 media containing 0.1 vol % DMSO for 1 h at 28 °C. In addition, iron-loaded zebrafish (10 μM and 40 μM FeCl<sub>3</sub> for 1-day incubation) were incubated with 10 μM NRPA in E3 media for 1 h at 28 °C. Alternatively, zebrafish were exposed to 100 μM SIH in E3 media containing 0.1 vol % DMSO for

1 h at 28°C. After washing with E3 media to remove the remaining SIH, the zebrafish were further incubated with 10  $\mu$ M NRPA in E3 media for 1 h at 28 °C. The treated zebrafish were imaged by a confocal microscope.

### 5.3 Results and discussion

#### 5.3.1 Design and synthesis

The initial goal of the synthesis of NRPA was to coordinate to  $\text{Fe}^{3+}$  ions with high binding constant and was designed based on the principles of coordination chemistry. The design of NRPA sensor was carefully developed with a coordination site of two nitrogen and two oxygen atoms to afford three five-membered rings. The sensor, NRPA, was synthesized in a four step procedure (synthesis of NIRh was explained in chapter 4) with overall yield of 17% (Scheme 5.1). The structure of NRPA was confirmed by  $^1\text{H}$  NMR and  $^{13}\text{C}$  NMR and mass spectrometry.



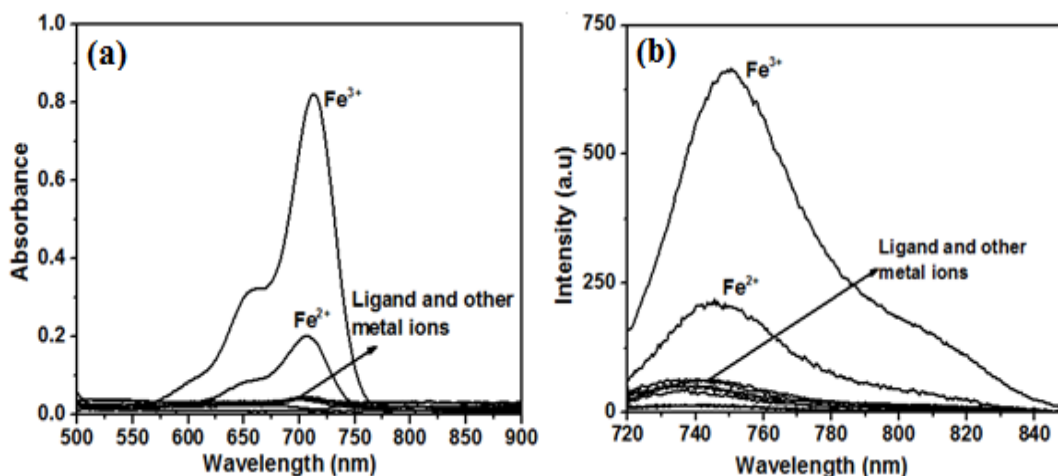
**Scheme 5.1** Synthesis route for NRPA

#### 5.3.2 Spectroscopic and Selectivity Studies

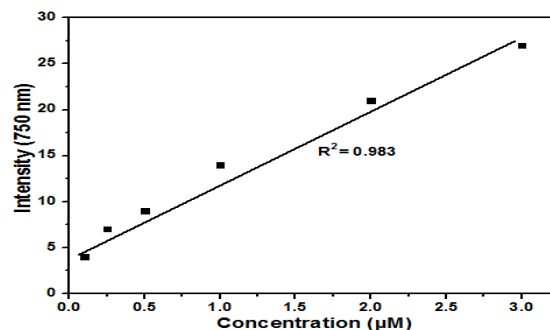
Absorption spectra of NRPA were evaluated in ACN/Tris-HCl buffer (10 mM, pH 7.3, v/v 2:1). A very weak absorption peak at 710 nm ( $\epsilon = 1.15 \times 10^3 \text{ M}^{-1} \text{ cm}^{-1}$ ) was observed in NRPA solution that was pale yellow color. The changes in UV-vis spectra in the presence of 1 equiv of metal ions,  $\text{Zn}^{2+}$ ,  $\text{Cr}^{3+}$ ,  $\text{Ni}^{2+}$ ,  $\text{Hg}^{2+}$ ,  $\text{Fe}^{3+}$ ,  $\text{Mn}^{2+}$ ,  $\text{Ag}^+$ ,  $\text{Pb}^{2+}$ ,  $\text{Fe}^{2+}$ ,  $\text{Cu}^+$ ,  $\text{Cu}^{2+}$ , and  $\text{Co}^{2+}$ , are shown in

Figure 5.1a. Only the addition of  $\text{Fe}^{3+}$  to the solution of NRPA increased the absorption peak at 710 nm ( $\epsilon = 4.0 \times 10^5 \text{ M}^{-1} \text{ cm}^{-1}$ ), and the color of the solution changed to green (result not shown). This can be explained with the ring-open form of spiro lactam<sup>[8]</sup> in NRPA. Compared with that of  $\text{Fe}^{3+}$ , other metal ions did not induce any changes in UV-vis absorption. Only  $\text{Fe}^{2+}$  showed minor response to NRPA.

The fluorescence responses of NRPA to different metal ions are shown in Figure 5.1b. NRPA solution showed very weak fluorescence at 738 nm. However, addition of 1 equiv of  $\text{Fe}^{3+}$  triggered an over 25-fold fluorescence enhancement with a detection limit of 0.1  $\mu\text{M}$  for  $\text{Fe}^{3+}$  (Figure 5.2), and with an emission peak at 750 nm ( $\Phi=0.198$ ) was observed with a blue shift about 7 nm compared with that of NRPA. However, little enhancement in fluorescence was observed for the other metal ions tested (only  $\text{Fe}^{2+}$  produced very weak enhancement). These data demonstrate that NRPA is a highly specific turn-on fluorescent sensor for  $\text{Fe}^{3+}$ .



**Figure 5.1** Absorption responses (a) and Fluorescence responses (b) of 20  $\mu\text{M}$  NRPA to various metal ions (20  $\mu\text{M}$   $\text{Zn}^{2+}$ ,  $\text{Cr}^{3+}$ ,  $\text{Ni}^{2+}$ ,  $\text{Hg}^{2+}$ ,  $\text{Fe}^{3+}$ ,  $\text{Mn}^{2+}$ ,  $\text{Ag}^+$ ,  $\text{Pb}^{2+}$ ,  $\text{Fe}^{2+}$ ,  $\text{Cu}^+$ ,  $\text{Cu}^{2+}$ , and  $\text{Co}^{2+}$ ; 100  $\mu\text{M}$  for  $\text{Na}^+$ ,  $\text{K}^+$ ,  $\text{Mg}^{2+}$ , and  $\text{Ca}^{2+}$ ) in ACN/Tris-HCl buffer (10 mM, pH 7.3, v/v 2:1)



**Figure 5.2** Fluorescence intensity versus increasing concentration of NRPA-Fe<sup>3+</sup> (1:1) in ACN/Tris-HCl buffer (10 mM, pH 7.3, v/v 2:1). Detection limit of 0.1 µM was obtained from the plot.

The interferences from the other metal ions were also examined with NRPA in its response to Fe<sup>3+</sup>. Even though the 15 metal ions tested do not turn-on the fluorescence of NRPA, they could quench the fluorescence of the complex (NRPA-Fe<sup>3+</sup>). Each of the 15 metal ions was pre-incubated with NRPA before 1 equiv of Fe<sup>3+</sup> was added, the fluorescence responses before and after the addition of Fe<sup>3+</sup> were measured. As shown in Figure 5.3, the fluorescent intensity of NRPA with Fe<sup>3+</sup> is not affected significantly in the presence of any of the other metal ions tested, demonstrating little interferences from the other metal ions.

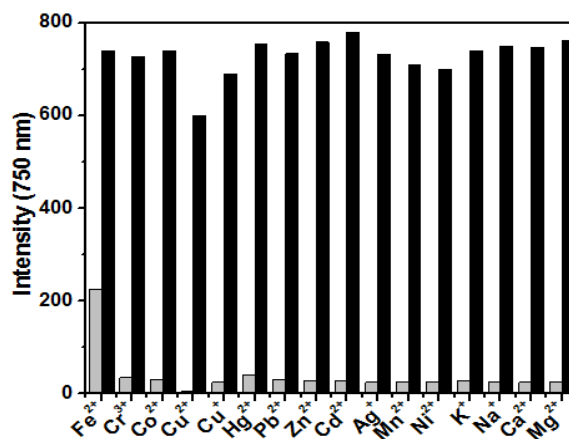


**Figure 5.3** Fluorescence responses of 20 µM NRPA to the presence of various metal ions (gray bar) and the subsequent addition of Fe<sup>3+</sup> (black bar) in the ACN/Tris buffer (10 mM, pH 7.3, v/v 2:1). The bars represent the fluorescence intensity at 750 nm.

One of the disadvantages of spirolactam-based sensors is that they also give response to hydrogen ions.<sup>[9, 10]</sup> The pH response of NRPA in ACN/water solution (2/1) was also evaluated as shown in Figure 5.3. The pH-dependent UV-vis and fluorescent experiments revealed that NRPA did not show any obvious and characteristic absorption and fluorescent (excited at 690 nm) in the pH range 5 to 9, suggesting that it can be studied in biological pH with a very low background fluorescence.

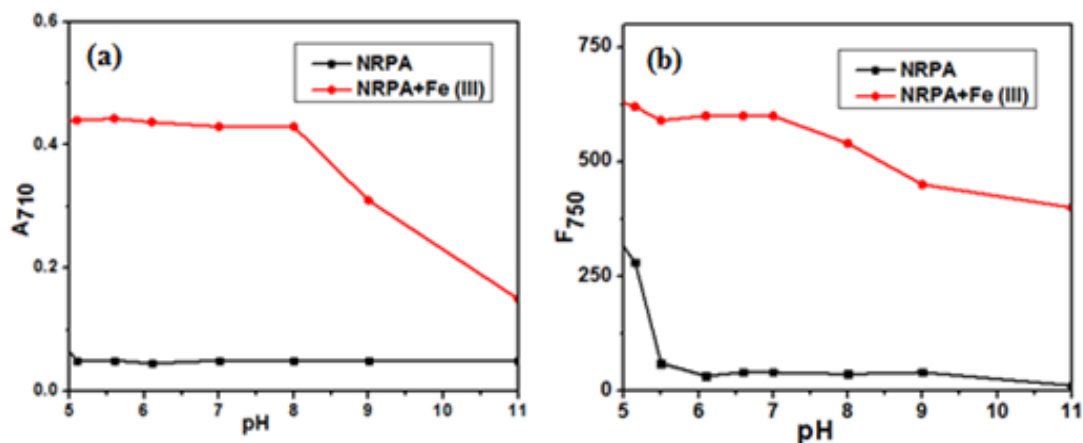


**Figure 5.4** (a) Absorption of NRPA and NRPA+Fe<sup>3+</sup> (20  $\mu$ M, the absorption intensity was measured at 710 nm) at various pH values in ACN/H<sub>2</sub>O (2/1, v/v) solution (b) Variation of fluorescence intensity (750 nm) of NRPA and NRPA+Fe(III) (20  $\mu$ M each) at various pH values in ACN/H<sub>2</sub>O (2/1, v/v) solution.

### 5.3.3 Binding Studies

Job's method and UV-vis titration spectra were applied to study the binding stoichiometry between NRPA and Fe<sup>3+</sup> and monitored by the absorbance at 710 nm. The titration curve (a plot of NRPA versus Fe<sup>3+</sup> concentration) increased linearly and plateaued at 1:1 ratio of the sensor and Fe<sup>3+</sup> (Figure 5.5), suggesting the formation of a 1:1 Fe<sup>3+</sup>-NRPA complex. The binding constant of this complex was calculated using absorption values at 710 nm by the equations described in chapter 4, and was determined to be  $6.76 \times 10^8 \text{ M}^{-1}$ .

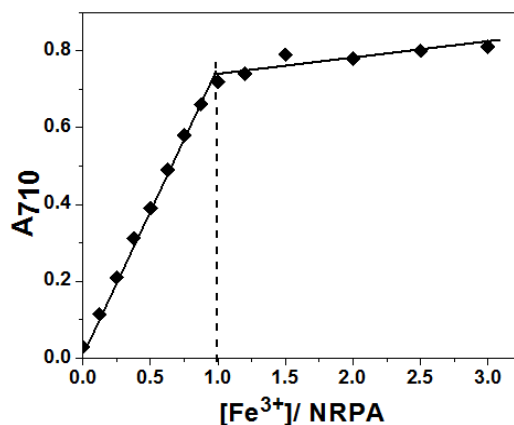


**Figure 5.5** Titration of 20  $\mu\text{M}$  NRPA with increasing concentrations of  $\text{FeCl}_3$  (2, 4, 6, 10, 12, 14, 16, 18, 20, 28, 36, 44, 52, 60, and 80  $\mu\text{M}$ , respectively) in ACN/Tris-HCl buffer (10 mM, pH 7.3, v/v 2:1). The absorption intensities were measured at 710 nm.

The Job's plot (Figure 5.6a) using a total concentration of 20  $\mu\text{M}$  NRPA and  $\text{Fe}^{3+}$  in ACN/Tris-HCl buffer (10 mM, pH 7.32, v/v 2:1) solution exhibited a maximum absorbance when the molecular fractions of  $\text{Fe}^{3+}$  and NRPA were close to 50 %, suggesting a 1:1 stoichiometry for the binding of NRPA and  $\text{Fe}^{3+}$ . Reversibility experiments were carried out by adding EDTA to the complex in ACN/Tris-HCl buffer (10 mM, pH 7.32, v/v 2:1). In the absence of EDTA, the complex was green and fluorescent. After adding EDTA, the absorption of the complex decreased in intensity and finally, disappeared (Figure 4.8b), suggesting a reversible binding between NRPA and  $\text{Fe}^{3+}$ . A possible mechanism for the reaction and the binding mode are shown in Scheme 5.2.

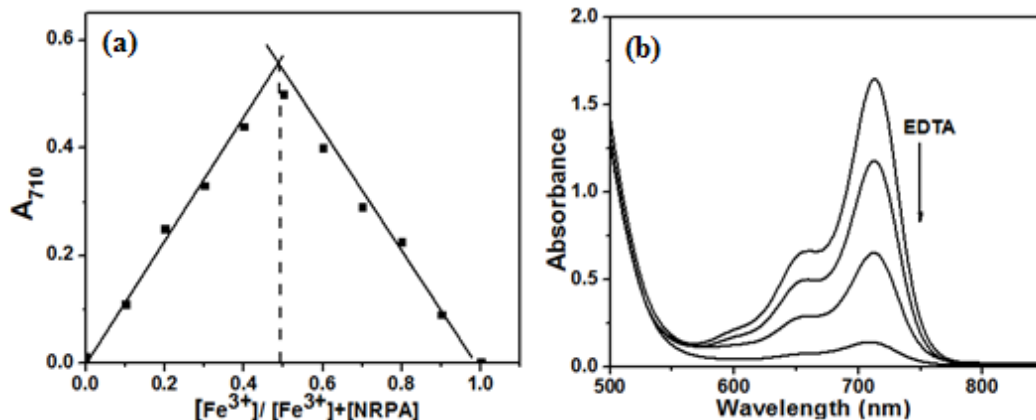
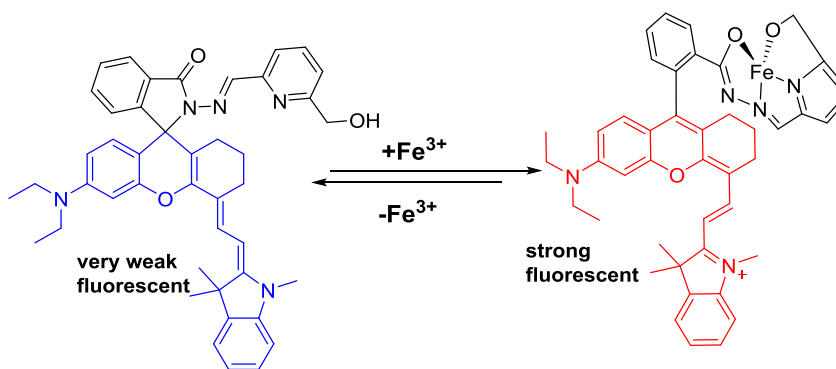


**Figure 5.6** (a) Job plot. The total concentrations of NRPA and  $\text{Fe}^{3+}$  were kept at constant  $25 \mu\text{M}$  and the absorbance intensity was measured at 710 nm in the ACN/Tris buffer (b) Treatment of  $40 \mu\text{M}$  NRPA- $\text{Fe}^{3+}$  complex with increasing concentration of EDTA (0 to  $40 \mu\text{M}$ , from top to bottom) in ACN/Tris-HCl buffer ( $10 \text{ mM}$ , pH 7.3, v/v 2:1).



**Scheme 5.2** Proposed 1:1 binding mode of NRPA with  $\text{Fe}^{3+}$  in ACN/Tris-HCl buffer ( $10 \text{ mM}$ , pH 7.3, v/v 2:1)

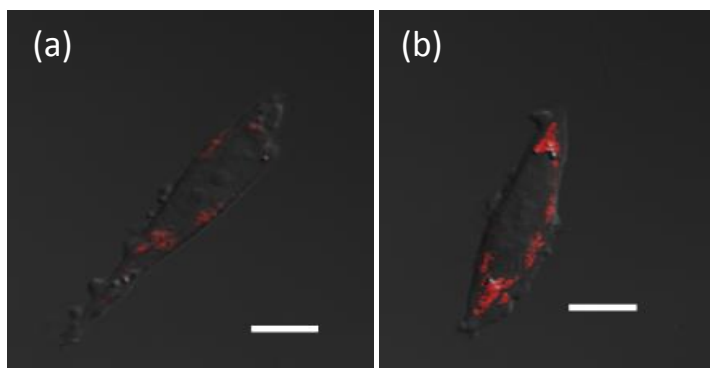
### 5.3.4 Cell Studies

Encouraged by the above promising results, we next tested the ability of NRPA to track  $\text{Fe}^{3+}$  in live human neuroblastoma SH-SY5Y cells via a laser scanning confocal microscope (Zeiss LSM 710). The cells were incubated with  $10 \mu\text{M}$  NRPA for 30 min.<sup>[10]</sup> We observed turn on fluorescence (Figure 5.7a) that is likely being triggered by endogenous labile  $\text{Fe}^{3+}$ . Another possibility might be the acidic environment of certain intracellular organelles (e.g., lysosomes/



endosomes), as low pH can also trigger the turn-on response of spirolactam based sensors.<sup>[10,11]</sup>

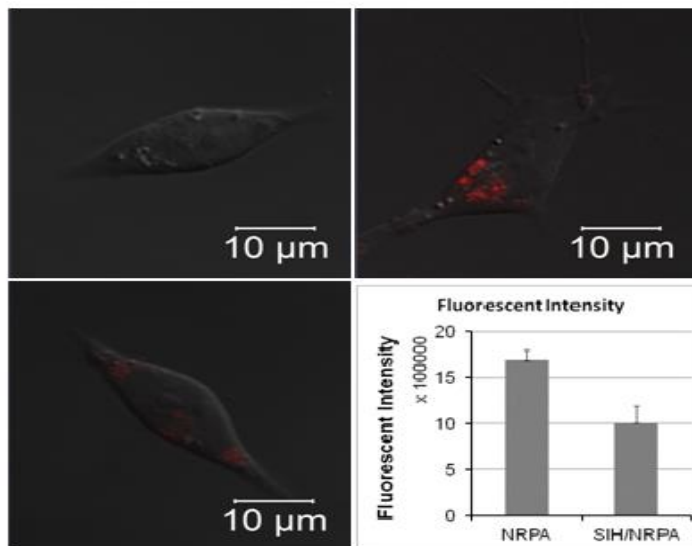
To look into these possibilities carefully, two approaches were used: first loading the cells with  $\text{Fe}^{3+}$  and second, depletion of  $\text{Fe}^{3+}$  by cell permeable  $\text{Fe}^{3+}$ -specific chelators. The fluorescence changes under both conditions were carefully monitored. Figure 5.7 compares the confocal fluorescence images of NRPA in human SH-SY5Y cells before and after being loaded with  $20\ \mu\text{M}$   $\text{Fe}^{3+}$ . The  $\text{Fe}^{3+}$ -loaded human SH-SY5Y cells clearly showed brighter and more widely distributed fluorescence signals in localized areas within the cytosol (Figure 5.7b), suggesting a positive response of NRPA to elevated labile  $\text{Fe}^{3+}$  levels in the  $\text{Fe}^{3+}$ -loaded cells.



**Figure 5.7** Confocal microscopy images (with DIC) of live human SH-SY5Y neuroblastoma cells treated with (a)  $20\ \mu\text{M}$  NRPA sensor after 30 min incubation (b) the cells were then incubated with  $\text{Fe}^{3+}$  ( $20\ \mu\text{M}$  Fe(8-HQ)) for 30 min. The brighter and more widely distributed fluorescence signals in (b) suggest elevated  $\text{Fe}^{3+}$  levels in  $\text{Fe}^{3+}$ -loaded human SH-SY5Y cells. Fluorescence intensity was collected at 680-750 nm (for NRPA) (DIC image of cells with  $10\text{-}\mu\text{m}$  scale bar).

To deplete the cellular labile  $\text{Fe}^{3+}$  from cells, the cells were pre-incubated with SIH (salicylaldehyde isonicotinoyl hydrazone, a cell permeable  $\text{Fe}^{3+}$ -chelator). The cells were then treated with NRPA and a decreased fluorescence response was observed (Figure 5.8c). These data, together with those from  $\text{Fe}^{3+}$ -loaded cells (Figure 5.7 and 5.8 ) demonstrate that the fluorescence response of NRPA in cells is triggered by cellular chelatable  $\text{Fe}^{3+}$ , not by acidic pH,

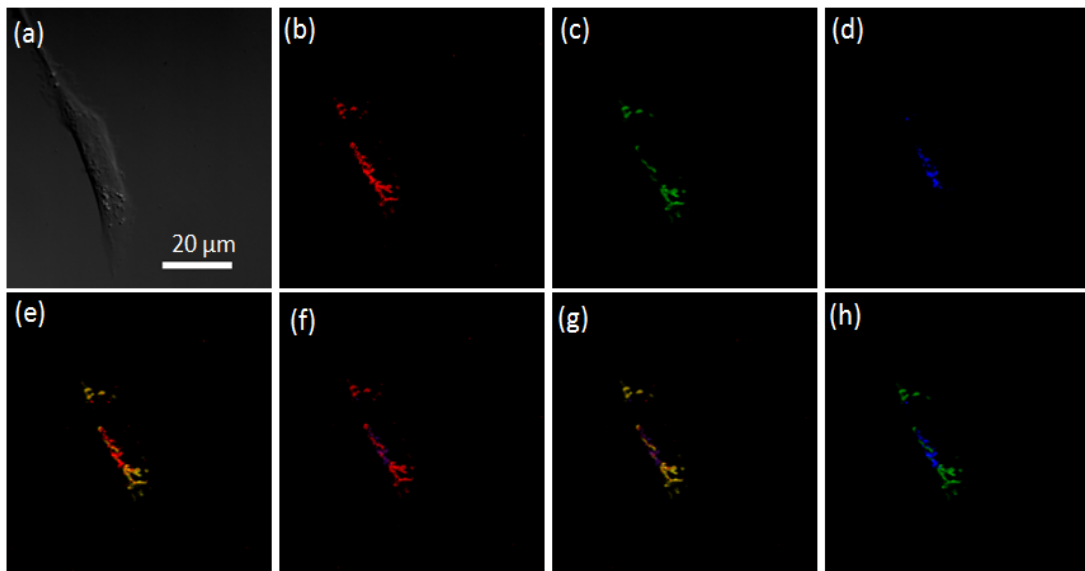
thus confirming that NRPA can detect not only endogenous labile  $\text{Fe}^{3+}$  in the cells but also the dynamic changes of  $\text{Fe}^{3+}$  in the cells.



**Figure 5.8** Confocal microscopy images (with DIC) of live human SH-SY5Y neuroblastoma cells with prior iron depletion by 100  $\mu\text{M}$  cell permeable  $\text{Fe}^{3+}$ -chelator salicylaldehyde isonicotinoyl hydrazine (SIH) for overnight and then treated with NRPA (10  $\mu\text{M}$ ) in 1:1 mixture of Eagles Minimal Essential medium (ATCC) and Ham's F12 medium (ATCC). (a) DIC image of cells with 10  $\mu\text{m}$  scale bar (b) 10  $\mu\text{M}$  NRPA sensor after 30 min incubation (c) 100  $\mu\text{M}$  cell permeable  $\text{Fe}^{3+}$ -chelator salicylaldehyde isonicotinoyl hydrazine (SIH) for overnight and then treated with NRPA, Fluorescence intensity was collected at 680-750 nm (for NRPA).

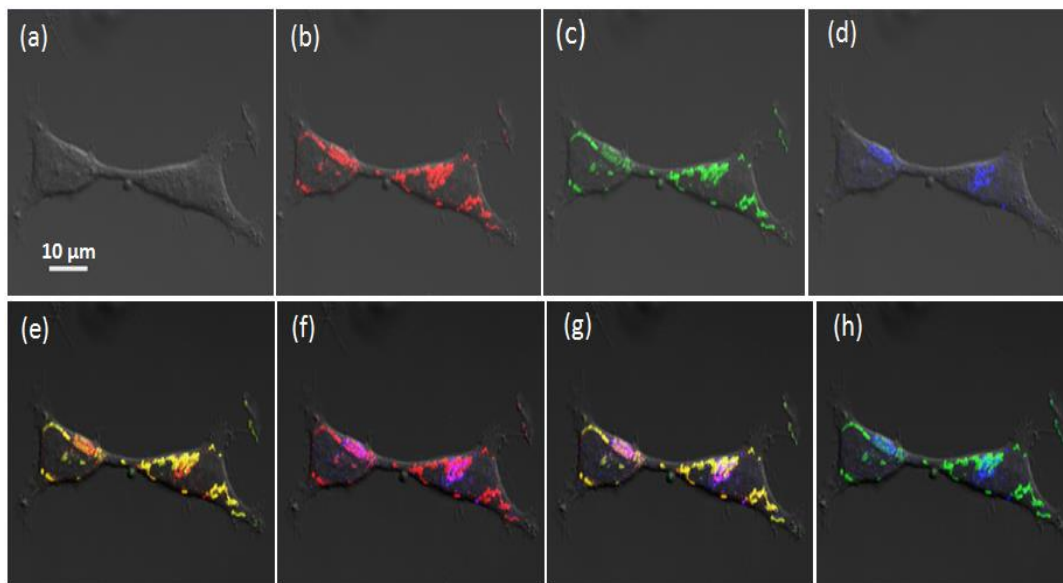
In Chapter 4, the NIRh-Ac sensor revealed that exogenous  $\text{Fe}^{3+}$  ions were located in mitochondria and lysosome of SH-SY5Y cells. Here, the capability of NRPA was tested to image endogenous  $\text{Fe}^{3+}$  ions at subcellular resolution. The subcellular distribution of exchangeable  $\text{Fe}^{3+}$  pools in live SH-SY5Y cells was investigated using NRPA and colocalization experiments with other dyes, MitoTracker Green FM (a green-fluorescent dye which localizes to mitochondria in live cells regardless of mitochondrial membrane potential) and LysoTracker blue DND-22 (a blue fluorescent dye that stains acidic compartments such as endosomes and lysosomes<sup>[10]</sup> in live cells). Human SH-SY5Y cells (without  $\text{Fe}^{3+}$  treatment) were treated with NRPA, MitoTracker

Green FM, and LysoTracker blue DND-22. As illustrated in Figure 5.9, there are partial colocalization between NRPA-Fe<sup>3+</sup> and the MitoTracker (Figure 5.9e) as well as that between NRPA-Fe<sup>3+</sup> and the LysoTracker (Figure 5.9f); however, a complete colocalization was observed among NRPA-Fe<sup>3+</sup>, MitoTracker and LysoTracker (Figure 5.9g). These data suggest that the exchangeable Fe<sup>3+</sup> pools in SH-SY5Y cells detectable by NRPA are localized in mitochondria and endosomes/lysosomes, not in cytosol. Additional experiments with NRPA and the trackers under Fe<sup>3+</sup> supplement conditions revealed again elevated levels of cellular chelatable Fe<sup>3+</sup> and that the labile Fe<sup>3+</sup> pools are still localized in mitochondria and endosomes/lysosomes (Figure 5.10). This finding is consistent with recent observations that cellular Fe<sup>3+</sup> directly transports from endosomes to mitochondria by a ‘kiss and run’ pathway, bypassing the cytosol.<sup>[12, 13]</sup>



**Figure 5.9** Representative confocal images of intracellular colocalization studies of 10 μM NRPA incubated with live human SH-SY5Y cells co-labeled with MitoTracker Green (100 nM) and LysoTracker Blue DND-22 (50 nM) (a) DIC image of cells with 20 μm scale bar (b) NRPA-Fe<sup>3+</sup> fluorescence collected at 680-750 nm (red) (c) MitoTracker fluorescence collected at 492-548 nm (green) (d) LysoTracker fluorescence collected at 409-484 nm (blue). (e) DIC image of (a) and fluorescence images of (b) and (c) were merged together. Colocalization regions are in yellow and non-overlapping regions remain in red (f) DIC image of (a) and fluorescence images of (b) and (d) were merged together. Overlapping regions are in purple and non-overlapping regions remain in red (g) Images of (a), (b), (c) and (d) were merged together, revealing that the NRPA-

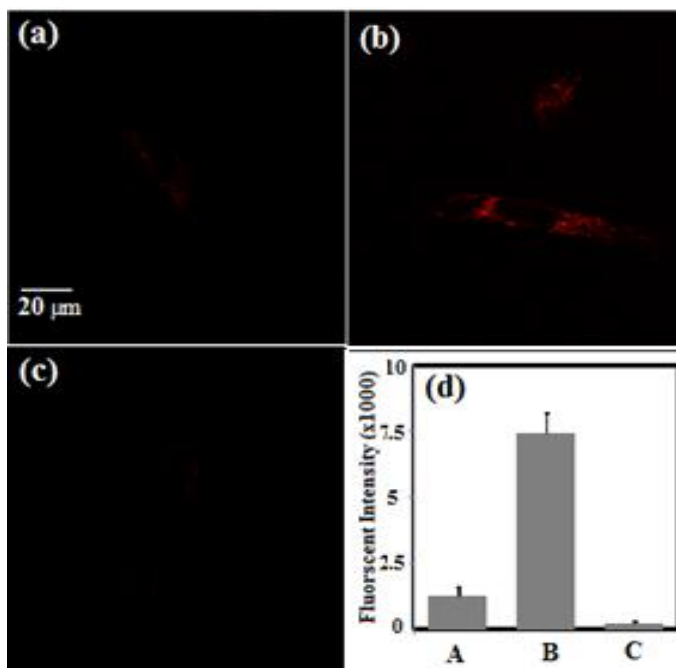
$\text{Fe}^{3+}$  images are 100% colocalized with the sum of those of MitoTracker and LysoTracker (h), Images of (a), (c) and (d) were merged together, showing no overlapping region between lysosomes and mitochondria.



**Figure 5.10** Representative confocal microscopy images of intracellular colocalization studies of 10  $\mu\text{M}$  NRPA incubated with  $\text{Fe}^{3+}$ -loaded human SH-SY5Y cells (pre-incubated with 10  $\mu\text{M}$   $\text{Fe}^{3+}$ ) co-labeled with MitoTracker Green FM (100 nM, incubated for 30 min) and LysoTracker Blue DND-22 (50 nM, incubated for 120 min) (a) DIC image of cells with 10  $\mu\text{m}$  scale bar (b) NRPA- $\text{Fe}^{3+}$  fluorescence collected at 680-750 nm (red) (c) MitoTracker fluorescence collected at 492-548 nm (green) (d) LysoTracker fluorescence collected at 409-484 nm (blue). (e) DIC image of (a) and fluorescence images of (b) and (c) were merged together. Colocalizations regions are in yellow and non-overlapping regions remain in red (f) DIC image of (a) and fluorescence images of (b) and (d) were merged together. Overlapping regions are in purple and non-overlapping regions remain in red (g) Images of (a), (b), (c) and (d) were merged together, revealing that the NRPA- $\text{Fe}^{3+}$  images are 100% colocalized with the sum of those of MitoTracker and LysoTracker. (h) Images of (a), (c) and (d) were merged together, showing no overlapping region between lysosomes and mitochondria.

Similar experiments were performed to investigate the ability of NRPA to detect  $\text{Fe}^{3+}$  in live human fibroblast ws1 cells by using confocal microscopy. First, it was tested if NRPA can detect endogenous  $\text{Fe}^{3+}$  and elevated levels of labile  $\text{Fe}^{3+}$  in live ws1 cells. To this end, ws1 cells were incubated with 20  $\mu\text{M}$   $\text{FeCl}_3$  for 8 h and then stained with 20  $\mu\text{M}$  NRPA for an additional 30 min. As shown in Figure 5.11b, clear fluorescence was observed in ws1 cells without  $\text{Fe}^{3+}$

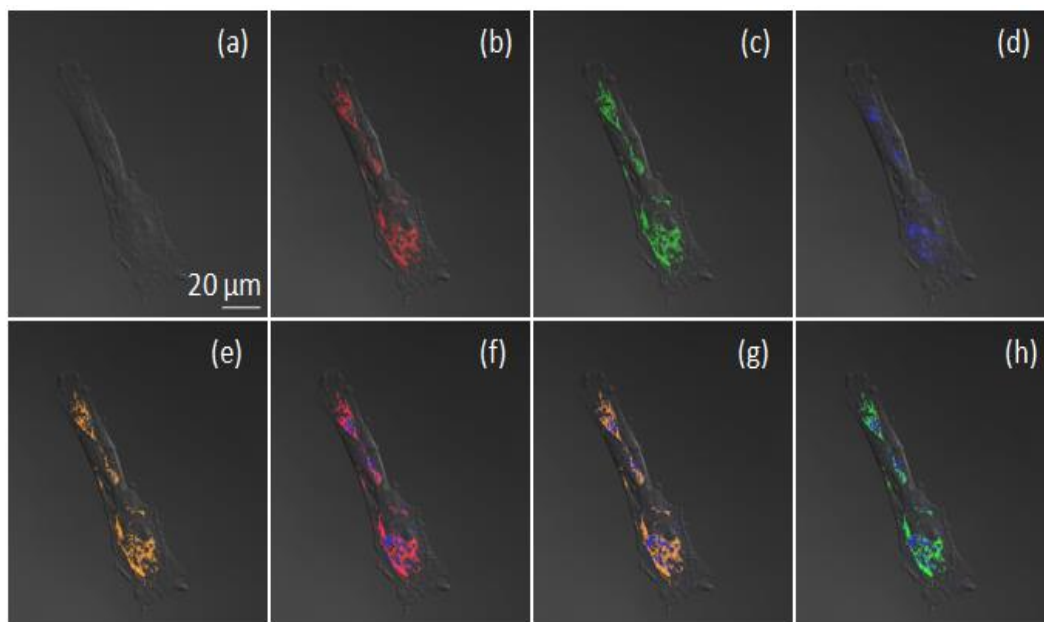
treatment (control) and a significant increase in intracellular fluorescence was observed in iron-loaded cells compared to control cells was observed (Figure 5.11a). To verify that the fluorescence increase was due to iron-dependent events, iron-loaded ws1 cells were treated with 100  $\mu\text{M}$  of iron chelator salicylaldehyde isonicotinoyl hydrazone (SIH) for overnight to reduce intracellular levels of labile iron. As expected, SIH reduced the cellular fluorescence (Figure 5.11b and 11.c), thus confirming that NRPA can detect not only endogenous labile  $\text{Fe}^{3+}$  in the cells but also the dynamic changes of  $\text{Fe}^{3+}$  in the cells.



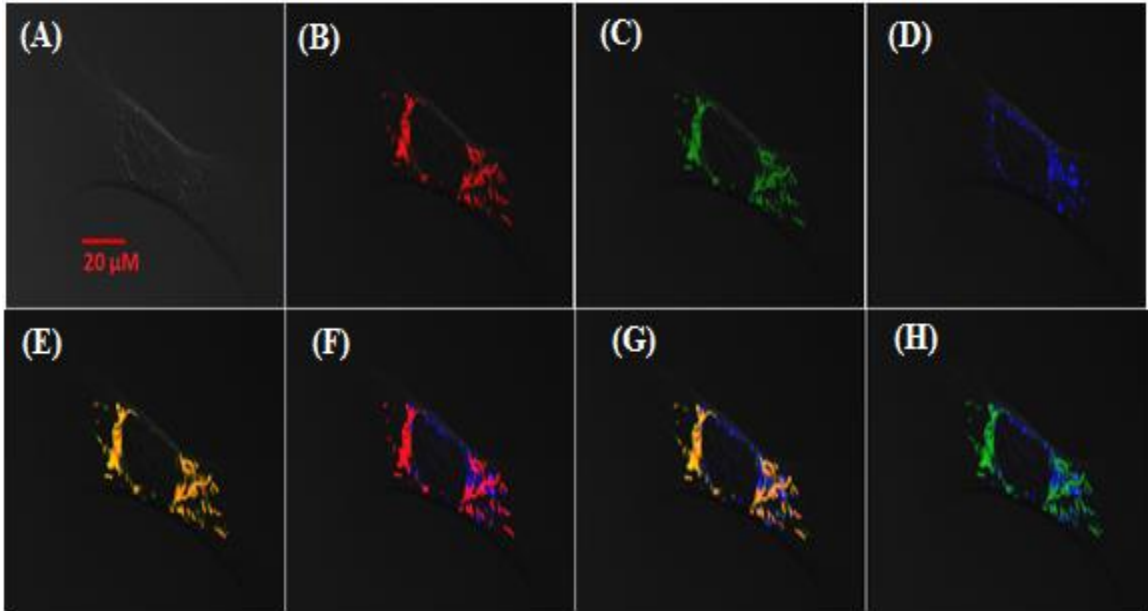
**Figure 5.11** Confocal microscopy images (with DIC) of live human skin fibroblast cells (ws1) (a) DIC image of cells with 20  $\mu\text{m}$  scale bar (a) 10  $\mu\text{M}$  NRPA sensor after 30 min incubation (b) Fibroblast cells (WS1) were then incubated with 20  $\mu\text{M}$   $\text{Fe}^{3+}$  for 8 h then the sensor was added (c) 100  $\mu\text{M}$  SIH for overnight and then treated with NRPA (d) Bar chart of fluorescent intensity of A, B, C (Fluorescence intensity was collected at 680-750 nm (for NRPA)).

Figure 5.12 shows the distribution of exchangeable  $\text{Fe}^{3+}$  pools in live fibroblast cells (ws1). The sensor NRPA- $\text{Fe}(\text{III})$  complex gives red fluorescent images and is shown in Figure 5.12b. Figure 5.12c shows the MitoTracker signals and Figure 5.12d LysoTracker signals in live

fibroblast cells (ws1). As shown in Figure 5.12e there is a complete colocalization between NIRh-Fe(III) and MitoTracker (red + green = yellowish-green). There was no co-localization observed between ws1-Fe<sup>3+</sup> and the lysosome (Figure 5.12f and g). However, when we repeated the experiments for the iron loaded ws1 cells, we observed that the NRPA-Fe<sup>3+</sup> images are 100% colocalized with the sum of those of MitoTracker and LysoTracker (Figure 5.12). These results also show that free Fe<sup>3+</sup> ions enter cells as described in chapter 4.



**Figure 5.12** Representative confocal images of intracellular colocalization studies of 10  $\mu\text{M}$  NRPA incubated with live human ws1 cells co-labeled with MitoTracker Green (100 nM) and LysoTracker Blue DND-22 (50 nM) (a) DIC image of cells with 20  $\mu\text{m}$  scale bar (b) NRPA-Fe<sup>3+</sup> fluorescence collected at 680-750 nm (red) (c) MitoTracker fluorescence collected at 492-548 nm (green) (d) LysoTracker fluorescence collected at 409-484 nm (blue) (e) DIC image of (a) and fluorescence images of (b) and (c) were merged together. Colocalization regions are in orange and no red colored region remained (f) DIC image of (a) and fluorescence images of (b) and (d) were merged together no overlapping (g) Images of (a), (b), (c) and (d) were merged together, revealing that the NRPA-Fe<sup>3+</sup> images are 100% colocalized with MitoTracker but not with LysoTracker. (h) Images of (a), (c) and (d) were merged together, showing no overlapping region between lysosomes and mitochondria.



**Figure 5.13** Representative confocal microscopy images of intracellular colocalization studies of 20  $\mu\text{M}$  NRPA incubated with  $\text{Fe}^{3+}$ -loaded fibroblast cells (ws1) (pre-incubated with 20  $\mu\text{M}$   $\text{Fe}^{3+}$ ) co-labeled with MitoTracker Green FM (100 nM, incubated for 30 min) (a) DIC image of cells with 20  $\mu\text{m}$  scale bar (b) NRPA fluorescence collected at 680-750 nm (red) (c) MitoTracker fluorescence collected at 492-548 nm (green) (d) LysoTracker fluorescence collected at 409-484 nm (blue) (e) DIC image of (a) and fluorescence images of (b) and (c) were merged together. Colocalizations regions are in yellow and non-overlapping regions remain in red (f) DIC image of (a) and fluorescence images of (b) and (d) were merged together. Overlapping regions are in purple and non-overlapping regions remain in red (g). Images of (a), (b), (c) and (d) were merged together, revealing that the NRPA- $\text{Fe}^{3+}$  images are 100% colocalized with the sum of those of MitoTracker and LysoTracker. (h) Images of (a), (c) and (d) were merged together, showing no overlapping region between lysosomes and mitochondria.

The results show that the endogenous iron levels and subcellular distribution in different cell lines are different. SH-SY5Y neuroblastoma cells are cancer cells and ws1 cells are primary healthy cells. Cancer cells need more iron than normal cells to keep their abnormal rapid growth<sup>[14]</sup>, so SH-SY5Y has a higher iron stock and in two pools.

### 5.3.5 Zebrafish Studies

We explored further whether NRPA could be used to monitor endogenous free  $\text{Fe}^{3+}$  ions in zebrafish in collaboration with Dr. Ferreira's Lab (Bioengineering Department). The

preliminary *in vivo* Fe<sup>3+</sup> imaging of intact two-day-old zebrafish larva with NRPA staining was performed using confocal microscopy. We observed turn on fluorescence response of NRPA which is likely being triggered by endogenous labile Fe<sup>3+</sup>. To confirm this and to test whether NRPA can image the dynamic changes of labile Fe<sup>3+</sup> levels in zebrafish; we did two control experiments. First, loading zebrafish with exogenous Fe<sup>3+</sup> and second, depletion of Fe<sup>3+</sup> by cell permeable Fe<sup>3+</sup>-specific chelator. However, the chelator SIH was toxic to zebrafish, and killed them even when it was incubated for 1 h. We decided to use different concentration of Fe<sup>3+</sup> to show that when iron concentration increases, turn-on fluorescence increases.

Figure 5.14 show some confocal images for 3- and 6-days-old zebrafish. The images in the first row belong to 3-days-old zebrafish. 3-days-old zebrafish itself did not show any fluorescence when it was excited at 633 nm under the confocal microscopy. When it was incubated with NRPA, a red colored region was observed. 2-days-old zebrafish were pre-incubated with FeCl<sub>3</sub> (10 and 40 μM) for 24 hours, washed, and then incubated with 10 μM NRPA for another 0.5 hour. The Fe<sup>3+</sup>-loaded zebrafish clearly showed brighter fluorescence (3 fold for 10 μM and 10 fold for 40 μM Fe<sup>3+</sup>), suggesting a positive response of NRPA to elevated labile Fe<sup>3+</sup> levels in the Fe<sup>3+</sup>-loaded zebrafish. However, organs in zebrafish have not been fully developed in this stage<sup>[15-16]</sup> (3-days-old). The red colored region seems to be the intestine area.

We repeated the same experiments with 6-days-old zebrafish and observed similar Fe<sup>3+</sup>-concentration dependent response as those with 3-days-old zebrafish. However, the red-colored region now was observed as a well-localized red round spot, being the liver/gall bladder region of the 6-days-old zebrafish.<sup>[14-15]</sup> These interesting data demonstrate that the NRPA sensor is able to image dynamic changes of labile Fe<sup>3+</sup> levels in zebrafish, as well its locations in different developmental stages.



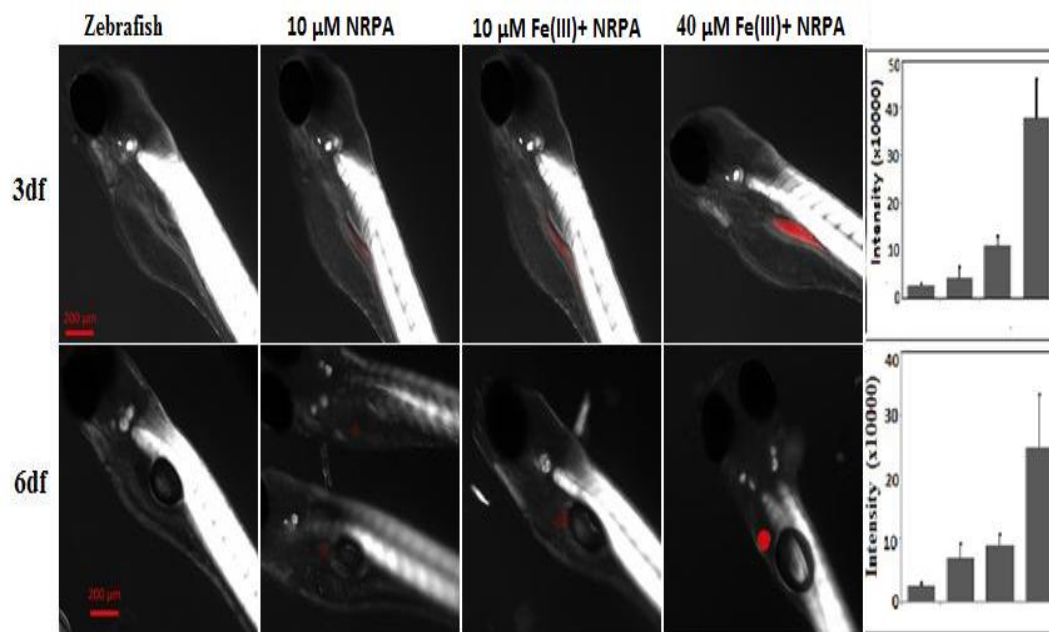


**Figure 5.14** Confocal microscopy images of 3 and 6 day old zebrafish larvae (a,e) Zebrafish only (b,f) Zebrafish larva was incubated with 10  $\mu\text{M}$  NRPA for 30 min (c,g) Zebrafish larva incubated with 10  $\mu\text{M}$  and (d,h) incubated with 40  $\mu\text{M}$   $\text{FeCl}_3$  for 3 days then 10  $\mu\text{M}$  NRPA was added and incubated for 30 min

#### 5. 4 Conclusion

In summary, we have developed a highly sensitive, highly selective, and reversible turn-on near infrared fluorescent  $\text{Fe}^{3+}$ -sensor, NRPA. The sensor gives a distinct rapid and reversible fluorescence response upon the alteration of intracellular  $\text{Fe}^{3+}$  levels with little interference from other biologically relevant metal ions. Confocal experiments show that NRPA can readily detect endogenous free  $\text{Fe}^{3+}$  in live human SH-SY5Y cells and live fibroblast cell (ws1) at subcellular resolution. However, results showed that chelatable  $\text{Fe}^{3+}$  pools were located in mitochondria and endosomes/lysosomes for SH-SY5 cells while in mitochondria only for ws1 cells. It was concluded that different cell lines store/handle iron in different ways. The ability of NRPA to detect endogenous free  $\text{Fe}^{3+}$  ions in zebrafish was also demonstrated and free  $\text{Fe}^{3+}$  ions were found located in liver/gall bladder of 6-days-old zebrafish.

## 5.5 References

1. Crichton R., *Inorganic Biochemistry of Iron Metabolism*, 2nd ed.), Wiley, Chichester, **2001**, pp. 167 - 175
2. Linder M.C., *Nutrients*, **2013**, 5, 4022-4050
3. Truty J., Malpe R., Linder M.C., *J. Biol. Chem.*, **2001**, 276, 48775-48780
4. Kidane T.Z., Sauble E., Linder M.C. *Am. J. Physiol. Cell Physiol.*, **2006**, 291, C445-C455
5. Epsztejn S., Glickstein H., Picard V., Slotki I. N., Breuer W., Beaumont C., Cabantchik Z. I., *Blood*, **1999**, 94, 1-12
6. Santra M., Ryu D., Chatterjee A., Ko S. K., Shin I., Ahn K. H., *Chem. Commun.*, **2009**, 2115-2117
7. Lister J.A., Robertson C.P., Lepage T., Johnson S.L., Raible D.W., *Development*, **1999**, 126, 3757-3767
8. Yuan L., Lin W., Yang Y., Chen H., *J. Am. Chem. Soc.*, **2012**, 134, 1200-1211
9. Kim H.N., Lee M.H., Kim H.J., Kim J.S., *Chem. Soc. Rev.*, **2008**, 37, 1465-1472
10. Wei Y., Zhang Y., Liu Z. and Guo M., *Chem. Comm.*, **2010**, 46, 4722-4726
11. Chartres J. D., Busby M., Riley M. L., Davis J. J., Bernhardt P. V., *Inorg. Chem.*, **2011**, 50, 9178 - 9183
12. Sheftel A. D., Zhang A. S., Brown C., Shirihai O. S., Ponka P., *Blood*, **2007**, 110, 125 - 132
13. Beckera E. M., Huang M. L.-H., Whitnalla M., Rahmantoa Y. S., Sheftel A. D., Ponkac P., *Proc. Natl. Acad. Sci. USA*, **2010**, 107, 10775 - 10782
14. Kiessling M. K., Klemke C. D., Kaminski M. M., Galani I. E., Krammer P. H., Gulow K., *Cancer Res.*, **2009**, 69, 2365-2374
15. Ko S.K., Chen X., Yoon J., Shin I., *Chem. Soc. Rev.*, **2011**, 40, 2120-2130
16. Wallace K. N., Pack M., *Dev. Biol.*, **2003**, 255, 12-29

## CHAPTER 6

### TURN-ON NEAR-INFRARED FLUORESCENT SENSORS NRP AND NRPK FOR IMAGING

#### ENDOGENOUS $\text{Fe}^{3+}$ IN LIVE ORGANISMS

##### 6.1 Introduction

Iron is the most abundant nutritionally essential transition metal found in the human body.<sup>[1-2]</sup> It is nutritionally essential because it is the key part in the prosthetic group in heme containing proteins as well as non-heme iron containing proteins and thereby plays important roles in various biological processes such as oxygen delivery, electron transport, enzymatic reactions and DNA synthesis and repair.<sup>[3]</sup> However, excess iron is highly toxic to cells as it promotes the abnormal production of reactive oxygen species (ROS).<sup>[4-5]</sup> Even though  $\text{Fe}^{3+}$  is a more stable form under aerobic conditions<sup>[6]</sup>, due to the reducing environment of the cell and greater aqueous solubility of  $\text{Fe}^{2+}$ ,  $\text{Fe}^{2+}$  ions are also found in cellular labile iron pools.<sup>[7-9]</sup> Thus it was attempted to design a Fe(II)-selective fluorescent sensor by introducing an “NNO” iron-binding motif; however, another Fe(III)-selective fluorescent sensor was obtained after *in vitro* experiments were performed.

In this chapter, I present the design, synthesis, characterization, and biological applications of another Fe(III) sensor NRPK, a modified rhodamine based (Changsha (CS) near infrared fluorophore) turn-on fluorescent sensor for monitoring exchangeable  $\text{Fe}^{3+}$  pools in aqueous solution and living cells. I also synthesized the sensor NRP to aid the understanding of the binding between  $\text{Fe}^{3+}$  and NRPK. The utility of NRPK in biological settings was demonstrated by showing that this probe could detect changes in exchangeable iron(III) stores in living cells upon iron supplementation or depletion. Moreover, NRPK can be used to visualize chelatable  $\text{Fe}^{3+}$  ions in zebrafish.

## 6.2 Experimental Part

Unless otherwise stated, similar procedures described in the previous chapters were used.

### 6.2.1 Materials and Reagents

2-(1,3,3-Trimethylindolin-2-ylidene) acetaldehyde was purchased from OChem Incorporation. 2-(4-Diethylamino-2-hydroxybenzoyl) benzoic acid, 2,6-diacetylpyridine, and benzotriazol-1-yloxytris(dimethylamino)-phosphonium hexafluorophosphate (BOP) were purchased from TCI America. 2-acetylpyridine was purchased from Aldrich. The other chemicals and the solvents used in the experiments were purchased commercially. The solution of metal ions were prepared from chloride salts of  $\text{Ni}^{2+}$ ,  $\text{Fe}^{3+}$ ,  $\text{Cu}^{2+}$ ,  $\text{Mn}^{2+}$ ,  $\text{Hg}^{2+}$ ,  $\text{Na}^+$ ,  $\text{Ca}^{2+}$ ,  $\text{Zn}^{2+}$ ,  $\text{Ag}^+$ , and nitrate salts of  $\text{Mg}^{2+}$ ,  $\text{Pb}^{2+}$ ,  $\text{K}^+$ ,  $\text{Co}^{2+}$ . Stock solutions of metal ions (10 mM) were prepared in deionized water, except for  $\text{Fe}^{3+}$  and  $\text{Fe}^{2+}$  that were dissolved in 0.1 M HCl solution. Solution of  $\text{Cu}^+$  was freshly prepared by dissolving tetrakis(acetonitrile) copper(I) (Sigma-Aldrich) into double-distilled water.

Stock solutions of NRP and NRPK (1 mM) were prepared in ACN. The solutions of the sensors were diluted to 25  $\mu\text{M}$  with ACN/Tris-HCl buffer (10 mM, pH 7.2, v/v 3:1). In selectivity experiments, the test samples were prepared by appropriate amount of metal ion stocks into 1 mL solution of sensors (25  $\mu\text{M}$ ).  $^1\text{H}$  and  $^{13}\text{C}$  NMR spectra were recorded on a Bruker Ascend-400 NMR spectrometer. ESI-MS analyses were performed using a Perkin Elmer API 150 EX mass spectrometer. UV/Vis spectra were recorded on a Perkin Elmer Lambda 25 spectrometer at 293 K. Fluorescence spectra were recorded on a Perkin Elmer LS55 luminescence spectrometer at 293 K. The pH measurements were carried out on a Corning pH meter equipped with a Sigma-Aldrich micro combination electrode calibrated with standard buffer solutions.

## 6.2.2 Synthesis

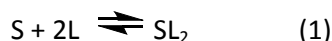
**Synthesis of NRPK:** NIRh (0.20 g, 0.35 mmol, 1 equiv) and 2,6-diacetylpyridine (0.115 g, 0.7 mmol, 2 equiv) were dissolved in ethanol (25 ml). The reaction mixture was then stirred and refluxed for 3 days. The mixture was evaporated to amount of 5 mL then hexane (20 mL) was added. A pale green compound was precipitated. The product was purified by a column chromatography (silica gel) using Hexane/EtOAc (1:2) to give NRPK (58 mg, yield 28 %).  $^1\text{H}$  NMR ( $\text{CDCl}_3$ , 400 MHz  $\delta(\text{ppm})$ ): 8.43 - 8.29 (m, 2H), 8.25 (s, 1H), 7.85 (s, 1H), 7.54 (s, 1H), 7.46 (d,  $J = 5.9$  Hz, 2H), 7.20 (d,  $J = 15.4$  Hz, 2H), 6.94 (s, 1H), 6.76 (s, 1H), 6.62 (s, 2H), 6.39 - 6.26 (m, 3H), 5.48 (s, 1H), 3.77 - 3.56 (m, 2H), 3.49 - 3.28 (m, 2H), 2.97 - 2.90 (m, 3H), 2.68 - 2.61 (m, 3H), 2.39 - 2.33 (m, 3H), 1.78 - 1.70 (m, 2H), 1.68 - 1.61 (m, 2H), 1.56 - 1.50 (m, 6H), 1.40 - 1.32 (m, 2H), 1.25 - 1.18 (m, 6H).  $^{13}\text{C}$  NMR ( $\text{CDCl}_3$ , 100 MHz  $\delta(\text{ppm})$ ): 12.55, 14.2, 15.43, 21.06, 22.28, 25.3, 25.7, 28.2, 28.36, 29.1, 35.80, 44.30, 45.44, 91.99, 97.93, 102.6, 102.8, 105.6, 108.3, 119.3, 119.6, 120.1, 121.59, 123.01, 123.45, 124.76, 125.7, 128.25, 137.97, 138.04, 145.96, 148.5, 148.8, 149.1, 152.69, 157.7, 166.38, 171.77, 199.40; ESI-MS: found:  $m/z = 718.1$   $[\text{M}+\text{H}]^+$ , calcd for  $\text{C}_{46}\text{H}_{47}\text{N}_5\text{O}_3 = 717.3$ .

**Synthesis of NRP:** NIRh (0.100 g, 0.175 mmol, 1 equiv) and 2-acetylpyridine (0.025 g, 0.21 mmol, and 1.2 equiv) were dissolved in ethanol (10 ml). The reaction mixture was then stirred and refluxed for overnight. The mixture was cooled to room temperature and the solvent was evaporated under reduced pressure. The crude product was purified by a column chromatography (silica gel) using Hexane/EtOAc (1:2) to obtain NRP (48 mg, yield 40 %).  $^1\text{H}$  NMR ( $\text{CDCl}_3$ , 400 MHz  $\delta(\text{ppm})$ ): 8.43 (s, 1H), 7.94 (s, 1H), 7.86 (d, 2H), 7.58 (s, 1H), 7.53 (s, 1H), 7.45 (d, 2H), 7.21 (d, 2H), 6.95 (s, 1H), 6.74 (s, 1H), 6.63 (s, 1H), 6.36 (d, 2H), 6.21 (s, 1H), 5.05 (s, 1H), 3.73 - 3.57 (m, 2H), 3.36 - 3.29 (m, 2H), 3.18 - 3.13 (m, 3H), 2.41 - 2.36 (m, 3H), 2.04 - 1.96 (m,

4H), 1.55 - 1.48 (m, 8H), 1.24 - 1.19 (m, 6H);  $^{13}\text{C}$  NMR ( $\text{CDCl}_3$ , 100 MHz  $\delta(\text{ppm})$ ): 13, 17.8, 24.4, 25.3, 27.6, 28.1, 33, 45, 48, 99, 101.2, 109.3, 114.1, 115.2, 118, 122, 123.6, 125.2, 126, 128.1, 130.9, 133.2, 134, 134.8, 135, 136.1, 143, 144, 148, 149, 150.6, 158, 158.9, 169.2; ESI-MS: found:  $m/z = 676.2$   $[\text{M}+\text{H}]^+$ , calcd for  $\text{C}_{44}\text{H}_{45}\text{N}_5\text{O}_2 = 675.36$ .

### 6.2.3 Binding Studies

UV-vis titration and Job's plot were obtained for NRPK and NRP to determine the stoichiometries between  $\text{Fe}^{3+}$  and the sensors. Similar processes described in Chapter 4 and 5 were used for Job's plot and UV-vis titration. We estimated the binding constant by using the absorption titration results. The equation below was used to calculate the binding constants for 2:1 complexes.



The apparent binding constant and the fraction of the ligand that participates in the complex are shown in equations (2) and (3)

$$K = \frac{[\text{FeS}_2]_e}{[\text{Fe}]_e [\text{S}]_e^2} \quad (2)$$

The subscript e means concentrations at equilibrium. The ratio of the equilibrium between the complex,  $[\text{SFe}]_e$ , and the initial concentration of the ligand,  $[\text{S}]_o$ , can be derived from the absorbance of the ligand at a chosen wavelength when the system is at equilibrium. The result of the derivation is shown in eq. (4).

$$F_c = \frac{\text{Au}-\text{Am}}{2\text{Au}-2\text{Ac}} \quad (3)$$

Finally, the integrated apparent binding constant equation is shown in equation (4) (for a complete derivation see ref 10).

$$K = \frac{Fc}{2 [S]_o [Fe]_e (1-Fc)^2} \quad (4)$$

#### 6.2.4 Cell and Zebrafish Studies

Bovine aortic endothelial cells (BAEC) were obtained from Dr. Keaney's research group (UMass Medical School). Primary cultured endothelial cells from bovine aorta were passaged in Endothelial Basal Medium (Lonza) containing 5% fetal bovine serum. Before the experiment, the cells were cultured to about 8<sup>th</sup> generation. For experiment preparation, the cells were routinely subcultured using 0.05% trypsin-EDTA solution. The cells were seeded on the 25 cm<sup>2</sup> flask and medium change every two days until 70% confluency before transferring into dishes. The cells were seeded on the 1 cm<sup>2</sup> dish and a medium change the next day. After incubation for 4 hrs, different test materials were added to the medium.

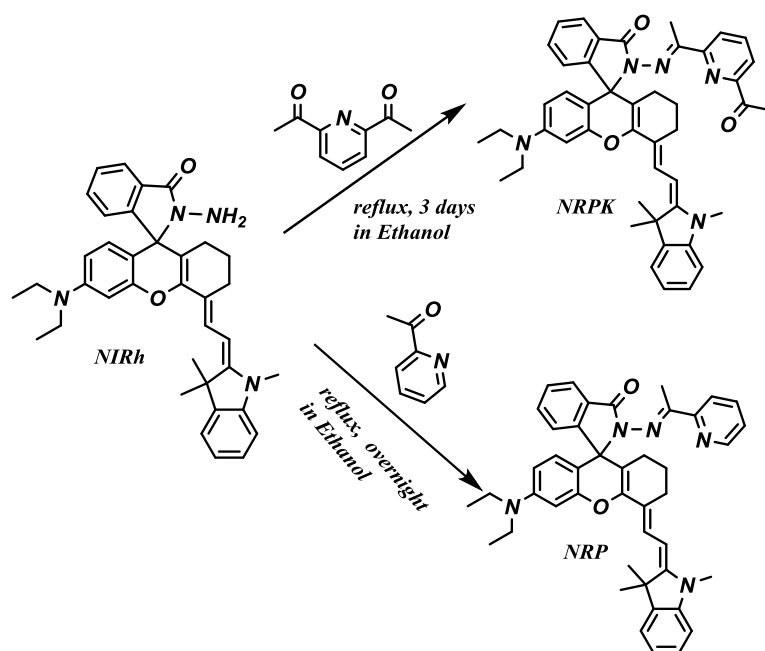
Zebrafish were maintained under standard conditions in collaborator Prof. T. Ferreira's lab (UMD, Bioengineering). Embryos were collected from natural spawning and raised up in embryo medium.<sup>[11]</sup> Zebrafish strain nacre was utilized because it lacks pigment, allowing better visualization. Zebrafish embryos at 2, 3, and 6 dpf were incubated with 10 μM NRPK in E3 media containing 0.1 vol % DMSO for 1 h at 28 °C. In addition, iron-loaded zebrafish (10 μM and 40 μM FeCl<sub>3</sub> for 1-day incubation) were incubated with 10 μM NRPK in E3 media for 1 h at 28 °C. Alternatively, zebrafish were exposed to 100-μM iron chelator SIH in E3 media containing 0.1 vol % DMSO for 1 h at 28°C. After washing with E3 media to remove the remaining SIH, the zebrafish were further incubated with 10 μM NRPK in E3 media for 1 h at 28 °C. The treated zebrafish were imaged by a confocal microscope Zeiss LSM 710.

## 6.3 Results and Discussion

### 6.3.1 Design and Synthesis

In chapter 5, the sensor NRPA showed a little turn-on fluorescence response to  $\text{Fe}^{2+}$  ions. This encouraged us to synthesize a fluorescent sensor for  $\text{Fe}^{2+}$  by incorporating a softer binding moiety. The carbonyl group in 2,6 diacetyl pyridine is softer than the -OH group in hydroxymethylpyridene moiety<sup>[12]</sup> in NRPA. Also 2,6 diacetylpyridine was linked to rhodamine B to obtain a Fe (II)-selective fluorescent sensor.<sup>[13]</sup> This reported article also encouraged us to use 2,6 diacetylpyridine as a binding moiety. It was expected that the sensor NRPK would bind to  $\text{Fe}^{2+}$  with O/N/N/O binding moiety. However, as seen in the results and discussion section, NRPK shows fluorescence response to  $\text{Fe}^{3+}$  ions, not  $\text{Fe}^{2+}$  ions. The sensor NRP was synthesized for better understanding of the binding between  $\text{Fe}^{3+}$  and NRPK. The sensors, NRPK and NRP, were synthesized in a four step procedure (synthesis of NIRh took 3 steps, see chapter 4) with overall yields of 28% for NRPK and 40% for NRP (Scheme 6.1). The structures of NRP and NRPK were confirmed by  $^1\text{H}$  NMR and  $^{13}\text{C}$  NMR and mass spectrometry.





**Scheme 6.1** Synthesis of the sensors, NRPK ad NRP

### 6.3.2 Spectroscopic and Selectivity Studies

In this section, the selectivity and spectroscopic properties of the sensors NRP and NRPK were investigated individually.

#### Spectroscopic and Selectivity Studies for NRPK

UV-vis spectra of NRPK with various metal ions were collected in ACN/Tris-HCl buffer (10 mM, pH 7.2, v/v 3:1). NRPK is a colorless compound showing very weak absorption in the 450-800 nm regions. When  $\text{Fe}^{3+}$  was added into the colorless solution of NRPK in ACN/Tris-HCl buffer (10 mM, pH 7.2, v/v 3:1), a strong absorption appeared with a maximum absorption wavelength at 715 nm (coefficient  $\epsilon = 2.32 \times 10^4 \text{ cm}^{-1} \text{ M}^{-1}$ ) with a color changed to green (Figure 6.1c). In contrast, other metal ions such as  $\text{Ni}^{2+}$ ,  $\text{Cu}^{2+}$ ,  $\text{Mn}^{2+}$ ,  $\text{Hg}^{2+}$ ,  $\text{Na}^+$ ,  $\text{Ca}^{2+}$ ,  $\text{Zn}^{2+}$ ,  $\text{Ag}^+$ ,  $\text{Mg}^{2+}$ ,  $\text{Pb}^{2+}$ ,  $\text{K}^+$ ,  $\text{Fe}^{2+}$  (prepared in 0.01 M HCl),  $\text{Co}^{2+}$ , and  $\text{Cr}^{3+}$  give little response to NRPK (Figure 6.1a). Only  $\text{Pb}^{2+}$  and  $\text{Cd}^{2+}$  showed minor response to NRPK.

The changes in fluorescence spectra of NRPK with the addition of different metal ions in ACN/Tris-HCl buffer (10 mM, pH 7.2, v/v 3:1) are shown in Figure 6.1b. NRPK shows very weak fluorescence in the 600-850 nm range in the absence of metal ions. When  $\text{Fe}^{3+}$  was added into the solution of NRPK, a large fluorescence enhancement at 750 nm was observed ( $\Phi_{\text{NRPK} + \text{Fe(III)}} = 0.189$ ), which attributed to the spirolactam ring opening, induced by the complexation of  $\text{Fe}^{3+}$ . The emission intensity enhancement at 750 nm is greater than 13-fold with 1.0 equiv of  $\text{Fe}^{3+}$ , which was red-shifted about 7 nm compared with that of NRPK, suggesting that NRPK is a great turn-on fluorescent sensor for  $\text{Fe}^{3+}$ . In contrast to  $\text{Fe}^{3+}$ , other metal ions such as  $\text{Zn}^{2+}$ ,  $\text{Cr}^{3+}$ ,  $\text{Ni}^{2+}$ ,  $\text{Hg}^{2+}$ ,  $\text{Fe}^{2+}$ ,  $\text{Mn}^{2+}$ ,  $\text{Ag}^+$ ,  $\text{Pb}^{2+}$ ,  $\text{Cu}^+$ ,  $\text{Cu}^{2+}$ ,  $\text{Co}^{2+}$ ,  $\text{Na}^+$ ,  $\text{K}^+$ ,  $\text{Mg}^{2+}$ , and  $\text{Ca}^{2+}$  did not induce any spectral response under identical conditions. Similar as that observed by UV-vis, only  $\text{Pb}^{2+}$  and  $\text{Cd}^{2+}$  showed a minor enhancement in fluorescence under these conditions.

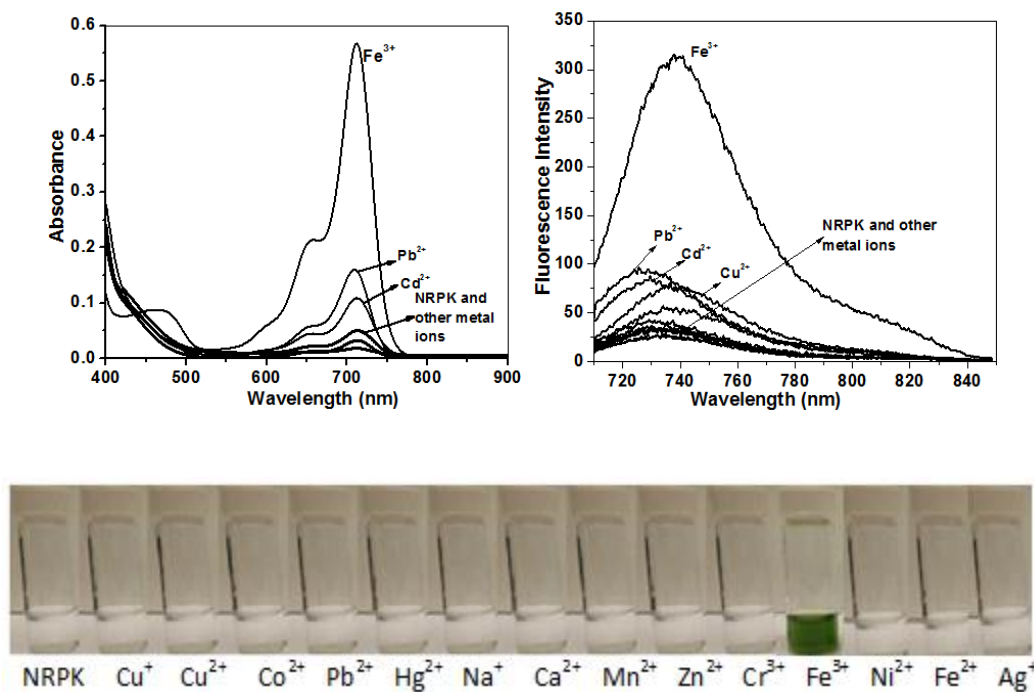


**Figure 6.1** (a) Absorption responses and (b) Fluorescence response and (c) Color changes of 25  $\mu\text{M}$  NRPK with various metal ions (25  $\mu\text{M}$  for  $\text{Zn}^{2+}$ ,  $\text{Cr}^{3+}$ ,  $\text{Ni}^{2+}$ ,  $\text{Hg}^{2+}$ ,  $\text{Fe}^{3+}$ ,  $\text{Mn}^{2+}$ ,  $\text{Ag}^+$ ,  $\text{Pb}^{2+}$ ,  $\text{Fe}^{2+}$ ,  $\text{Cu}^+$ ,  $\text{Cu}^{2+}$ , and  $\text{Co}^{2+}$ ; 100  $\mu\text{M}$  for  $\text{Na}^+$  and  $\text{Ca}^{2+}$ ) in ACN/Tris-HCl buffer (10 mM, pH 7.2, v/v 3:1)

In cells, there is a number of other metal cations that may potentially interfere with the sensor's response.<sup>[14]</sup> Also, these cations may affect the fluorescent intensity of the sensors' response to  $\text{Fe}^{3+}$ . For example,  $\text{Cu(II)}$  is a paramagnetic element that may cause an intensity decreasing (quenching). We examined the interferences from a few other metal ions with NRPK in their responses to  $\text{Fe}^{3+}$ . Figure 6.2 shows the result of interference studies on NRPK. The intensity of NRPK with  $\text{Fe}^{3+}$  was not changed by the addition of other metal ions in the solution. The presence of  $\text{Cu}^{2+}$  appears to quench the fluorescence slightly, presumably owing to the paramagnetic effect.

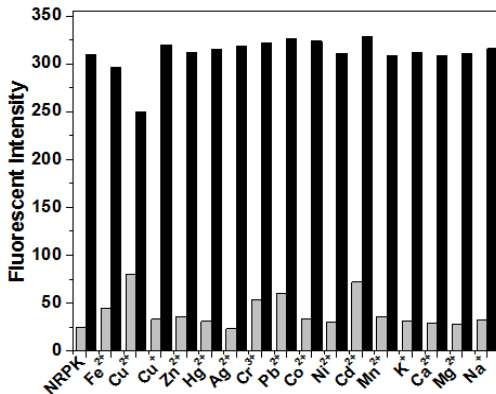


**Figure 6.2** Fluorescence responses of 25  $\mu\text{M}$  NRPK to the presence of various metal ions (gray bar) and the subsequent addition of  $\text{Fe}^{3+}$  (black bar) in the ACN/Tris buffer (10 mM, pH 7.3, v/v 3;1). The bars represent the fluorescence intensity at 740 nm.

The preliminary investigations indicated that the spirolactam ring of near infrared rhodamine based sensors is pH-dependent. Optical absorption and fluorescence emission for NRPK and NRPK- $\text{Fe}^{3+}$  complex are shown Figure 6.3 at pH 5-11. NRPK did not show any obvious and characteristic absorption and fluorescent (excited 690 nm) in the pH range (Figure 6.4a and 4b), suggesting that it can be studied in biological pH with a very low background fluorescence.

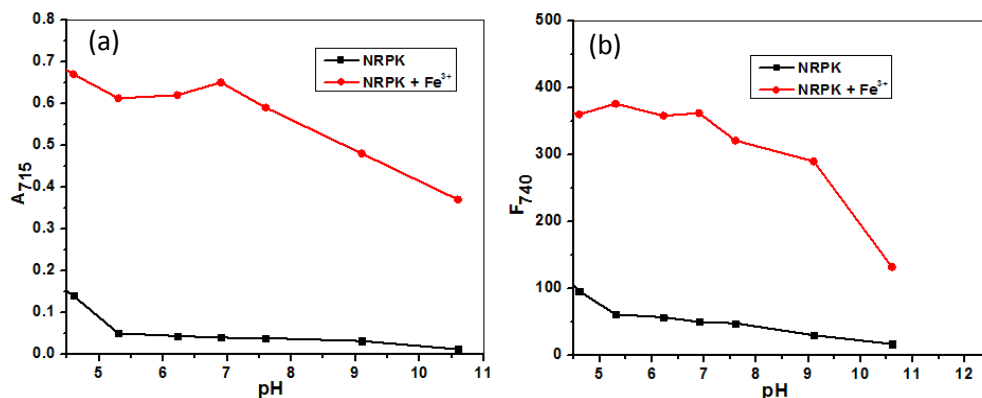


**Figure 6.3** (a) Variation of absorption (715 nm) of NRPK and NRPK + Fe<sup>3+</sup> (25  $\mu$ M each) at various pH values in ACN/H<sub>2</sub>O (3/1, v/v) solution (b) Variation of intensity (740 nm) of NRPK and NRPK + Fe<sup>3+</sup> (25  $\mu$ M each) at various pH values in ACN/H<sub>2</sub>O (3/1, v/v) solution. pH's were adjusted by adding HCl or NaOH.

### Spectroscopic and Selectivity Studies for NRP

Similar *in vitro* selective experiments were performed for the sensor, NRP. Figure 6.4a shows the absorption spectra of NRP and those in the presence of different metal ions such as Ni<sup>2+</sup>, Fe<sup>3+</sup>, Cu<sup>2+</sup>, Mn<sup>2+</sup>, Hg<sup>2+</sup>, Na<sup>+</sup>, Ca<sup>2+</sup>, Zn<sup>2+</sup>, Ag<sup>+</sup>, Mg<sup>2+</sup>, Pb<sup>2+</sup>, K<sup>+</sup>, Co<sup>2+</sup>, Cu<sup>+</sup> in ACN/Tris buffer (10 mM, pH=7.3, v/v 3:1). The free ligand scarcely shows absorption at 500-900 nm. After adding Fe<sup>3+</sup> into the solution of NRP, a strong absorption appeared at 714 nm with a color change (Figure 6.4c). The ligand also gave responses to Cr<sup>3+</sup>. However, the absorption intensity is little weaker for Cr<sup>3+</sup> ( $\epsilon = 5.6 \times 10^5 \text{ cm}^{-1} \text{ M}^{-1}$ ) compared to that for Fe<sup>3+</sup> ( $\epsilon = 8.0 \times 10^5 \text{ cm}^{-1} \text{ M}^{-1}$ ).

The changes in fluorescence responses of NRP with the addition of different metal ions (1 equiv) in ACN/Tris buffer (10 mM, pH=7.3, v/v 3: 1) are shown in Figure 6.4b. In the absence of metal ions, the ligand is almost non-fluorescent. However, addition of Fe<sup>3+</sup>, Cd<sup>2+</sup>, and Cr<sup>3+</sup> leads to an appearance of fluorescence at 745 nm. The fluorescence enhancements of Fe<sup>3+</sup>, Cd<sup>2+</sup>, and Cr<sup>3+</sup> are 10-fold, 7-fold, 13-fold, respectively, with a 10 nm red-shift for NRP-Fe<sup>3+</sup> and a 15 nm red-shift for NRP-Cr<sup>3+</sup> compared with that of NRP. Even though NRP give response to Cr<sup>3+</sup> and

$\text{Cd}^{2+}$ , it can be used as an  $\text{Fe}^{3+}$  selective sensor for cell application because the concentration of  $\text{Cr}^{3+}$  and  $\text{Cd}^{2+}$  in cells are usually very low.<sup>[15]</sup>

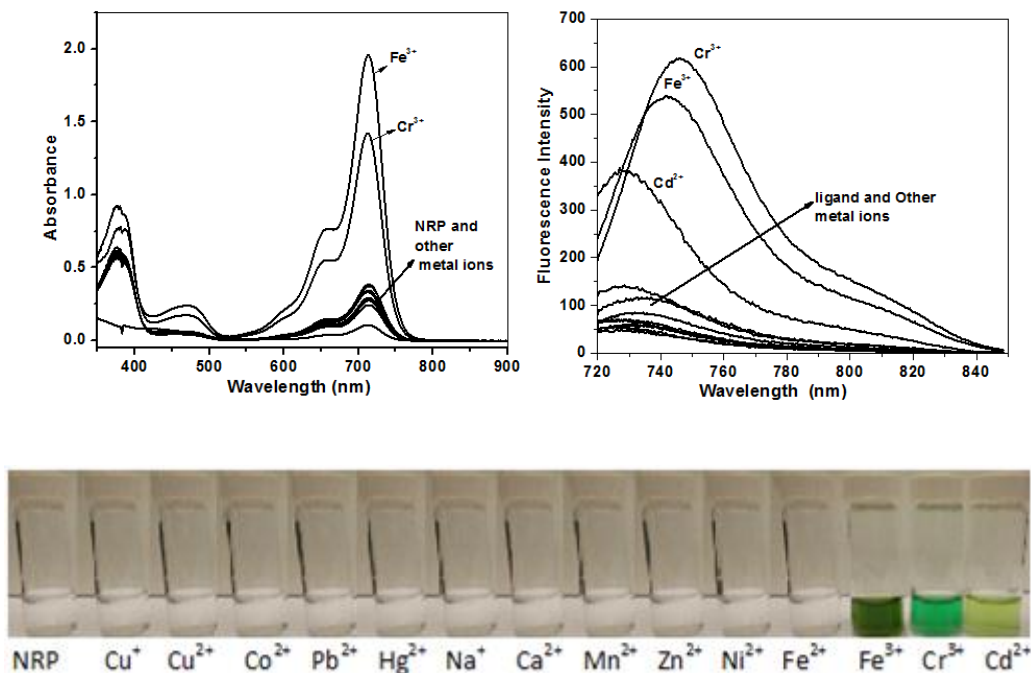


**Figure 6.4** (a) Absorption responses and (b) Fluorescence response and (c) Color changes of 25  $\mu\text{M}$  NRP with various metal ions (25  $\mu\text{M}$  for  $\text{Zn}^{2+}$ ,  $\text{Cr}^{3+}$ ,  $\text{Ni}^{2+}$ ,  $\text{Hg}^{2+}$ ,  $\text{Fe}^{3+}$ ,  $\text{Mn}^{2+}$ ,  $\text{Ag}^+$ ,  $\text{Pb}^{2+}$ ,  $\text{Fe}^{2+}$ ,  $\text{Cu}^+$ ,  $\text{Cu}^{2+}$ , and  $\text{Co}^{2+}$ ; 100  $\mu\text{M}$  for  $\text{Na}^+$  and  $\text{Ca}^{2+}$ ) in ACN/Tris buffer (10 mM, pH 7.3, v/v 3;1)

### 6.3.3 Binding Studies

In this section, the binding properties of the complexes  $\text{NRP-Fe}^{3+}$  and  $\text{NRPK-Fe}^{3+}$  were investigated together for a better understanding of the complexation between  $\text{NRPK}$  and  $\text{Fe}^{3+}$ . To investigate the binding mode of  $\text{NRPK}$  and  $\text{Fe}^{3+}$ , Job's plot and absorption titration were carried out. Typical UV-vis titration spectra for  $\text{NRPK}$  with  $\text{Fe}^{3+}$  in ACN/Tris-HCl buffer (10 mM, pH 7.32, v/v 2:1) were shown in Figure 6.5. With the addition of  $\text{Fe}^{3+}$ , the solution became green and an absorption band appeared at 715 nm and increased in intensity. The absorbance titration curve showed a typical sigmoidal curve; inflecting at 0.5 equiv of  $\text{Fe}^{3+}$  and saturation of the

absorbance was at  $\sim 0.5$  equiv of  $\text{Fe}^{3+}$ . The titration experiments indicated that a 2:1 complex was formed between NRPK and  $\text{Fe}^{3+}$ . The binding constant of this complex was calculated using absorption values at 715 nm by the equations described in the experimental section, and was determined to be  $5.11 \times 10^{11} \text{ M}^{-2}$ .

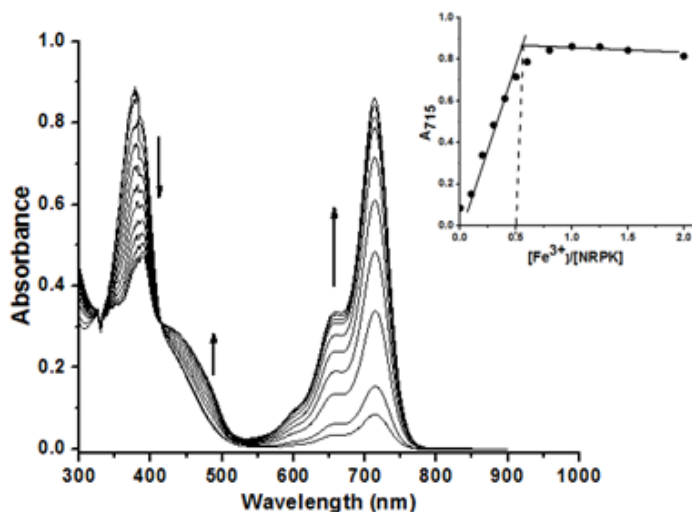


**Figure 6.5** Titration of 25  $\mu\text{M}$  NRPK with increasing concentrations of  $\text{FeCl}_3$  (2.5, 5, 7.5, 10, 12.5, 15, 20, 25, 31.25, 37.5, and 50  $\mu\text{M}$  respectively) in ACN/Tris-HCl buffer (10 mM, pH 7.2, v/v 3:1). Inset is a plot of absorbance at 715 nm versus the ratio of  $[\text{Fe}^{3+}]/[\text{sensor}]$ .

Job's method was also applied to study the binding stoichiometry of NRPK and  $\text{Fe}^{3+}$ . The Job's plot (Figure 6.6a) using a total concentration of 50  $\mu\text{M}$  NRPK and  $\text{Fe}^{3+}$  in ACN/Tris-HCl buffer (10 mM, pH 7.2, v/v 3:1) solution exhibited a maximum absorbance (at 715 nm) when the molecular fraction of  $\text{Fe}^{3+}$  and NRPK was close to 2:1, suggesting a 2:1 stoichiometry for the binding of NRPK and  $\text{Fe}^{3+}$ .

To be a good fluorescent sensor, the binding reversibility is an important requirement. The reversibility of the binding between NRPK and  $\text{Fe}^{3+}$  were tested in ACN/Tris buffer (10 mM, pH=7.3, v/v 3:1) in the presence of  $\text{Fe}^{3+}$  and EDTA (2.0 equiv.). The addition of EDTA (2.0 equiv.) to the solution of NRPK containing  $\text{Fe}^{3+}$  caused the disappearance of the absorption (Figure 6.6b)

at 715 nm as well as the fluorescence signals (data not shown) of NRPK-Fe<sup>3+</sup>, suggesting that the chelation process is reversible.

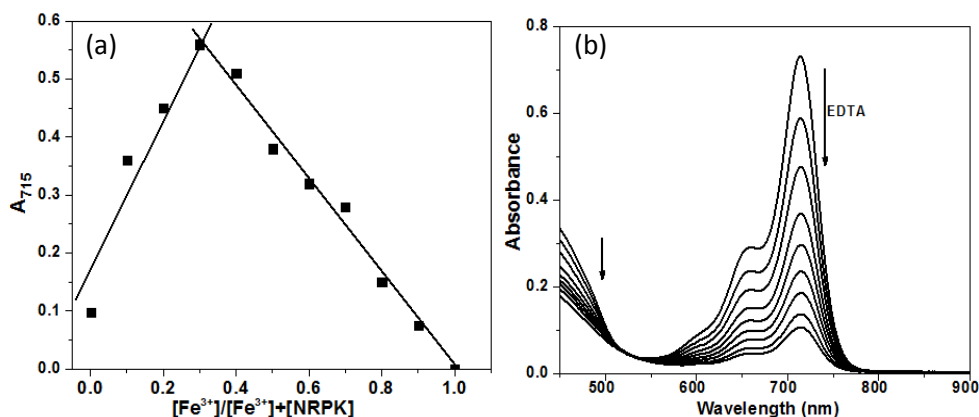


**Figure 6.6** (a) Job's plot: the total concentrations of NRPK and Fe<sup>3+</sup> were kept at constant 50 μM and the absorption intensity was measured at 715 nm in ACN/Tris-HCl buffer (10 mM, pH 7.2, v/v 3:1). (b) Treatment of 25 μM NRPK-Fe<sup>3+</sup> complex with increasing concentration of EDTA (0 to 50 μM, from top to bottom) in ACN/Tris-HCl buffer (10 mM, pH 7.2, v/v 3:1).

NRPK was originally designed to coordinate Fe<sup>3+</sup> in 1:1 binding ratio with its “ONNO” tetradentate-binding motif; however, the above results suggest that NRPK binds to Fe<sup>3+</sup> in 2:1 ratio. For a better understanding for the binding between NRPK and Fe<sup>3+</sup>, it was decided to investigate the binding properties of Fe<sup>3+</sup> and NRP which contains an “ONN” tridentate binding motif. Job's method and UV-vis titration were applied to study the binding stoichiometry between NRP and Fe<sup>3+</sup> in ACN/Tris-HCl buffer (10 mM, pH 7.2, v/v 3:1). With the addition of Fe<sup>3+</sup>, the solution became green and an absorption band appeared at 714 nm and increased in intensity. Figure 6.7a displays a plot of NRP versus Fe<sup>3+</sup> concentration. The titration curve increased linearly and plateaued at 2:1 ratio of the sensor and Fe<sup>3+</sup> (Figure 6.7b), suggesting the formation of a 2:1 Fe<sup>3+</sup>-NRP complex. The binding constant of this complex was calculated using absorption values at 714 nm by the equations described in the experimental section, and was determined to be  $2.16 \times 10^{12} \text{ M}^{-2}$ .

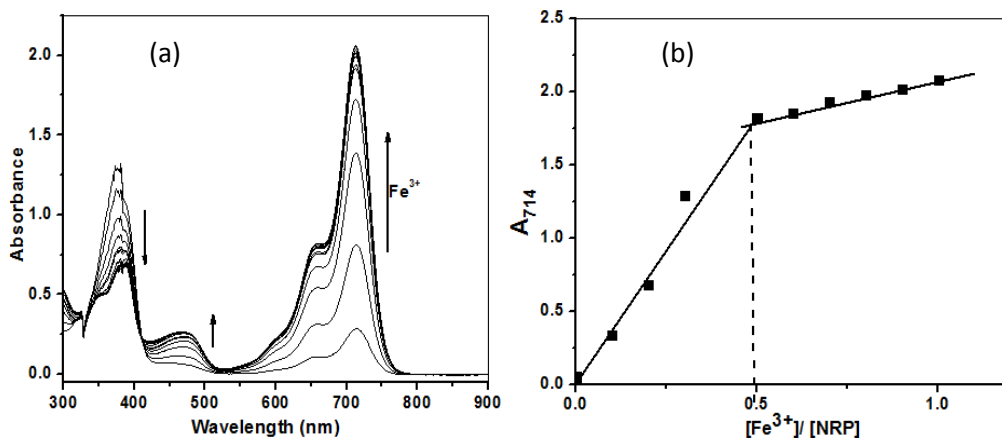


**Figure 6.7** (a) Titration of 25  $\mu\text{M}$  NRP with increasing concentrations of  $\text{FeCl}_3$  (2.5, 5, 7.5, 10, 12.5, 15, 20, 25, 31.25, 37.5, and 50  $\mu\text{M}$  respectively) in ACN/Tris-HCl buffer (10 mM, pH 7.2, v/v 3:1) (b) a plot of absorbance at 714 nm versus the ratio of  $[\text{Fe}^{3+}]/[\text{sensor}]$

Job's method was also applied to study the binding stoichiometry of NRP and  $\text{Fe}^{3+}$ . The Job's plot (Figure 6.8a) using a total concentration of 50  $\mu\text{M}$  NRP and  $\text{Fe}^{3+}$  in ACN/Tris-HCl buffer (10 mM, pH 7.2, v/v 3:1) solution exhibited a maximum absorbance (at 714 nm) when the molecular fraction of  $\text{Fe}^{3+}$  and NRP was close to 2:1, suggesting a 2:1 stoichiometry for the binding of NRP and  $\text{Fe}^{3+}$ . The reversibility of the recognition of NRP was performed by adding EDTA to the complex, NRP- $\text{Fe}^{3+}$ . Due to the strong affinity of EDTA for  $\text{Fe}^{3+}$  ions, a  $\text{Fe}^{3+}$ -EDTA complex was formed, resulting in a disassociation of the NRP-  $\text{Fe}^{3+}$  and consequently absorption decrease at 714 nm (Figure 6.8b). Thus, the complexation between NRP and  $\text{Fe}^{3+}$  is reversible.



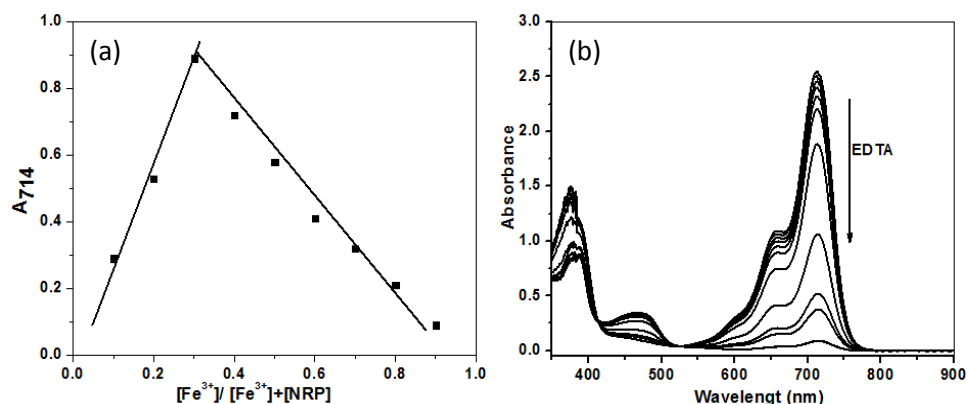
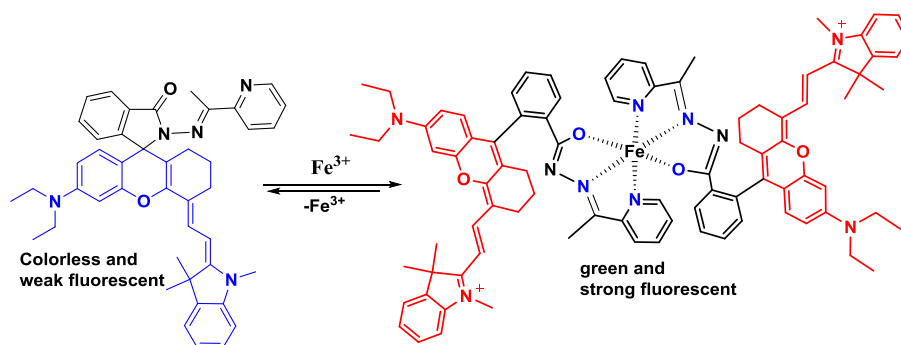
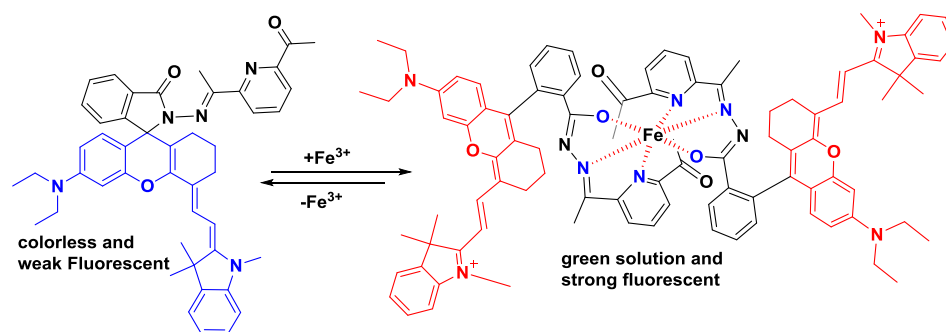


**Figure 6.8** (a) Job's plot: the total concentrations of NRP and  $\text{Fe}^{3+}$  were kept at constant  $50 \mu\text{M}$  and the absorption intensity was measured at  $714 \text{ nm}$  in ACN/Tris-HCl buffer ( $10 \text{ mM}$ ,  $\text{pH } 7.2$ ,  $v/v \text{ } 3:1$ ) (b) Treatment of  $25 \mu\text{M}$  NRP- $35 \mu\text{M}$   $\text{Fe}^{3+}$  complex with increasing concentration of EDTA ( $0$  to  $50 \mu\text{M}$  from top to bottom) in ACN/Tris-HCl buffer ( $10 \text{ mM}$ ,  $\text{pH } 7.2$ ,  $v/v \text{ } 3:1$ ).

From the above results, both NRP and NRPK show similar binding properties with  $\text{Fe}^{3+}$ , with the formation of  $\text{NRP}_2\text{-Fe}^{3+}$  and  $\text{NRPK}_2\text{-Fe}^{3+}$  complexes in a 2:1 binding mode. The spectroscopic changes and binding constants for the two complexes are also very similar. As it can be concluded that NRP coordinates  $\text{Fe}^{3+}$  with O/N/N, so NRPK probably used O/N/N, not O/N/N/O, to bind to  $\text{Fe}^{3+}$ . The carbonyl group linked to pyridine ring is not involved in  $\text{Fe}^{3+}$  binding. The proposed 2:1 reversible binding modes of  $\text{NRP-Fe}^{3+}$  and  $\text{NRPK-Fe}^{3+}$  are shown in Scheme 6.2 and Scheme 6.3, respectively.



**Scheme 6.2** Proposed 2:1 binding mode of NRP with  $\text{Fe}^{3+}$  in ACN/Tris-HCl buffer ( $10 \text{ mM}$ ,  $\text{pH } 7.3$ ,  $v/v \text{ } 3:1$ )



**Scheme 6.3** Proposed 2:1 binding mode of NRPK with  $\text{Fe}^{3+}$  in ACN/Tris-HCl buffer (10 mM, pH 7.3, v/v 3:1).

#### 6.3.4 Cell Studies

The *in vitro* data above strongly encourage us to test the usefulness of the sensor NRPK in detecting  $\text{Fe}(\text{III})$  ions in living cells. The ability of NRPK to detect  $\text{Fe}^{3+}$  in live bovine aortic endothelial cells (BAEC) was investigated by using confocal microscopy. BAEC cells were incubated with 10  $\mu\text{M}$  of ferric chloride ( $\text{FeCl}_3$ ) at 37° C for overnight followed by washing with EMEM medium to remove excess  $\text{Fe}^{3+}$ . Then 10  $\mu\text{M}$  of NRPK was added to BAEC cells and was incubated at 37° C for 30 min. The  $\text{Fe}^{3+}$ -treated BAEC cells showed significant increase in fluorescent signal (Figure 6.9c) compared to that without  $\text{Fe}^{3+}$  supplementation (Figure 6.9b), suggesting a positive response of NRPK to increased labile  $\text{Fe}^{3+}$  in  $\text{Fe}^{3+}$ -treated cells. To test the response to iron depleting, chelation experiment was performed. Salicylaldehyde isonicotinoyl hydrazone (SIH) which is known to be an  $\text{Fe}^{3+}$ -chelator was used to depleting  $\text{Fe}^{3+}$  from the cells.<sup>[16]</sup> BAEC cells treated with 100  $\mu\text{M}$  of SIH showed small decrease in fluorescence signal which is lower than that of signals of NRPA-treated cells (Figure 6.9e), suggesting NRPK can detect the decrease in  $\text{Fe}^{3+}$  levels as well as basal level of labile  $\text{Fe}^{3+}$  in BAEC cells. The BAEC cells treated with 20  $\mu\text{M}$  of  $\text{Fe}^{3+}$  overnight first followed by washing with EMEM medium and then

treated with 100  $\mu\text{M}$  of SIH and subsequent addition of 10  $\mu\text{M}$  of NRPK showed large decrease in fluorescence signal (Figure 6.9d) compare to that of cells with Fe(III) supplement and is almost same level as that of the signal of cells without Fe<sup>3+</sup> and SIH, clearly indicates that NRPK has the ability to detect endogenous level of labile Fe<sup>3+</sup> as well as the dynamic changes in Fe<sup>3+</sup> in BAEC cells.

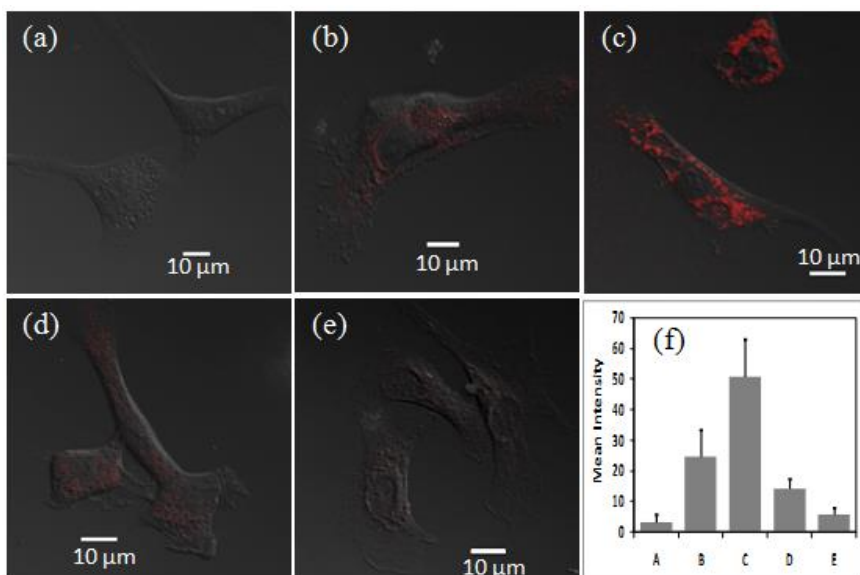


**Figure 6.9** Confocal microscopy images (with DIC) of BAEC treated with (a) cell only (b) the sensor after 30 min incubation (c) the cells were then incubated with 10  $\mu\text{M}$  Fe<sup>3+</sup> for 30 min then the sensor was added. (d) the cells were then incubated with 10  $\mu\text{M}$  Fe<sup>3+</sup> for 30 min then the sensor was added the SIH for overnight (e) the cells were incubated with SIH (Fe<sup>3+</sup>-chelator) (100  $\mu\text{M}$ ) overnight then sensor was added. (f) Bar chart of the mean intensity of (a), (b), (c), (d) and (e) Fluorescence intensity was collected at 680-750 nm (Excited at 633 nm).

The discrete fluorescent signals detected by NRPK in BAEC cells suggest that labile Fe<sup>3+</sup> ions are located in certain subcellular compartments in the cells. BAEC cells (without Fe<sup>3+</sup> treatment) were treated with NRPK, MitoTracker Green FM, and LysoTracker blue DND-22. As illustrated in Figure 6.10, there are partial colocalization between NRPK-Fe<sup>3+</sup> and the MitoTracker (Figure 6.10e) as well as that between NRPK-Fe<sup>3+</sup> and the LysoTracker (Figure

6.10f); however, a complete colocalization was observed among NRPK-Fe<sup>3+</sup>, MitoTracker and LysoTracker (Figure 6.10g). These data suggest that the exchangeable Fe<sup>3+</sup> pools in BAEC cells detectable by NRPK are localized in mitochondria and endosomes/lysosomes, not in cytosol. Additional experiments with NRPK and the trackers under Fe<sup>3+</sup> supplement conditions revealed again elevated levels of cellular chelatable Fe<sup>3+</sup> and that the labile Fe<sup>3+</sup> pools are still localized in mitochondria and endosomes/lysosomes (Figure 6.11).

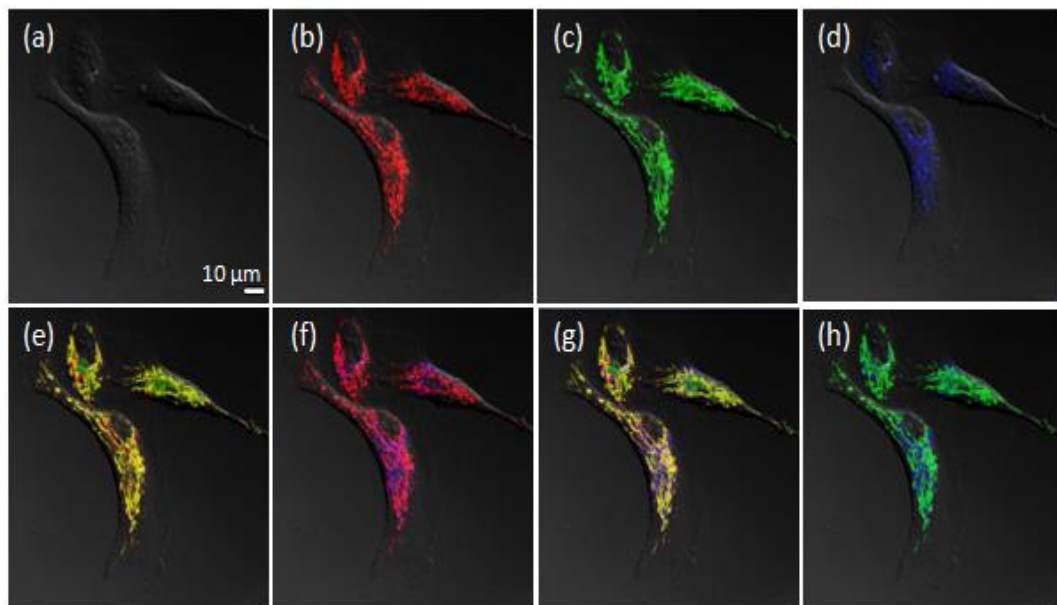


**Figure 6.10** Representative confocal images of intracellular colocalization studies of 10  $\mu\text{M}$  NRPK incubated with live BAEC cells co-labeled with MitoTracker Green (100 nM) and LysoTracker Blue DND-22 (50 nM) (a) DIC image of cells with 10  $\mu\text{m}$  scale bar (b) NRPK-Fe<sup>3+</sup> fluorescence collected at 680-750 nm (red) (c) MitoTracker fluorescence collected at 492-548 nm (green) (d) LysoTracker fluorescence collected at 409-484 nm (blue) (e) DIC image of (a) and fluorescence images of (b) and (c) were merged together. Colocalization regions are in yellow and non-overlapping regions remain in red (f) DIC image of (a) and fluorescence images of (b) and (d) were merged together. Overlapping regions are in purple and non-overlapping regions remain in red (g) Images of (a), (b), (c) and (d) were merged together, revealing that the NRPK-Fe<sup>3+</sup> images are 100% colocalized with the sum of those of MitoTracker and LysoTracker (h) Images of (a), (c) and (d) were merged together, showing no overlapping region between lysosomes and mitochondria.

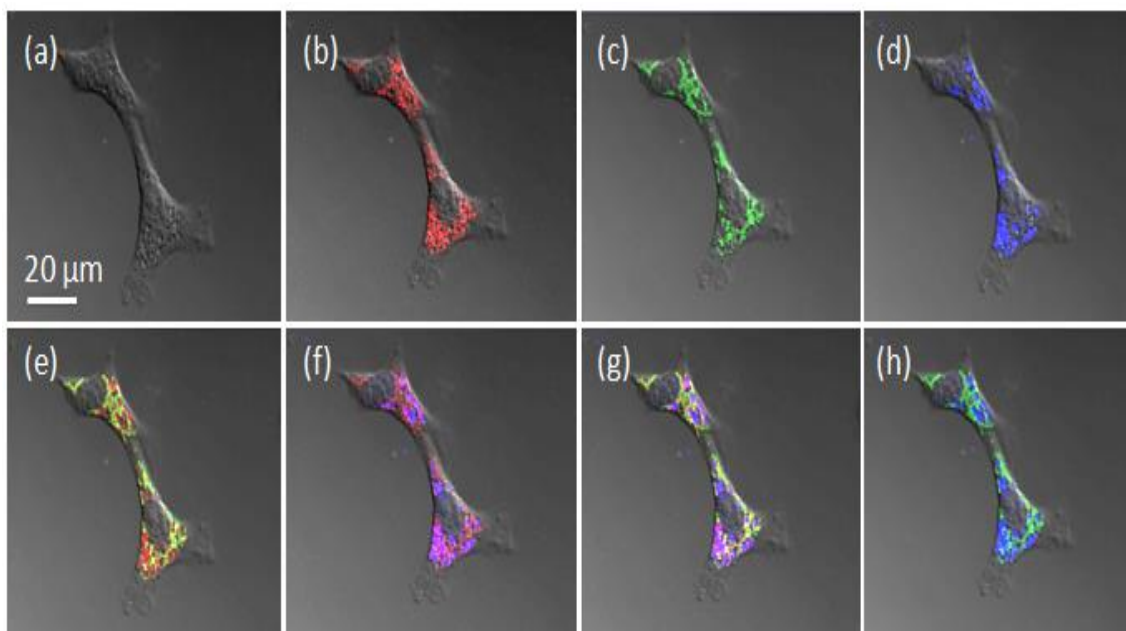


**Figure 6.11** Representative confocal microscopy images of intracellular colocalization studies of 10  $\mu\text{M}$  NRPK incubated with  $\text{Fe}^{3+}$ -loaded BAEC cells (pre-implemented with 10  $\mu\text{M}$   $\text{Fe}^{3+}$ ) co-labeled with MitoTracker Green FM (100 nM, incubated for 30 min) and LysoTracker Blue DND-22 (50 nM, incubated for 120 min) (a) DIC image of cells with 20  $\mu\text{m}$  scale bar (b) NRPK- $\text{Fe}^{3+}$  fluorescence collected at 680-750 nm (red) (c) MitoTracker fluorescence collected at 492-548 nm (green) (d) LysoTracker fluorescence collected at 409-484 nm (blue) (e) DIC image of (a) and fluorescence images of (b) and (c) were merged together. Colocalization regions are in yellow and non-overlapping regions remain in red (f) DIC image of (a) and fluorescence images of (b) and (d) were merged together. Overlapping regions are in purple and non-overlapping regions remain in red. (g) Images of (a), (b), (c) and (d) were merged together, revealing that the NRPK- $\text{Fe}^{3+}$  images are 100% colocalized with the sum of those of MitoTracker and LysoTracker. (h) Images of (a), (c) and (d) were merged together, showing no overlapping region between lysosomes and mitochondria.

In the previous chapters, we tested the ability of the sensors RPE, NIRh-Ac, and NRPA to detect  $\text{Fe}^{3+}$  in Human SH-SY5Y neuroblastoma cells. The results showed that chelatable iron pools in Human SH-SY5Y neuroblastoma cells are in mitochondria and lysosome. We decided to apply the sensor NRPK into SH-SY5Y cells and compare to the results with BAEC cells. SH-SY5Y cells (with  $\text{Fe}^{3+}$  treatment) were treated with NRPK, MitoTracker Green FM, and LysoTracker blue DND-22. As illustrated in Figure 6.12, there are partial colocalization between NRPK- $\text{Fe}^{3+}$

and the MitoTracker (Figure 6.12e) as well as that between NRPK-Fe<sup>3+</sup> and the LysoTracker (Figure 6.12f); however, a complete colocalization was observed among NRPK-Fe<sup>3+</sup>, MitoTracker and LysoTracker (Figure 6.12g). These data suggest that the exchangeable Fe<sup>3+</sup> pools in SH-SY5Y cells detectable by NRPK are localized in mitochondria and endosomes/lysosomes, not in cytosol.

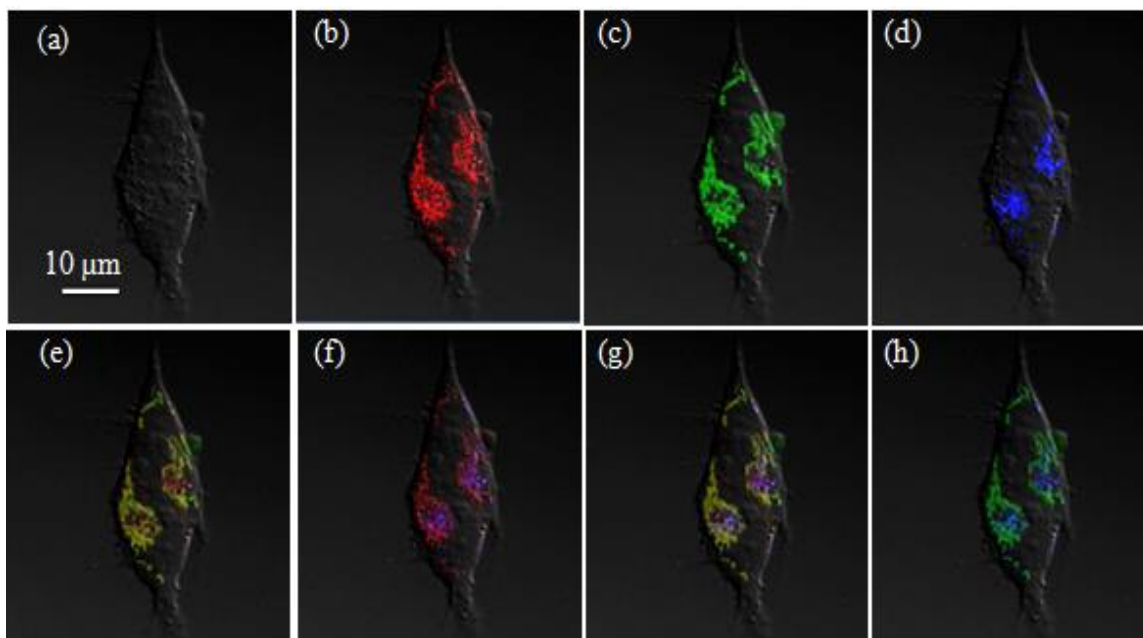


**Figure 6.12** Representative confocal microscopy images of intracellular colocalization studies of 10  $\mu\text{M}$  NRPK incubated with Fe<sup>3+</sup>-loaded human SH-SY5Y cells (pre-implemented with 10  $\mu\text{M}$  Fe<sup>3+</sup>) co-labeled with MitoTracker Green FM (100 nM, incubated for 30 min) and LysoTracker Blue DND-22 (50 nM, incubated for 120 min)(a) DIC image of cells with 10  $\mu\text{m}$  scale bar (b) NRPK-Fe<sup>3+</sup> fluorescence collected at 680-750 nm (red) (c) MitoTracker fluorescence collected at 492-548 nm (green) (d) LysoTracker fluorescence collected at 409-484 nm (blue) (e) DIC image of (a) and fluorescence images of (b) and (c) were merged together. Colocalization regions are in yellow and non-overlapping regions remain in red. (f) DIC image of (a) and fluorescence images of (b) and (d) were merged together. Overlapping regions are in purple and non-overlapping regions remain in red. (g) Images of (a), (b), (c) and (d) were merged together, revealing that NRPK-Fe<sup>3+</sup> images are 100% colocalized with the sum of those of MitoTracker and LysoTracker. (h) Images of (a), (c) and (d) were merged together, showing no overlapping region between lysosomes and mitochondria.

### 6.3.5 Zebrafish Studies

We explored further whether NRPK could be used to monitor exchangeable free  $\text{Fe}^{3+}$  ions in zebrafish. The preliminary *in vivo*  $\text{Fe}^{3+}$  imaging of intact 2-days-old zebrafish larva with NRPK staining was performed using confocal microscopy. We observed turn on fluorescence which is likely being triggered by endogenous labile  $\text{Fe}^{3+}$  for 2-days-old zebrafish. To confirm this, two control experiments were performed to verify that this turn-on fluorescence is caused by the coordination of  $\text{Fe}^{3+}$  with NRPK. First, loading zebrafish with  $\text{Fe}^{3+}$  and second, depletion of  $\text{Fe}^{3+}$  by cell permeable  $\text{Fe}^{3+}$ -chelator SIH. However, the chelator SIH was toxic to zebrafish, and killed them even when it was incubated for 1 h. We then decided to use different concentrations of  $\text{Fe}^{3+}$  to show that when iron concentration increases, turn-on fluorescence increases.

Figure 6.13 show some confocal images for 3- and 6-days-old zebrafish. The images in the first row belong to 3-day-old zebrafish. 3-days-old zebrafish itself did not show any fluorescence when it was excited at 633 nm under confocal microscopy. When it was incubated with NRPK, a red colored region was observed. When 2-days-old zebrafish were pre-incubated with  $\text{FeCl}_3$  (10 and 40  $\mu\text{M}$ ) for 24 hours then incubated with 10  $\mu\text{M}$  NRPK for another 0.5 hour, the  $\text{Fe}^{3+}$ -loaded zebrafish clearly showed brighter (3 fold for 10  $\mu\text{M}$  and 10 fold for 40  $\mu\text{M}$   $\text{Fe}^{3+}$ ) fluorescent images, suggesting a positive response of NRPK to elevated labile  $\text{Fe}^{3+}$  levels in the  $\text{Fe}^{3+}$ -loaded zebrafish. However, organs in zebrafish do not develop at this stage<sup>[18-19]</sup> (3-days-old). The red colored region is likely to be the intestine area.

We repeated the same experiments for 6-days-old zebrafish and observed similar concentration-dependent response as those for 3-days-old zebrafish but the red-colored region

observed in 3-day zebrafish became a smaller and a well-colocalized red dot that lies in the liver/gall bladder region<sup>[18-19]</sup> was observed in 6-days-old zebrafish.

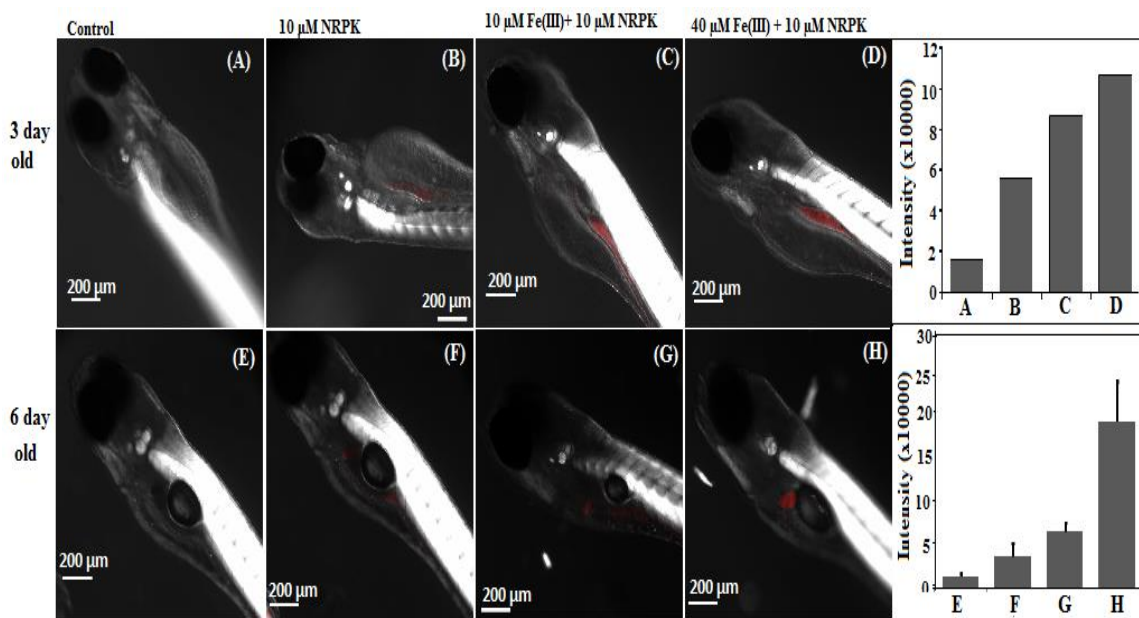


**Figure 6.13** Confocal microscopy images of 3 and 6 day old zebrafish larvae (a,e) Zebrafish only (b,f) Zebrafish larva was incubated with 10 μM NRPK for 30 min (c,g) Zebrafish larva incubated with 10 μM and (d,h) incubated with 40 μM FeCl<sub>3</sub> for 3 days then 10 μM NRPK was added and incubated for 30 min.

## 6.4 Conclusions

In summary, highly sensitive, highly selective, and reversible turn-on near infrared fluorescent Fe<sup>3+</sup>-sensors, NRPK and NRP have been developed. The initial goal was to synthesize Fe(II)-selective fluorescence sensor; however, NRPK turned out to be a sensor for Fe(III). Both NRP and NRPK coordinate with Fe<sup>3+</sup> with O/N/N binding motif with 2:1 ratio. The NRPK appears not using the carbonyl group linked to the pyridine ring for coordination. Cell imaging experiments with NRPK showed that it could readily detect endogenous free Fe<sup>3+</sup> in live bovine aortic endothelial cells (BAEC) and human SH-SY5Y cells at subcellular resolution, with free



iron(III) ions located in mitochondria and endosomes/lysosomes for both BAEC and SH-SY5 cells.

Finally, NRPK demonstrated the ability to detect exchangeable free iron(III) in zebrafish *in vivo*.

## 6.5 References

1. Lippard S. J., J. M. Berg, Principles of Bioinorganic Chemistry, University Science Books, Mill Valley, CA, **1994**
2. Domaille D. W., Que E. L., Chang C. J., Nat. Chem. Biol., **2008**, 4, 168-175
3. Aisen P., Wessling-Resnick M., Leibold E. A., Curr. Opin. Chem. Biol., **1999**, 3, 200-206
4. Halliwell B., J. M. C. Gutteridge, FEBS Lett., **1992**, 307,108-112
5. Xu J., Jia Z., Knutson M. D., Leeuwenburgh C., Int. J. Mol.Sci., **2012**, 13, 2368-2386
6. Crichton R., Ed. Inorganic biochemistry of iron metabolism, 2nd ed.; John Wiley & Sons Ltd.: U.K., **2001**, pp. 1-10
7. Breuer W., Shvartsman M., Cabantchik, Z. I., Int. J. Biochem.Cell Biol., **2008**, 40 , 350-354
8. Petrat F.I., de Groot H., Rauen U., Biochem. J., **2001**, 356, 61-69
9. Richardson D. R., Lane D. J. R., Becker E. M., Huang M. L.H., Whitnall M., Rahmanto Y. S., Sheftel A. D., Ponka P., Proc. Natl. Acad. Sci. U.S.A., **2010**, 107 , 10775-10782
10. Perez C. A., Wei Y., Guo M., J. Inorg. Biochem., **2009**, 103, 326-322
11. Santra M., Ryu D., Chatterjee A., Ko S. K., Shin I., Ahn K. H., Chem. Commun., **2009**, 2115-2117
12. Pearson R. G., J. Am. Chem. Soc., **1963**, 85, 3533-3539
13. Hou G. G., Wang C. H., Sun J. F., Yang M. Z., Lin D., Li H.J., Biochem. Biophys. Res. Commun., **2013**, 439, 459-463
14. Domaille D. W., Que E. L., Chang C. J., Nat. Chem. Biol. **2008**, 4, 168-175
15. Bertini I., Gray H. B., Stiefel E. I., Valentine J. S., Biological Inorganic Chemistry; Structure and Reactivity, Sausalite, California, **2007**, pp. 60-61
16. Wei Y., Guo M., Angew. Chem. Int. Ed., **2007**, 46, 4722-4725
17. Kim H.N., Lee M.H., Kim H.J., Kim J. S., Chem. Soc. Rev., **2008**, 37, 1465-1472
18. Wallace K. N., Pack M., Dev. Biol., **2003**, 255, 12-29
19. Ko S.K., Chen X., Yoon J., Shin I., Chem. Soc. Rev., **2011**, 40, 2120-2130

## CHAPTER 7

### DEVELOPING RATIO METRIC SENSORS FOR DETERMINATION OF IRON(III) CONCENTRATION IN LIVING SYSTEMS

#### 7.1 Introduction

Intracellular iron homeostasis is strictly regulated in cells. Cellular iron homeostasis is a well-coordinated process consisting of iron uptake, intracellular transport, utilisation, and storage.<sup>[1-4]</sup> A transit exchangeable “labile iron pool (LIP)” has been proposed to play a central role in this process.<sup>[1-4]</sup> This loosely bound iron in cells can potentially participate in redox-cycling and damage lipids and other biomolecules.<sup>[5-7]</sup> Determination of this labile iron in living systems may contribute to the understanding of the cell biology of iron under physiological and pathological conditions. There are mainly two questions concerning the LIP, (1) where is it located in cells? (2) What is the concentration of iron in the LIP?<sup>[8]</sup> In previous chapters, we focused on answering the question #1. Our results show that free  $\text{Fe}^{3+}$  ions are located in mitochondria and endosomes/lysosomes of live bovine aortic endothelial cells (BAEC) and live human SH-SY5Y neuroblastoma cells, but in only mitochondria of human fibroblast ws1 cells. Even though we showed where free  $\text{Fe}^{3+}$  ions are located in the cells, still one question is remaining. "Are we sure that the images observed reflect the true locations of labile  $\text{Fe}^{3+}$ , not instead the locations of our sensors such as RPE, NIRh-Ac, NRPA, NRPK as the sensors themselves may preferentially localized in certain organelles of the cells. In this chapter, I will focus on addressing the second question, the determination of the concentration of  $\text{Fe}^{3+}$  in LIP by developing a novel ratio metric  $\text{Fe}^{3+}$  sensor. Moreover, the two bands absorption/fluorescence nature of the ratio metric sensor enables the tracing of the cellular distribution of the sensor itself, in addition to detecting  $\text{Fe}^{3+}$ , allowing the unambiguous determination of the subcellular distributions of the sensor and the labile  $\text{Fe}^{3+}$  pools.

Ratiometric sensors were first used by Tsien and coworkers in 1985 in context of calcium sensing.<sup>[9]</sup> Recently, ratiometric sensors have been used for determination of concentrations of a few other metal ions in cells.<sup>[10-12]</sup> If the fluorescence spectra shift upon binding metal ions, the ratio R of the fluorescence intensities at the two different emission or excitation wavelengths  $\lambda_1$  and  $\lambda_2$  is directly related to the free metal ion concentration, according to the following equation shown below.<sup>[11-12]</sup>

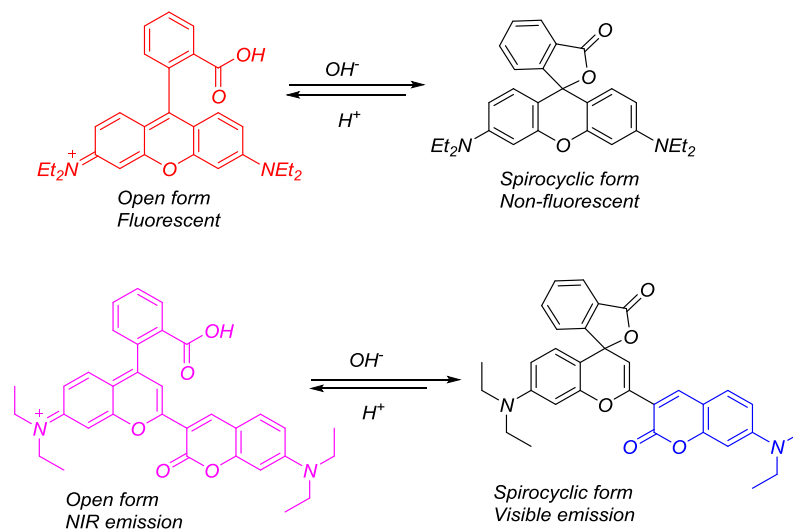
$$R = (R_{\min} K_d + R_{\max} [M^{n+}]) / (K_d + [M^{n+}]) \quad (1)$$

Where  $M^{n+}$  refers to metal ions,  $K_d$  is the dissociation constant for  $M^{n+}$ ,  $R_{\max}$  is the maximum fluorescence ratio at saturating  $M^{n+}$ , and  $R_{\min}$  is the fluorescence ratio in the absence of  $M^{n+}$ .

In chapter 3, the sensor IRPE was a ratiometric fluorescent sensor for  $Fe^{3+}$  ions; however, it was not able to detect  $Fe^{3+}$  ions in cells. Here, a spiro lactam-based sensor is developed as a ratiometric sensor for  $Fe^{3+}$  (Scheme 7.1). The compound 2-(7-diethylamino-2-oxo-2H-1-benzopyran-3-yl)-4-(2-carboxyphenyl)-7-diethylamino-1-benzopyrylium (called "CR" in this chapter) was synthesized in 1995 by Czerney *et al.* and it showed a near-infrared fluorescence.<sup>[13]</sup> Liu *et al.* showed that CR exhibits a near-infrared absorbance and fluorescence in neutral conditions but shows coumarin dye properties in basic solutions.<sup>[14]</sup> This was found to be due to the cyclization of C-4 atom at its benzopyrylium, decreasing the  $\pi$ -conjugation of the CR (Scheme 7.1). This is similar to the "on-off" fluorescence mechanism of rhodamine dyes. However, it is yellow and fluorescence in the spirocyclic form. It means that CR shows NIR emission in its spirocyclic ring-opened form while visible emission in the ring-closed form.

Recently, this mechanism has been used to develop  $Hg^{2+}$  and cysteine /homocysteine selective ratiometric fluorescent sensors.<sup>[14-15]</sup> As shown in Figure 7.1, the sensor 1 exhibits near infrared fluorescence. However, after binding to cysteine/homocysteine, the spiro lactam of the

sensor is closed and exhibits visible fluorescence. For the sensor 2, it is opposite. It is in spirocyclic-closed form. When it coordinates with  $\text{Hg}^{2+}$ , it exhibits a near infrared fluorescence. Both of them are ratiometric fluorescent sensors.



**Scheme 7.1** Equilibrium between the open form and spirocyclic form of rhodamine (a) and dye CR (b)

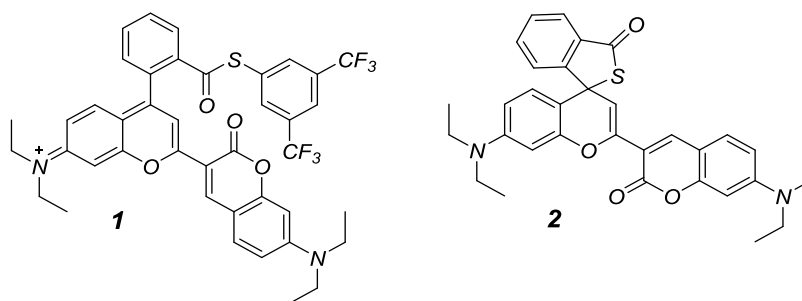


**Figure 7.1** Structure of the ratiometric CR-based fluorescent sensors (1) cysteine and homocysteine-selective and (2)  $\text{Hg}^{2+}$ -selective sensors

In this chapter, a highly selective and highly sensitive reversible ratiometric fluorescent  $\text{Fe}^{3+}$  sensor CR-PK (Scheme 7.2) is developed and its physicochemical properties described. With

this sensor, the concentration of free  $\text{Fe}^{3+}$  ions (endogenous) in live bovine aortic endothelial cells (BAEC) cells, human neuronal cells (SH-SY5H) and fibroblast cells (ws1) was determined.

## 7.2 Experimental

Unless otherwise stated, similar procedures described in the previous chapters were used.

### 7.2.1 Materials and Instruments

4-diethylamino-salicylaldehyde, ethyl acetoacetate, hydrazine monohydrate, and benzotriazol-1-yloxytris (dimethylamino)-phosphonium hexafluorophosphate (BOP) were purchased from TCI America. Piperidine was purchased from Aldrich. MitoTracker Green FM, LysoTracker Blue DND-99, and the nuclear stain Hoechst 33258 were purchased from Life Technologies and used in accordance with the manufacturer's protocols. The other chemicals and the solvents used in the experiments were purchased commercially.

$^1\text{H}$  and  $^{13}\text{C}$  NMR spectra were recorded on a Bruker AVANCE III HD 400 at ambient temperature (298K). Chemical shifts are reported in delta ( $\delta$ ) unit per million (ppm) downfield tetramethylsilane. Splitting patterns are abbreviated as follows: s, singlet; d, doublet; t, triplet; q, quartet; m, multiplet; br, broad. ESI-MS analyses were performed on a Perkin Elmer API 150 EX mass spectrometer. UV/Vis spectra were recorded on a Perkin Elmer Lambda 25 spectrometer at 298 K. Fluorescence spectra were recorded on a Perkin Elmer LS55 luminescence spectrometer at 293 K. The excitation wavelengths and filters used were indicated in the figures. The pH measurements were carried out on a Corning pH meter equipped with a Sigma-Aldrich micro combination electrode calibrated with standard buffer solution.

### 7.2.2 Synthesis of CR-PK

CR was synthesized according to the published methods,<sup>[13]</sup> and described briefly below.

**Synthesis of 3-acetyl-7-(diethylamino)-2H-chromen-2-one.** A solution of 4-diethylamino-salicylaldehyde (1.93 g, 10 mmol) and ethyl acetoacetate (1.95 g, 15 mmol) in EtOH (15 mL) was treated with piperidine (0.2 mL) and glacial acetic acid (2 drops) and refluxed for 6 h. The mixture was cooled to room temperature and the yellow crystalline solid was filtered. The product was pure enough to be used in the next procedure (yield, 75%). <sup>1</sup>H NMR (CDCl<sub>3</sub>, 400 MHz δ(ppm)): 8.46 (s, 1H), 7.45 (d, 1H), 6.68 (d, 1H), 6.50 (s, 1H), 3.52 (q, 4H), 2.67 (s, 3H), 1.26 (t, 6H); ESI-MS: found:  $m/z = 259.1$  [M+H]<sup>+</sup>, calcd for C<sub>15</sub>H<sub>17</sub>NO<sub>3</sub> = 259.3.

**Synthesis of 2-(7-diethylamino-2-oxo-2H-1-benzopyran-3-yl)-4-(2-carboxyphenyl)-7-diethylamino-1-benzopyrylium (CR).** 1 (0.939 g, 3 mmol) and 2 (0.777 g, 3 mmol) were dissolved in conc. H<sub>2</sub>SO<sub>4</sub> (15 mL) and stirred at 90 °C for 6 h. After cooling to room temperature, the solution was added into ice (30 g) then 70% perchloric acid (1.5 mL) was added, filtered, and washed with water to afford crude product. The crude product was purified by silica gel flash chromatography using CH<sub>2</sub>Cl<sub>2</sub>/CH<sub>3</sub>OH (50 : 1 to 20 : 1) as eluent to afford pure CR as a blue solid (yield 65%). <sup>1</sup>H NMR (CDCl<sub>3</sub>, 400 MHz δ(ppm)): 9.06 (s, 1H), 8.2 (d, 1H), 7.60-7.71 (m, 3H), 7.4 (d, 1H), 7.28 (d, 1H), 7.21 (d, 1H), 7.1 (d, 1H), 6.81 (d, 1H), 6.61 (s, 1H), 3.61 (q, 4H), 1.42 (t, 6H), 1.29 (t, 6H); ESI-MS: found:  $m/z = 537.1$  [M]<sup>+</sup>, calcd for C<sub>33</sub>H<sub>33</sub>N<sub>2</sub>O<sub>5</sub> = 537.24 (without ClO<sub>4</sub><sup>-</sup>)

**Synthesis of CR-NH<sub>2</sub>.** CR (0.50 g, 0.07 mmol, 1 equiv) and BOP (1.2 equiv) were dissolved in DCM and stirred at room temperature for 10 min. Then hydrazine monohydrate (0.195 g, 0.35 mmol, 5 equiv) was added. The mixture was stirred at room temperature for 5 h. The solvent was evaporated under reduced vacuum and the crude product was purified by alumina gel column using CH<sub>2</sub>Cl<sub>2</sub> to CH<sub>2</sub>Cl<sub>2</sub>/MeOH as eluent to obtain a yellow product (second yellow fraction from

the column) (0.130 g, yield 30%).  $^1\text{H}$  NMR ( $\text{CDCl}_3$ , 400 MHz  $\delta(\text{ppm})$ ): 8.43 (s 1H), 7.72 (s, 1H), 7.5-7.27 (m, 6H), 6.41-6.22 (m, 3H), 3.47 - 3.38 (q, 4H), 3.36 - 3.32 (q, 4H), 1.24-1.20 (t, 6H), 1.19 - 1.17 (t, 6H);  $^{13}\text{C}$  NMR ( $\text{CDCl}_3$ , 100 MHz  $\delta(\text{ppm})$ ): 165.89, 156.43, 156.15, 153.5, 151.3, 150.6, 148.8, 147.4, 139.6, 132.3, 129.9, 129.86, 128.4, 127.7, 124.03, 123.93, 111.7, 109.3, 108.2, 104.1, 1007.7, 99.8, 96.1, 64.53, 44.9, 44.33, 12.62, 12.46; ESI-MS: found:  $m/z = 551.1$   $[\text{M}+\text{H}]^+$ , calcd for  $\text{C}_{33}\text{H}_{34}\text{N}_4\text{O}_4 = 550.2$ .

**Synthesis of CR-PK.** CR-NH<sub>2</sub> (0.130 g, 0.2 mmol) and 2,6-diacetylpyridine (0.078 g, 0.4 mmol, 2 equiv) were dissolved in ethanol (15 ml). The reaction mixture was then stirred and refluxed for overnight. The solvent was evaporated under reduced vacuum and the crude product was purified by alumina gel column using  $\text{CH}_2\text{Cl}_2$  to  $\text{CH}_2\text{Cl}_2/\text{MeOH}$  as eluent to afford CR-PK as yellow solid. (0.065 g, yield 46%).  $^1\text{H}$  NMR ( $\text{CDCl}_3$ , 400 MHz  $\delta(\text{ppm})$ ): 8.43 (s 1H), 7.72 (s, 1H), 7.5-7.27 (m, 6H), 6.41-6.22 (m, 3H), 3.47 - 3.38 (q, 4H), 3.36 - 3.32 (q, 4H), 1.24-1.20 (t, 6H), 1.19 - 1.17 (t, 6H);  $^{13}\text{C}$  NMR ( $\text{CDCl}_3$ , 100 MHz  $\delta(\text{ppm})$ ): 196.4, 165.89, 156.43, 156.15, 153.5, 151.3, 150.6, 148.8, 147.4, 139.6, 132.3, 129.9, 129.86, 128.4, 127.7, 124.03, 123.93, 111.7, 109.3, 108.2, 104.1, 1007.7, 99.8, 96.1, 64.53, 44.9, 44.33, 34.3, 23.4 12.62, 12.46; ESI-MS: found:  $m/z = 696.1$   $[\text{M}+\text{H}]^+$ , calcd for  $\text{C}_{42}\text{H}_{41}\text{N}_5\text{O}_5 = 695.3$ .

### 7.2.3 Procedures for Metal Ion Sensing

The solution of metal ions were prepared from chloride salts of  $\text{Ni}^{2+}$ ,  $\text{Fe}^{3+}$ ,  $\text{Cu}^{2+}$ ,  $\text{Mn}^{2+}$ ,  $\text{Hg}^{2+}$ ,  $\text{Na}^+$ ,  $\text{Ca}^{2+}$ ,  $\text{Zn}^{2+}$ ,  $\text{Ag}^+$ , and nitrate salts of  $\text{Mg}^{2+}$ ,  $\text{Pb}^{2+}$ ,  $\text{K}^+$ ,  $\text{Co}^{2+}$  and ammonium sulfate salt of  $\text{Fe}^{2+}$ . Stock solutions of metal ions (10 mM) were prepared in deionized water, except for  $\text{Fe}^{3+}$  and  $\text{Fe}^{2+}$  in 0.1 M HCl. Solution of  $\text{Cu}^+$  was freshly prepared by dissolving tetrakis(acetonitrile) copper(I) (Sigma-Aldrich) into double-distilled water.

A stock solution of CR-PK (1 mM) was prepared in ethanol. The solution of CR-PK was diluted to 10  $\mu\text{M}$  with ethanol/HEPES buffer (10 mM, pH 7.4, v/v 1:4). Before spectroscopic measurements, solutions were freshly prepared by diluting the corresponding high-concentration stock solution. For each spectrum, 1 mL of a probe solution was added to a 1-cm quartz cell, to which different stock solutions of cations were gradually added by using a micropipette. All spectroscopic measurements were done under simulated physiological pH, and measurements were performed at least triplicate and resulting averages are reported.

#### 7.2.4 Quantum Yield

Stock solutions of 40  $\mu\text{M}$  CR-PK, 40  $\mu\text{M}$  rhodamine B (standard), and 40  $\mu\text{M}$  CR-PK+  $\text{Fe}^{3+}$  were prepared. Dilutions of CR-PK, rhodamine B, CR-PK+ $\text{Fe}^{3+}$  were prepared in EtOH at concentrations such that their absorbance at 425 nm for CR-PK, 650 nm for CR-PK+  $\text{Fe}^{3+}$  and 540 nm for rhodamine b, equaled 0.1, 0.2, 0.3, 0.4, and 0.5  $\mu\text{M}$ . Excitation was performed at 420, 510, and 633 nm, respectively, and collected emission was normalized to the EtOH blank and then integrated from 480-650, 560-750 and 680-850 nm for CR-PK, rhodamine b, and CR-PK+  $\text{Fe}^{3+}$  respectively. A plot of the integrated fluorescence intensity vs. the absorbance for each concentration was prepared and the positive slope of the linear fit was calculated. The data were compared to the rhodamine b standard using the following equation, where  $\Phi_R$  is the quantum yield of the standard (0.97), Grad is the slope of the absorbance vs. emission line found for each compound, GradR is the slope found for the rhodamine standard,  $\eta$  is the refractive index of the sample solutions (1.33) and  $\eta_R$  is the refractive index of the rhodamine solution (1.33):

$$\Phi = \Phi_R (\text{Grad}/\text{Grad}_R) \times (\eta^2/\eta_R^2)$$

$$\Phi_{\text{CR-PK}} = 0.582$$



$$\Phi_{\text{CR-PK} + \text{Fe(III)}} = 0.164$$

## 7.2 .5 Cell culture

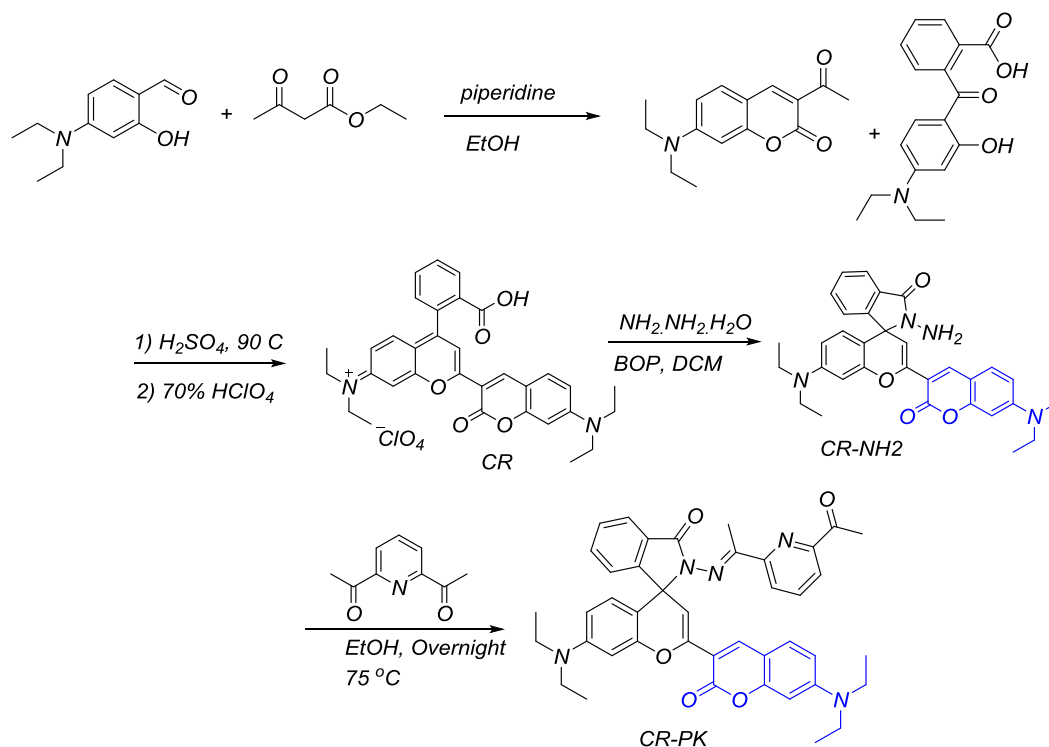
Bovine aortic endothelial cells (BAEC) were obtained from Dr. Keaney's research group (UMass Medical School). Primary cultured endothelial cells from bovine aorta were passaged in Endothelial Basal Medium (Lonza) containing 5% fetal bovine serum. Before the experiment, the cells were cultured to about 8<sup>th</sup> generation. For experiment preparation, the cells were routinely subcultured using 0.05% trypsin-EDTA solution. The cells were seeded on the 25 cm<sup>2</sup> flask and medium change every two days until a 70% confluency before transferring into dishes. The cells were seeded on the 1 cm<sup>2</sup> dish and a medium change the next day. After incubation for 4 hrs, different test materials were added to the medium. Fluorescence imaging was performed with a Zeiss LSM 710 laser scanning confocal microscope. Typically, three experiments were carried out: (1) the cells were incubated with CR-PK for 30 min; (2) cells were first incubated with a cell permeable iron source (Fe-citrate) then incubated with CR-PK and (3) cells were pre-incubated with an iron chelator (SIH) then incubated with CR-PK. Cell imaging was then carried out after changing cells media. Emission was collected at 460-540 nm for blue channel (excited at 458 nm) and 650-750 nm for red channel (excited at 633 nm).

## 7.3 Results and Discussion

### 7.3.1 Design and synthesis

One of the initial goals creating a ratiometric sensor was to trace the cellular distribution of my sensors and the true locations of free iron(III) ions in cells. Encouraged by the report by Lui *et al.*<sup>[14]</sup>, I modified CR for the purpose. First, CR was reacted with hydrazine monohydrate to obtain CR-NH<sub>2</sub>. This step requires BOP to be used to make an amide bond between carboxylic

acid of CR and hydrazine. CR-NH2 can then react with ketones or aldehydes to make the desired product. Second, I choose binding groups that were used in previous chapters to react with CR-NH2. Acetylacetate (used in chapter 4) was initially linked to CR-NH2, but a  $\text{Cu}^{2+}$ -selective ratiometric sensor was obtained (data not shown). Then, it was decided to use 2,6-diacetylpyridine to create a  $\text{Fe}^{3+}$  binding moiety. The sensor, CR-PK, was synthesized in a five-step procedure with overall yields of 46% (Scheme 7.2). The structure of CR-PK was confirmed by  $^1\text{H}$  NMR and  $^{13}\text{C}$  NMR and mass spectrometry.



**Scheme 7.2** Synthesis route for CR-PK

### 7.3.2 Spectroscopic and Selectivity Studies

The absorption spectra of CR-PK upon coordination with  $\text{Fe}^{3+}$  in EtOH/HEPES at pH 7.4 (1/4, v/v) were monitored first. As shown in Figure 7.2a, the solution of CR-PK alone ( $10.0 \mu\text{M}$ )

exhibits an absorption maximum at 425 nm, which is responsible for the yellow color of the solution. With increasing  $\text{Fe}^{3+}$  concentration, the absorbance at 425 nm ( $\epsilon = 3.9 \times 10^4 \text{ M}^{-1} \text{ cm}^{-1}$ , CR-PK only) decreased, while the absorbance at 647 nm ( $\epsilon = 8.3 \times 10^3 \text{ M}^{-1} \text{ cm}^{-1}$ , CR-PK and  $\text{Fe}^{3+}$  at 1:1 ratio) increased concomitantly. This pronounced red shift of the maximum absorption wavelength can be ascribed to the coordination of  $\text{Fe}^{3+}$ . Meanwhile, an isosbestic point was clearly observed around 454 nm, indicating the conversion of the free dye into the Fe(III)-complex is a clean reaction. In contrast, other metal ions such as  $\text{Ni}^{2+}$ ,  $\text{Cu}^{2+}$ ,  $\text{Mn}^{2+}$ ,  $\text{Hg}^{2+}$ ,  $\text{Na}^+$ ,  $\text{Ca}^{2+}$ ,  $\text{Zn}^{2+}$ ,  $\text{Ag}^+$ ,  $\text{Mg}^{2+}$ ,  $\text{Pb}^{2+}$ ,  $\text{K}^+$ ,  $\text{Fe}^{2+}$ ,  $\text{Co}^{2+}$ , and  $\text{Cr}^{3+}$  give little response to CR-PK (Figure 7.2b). In addition, such a large red-shift of 222 nm in the absorption behavior changes the color of the resultant solution from yellow to greenish blue, allowing “naked-eye” detection (Figure 7.2c).<sup>[14]</sup>

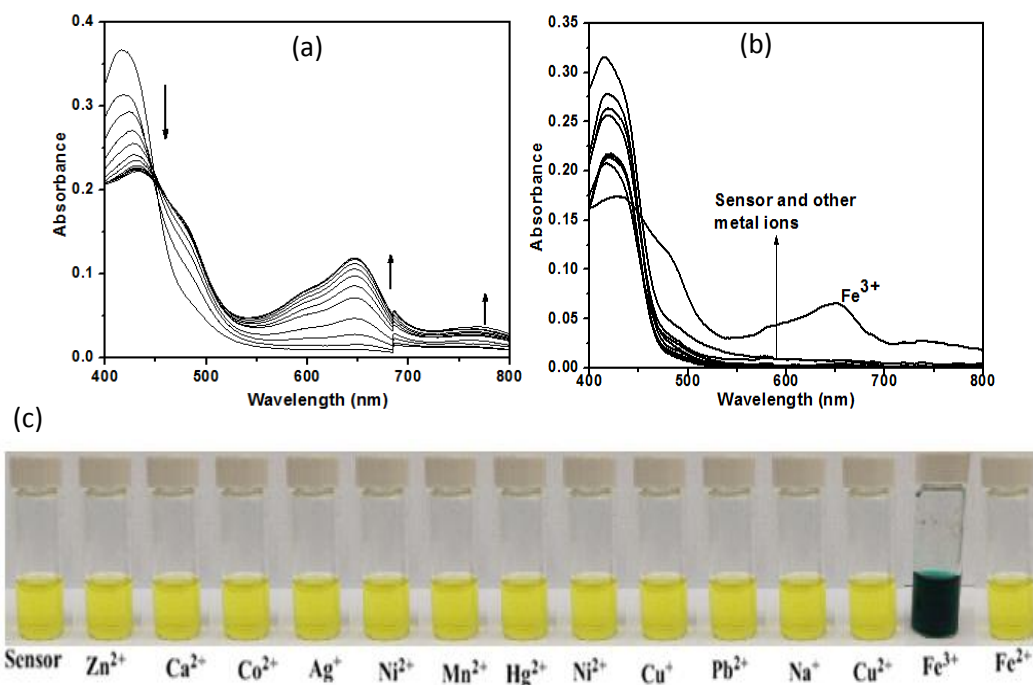


**Figure 7.2** (a) Absorbance responses of 10  $\mu\text{M}$  CR-PK to increasing concentration of  $\text{Fe}^{3+}$  (top to bottom, 0, 0.05, 0.1, 0.15, 0.2, 0.3, 0.5, 0.7, 0.8, 0.9, 1.0, 1.2, 1.5, and 2 equiv in EtOH/HEPES buffer (10 mM, pH 7.4, v/v 1:4) (b) UV-vis spectra of 20  $\mu\text{M}$  CR-PK to various metal ions (10  $\mu\text{M}$  for  $\text{Zn}^{2+}$ ,  $\text{Cr}^{3+}$ ,  $\text{Ni}^{2+}$ ,  $\text{Hg}^{2+}$ ,  $\text{Fe}^{3+}$ ,  $\text{Mn}^{2+}$ ,  $\text{Ag}^+$ ,  $\text{Pb}^{2+}$ ,  $\text{Fe}^{2+}$ ,  $\text{Cu}^+$ ,  $\text{Cu}^{2+}$ , and  $\text{Co}^{2+}$ ; 15  $\mu\text{M}$  for  $\text{Na}^+$ ,  $\text{K}^+$ ,  $\text{Mg}^{2+}$  and  $\text{Ca}^{2+}$ ) in EtOH/HEPES buffer (10 mM, pH 7.4, v/v 4:1) (c) Color changes of 20  $\mu\text{M}$  CR-PK with various metal ions.

To examine the fluorescent response to  $\text{Fe}^{3+}$ , a solution of CR-PK in EtOH/HEPES buffer (10 mM, pH 7.4, v/v 4:1) was titrated with various concentrations of  $\text{Fe}^{3+}$  and monitored with a fluorometer by excitation at 450 and 633 nm, individually. When excited at 633 nm, CRPK is yellowish and non-fluorescent. When  $\text{Fe}^{3+}$  was added to the CR-PK solution, the spirolactam ring opened and it displayed an emission peak with the maximum at 704 nm (Figure 7.3a). When it was excited at 450 nm, CR-PK solution displayed three emission peaks, one at 470 nm and two peaks at  $\sim 520$  nm and 704 nm (Figure 7.3b). When  $\text{Fe}^{3+}$  was added to CR-PK solution, a decrease in intensity of the 470 nm and 520 nm emissions and an increase in intensity of the fluorescence at 704 nm were observed. Compared to the other peaks, the  $\sim 520$  nm peak was less affected in the titration process.

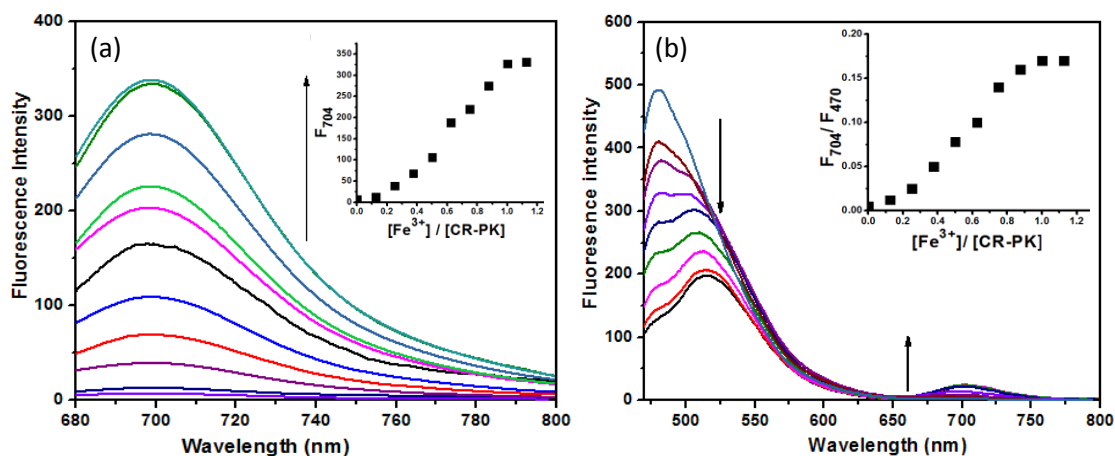


**Figure 7.3** (a) Fluorescence response of 10  $\mu\text{M}$  CR-PK to increasing concentration of  $\text{Fe}^{3+}$  ( $\lambda_{\text{Ex}} = 650$  nm) (b) Fluorescence response of 10  $\mu\text{M}$  CR-PK to increasing concentration of  $\text{Fe}^{3+}$  ( $\lambda_{\text{Ex}} = 450$  nm)(top to bottom, 0, 0.125, 0.250, 0.375, 0.50, 0.625, 0.750, 0.875, 1.0, 1.25, equiv in EtOH/HEPES buffer (10 mM, pH 7.4, v/v 1:4).

Then, the ratiometric fluorescence response of CR-PK was analyzed to determine its selectivity. As shown in Figure 7.4 (gray bars), the solution of CR-PK exhibits a very low fluorescent ratiometric value ( $F_{704}/F_{470}$ ), but upon the addition of 1 equiv of  $\text{Fe}^{3+}$ , there is a strong enhancement of this value. The addition of the other metal ions resulted in very little

increases in this value. I also examined the interferences from the other metal ions with CR-PK in its response to  $\text{Fe}^{3+}$ . Each of the metal ions was pre-incubated with CR-PK before 1 equiv  $\text{Fe}^{3+}$  was added, the fluorescence response was then measured. As shown in Figure 7.4 (black bars), the fluorescent ratiometric value of CR-PK with  $\text{Fe}^{3+}$  was not affected significantly in the presence of any of the other metal ions tested, demonstrating little interferences from other metal ions.

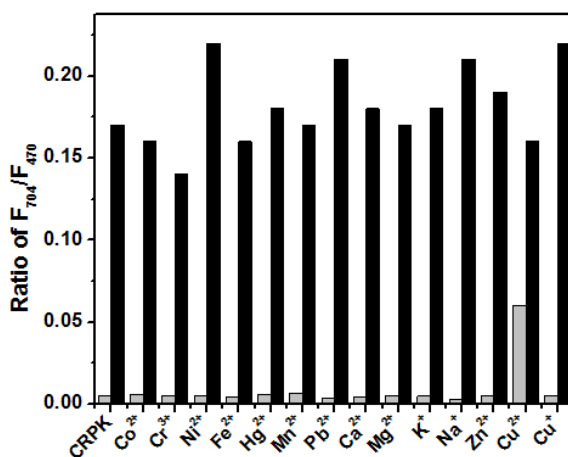


**Figure 7.4** Fluorescence responses  $F_{704}/F_{470}$  of 10  $\mu\text{M}$  CR-PK ( $\lambda_{\text{ex}}=450$  nm) to the presence of various metal ions (gray bars) and the subsequent addition of  $\text{Fe}^{3+}$  (black bar) in the EtOH/HEPES buffer (10 mM, pH 7.4, v/v 1:4).

One of the disadvantages of spirolactam- based sensors is that they also give response to hydrogen ions.<sup>[16,17]</sup> The ratio between the emission/absorption intensities provide built-in correction for environmental effects, so ratiometric sensors can eliminate the pH issues of sensors. The pH response of CR-PK in EtOH/water solution (1/4) was evaluated as shown in Figure 7.5. The pH-dependent UV-vis and fluorescent experiments revealed that CR-PK did not show any obvious and characteristic absorption and fluorescent (excited at 450 or 633 nm) in the pH range 4 to 11, suggesting that it can be studied in biological pH with a very low background fluorescence.

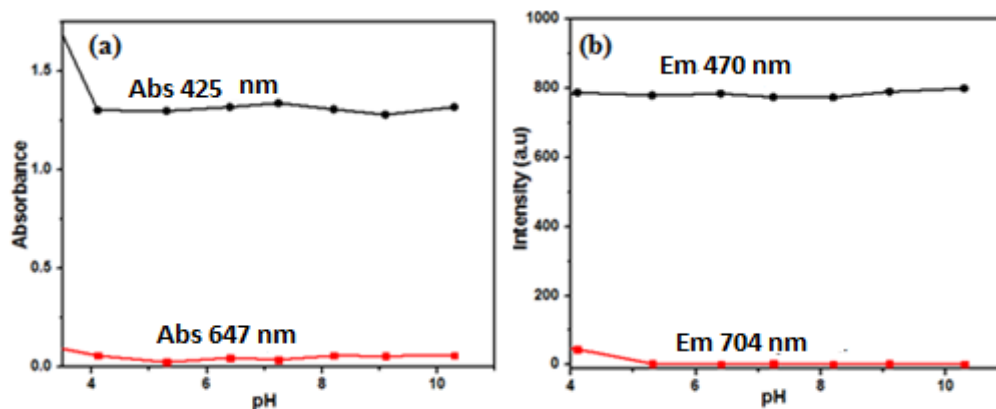


**Figure 7.5** (a) Variation of absorption and (b) fluorescent intensity of CR-PK in response to different pH.

### 7.3.3 Binding Studies

The binding stoichiometry of CR-PK and  $\text{Fe}^{3+}$  was determined by Job's method and UV-titration. Job's plot (Figure 7.6a) using continuous variation with a total concentration of  $20 \mu\text{M}$  of CR-PK and  $\text{Fe}^{3+}$  exhibited two maximum absorbances (at 425 and 647 nm). The results showed that the ratiometric values of the absorbance ( $A_{647}/A_{425}$ ) of the system (CR-PK +  $\text{Fe}^{3+}$ ) reached a maximum value when the molecular fraction of  $\text{Fe}^{3+}$  was close to 0.5, indicating a 1:1 stoichiometry. The titration curves (a plot of absorption versus the ratio of CR-PK/ $\text{Fe}^{3+}$ ) increased at 647 nm and decreased at 425 nm (Figure 7.3b and Figure 7.6b) linearly and plateaued at 1:1 ratio of the sensor and  $\text{Fe}^{3+}$ , also suggesting the formation of a 1:1 of CRPK- $\text{Fe}^{3+}$  complex also (inset graphs in Figure 7.3 a and b also provided that the binding mode is 1:1). The binding constant of this complex was calculated following the method explained in chapter 2 and chapter 4, using absorption values at 647 nm, and was determined to be  $2.94 \times 10^7 \text{ M}^{-1}$ .

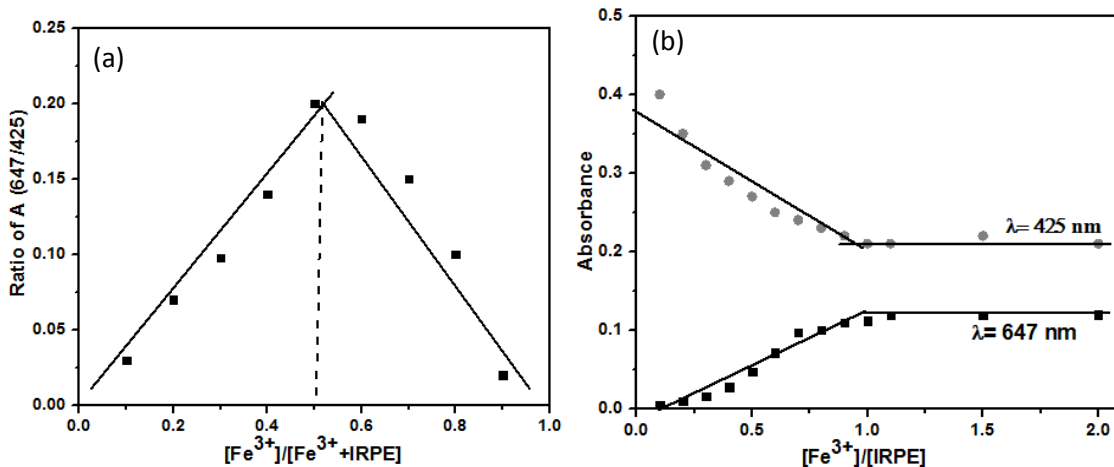


**Figure 7.6** (a) Job's plot of the complexation between CR-PK and  $\text{Fe}^{3+}$  [ $\text{CR-PK}$ ] + [ $\text{Fe}^{3+}$ ] = 20  $\mu\text{M}$  in EtOH/HEPES buffer (10 mM, pH 7.4, v/v 1:4) (b) Titration of 10  $\mu\text{M}$  CR with increasing concentrations of  $\text{FeCl}_3$  (1.0, 2.0, 3.0, 4.0, 5.0, 6.0, 7.0, 8.0, 9.0, 10.0, 11.0, 15.0, and 20  $\mu\text{M}$ , respectively) in EtOH/HEPES buffer (10 mM, pH 7.4, v/v 1:4). The absorption intensities increased at 647 nm and decreased at 425 nm.

In addition, reversibility experiments were carried out by adding EDTA to the CR-PK- $\text{Fe}^{3+}$  complex in the EtOH/HEPES buffer (10 mM, pH 7.4, v/v 1:4). In the absence of EDTA, the complex was greenish-blue and fluorescent at 704 nm. After adding 2 equiv of EDTA, fluorescent intensity decreased to that similar to CR-PK alone (Figure 7.7), suggesting a reversible binding between CR-PK and  $\text{Fe}^{3+}$  and that the spiro lactam ring is closed in the presence of EDTA.

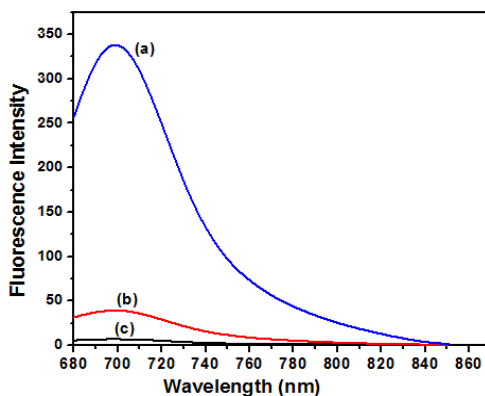
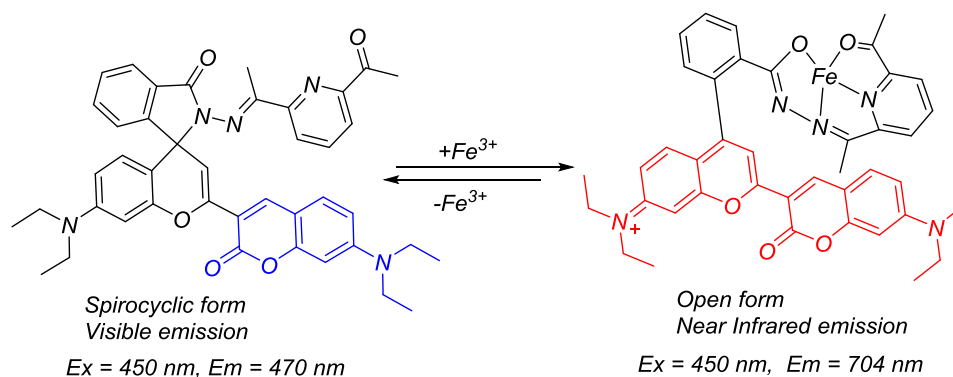


**Figure 7.7** Reversibility of CR-PK (10  $\mu\text{M}$ ) to  $\text{Fe}^{3+}$  ions by EDTA: (a) CR-PK + 1 equiv of  $\text{Fe}^{3+}$ , (b) CR-PK + 1 equiv of  $\text{Fe}^{3+}$  + 2 equiv of EDTA, (c) free CR-PK (10  $\mu\text{M}$ ).

A possible mechanism for the reaction and the binding mode between CR-PK and  $\text{Fe}^{3+}$  is shown in Scheme 7.3.



**Scheme 7.3** Proposed reversible 1:1 binding mode between CR-PK and  $\text{Fe}^{3+}$

#### 7.3.4 Cell Studies

The *in vitro* studies have shown that CR-PK can detect  $\text{Fe}^{3+}$  with excellent selectivity. To examine whether it can detect  $\text{Fe}^{3+}$  in living systems, live bovine aortic endothelial cells (BAEC) were used to test its ability in detecting endogenous  $\text{Fe}^{3+}$  ions in live cells. The cells were treated with 20  $\mu\text{M}$  of CR-PK for 30 min at 37  $^{\circ}\text{C}$ . Since CR-PK is cell permeable, the cells exhibited a strong fluorescence in the blue channel (Figure 7.9a) but very weak fluorescence in the red channel (Figure 7.9d). As seen in Figure 7.8a, CR-PK (blue color) was located almost everywhere in the cytosol of the cells but not the nucleus. However, in Figure 7.9d, similar to those observed with the other  $\text{Fe(III)}$  sensors RPE, NIRh-Ac, NRPA, and NRPK, red color images are located in certain organelles of the cells.

The equation (1) was then used to determine the concentration of  $\text{Fe}^{3+}$  ions in cells. Here,  $R_{\text{max}}$  is the maximum fluorescence ratio at saturating  $\text{Fe}^{3+}$  in cells. To measure the saturation of  $\text{Fe}^{3+}$  in cells for the sensor CR-PK (20  $\mu\text{M}$ ), a  $\text{Fe}^{3+}$  titration experiment was



performed with live bovine aortic endothelial cells (BAEC). The cells were pre-incubated with different concentrations of  $\text{Fe}^{3+}$ -citrate (0, 2, 5, 10, 15, 20, and 40  $\mu\text{M}$ ) for 30 min at 37 °C, then dyed with the  $\text{Fe}^{3+}$  sensor NRPA (20  $\mu\text{M}$ ) for another 30 min. Cell images were then collected by a confocal microscope immediately. NRPA was chosen for these experiments because it is a turn-on fluorescent sensor that makes it easier to measure the changes in image intensity than that with a ratiometric sensor. As seen in Figure 7.8, the cellular fluorescence intensity increased linearly and the sensor was saturated with  $\text{Fe}^{3+}$  at 20  $\mu\text{M}$ . It was then decided to use 40  $\mu\text{M}$  of ferric citrate loading the cells to saturate the cells with  $\text{Fe}^{3+}$ .

When the cells were pre-incubated with ferric citrate (40  $\mu\text{M}$  for 30 min at 37 °C), the blue imaging of the sensor decreased in intensity (Figure 7.9b, ~30 % turn-off), but, on the other hand, red imaging of the sensor increased in intensity (Figure 7.9e, ~6 fold). Again, as observed with the RPE sensor, the red colored regions are located in certain discrete areas in the cells, suggesting that  $\text{Fe}^{3+}$  is located in certain organelles, not in cytosol. When  $\text{Fe}^{3+}$  depletion was introduced via incubation the cells with a  $\text{Fe}^{3+}$  chelator SIH (salicylaldehyde isonicotinoyl hydrazon, 200  $\mu\text{M}$ , for 30 min.), a marked decrease in fluorescent intensity in the red channel with a strong increase in fluorescent intensity in the blue channel were observed (Figure 7.9c). These experiments showed that the sensor CR-PK could detect endogenous  $\text{Fe}^{3+}$  as well as the dynamic changes in  $\text{Fe}^{3+}$  concentration in live BAEC cells.

These results also suggest that CR-PK can be used for ratiometric fluorescence imaging of  $\text{Fe}^{3+}$  in living cells. Figures 7.9 g-h are the ratiometric images of CR-PK and the subsequent treatment with  $\text{Fe}^{3+}$  or SIH. By using the equation (1)<sup>[9]</sup>, the images obtained were then used to determine the concentration of  $\text{Fe}^{3+}$  in the cells. The ratios between the red channels and the blue channels,  $R$ ,  $R_{\min}$ , and  $R_{\max}$  were presented in Table 7.1. An accurate determination of  $K_d$

value in intracellular environment is critical for an accurate determination of  $\text{Fe}^{3+}$  concentration in cells. The  $K_d$  value found in this study is determined in EtOH/HEPES buffer (10 mM, pH 7.4, v/v 1:4) which is not the same as those in the intracellular environment as millimolar levels of  $\text{Fe}^{3+}$ -chelators such as ATP, phosphate are present in cells. Using a buffer, more closely mimic the cellular buffer condition to determine a more accurate apparent  $K_d$  value can improve the accuracy of this method (Method 1). The  $K_d$  value under this buffer condition<sup>[18]</sup> was determined to be  $6.30 \mu\text{M}$ . With this  $K_d$  value, the  $\text{Fe}^{3+}$  concentration in BAEC cells was determined to be  $2.18 \pm 0.35 \mu\text{M}$ .

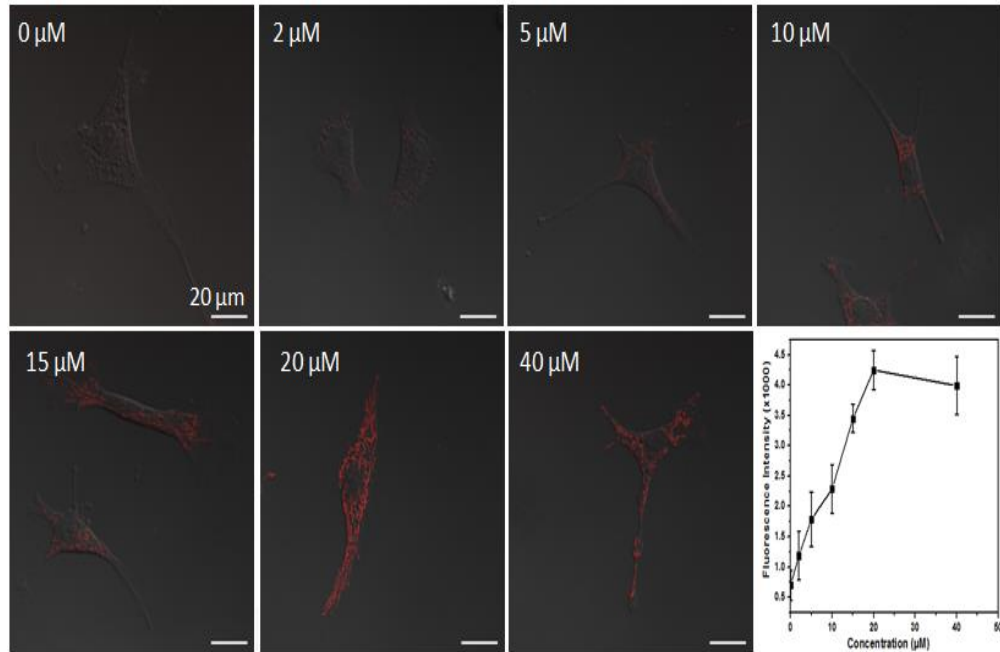


**Figure 7.8** Confocal microscopy images of live aortic endothelial cells (BAEC) cells treated with different concentration of  $\text{Fe}^{3+}$  (ferric citrate) for 30 min, and then incubated with NRPA (20  $\mu\text{M}$ ) in 1:1 mixture of Eagles Minimal Essential medium (ATCC) and Ham's F12 medium (ATCC). Fluorescence intensity collected at 680-750 nm (NRPA was excited at 633 nm).

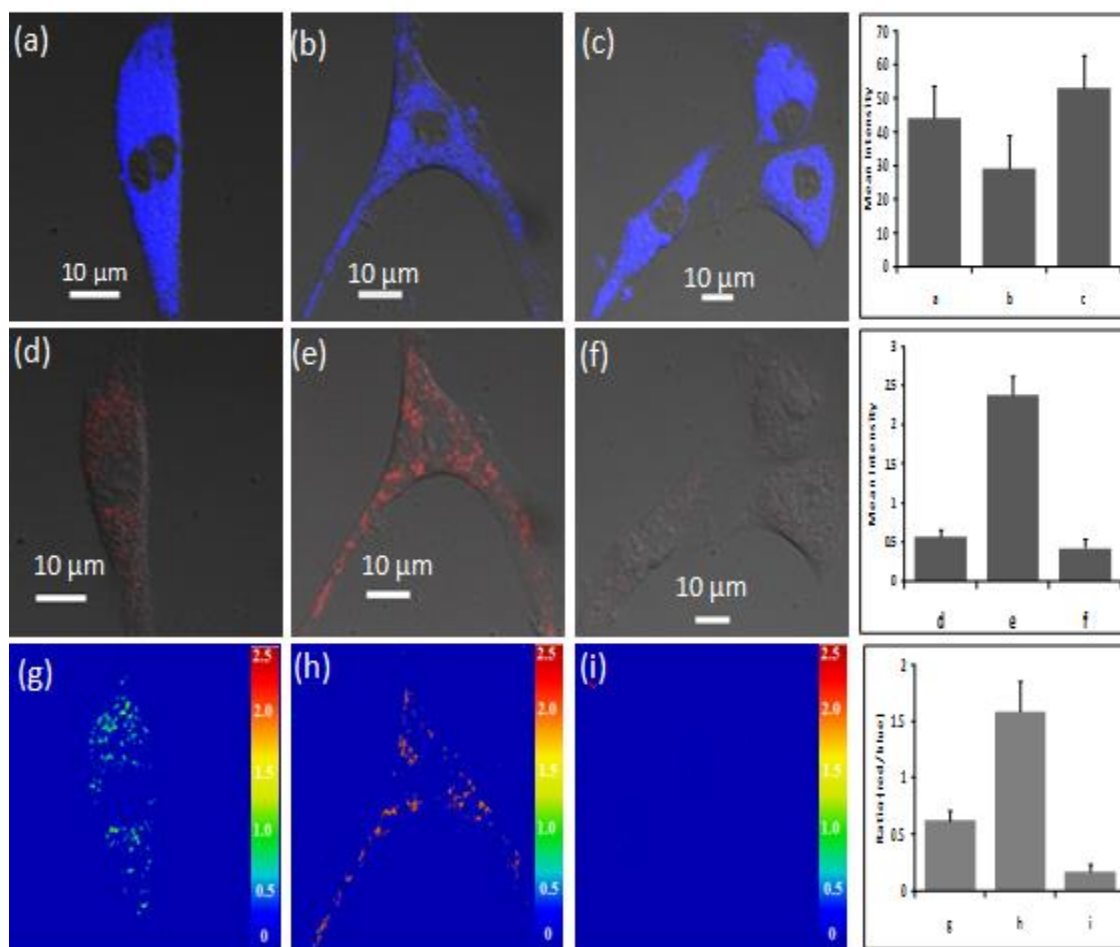


**Figure 7.9** Confocal microscopy images (with DIC) of BAEC treated with (a,d) 10 μM CR-PK sensor after 30 min incubation (b,e) the cells were incubated with Fe<sup>3+</sup> (20 μM) for 8 h then incubate with the sensor for 30 min (c,f) the cells were incubated with SIH (100 μM) for 8 h then incubated with the sensor for 30 min. (Excitation wavelength was 458 nm for a,b,c and 633 nm for (d,e,f), (g,h,i) ratio images of a,d; b,e; c,f. The ratio images were obtained for the regions where Fe<sup>3+</sup> ions are located. Confocal fluorescence ratiometric images are the average ratio in regions of interest.

**Table 7.1** Confocal fluorescence ratiometric images averages (a) BAEC cells incubated with CR-PK (10  $\mu\text{M}$ ) for 30 min. (b) BAEC cells were first pre-incubated with ferric citrate(10  $\mu\text{M}$ ) for 30 min, then incubated with CR-PK (10  $\mu\text{M}$ ) for another 30 min. (c) BAEC cells were first pre-incubated with SIH (200  $\mu\text{M}$ ) for 30 min, then incubated with CR-PK (10  $\mu\text{M}$ ) for another 30 min. Confocal fluorescence ratiometric images are the average ratio in regions of interest.

Ratio	1	2	3	4	5	Average	Standard Deviation
<b>R (CR-PK only (10 <math>\mu\text{M}</math>))</b>	0.5	0.63	0.78	0.78	0.51	0.64	0.15
<b><math>R_{\text{max}}</math> (Fe(III) (40 <math>\mu\text{M}</math>) incubation first + CR-PK (10 <math>\mu\text{M}</math>))</b>	1.71	1.48	1.38	1.84	1.54	1.59	0.18
<b><math>R_{\text{min}}</math> (SIH (200 <math>\mu\text{M}</math>) + CR-PK (10 <math>\mu\text{M}</math>))</b>	0.17	0.16	0.21	0.09	0.22	0.17	0.06

$$R = (R_{\text{min}} K_d + R_{\text{max}} [M^{n+}]) / (K_d + [M^{n+}])$$

$$[\text{Fe}^{3+}] = 2.18 \pm 0.35 \mu\text{M}$$

Beside the method using  $K_d$  and equation 1 to calculate the concentration, a second method by fitting a calibration curve to calculate cellular concentration has also been described in the literature.<sup>[11]</sup> Using this method, an *in vitro* calibration curve was obtained by titration of the sensor, CR-PK (10  $\mu\text{M}$ ), with different concentrations of  $\text{Fe}^{3+}$  and a calibration curve was obtained by plotting  $[\text{Fe}^{3+}]$  versus fluorescent ratio ( $F_{704}/F_{470}$ ) (Figure 7.10). Fitting the ratio determined by the cell imaging data to this calibration curve give a  $\text{Fe}^{3+}$  concentration in BAEC cells  $1.38 \pm 0.35 \mu\text{M}$ . The labile  $\text{Fe}^{3+}$  concentration in untreated BAEC cells determined by methods 1 and 2 are quite close, with an average of 1.76  $\mu\text{M}$  that is within the error ranges of data in both the methods. As far as I know, this is the first determination of labile  $\text{Fe}^{3+}$  concentration in cells.

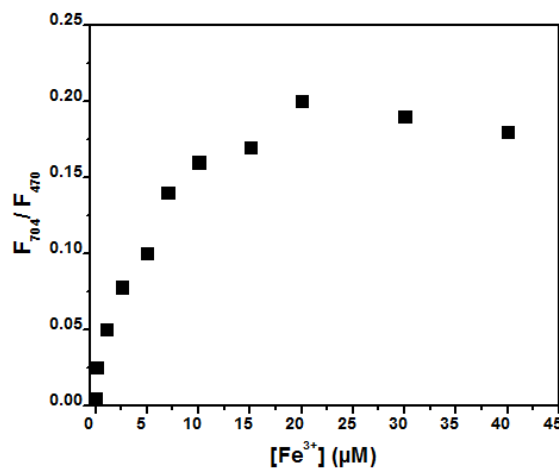


**Figure 7.10** *In vitro* calibration of CR-PK with  $[\text{Fe}^{3+}]$

The same experiments were used to determine the concentration of free  $\text{Fe}^{3+}$  ions in human neuroblastoma cells (SH-SY5H) and fibroblast cells (ws1). The cell images and the ratio between the channels were shown Figures 7.11 and 7.12, and the results were summarized in Table 7.2.

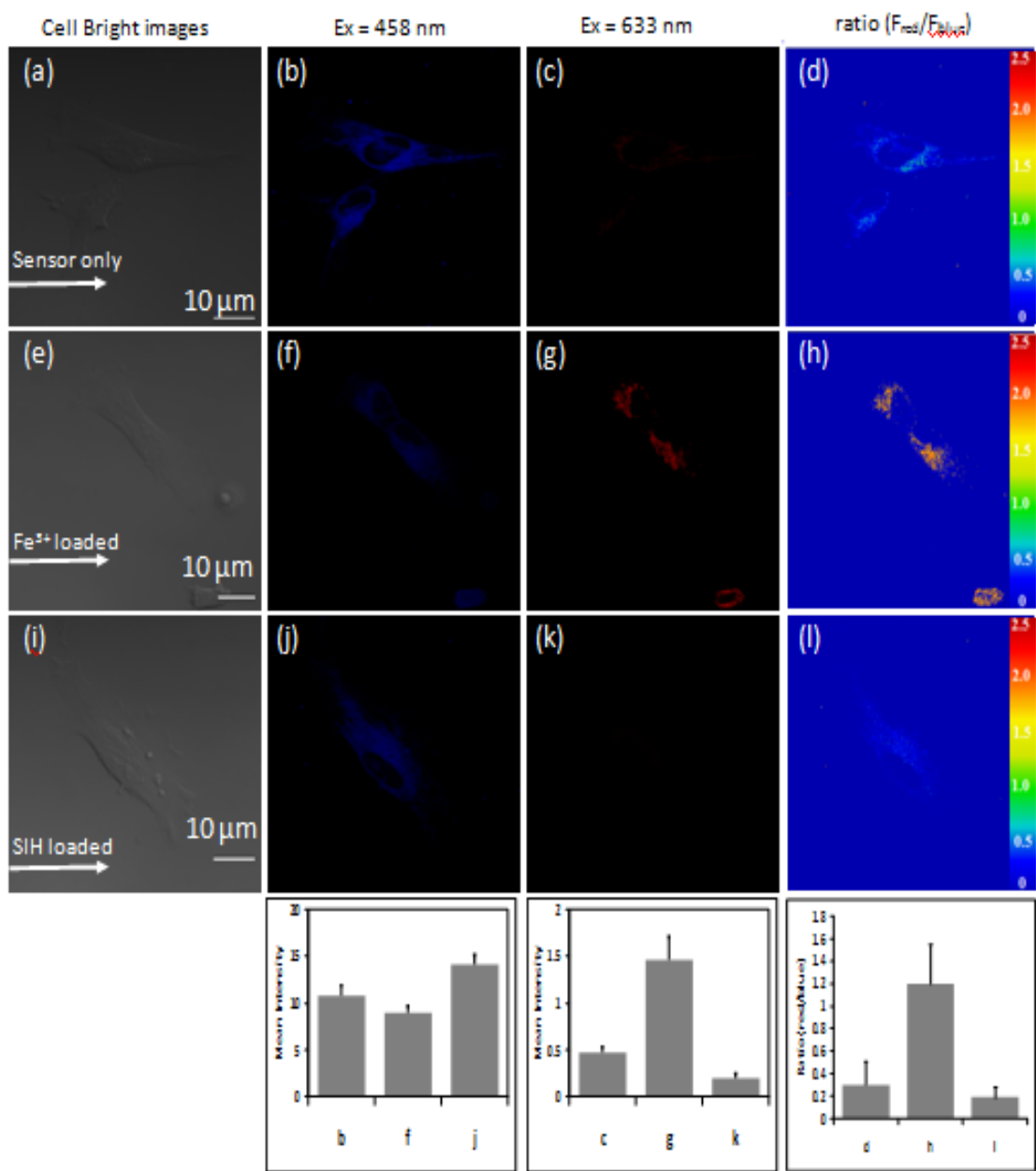


**Figure 7.11** Confocal microscopy images (with DIC) of *ws1* treated with (b,c) 10  $\mu M$  CR-PK sensor after 30 min incubation (f,g) the cells were incubated with  $Fe^{3+}$  (20  $\mu M$ ) for 1 h then incubated with the sensor for 30 min (j,k) the cells were incubated with SIH (100  $\mu M$ ) for 8 h then incubate with the sensor for 30 min (Excitation wavelength was 458 nm for (b,f,j) and 633 nm for (c,g,k), (d,h,l) ratio images of b,c; f,g; j,k. Confocal fluorescence ratiometric images are the average ratio in regions of interest.

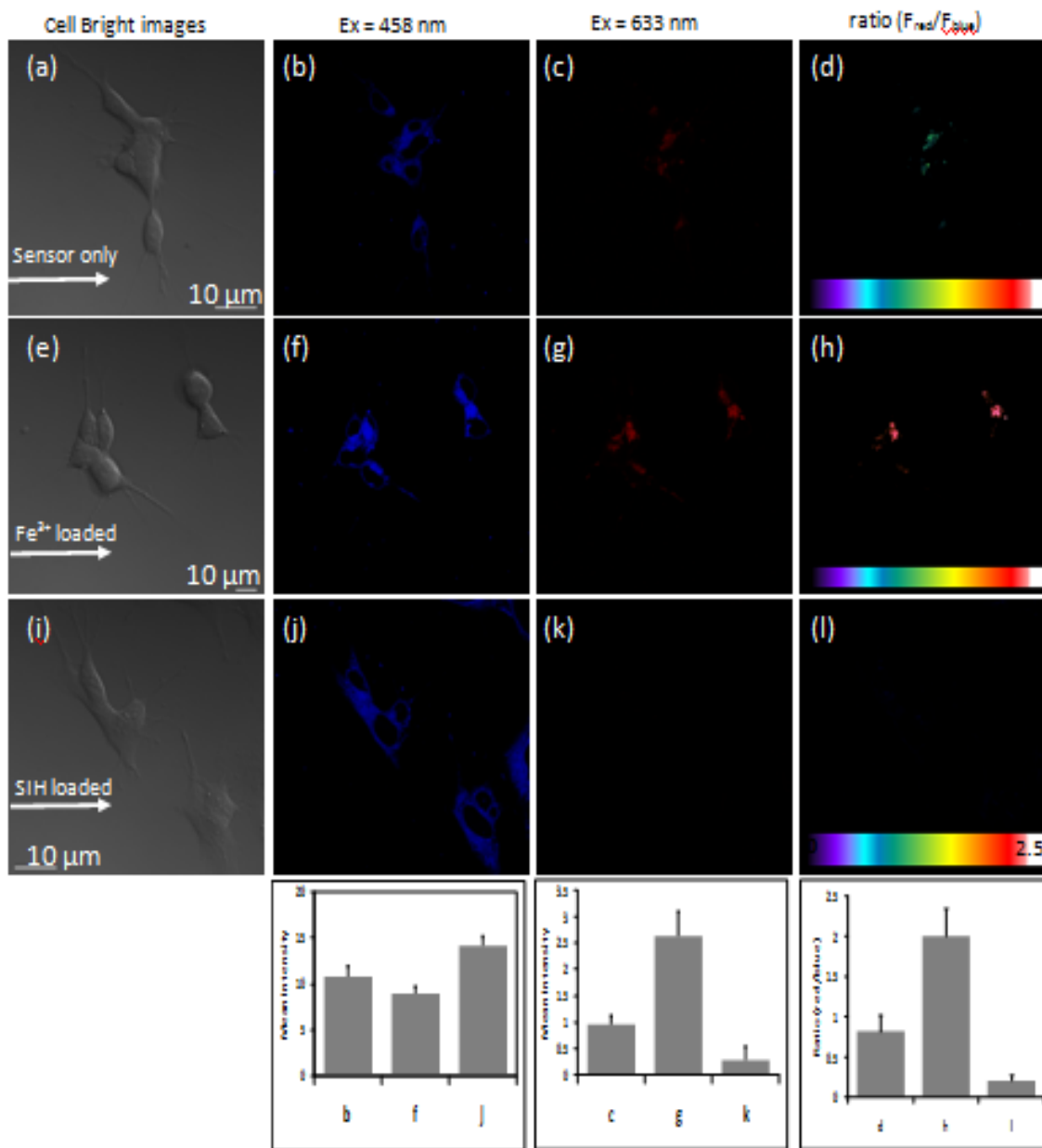


**Figure 7.12** Confocal microscopy images (with DIC) of SH-SY5H treated with (b,c) 10  $\mu\text{M}$  CR-PK sensor after 30 min incubation (f,g) the cells were incubated with  $\text{Fe}^{3+}$  (20  $\mu\text{M}$ ) for 1 h then incubate with the sensor for 30 min (j,k) the cells were incubated with SIH (100  $\mu\text{M}$ ) for 8 h then incubate with the sensor for 30 min. Excitation wavelength was 458 nm for (b,f,j) and 633 nm for (c,g,k), (d,h,l) ratio images of b,c; f,g; j,k. Confocal fluorescence ratiometric images are the average ratio in regions of interest.

**Table 7.2** Free Fe<sup>3+</sup> concentration in the cells

Cell Type	Method 1 (μM)	Method 2 (μM)
<b>WS1</b>	0.8 ± 0.28	0.43 ± 0.23
<b>BAEC</b>	2.18 ± 0.35	1.38 ± 0.47
<b>SH-SY5H</b>	3.2 ± 0.63	3.1 ± 0.52

The images from the red channels showed scattered patterns, implying that the labile Fe<sup>3+</sup> in the cells (BAEC, Ws1, and SH-SY5Y) may be localized in certain subcellular compartments (organelles) and that CR-PK may be capable of imaging Fe<sup>3+</sup> at subcellular resolution. To explore this, the distribution of exchangeable Fe<sup>3+</sup> pools in the cells was further investigated using CR-PK, together with colocalization experiments using other dyes—MitoTracker Green FM (a green fluorescent dye which localizes to mitochondria in live cells regardless of mitochondrial membrane potential) and LysoTracker Blue DND-99 (a blue fluorescent dye that stains acidic compartments such as endosomes and lysosomes<sup>[19,20]</sup> in live cells). The cells (without Fe<sup>3+</sup> treatment) were treated with CR-PK, MitoTracker Green FM, and LysoTracker Blue DND-99. For BAEC cells, as illustrated in Figure 7.13 partial colocalization between CR-PK-Fe<sup>3+</sup> and the MitoTracker (Figure 7.13e) as well as between CR-PK-Fe<sup>3+</sup> and the LysoTracker (Figure 7.13f) occurred whereas complete colocalization of CR-PK-Fe<sup>3+</sup>, MitoTracker and LysoTracker (Figure 7.13g) was observed. These data suggest that the exchangeable Fe<sup>3+</sup> pools in BAEC cells detectable by CR-PK are localized in mitochondria and endosomes/lysosomes. These results also showed that the iron levels in mitochondria and lysosome are different (red signal in mitochondria is brighter than those in lysosomes). As seen in Figure 7.9g, there are two different colors: greenish (ratio ~1.2) and blue (ratio ~0.5). Using these colors, Fe<sup>3+</sup>-levels in mitochondria



and lysosomes were calculated and determined to be  $2.69 \pm 0.43 \mu\text{M}$  and  $1.67 \pm 0.17 \mu\text{M}$  respectively by Method 1.

The same co-localization experiments were carried out for SH-SY5H and ws1 cells. It is clear from Figure 7.14 d-f that  $\text{Fe}^{3+}$  pools in ws1 cells detectable by CR-PK are localized in mitochondria only. For SH-SY5H cells,  $\text{Fe}^{3+}$  pools in the cells detectable by CR-PK are localized in mitochondria and endosomes/lysosomes (Figure 7.15).  $\text{Fe}^{3+}$  levels in these organelles were calculated and shown in Table 7.3.

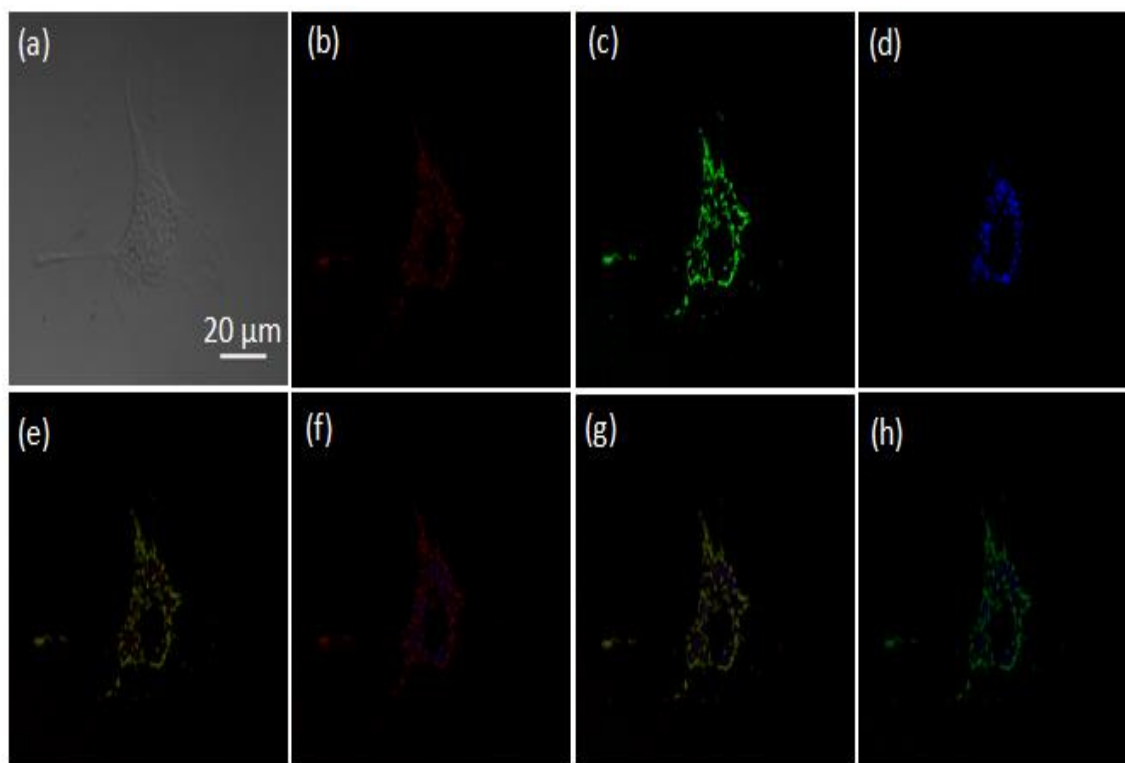


**Figure 7.13** Representative confocal microscopy images of intracellular colocalization studies of  $10 \mu\text{M}$  CR-PK incubated with live BAEC cells co-labeled with MitoTracker Green FM ( $100 \text{ nM}$ , incubated for  $30 \text{ min}$ ) and LysoTracker Blue DND-99 ( $50 \text{ nM}$ , incubated for  $30 \text{ min}$ ). (a) DIC image of cells with  $20\text{-}\mu\text{m}$  scale bar. (b) CR-PK- $\text{Fe}^{3+}$  fluorescence collected at  $680\text{-}750 \text{ nm}$  (red). (c) MitoTracker fluorescence collected at  $492\text{-}540 \text{ nm}$  (green). (d) LysoTracker fluorescence collected at  $547\text{-}630 \text{ nm}$  (blue). (e) DIC image of (a) and fluorescence images of (b) and (c) were merged together. Colocalization regions are in yellow and non-overlapping regions remain in red. (f) DIC image of (a) and fluorescence images of (b) and (d) were merged together. Overlapping regions are in purple and non-overlapping regions remain in red; (g) Images of (a), (b), (c) and (d) were merged together, revealing that the CR-PK- $\text{Fe}^{3+}$  images are 100% colocalized

with MitoTracker and LysoTracker. (h), Images of (a), (c) and (d) were merged together, showing no overlapping region between lysosomes and mitochondria

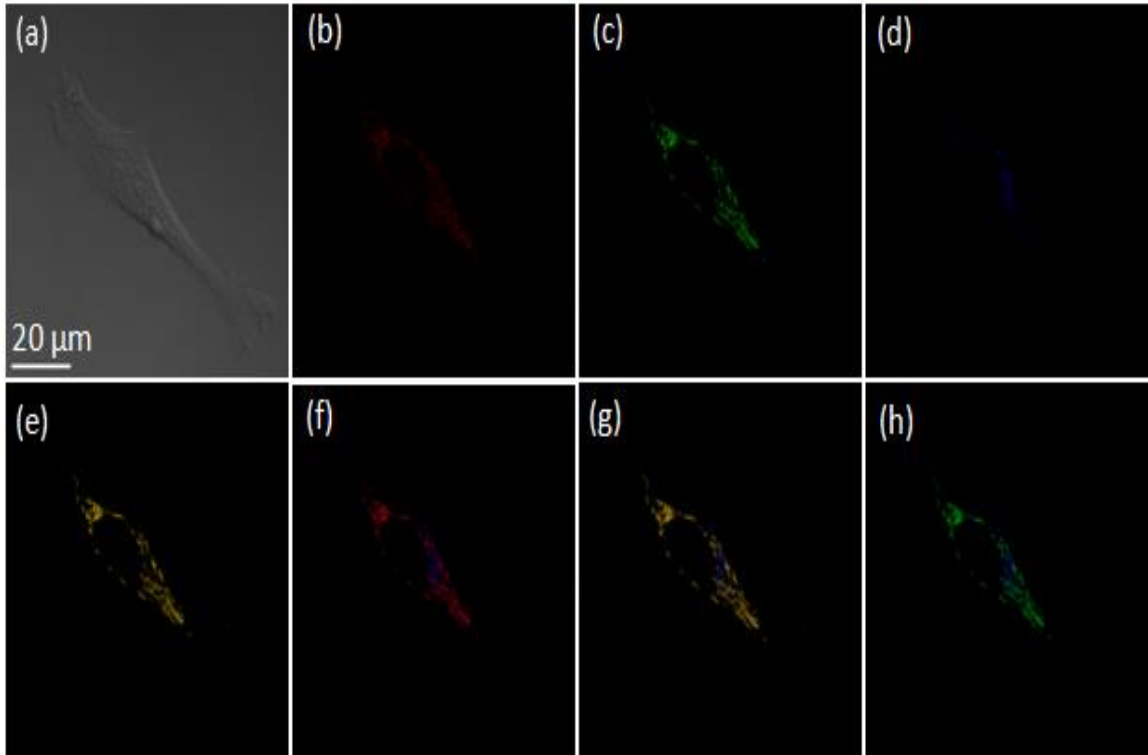


**Figure 7.14** Representative confocal microscopy images of intracellular colocalization studies of 10  $\mu\text{M}$  CR-PK incubated with live ws1 cells co-labeled with MitoTracker Green FM (100 nM, incubated for 30 min) and LysoTracker Blue DND-99 (50 nM, incubated for 30 min). (a) DIC image of cells with 20- $\mu\text{m}$  scale bar (b) CR-PK- $\text{Fe}^{3+}$  fluorescence collected at 680-750 nm (red). (c) MitoTracker fluorescence collected at 492-540 nm (green). (d) LysoTracker fluorescence collected at 547-630 nm (blue). (e) DIC image of (a) and fluorescence images of (b) and (c) were merged together. Colocalization regions are in yellowish green and no red colored region remain (f) DIC image of (a) and fluorescence images of (b) and (d) were merged together no overlapping (g) Images of (a), (b), (c) and (d) were merged together, revealing that the CR-PK- $\text{Fe}^{3+}$  images are 100% colocalized with MitoTracker but not with LysoTracker. (h) Images of (a), (c) and (d) were merged together, showing no overlapping region between lysosomes and mitochondria.

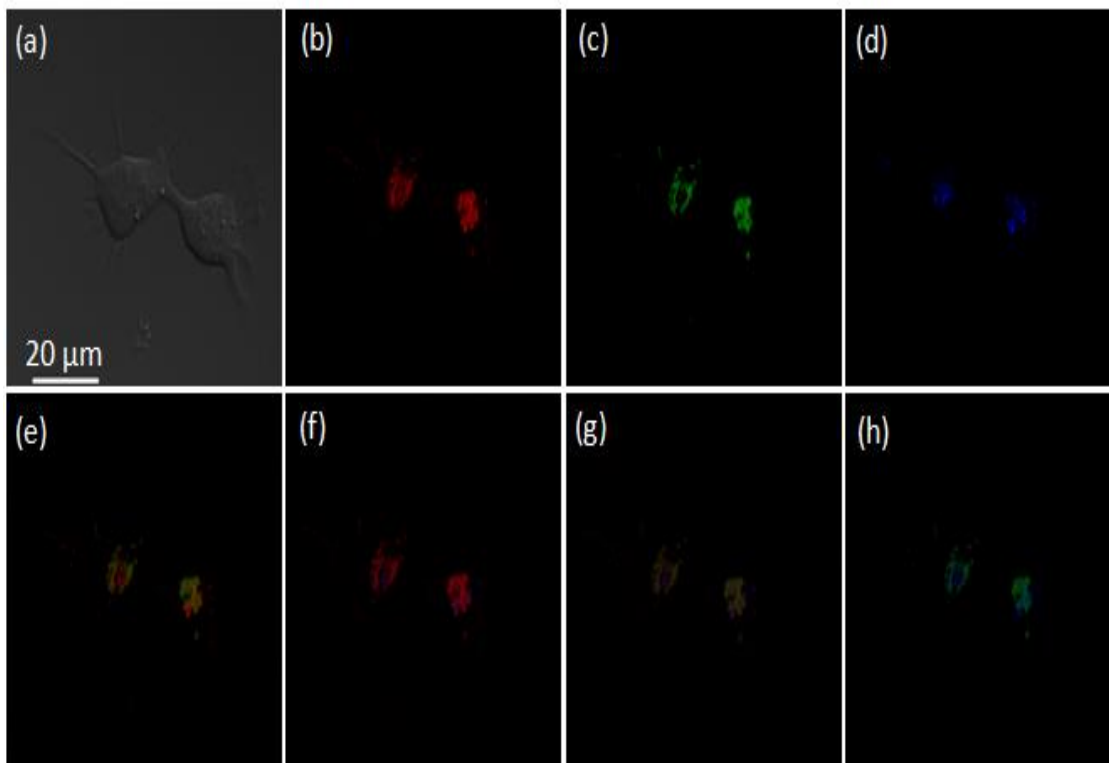


**Figure 7.15** Representative confocal microscopy images of intracellular colocalization studies of 10  $\mu\text{M}$  CR-PK incubated with live SH-SY5H cells co-labeled with MitoTracker Green FM (100 nM, incubated for 30 min) and LysoTracker Blue DND-99 (50 nM, incubated for 30 min). (a) DIC image of cells with 20  $\mu\text{m}$  scale bar. (b) CR-PK- $\text{Fe}^{3+}$  fluorescence collected at 680-750 nm (red). (c) MitoTracker fluorescence collected at 492-540 nm (green). (d) LysoTracker fluorescence collected at 547-630 nm (blue). (e) DIC image of (a) and fluorescence images of (b) and (c) were merged together. Colocalization regions are in yellow and non-overlapping regions remain in red. (f) DIC image of (a) and fluorescence images of (b) and (d) were merged together. Overlapping regions are in purple and non-overlapping regions remain in red. (g) Images of (a), (b), (c) and (d) were merged together, revealing that the CR-PK- $\text{Fe}^{3+}$  images are 100% colocalized with MitoTracker and LysoTracker. (h), Images of (a), (c) and (d) were merged together, showing no overlapping region between lysosomes and mitochondria.

**Table 7.3** Free  $\text{Fe}^{3+}$  concentration in the organelles of the cells\*

Cell Type	Mitochondria ( $\mu\text{M}$ )	Lysosomes ( $\mu\text{M}$ )
WS1	$0.8 \pm 0.28$	N.D.**
BAEC	$2.69 \pm 0.43$	$1.67 \pm 0.17$
SH-SY5H	$3.8 \pm 0.72$	$2.01 \pm 0.36$

\* Only Method 1 was used for the calculations; \*\* Not Detected

## 7.4 Conclusions

In summary, a highly sensitive, highly selective, and reversible ratiometric fluorescent  $\text{Fe}^{3+}$ -sensor CR-PK has been developed. The CR-PK sensor shows NIR and visible emission in its spirocyclic ring-open and closed forms, respectively. The reaction of CR-PK with  $\text{Fe}^{3+}$  leads to the ring-opening of the spirocyclic moiety of CR-PK, causing a huge red shift  $\sim 222$  nm. Cell imaging experiments with CR-PK revealed that CR-PK is evenly distributed in the cells except the nuclei region; however, chelatable labile  $\text{Fe}^{3+}$  ions are located in certain organelles in live bovine aortic endothelial cells (BAEC), human neuroblastoma cell (SH-SY5Y), and fibroblast (ws1) cells. The ratiometric sensor CR-PK enables the direct determination of endogenous labile  $\text{Fe}^{3+}$  concentration in cells for the first time, with a value of  $\sim 0.6$   $\mu\text{M}$  determined ( $0.43 \pm 0.23$   $\mu\text{M}$  by Method 1 and  $0.8 \pm 0.28$   $\mu\text{M}$  by Method 2) for ws1 cells,  $\sim 1.78$   $\mu\text{M}$  determined ( $2.18 \pm 0.35$   $\mu\text{M}$  by Method 1 and  $1.38 \pm 0.47$   $\mu\text{M}$  by Method 2) for BAEC cells, and  $\sim 3.15$   $\mu\text{M}$  determined ( $3.2 \pm 0.63$   $\mu\text{M}$  by Method 1 and  $3.1 \pm 0.53$   $\mu\text{M}$  by Method 2) for SH-SY5Y cells. Confocal experiments also show that CR-PK can readily detect endogenous chelatable  $\text{Fe}^{3+}$  in live BAEC, ws1, and SH-SY5Y cells at subcellular resolution in real time, with two labile  $\text{Fe}^{3+}$  pools being successfully located in mitochondria and endosomes/lysosomes of BAEC and SH-SY5Y cells and only in mitochondria of ws1 cells.

## 7.5 References

1. Greenberg G. R., Wintrare M. M., J. Biol. Chem., **1946**, 165, 397-398
2. Breuer W., Shvartsman M., Cabantchik Z. I., Int. J. Biochem. Cell. Biol., **2008**, 40, 350-354
3. Andrews N. C., Nat. Rev. Genet., **2000**, 1, 208-217
4. Rouault T. A., Nat. Chem. Biol., **2006**, 8, 406-414
5. Toyokuni S., Free Radic Biol. Med., **1996**, 20, 553-566

6. Kakhlon O., Cabantchik Z.I., *Free Radic. Biol. Med.*, **2002**, 33, 1037-1046
7. Xu J., Jia Z., Knutson M. D., Leeuwenburgh C., *Int. J. Mol. Sci.*, **2012**, 13, 2368-2386
8. Crichton R., Ed. *Inorganic biochemistry of iron metabolism*, 2nd ed.; John Wiley & Sons Ltd.: U.K., **2001**, pp. 160-180
9. Grynkiewicz G., Poenie M., Tsien R. Y., *J. Biol. Chem.*, **1985**, 260, 3440-3450
10. Liu Z., Zhang C., Chen Y., Fang Q., Bai Y., He W., Guo Z., *Chem. Commun.*, **2014**, 50, 1253-1255
11. Atar D., Backx P. H., Appel M. M., Gao W. D., Marban E., *J. Biol. Chem.*, **1995**, 270, 2473-2477
12. Taki M., Wolford J. L. O'Halloran T. V., *J. Am. Chem. Soc.*, **2004**, 126, 712-713
13. Czerney P., Grane B. G., Birckner E., Vollmer F., Rettig W., *J. Photochem. Photobiol. B*, **1995**, 89, 31-36
14. Lui J., Sun Y. Q., Wang P., Zhang J., Guo W., *Analyst*, **2013**, 138, 2654-2660
15. Lv H., Yang X. F., Zhang Y., Guo Y., Li Z., Li H., *Anal. Chem.*, **2014**, 86, 1800-1807
16. Yuan L., Lin W., Yang Y., Chen, H.J., *Am. Chem. Soc.*, **2012**, 134, 1200-1211
17. Kim H.N., Lee M.H., Kim H.J., Kim J.S., *Chem. Soc. Rev.*, **2008**, 37, 1465-1472
18. Breuer W., Epstein S., Milligram P., Cabantchik Z.I., *Am. J. Physiol.*, **1995**, 268, C1354-C1361
19. Desai S. D., Reed R. E., Babu S., Lorio E. A., *J. Biol. Chem.*, **2013**, 288, 2388-2402
20. Kazmi F., Hensley T., Pope C., Funk R. S., Loewen G. J., Buckley D. B., Parkinson A., *Drug Metab. Dispos.*, **2013**, 41, 897-905

## APPENDIX A

### OTHER SYNTHETIC ATTEMPTS TO MAKE IRON SENSORS

#### A1.1 Introduction

In this section, some other fluorescent sensors were prepared and characterized. These compounds were designed for either  $\text{Fe}^{3+}$  or  $\text{Fe}^{2+}$ . However, they are selective for other metal ions. This Appendix details synthesis and characterization of the other (5 heptamethine cyanine-based, 2 rhodamine based) sensors mentioned in the dissertation. Here, selectivity of the sensors will not be presented.

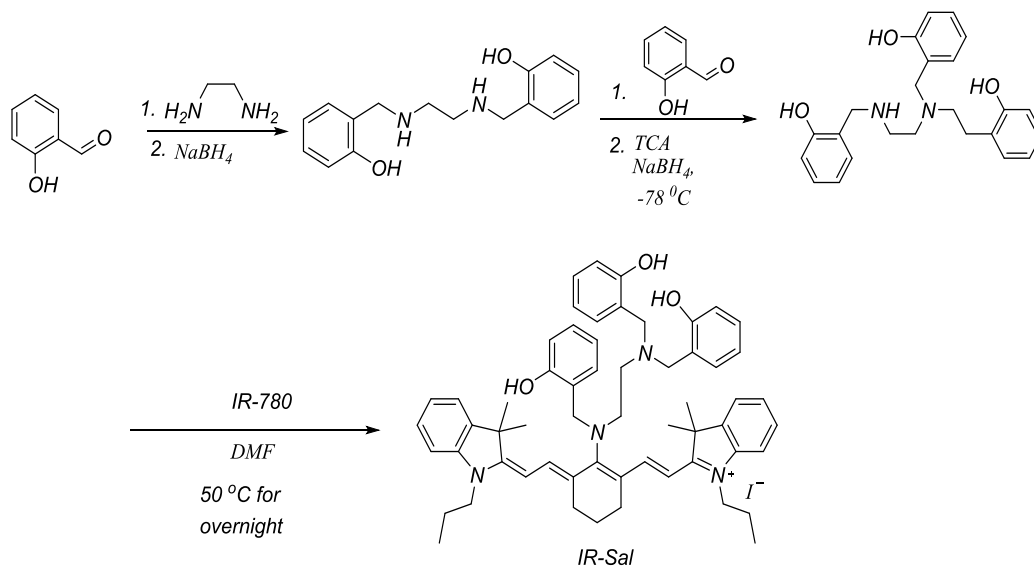
#### A1.2 Synthesis and Characterization

##### A1.2.1 Heptamethine Cyanine-Based Sensors

###### A1.2.1.1 Synthesis of IR-Sal

We designed the sensor IR-Sal (see Scheme A1.1) for  $\text{Fe}^{3+}$ ; however, it gives response to  $\text{Cu}^{2+}$  ions. N,N,N'-Tris(2-hydroxybenzyl)-1,2-diaminoethane binding moiety was synthesized according to the published method.<sup>[1]</sup>

**Synthesis of IR-Sal:** IR-780 (200 mg, 0.3 mmol) and N,N,N'-tris(2-hydroxybenzyl)-1,2-diaminoethane (120 mg, 0.4 mmol) were dissolved in anhydrous N,N-dimethylformamide (DMF) (20 mL). The mixture was stirred at 85 °C for overnight under an argon atmosphere. The solvent was removed under reduced vacuum. Mass spectrum of the crude product was obtained. The targeted-compound was in the crude product. DCM/MeOH (40/1) was used for the eluent for the column chromatography. However, the pure IR-Sal could not be obtained (70% pure of IR-Sal). ESI m/z (positive mode) ( $\text{C}_{59}\text{H}_{69}\text{O}_3\text{N}_4^+$ ), calc: 881.5; found: 881.3 (without  $\text{I}^-$ ).



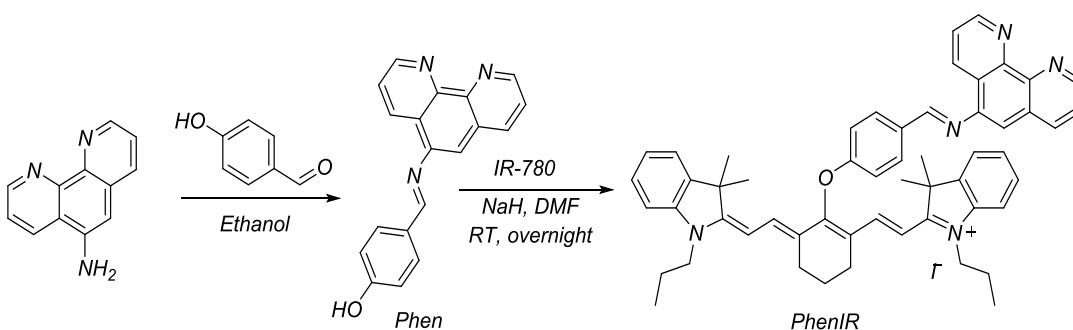
**Scheme A1.1** Synthesis route for IR-Sal

#### A1.2.1.2 Synthesis of IRPhen

Even though IRPhen was the one of the sensors designed for  $\text{Fe}^{2+}$ , it showed a decreased emission fluorescence response to  $\text{Cu}^{2+}$ . The binding receptor was synthesized according to the published method.<sup>[2]</sup>

**Synthesis of IRPhen:** Under nitrogen atmosphere, slurry of NaH (60% in mineral oil, 15.2 mg 0.38 mmol) and DMF (1 mL) was added to a stirring solution of Phen (0.120 g, 0.4 mmol) in anhydrous DMF (2 mL) at 0 °C. After 30 min., the reaction was allowed to warm up to ambient temperature. This was added to a solution of IR-780 (200 mg, 0.3 mmol) in DMF (3 mL). The reaction was stirred for overnight, and then quenched with water. The solution was evaporated by vacuum not over 40 °C to get dark green solid crude product. The crude product was purified by column chromatography on silica gel (DCM/MeOH; 100/0 to 90/10) to yield IRPhen (40 mg, yield 15%).  $^1\text{H}$  NMR (300 MHz,  $\text{CDCl}_3$ )  $\delta$ (ppm): 9.18- 9.05 (d, 1H), 8.84 (d, 1H), 8.51 (d, 1H), 8.22 (d, 2H), 8.13 - 7.85 (m, 2H), 7.79 (d, 1H), 7.71 - 7.54 (m, 2H), 7.51 - 6.99 (m, 9H), 6.96 (s, 1H),

6.11 (d, 1H), 4.18 - 3.62 (m, 4H), 3.48 (s, 2H), 3.17 (t, 2H), 1.96 (t, 2H), 1.96 (t, 4H), 1.49 (s, 6h), 1.37 (m, 2H), 0.95 (t, 6H).  $^{13}\text{C}$  NMR (75 MHz,  $\text{CDCl}_3$ )  $\delta$ (ppm): 170.3, 167.84, 164.33, 154.54, 149.43, 147, 146, 141.6, 140.9, 139, 138.3, 137, 136.3, 135, 133.6, 132, 131.93, 130.4, 128.4, 125.3, 124.4, 123.3, 122.2, 121.8, 121.2, 120.6, 117.4, 114.5, 112, 111, 97.1, 52.4, 50.1, 49.2, 45.3, 28.1, 28, 26.9, 26.2, 23.2, 21.5, 20.4, 12.1, 11.4; ESI m/z (positive mode) ( $\text{C}_{55}\text{H}_{56}\text{ON}_5^+$ ), calc: 802.4; found: 802.3 (without I<sup>-</sup>).



**Scheme A1.2** Synthesis route for IRPhen

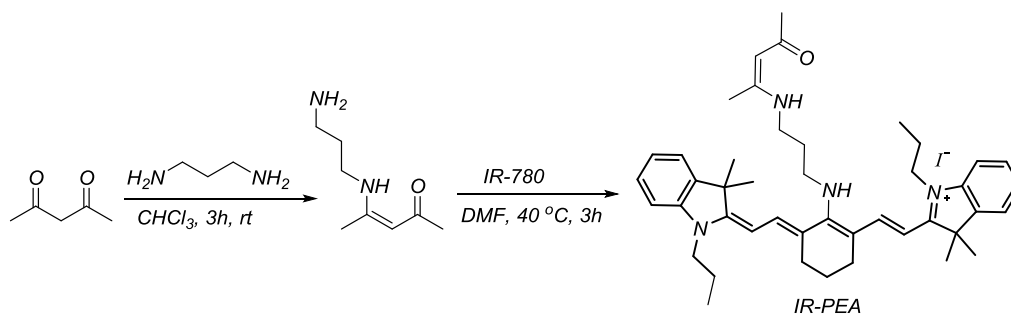
### A1.2.1.3 Synthesis of IR-PEA

IR-PEA is a turn-off  $\text{Cu}^{2+}$ -selective sensor. The binding moiety (Z)-4-(3-aminopropylamino)pent-3-en-2-one was synthesized according to the published method.<sup>[3]</sup>

**Synthesis Of IR-PEA:** IR-780 (200 mg, 0.3 mmol) and N,N,N'-tris(2-hydroxybenzyl)-1,2-diaminoethane (120 mg, 0.4 mmol) were dissolved in anhydrous N,N-dimethylformamide (DMF) (20 mL). The mixture was stirred at room temperature for 4 h under an argon atmosphere. The solvent was removed under reduced vacuum to deep blue-colored solid crude product. The crude product was purified by column chromatography on silica gel (DCM/MeOH; 100/0 to 95/5) to yield IR-PEA (68 mg, yield 29%).  $^1\text{H}$  NMR (300 MHz,  $\text{CDCl}_3$ )  $\delta$ (ppm): 7.6-6.8 (Ar-H, 8H), 6.54 (d, 1H), 5.46 (d, 1H), 5.3 (d, 1H), 3.1 (s, 6H), 3.02 (m, 2H), 1.56 (m, 2H), 1.49 (s, 6H), 1.4 (m,



2H), 1.3 (m, 4H), 0.96 (t, 6H):  $^{13}\text{C}$  NMR (75 MHz,  $\text{CDCl}_3$ )  $\delta$ (ppm): 199.8, 176.9, 175.9, 151.2, 146.8, 144.7, 143.1, 142.1, 131.2, 129.2, 128.9, 126.6, 124.3, 121.2, 119.9, 109, 106.4, 104.8, 104, 55, 54.9, 47.3, 44.3, 40.9, 31.6, 28.8, 27.4, 26.3, 25.4, 22.4, 21.9, 12.8, 11.4: ESI  $m/z$  (positive mode) ( $\text{C}_{44}\text{H}_{59}\text{ON}_4^+$ ) calc: 659.5; found: 659.3 (without I $^-$ ).



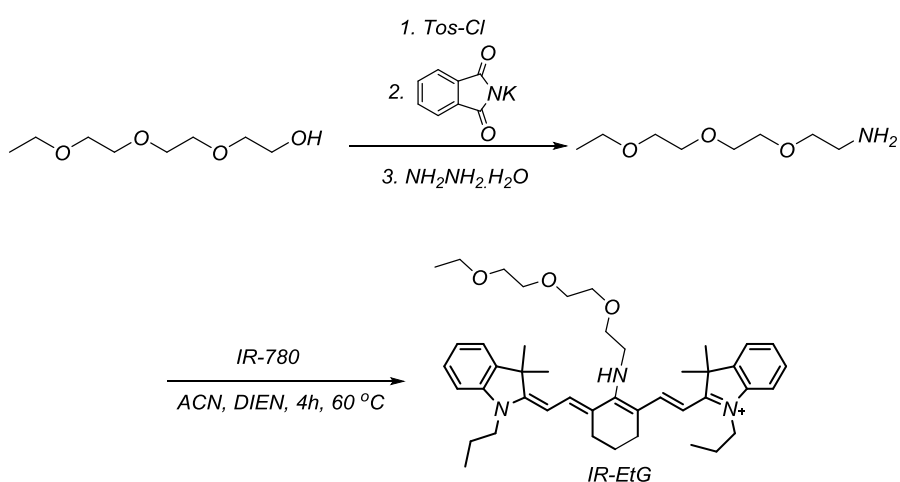
**Scheme A1.3** Synthesis route for IR-PEA

#### A1.2.1.4 Synthesis of IR-EtG

The sensor, IR-EtG was designed to bind  $\text{Fe}^{3+}$  with 3 oxygen and a nitrogen atoms. However, it showed a decreased fluorescence with  $\text{Cu}^{2+}$ . 2-(2-(2-ethoxyethoxy)ethoxy)ethanamine was synthesized according to the published method.<sup>[4]</sup>

**Synthesis Of IR-EtG:** IR-780 iodide (200 mg, 0.3 mmol) and 2-(2-(2-ethoxyethoxy)ethoxy)ethanamine (106 mg, 0.6 mmol) were dissolved in ACN (15 mL), and N,N-disopropylethylamine (DIEA) (77  $\mu\text{L}$ , 0.6mmol, 2 equiv.) was added. The reaction was stirred at 70 °C for 4 h under nitrogen atmosphere. The resulting blue color crude mixture was neutralized with 0.1 M HCl, and concentrated under vacuum. The crude product was purified by column chromatography on alumina gel (DCM/MeOH; 100/0 to 95/5) to yield IR-EtG (56 mg, yield 23%).  $^1\text{H}$  NMR (300 MHz,  $\text{CDCl}_3$ )  $\delta$ (ppm): 7.48-7.04 (m, 4H), 6.98 (s, 1H), 6.63 (d, 2H), 6.33 (s, 1H), 6.32 (s, 1H), 5.42 (s, 1H), 5.03 (s, 1H), 4.52(d, 2H), 3.43 (s, 1H), 3.37-3.11 (m, 10H), 3.07 (d, 4H), 2.98 (s, 1H), 2.87 (d, 2H),

2.19 - 2.04 (m, 2H), 2.00-1.95 (m, 2H), 1.84-1.79 (m, 1H), 1.63 - 1.56 (m, 4H), 1.55 -1.50 (m, 6H), 1.27-1.22 (m, 6H), 1.22-1.17 (m, 3H), 1.06- 1.01 (m, 6H);  $^{13}\text{C}$  NMR (75 MHz,  $\text{CDCl}_3$ )  $\delta$ (ppm): 172.1, 163.6, 141.3, 140.9, 140.2, 139.9, 139.3, 138.7, 123.7, 123.3, 122.9, 122.6, 122.1, 111.9, 111.3, 109.6, 102.1, 95.6, 70.9, 68.6, 68.1, 67.9, 65.8, 50.6, 49.8, 48.8, 43.1, 42.9, 26.9, 26.3, 25.8, 24.9, 24.6, 24.1, 22.3, 19.6, 18.1, 14.9, 12.1, 11.9: ESI  $m/z$  (positive mode) ( $\text{C}_{44}\text{H}_{62}\text{O}_3\text{N}_3^+$ ), calc: 680.4; found: 680.2 (without I<sup>-</sup>).



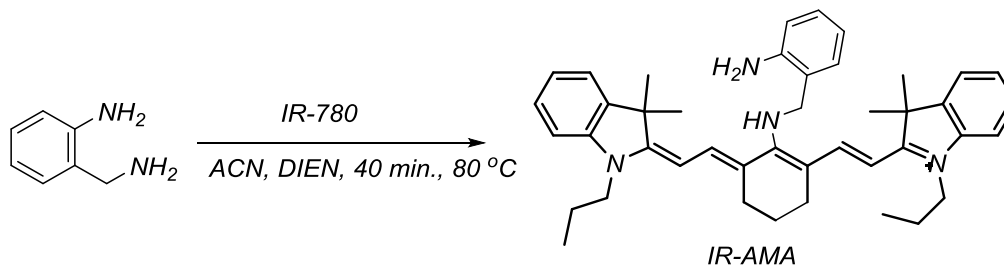
**Scheme A1.4** Synthesis route for IR-EtG

#### A1.2.1.4 Synthesis of IR-AMA

IR-AMA is a ratiometric sensor for NO, and shows a decreased emission for  $\text{Cu}^{2+}$ .

**Synthesis of IR-AMA:** A mixture of IR-780 (100 mg, 0.15 mmol), 2-amino-Benzenemethanamine (70 mg, 0.57 mmol) and N,N-disopropylethylamine (DIEA) (77  $\mu\text{L}$ , 0.6mmol, 4 equiv) were dissolved in ACN (15 mL) and heated at 80 °C for 40 min. The resulting blue colored crude mixture was neutralized with 0.1 M HCl, and concentrated under vacuum. The crude product was purified by normal phase chromatography on alumina gel (DCM/MeOH; 98/2) to yield IR-AMA (39 mg, yield 35%).  $^1\text{H}$  NMR (300 MHz,  $\text{CDCl}_3$ )  $\delta$  (ppm): 7.66 (d, 2H), 6.58-7.27 (m, 12H),

5.64 (d, 2H), 5.06 (s, 2H), 4.01 (s, 1H), 3.78 (s, 4H), 2.45 (m, 4H), 1.80 (d, 6H), 1.54 (d, 12H), 1.29 (m, 4H), 1.02 (t, 6H);  $^{13}\text{C}$  NMR (75 MHz,  $\text{CDCl}_3$ )  $\delta$  (ppm): 170.2, 168.4, 168.1, 145.2, 143.2, 141.5, 140.6, 140.4, 139.2, 129.4, 128.5, 128.1, 127.7, 126.4, 124.1, 123.1, 122.9, 121.6, 120.4, 118.9, 117.4, 116.7, 109.7, 106.6, 97.4, 94.8, 52.5, 48.5, 48, 45, 44.9, 28.9, 28.5, 27.5, 24.8, 21.7, 20.6, 20.2, 11.9; ESI  $m/z$  (positive mode) ( $\text{C}_{43}\text{H}_{53}\text{N}_4^+$ ), calc: 625.4; found: 625.2 (without  $\text{I}^-$ ).



**Scheme A1.5** Synthesis route for IR-AMA

### A1.2.2 Rhodamine-Based Sensors

Here, two rhodamine based fluorescent sensors, Rh-2S and Rh-3S were designed for  $\text{Fe}^{2+}$  ions, but Rh-2S was a  $\text{Cu}^{2+}$ -selective and Rh-3S was an  $\text{Hg}^{2+}$ -selective turn-on sensors. Rhodamine b hydrazine was synthesized according to the published method.<sup>[5]</sup>

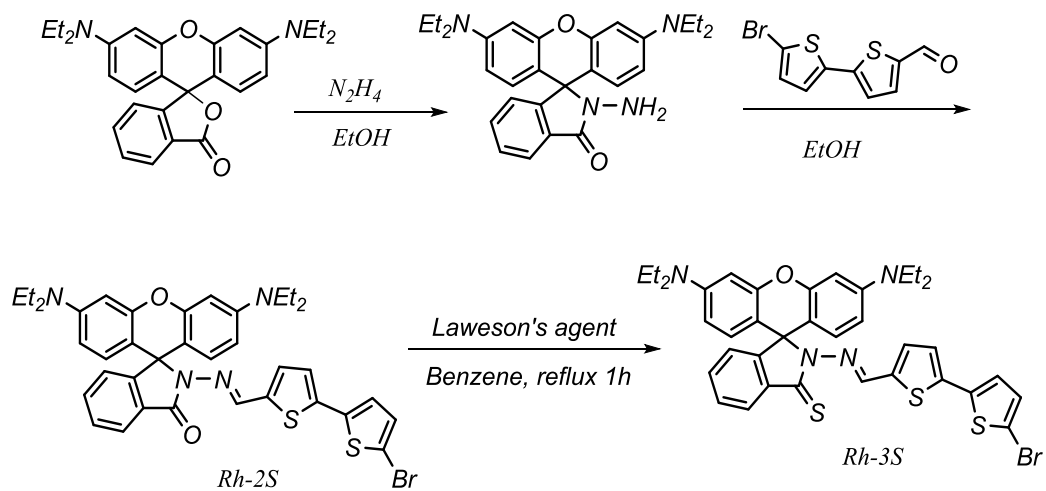
#### A1.2.2.1 Synthesis of Rh-2S

Rhodamine b hydrazine (0.5 mmol, 0.278 g) and 5-Bromo-2,2'-bithiophene-5'-carboxaldehyde (0.5 mmol, 0.137 g) were mixed in boiling ethanol then the mixture was refluxed for 6 h. After that, the solution was cooled and allowed to stand at room temperature overnight. The precipitate that appeared next day was filtered and washed 3 times with 10 mL cold ethanol. After drying under reduced pressure, it was recrystallized in MeOH to afford 0.21 g Rh-2S (60%) as pale yellow solid.  $^1\text{H}$  NMR (300 MHz,  $\text{CDCl}_3$ )  $\delta$ (ppm): 8.78 (1 H, s, CH=N), 7.98 (1 H, t, rh-H,  $J=6.2$  Hz), 7.49 (2H, d, tiol-H,  $J=2.7$  Hz), 7.25 (2H, t, rh-H,  $J=4.0$  Hz), 7.13 (1H, br,

rh-H) 6.92(2 H, d, rh-H, J = 8.8 Hz), 6.57(2 H, d, rh-H, J = 8.8 Hz), 6.52(2H, s, rh-H), 6.23 (2H, br, tiol-H), 3.39 (8 H, q, N-CH<sub>2</sub>, J = 9.6 Hz) 1.23 (12 H, t, -CH<sub>3</sub>, J=6.6 Hz). <sup>13</sup>C NMR (75 MHz, CDCl<sub>3</sub>) δ(ppm):164, 153, 151, 148, 141, 140, 138.8,138.2, 133, 130.7, 130.2, 129, 128, 127, 124, 123.8, 123.3, 111, 107, 105, 97, 66, 44, 12. MS: m/z 710.3 for [Rh-2S+H]<sup>+</sup> 711.4.

#### **A1.2.2.1 Synthesis of Rh-3S**

Rh-2S (0.08 g, 0.11 mmol) and Lawesson's reagent (0.045 g, 0.15 mmol) were dissolved in dry benzene, and the reaction mixture was stirred at 80 °C for 1 h under N<sub>2</sub> atmosphere. After removing the solvent under reduced pressure, the residue was purified by column chromatography using EtOAc/Hexane (2;1) as eluent to afford 36 mg Rh-3S as a yellow solid (37%). <sup>1</sup>H NMR (300 MHz, CDCl<sub>3</sub>) δ (ppm): 8.78 (1 H, s, CH=N), 7.98 (1 H, t, rh-H, J=6.2 Hz), 7.49 (2H, d, tiol-H, J=2.7 Hz), 7.25 (2H, t, rh-H, J=4.0 Hz), 7.13 (1H, br, rh-H) 6.92(2 H, d, rh-H, J = 8.8 Hz), 6.57 (2 H, d, rh-H, J = 8.8 Hz), 6.52 (2H, s, rh-H), 6.23 (2H, br, tiol-H), 3.39 (8 H, q, N-CH<sub>2</sub>, J = 9.6 Hz) 1.23 (12 H, t, -CH<sub>3</sub>, J=6.6 Hz). <sup>13</sup>C NMR (75 MHz, CDCl<sub>3</sub>) δ( ppm): 152.2, 152.1, 148.4, 148.1, 134,132.5, 132.4, 132.1, 131, 130.5, 130.3, 127.8, 124, 124.7, 124.1, 122, 110, 108, 97.1, 97, 66, 44, 12. MS: m/z 726.3 for [Rh-3S+H]<sup>+</sup> 727.4.



**Scheme A1.6** Synthesis route for Rh-2S and Rh-3S

### A1.3 References

1. Schmitt H., Lomoth R., Magnuson A., Park J., Fryxellus J., Kritikos M., Martensson J., Hammarstrom L., Sun L., Akermark B., *Chem. Eur. J.* **2002**, 8, 3757-3768
2. Cheng F., Tang N., Chen L., *Z. Anorg. Allg. Chem.*, **2008**, 634, 1608-1612
3. Biswas A., Drew M. G. B., Ghosh A., *Polyhedron*, **2010**, 29, 1029-1034
4. Harjani J. R., Liang C., Jessap P. G., *J. Org. Chem.*, **2011**, 76, 1683-1691
5. Xiang Y., Tong A., Jin P., Ju Y., *Org. Lett.*, **2006**, 8, 2863-2866.

## APPENDIX B

### TABLE SUMMARIZING THE MAJOR PROPERTIES OF THE IRON SENSORS

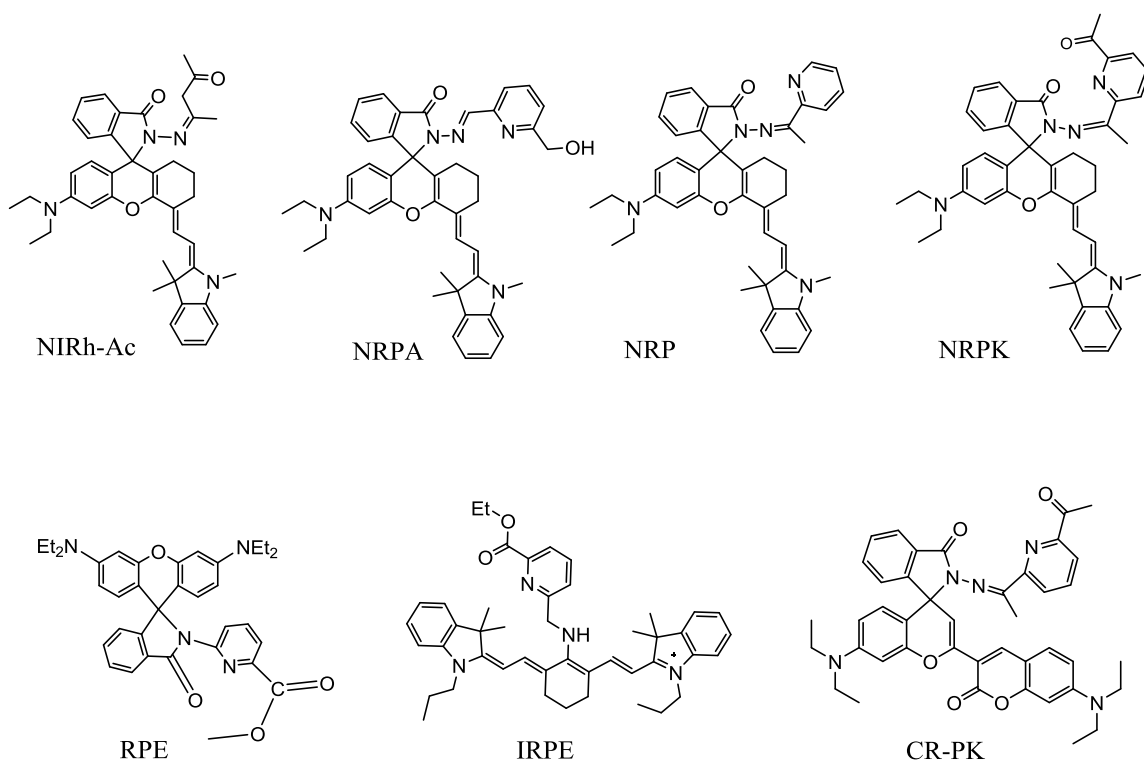


**Figure B.1** Molecular structures of the Fe<sup>3+</sup>-selective fluorescent sensors presented in this thesis

**Table B.1** The major properties of the sensors

Sensor	Sensor type	Ex (with Fe <sup>3+</sup> ) (nm)	Em (with Fe <sup>3+</sup> ) (nm)	Binding Constant	Quantum yield	Cell types	Endogenous/ Exogenous	Colocalization	Zebrafish Studies
RPE	Turn-on	559	584	$2.0 \times 10^7$ M <sup>-1</sup>	0.20	Human neuroblastoma cells (SH-SY5Y)	Endogenous	Lyso/mito	N.A
IRPE	Ratio-metric	664 (without Fe <sup>2+</sup> ) 523	760 (without Fe <sup>2+</sup> ) 580	$2.0 \times 10^8$ M <sup>-1</sup>	N.C	Not capable of detecting Fe <sup>2+</sup> ions in cells	-----	-----	-----
NIRh-Ac	Turn-on	713	735	$5.02 \times 10^8$ M <sup>-1</sup>	0.0194 (sensor) 0.236 (+Fe <sup>2+</sup> )	Fibro cells (ws1) Human neuroblastoma cells (SH-SY5Y)	Exogenous	Lyso/Mito for SH-SY5Y Only Mito for WS1	Liver/gall bladder And head
NRPA	Turn-on	710	750	$6.76 \times 10^8$ M <sup>-1</sup>	0.198 (+Fe <sup>2+</sup> )	ws1 SH-SY5Y	Endogenous	Lyso/Mito for SH-SY5Y Only Mito for WS1	Liver/gall bladder
NRPK	Turn-on	715	740	$2.16 \times 10^{12}$ M <sup>-2</sup>	0.189 (+Fe <sup>2+</sup> )	Bovine aortic endothelial cells (BAEC) And SH-SY5Y	Endogenous	Lyso/Mito for SH-SY5Y and BAEC	Liver/gall bladder
NRP	Turn-on	714	745	$5.6 \times 10^{12}$ M <sup>-2</sup>	0.174 (+Fe <sup>2+</sup> )	BAEC	Endogenous	Lyso/Mito for BAEC	N.A
CR-PK	Ratio-metric	425 (without Fe <sup>2+</sup> ) 647	470 (without Fe <sup>2+</sup> ) 704	$2.94 \times 10^7$ M <sup>-1</sup>	0.582 (sensor) 0.164 (+Fe <sup>2+</sup> )	SH-SY5Y WS1 BAEC	Endogenous	Lyso/Mito for SH-SY5Y and BAEC cells Only Mito for WS1	N.A

N. C.: not calculated; N.A: not applied; Lyso: lysosome; mito: mitochondria

## APPENDIX C

### DISTINGUISHING THE OXIDATION STATE OF IRON IN CELLS WITH THE SENSOR CR-PK

The sensors, CR-PK and NRPK were used to detect labile  $\text{Fe}^{3+}$  ions in BAEC cells. We decided to use CR-PK to show that CR-PK is selective for only  $\text{Fe}^{3+}$  not  $\text{Fe}^{2+}$  in BAEC cells. To do this, BAEC cells were incubated with  $\text{Fe}^{2+}$  (20  $\mu\text{M}$ , ferrous ammonium) and  $\text{Fe}^{3+}$  (20  $\mu\text{M}$ , ferric chloride) separately and, then the results were compared to ones gotten from the control (the cells were incubated with CR-PK (20  $\mu\text{M}$ )). The  $\text{Fe}^{3+}$ -treated BAEC cells showed significant increase in fluorescent signal (Figure C.1c, ~5 fold) compared to that without  $\text{Fe}^{3+}$  supplementation. On the other hand, the  $\text{Fe}^{2+}$ -treated BAEC cells did not exhibit any significant increased fluorescent intensity (Figure C1.b, ~1.5 fold). These results show that CR-PK is only capable of detecting  $\text{Fe}^{3+}$  ions in cells.

We repeated the same experiments for live human fibroblast (ws1) cells. Ws1 cells were incubated with 20  $\mu\text{M}$  of ferric chloride ( $\text{FeCl}_3$ ) and 20  $\mu\text{M}$  of ferrous ammonium sulfate separately at 37° C for overnight followed by washing with EMEM medium to remove excess  $\text{Fe}^{3+}$  and  $\text{Fe}^{2+}$ . Then 20  $\mu\text{M}$  of CR-PK was added to ws1 cells and was incubated at 37° C for 30 min. The  $\text{Fe}^{3+}$ -treated ws1 cells showed significant increase in fluorescent signal (Figure C.2c, ~4 fold) compared to that without  $\text{Fe}^{3+}$  supplementation (Figure C.2a), suggesting a positive response of CR-PK to increased labile  $\text{Fe}^{3+}$  in  $\text{Fe}^{3+}$ -treated cells. However, the  $\text{Fe}^{2+}$ -treated ws1 cells did not give any positive response with CR-PK. These results show that CR-PK is only capable of detecting  $\text{Fe}^{3+}$  ions in cells.



These control experiments prove that CR-PK can capture only iron(III) in the cells, not iron(II) ions.

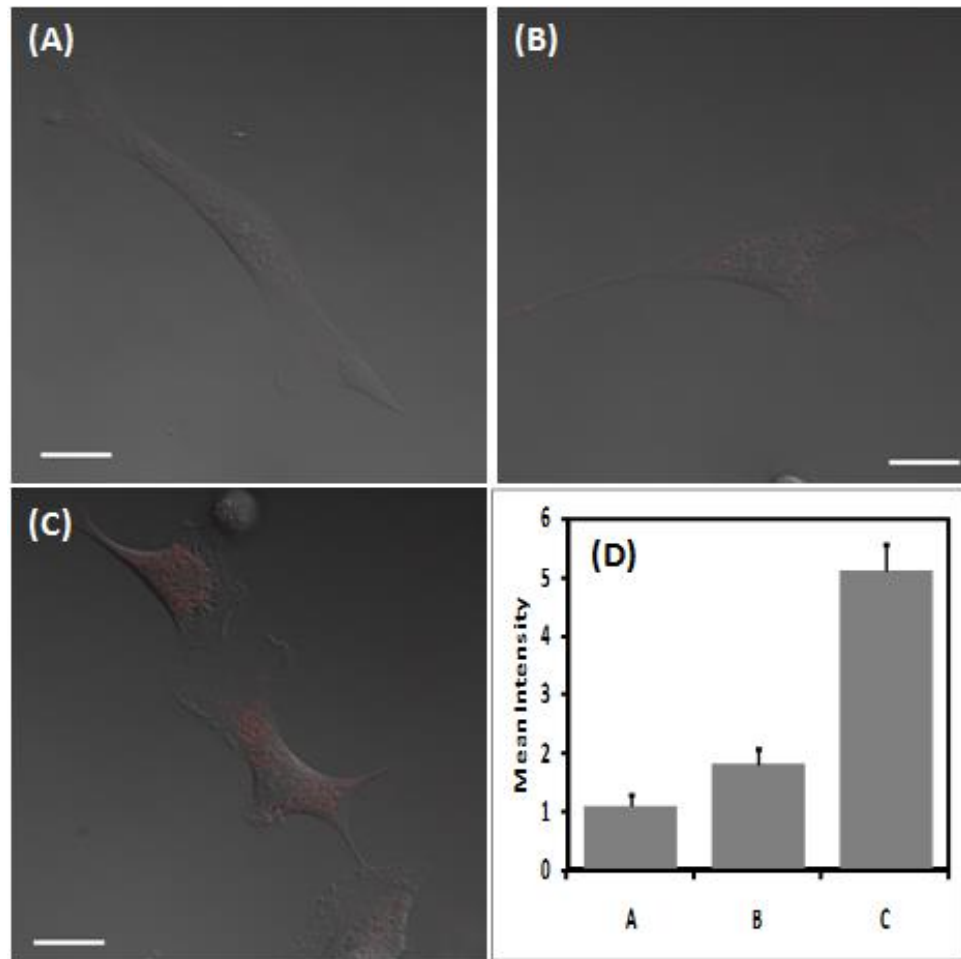


**Figure C.1** Confocal microscopy images (with DIC) of live bovine aortic endothelial cells (BAEC) treated with (a) incubated 20  $\mu\text{M}$  CR-PK (30 min) (b) were pre-incubated with 20  $\mu\text{M}$   $\text{Fe}^{2+}$  (ferrous ammonium sulfate) for overnight then 20  $\mu\text{M}$  CR-PK sensor was added and the images were taken after 30 min incubation (c) were pre-incubated with 20  $\mu\text{M}$   $\text{Fe}^{3+}$  for overnight then 20  $\mu\text{M}$  CR-PK sensor was added and the images were taken after 30 min incubation (d) Bar chart of fluorescent intensities of (a), (b) and (c). (CR-PK was excited at 633 nm, and the fluorescent intensities were collected from 650 nm to 750 nm) (DIC image of cells with 20- $\mu\text{m}$  scale bar)

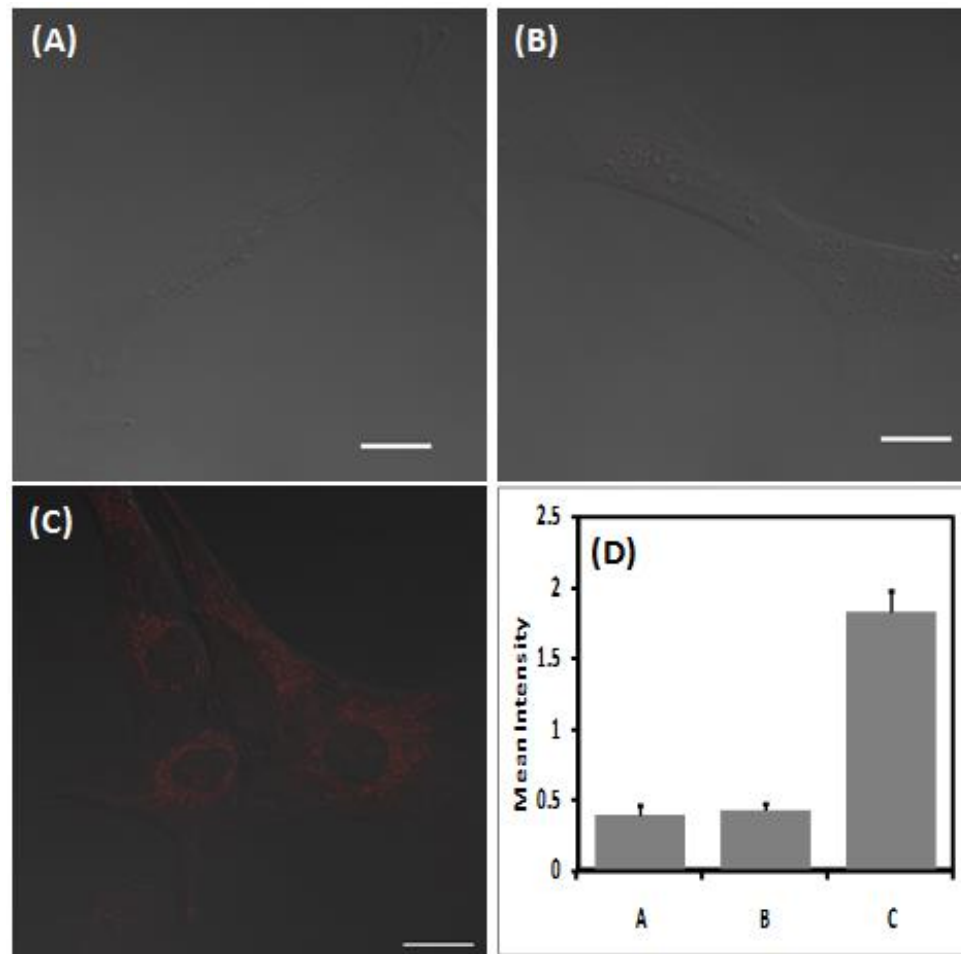


**Figure C.2** Confocal microscopy images (with DIC) of live human fibroblast cells (ws1) treated with (a) incubated 20 μM CR-PK (30 min) (b) pre-incubated with 20 μM Fe<sup>2+</sup> for overnight then 20 μM CR-PK sensor was added and the images were taken after 30 min incubation (c) pre-incubated with 20 μM Fe<sup>3+</sup> for overnight then 20 μM CR-PK sensor was added and the images were taken after 30 min incubation (d) Bar chart of fluorescent intensities of (a), (b) and (c). (CR-PK was excited at 633 nm, and the fluorescent intensities were collected from 650 nm to 750 nm) (DIC image of cells with 20-μm scale bar)

## APPENDIX D

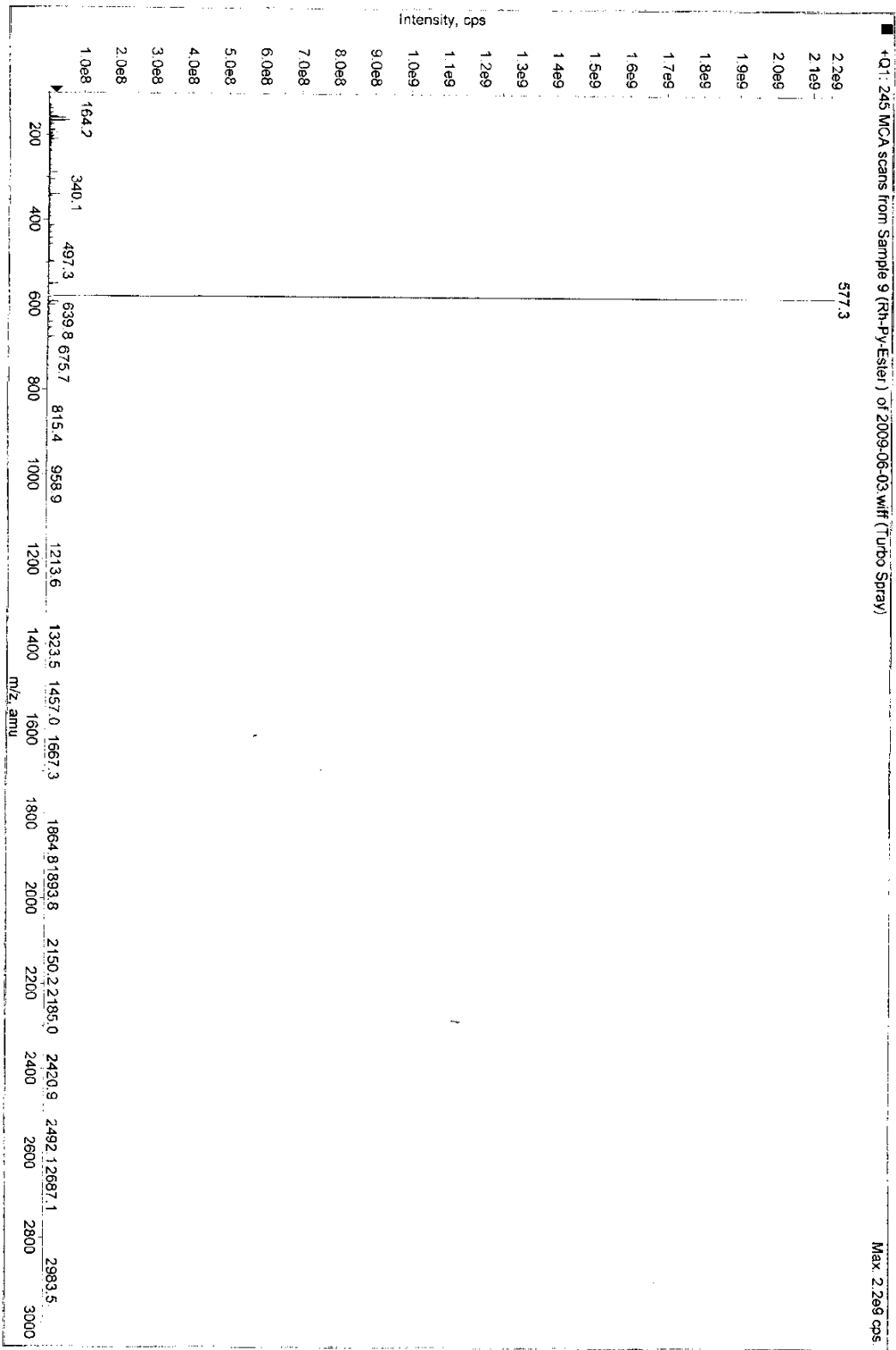
### SPECTROSCOPIC DATA

Shown below are ESI-MS,  $^1\text{H}$  NMR, and  $^{13}\text{C}$  NMR spectra of the sensors and some important intermediate compounds presented throughout this dissertation.  $^1\text{H}$  NMR and  $^{13}\text{C}$  NMR spectra were recorded on a Bruker DRX-300 spectrometer or a Bruker Ascend-400 at ambient probe temperature, 298 K, and ESI-MS analyses were performed on a Perkin Elmer API 150 EX mass spectrometer.

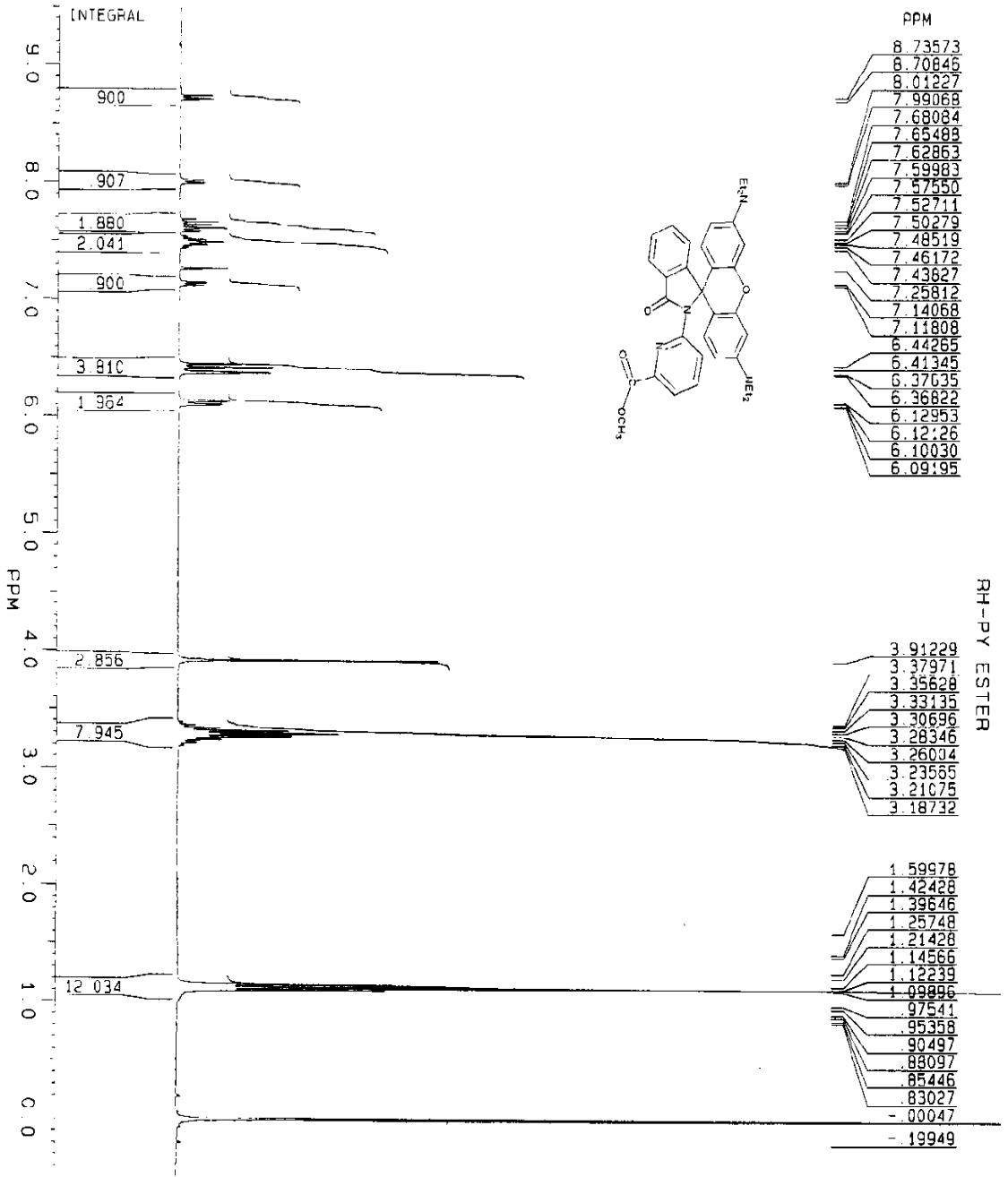
Acq. Date: Wednesday, June 03, 2009  
Acq. Time: 15:35


University of Massachusetts - API150EX S/N 104904  
\*Install Testing: PEG Standard 1x10<sup>-4</sup> M @ 10µL/min

Modelation: API150A  
Operator: API-150A



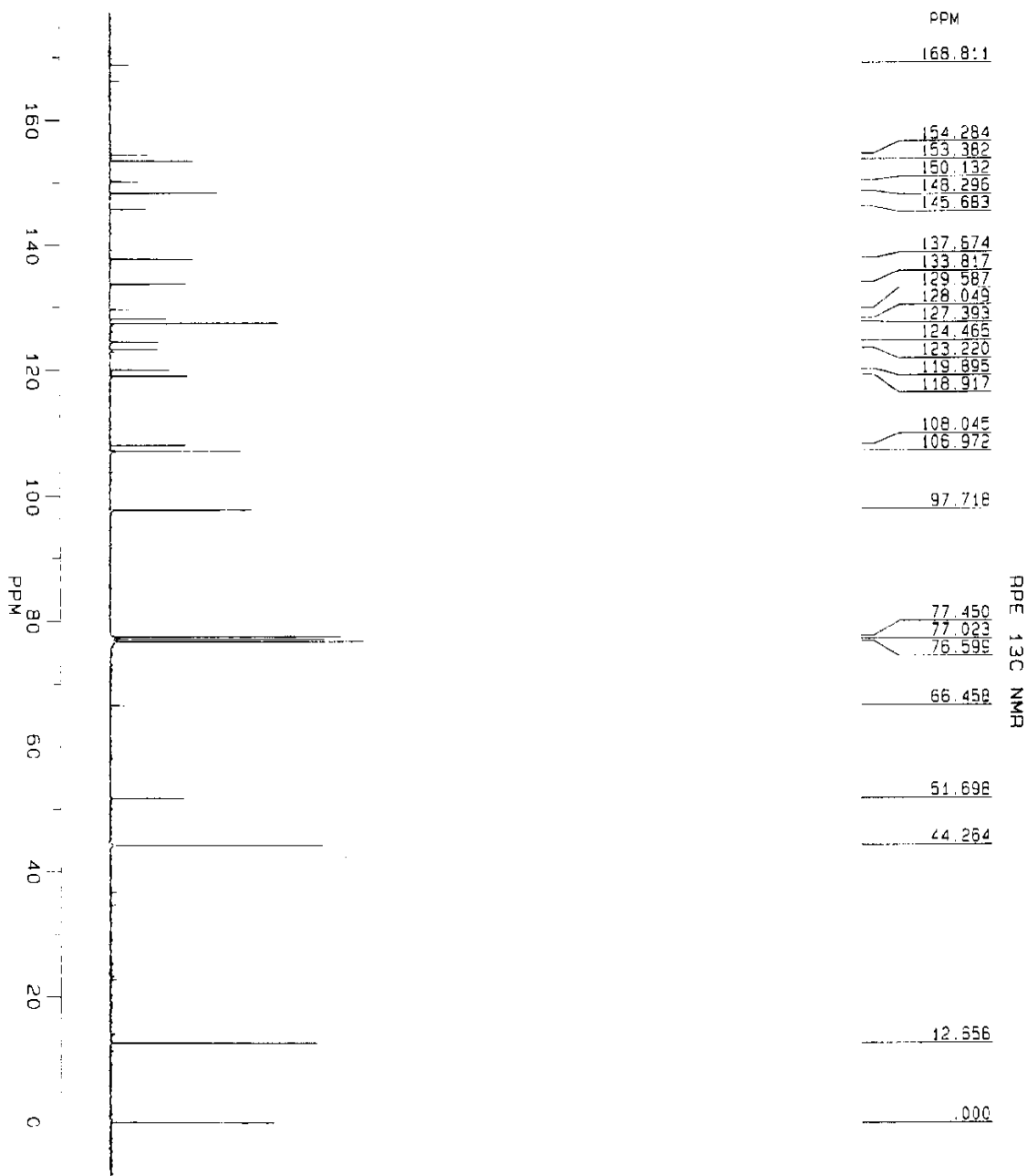
D.1 ESI-Mass spectrum of the sensor RPE





MG031210.100  
 DATE 12-3-10  
 SF 299.0  
 01 4680.000  
 SI 32768  
 TD 32768  
 SW 5376.344  
 HZ/PT .328  
 PW 6.5  
 RD 0.0  
 AG 3.047  
 RG 20  
 NS 32  
 TE 300  
 FW 6800  
 OZ 0.0  
 DP 63L P0  
 LB 300  
 GB 0.0  
 CX 20.00  
 CY 20.00  
 F1 9.500P  
 F2 -500P  
 HZ/CM 150.061  
 PPM/CM 500  
 SR 3369.73

D.2 <sup>1</sup>H-NMR spectrum of the sensor RPE in CDCl<sub>3</sub>



RPE 13C NMR



MG031210.103  
DATE 13-3-10

SF 75.469  
SY 75.0  
O1 6950.000  
S1 32768  
TD 32768  
SW 19230.769  
HZ/PT 1.174

PW 3.0  
RD 1.000  
AQ .852  
RG 200  
NS 12078  
TC 297

FW 24100  
O2 4680.000  
DP 24H CPD

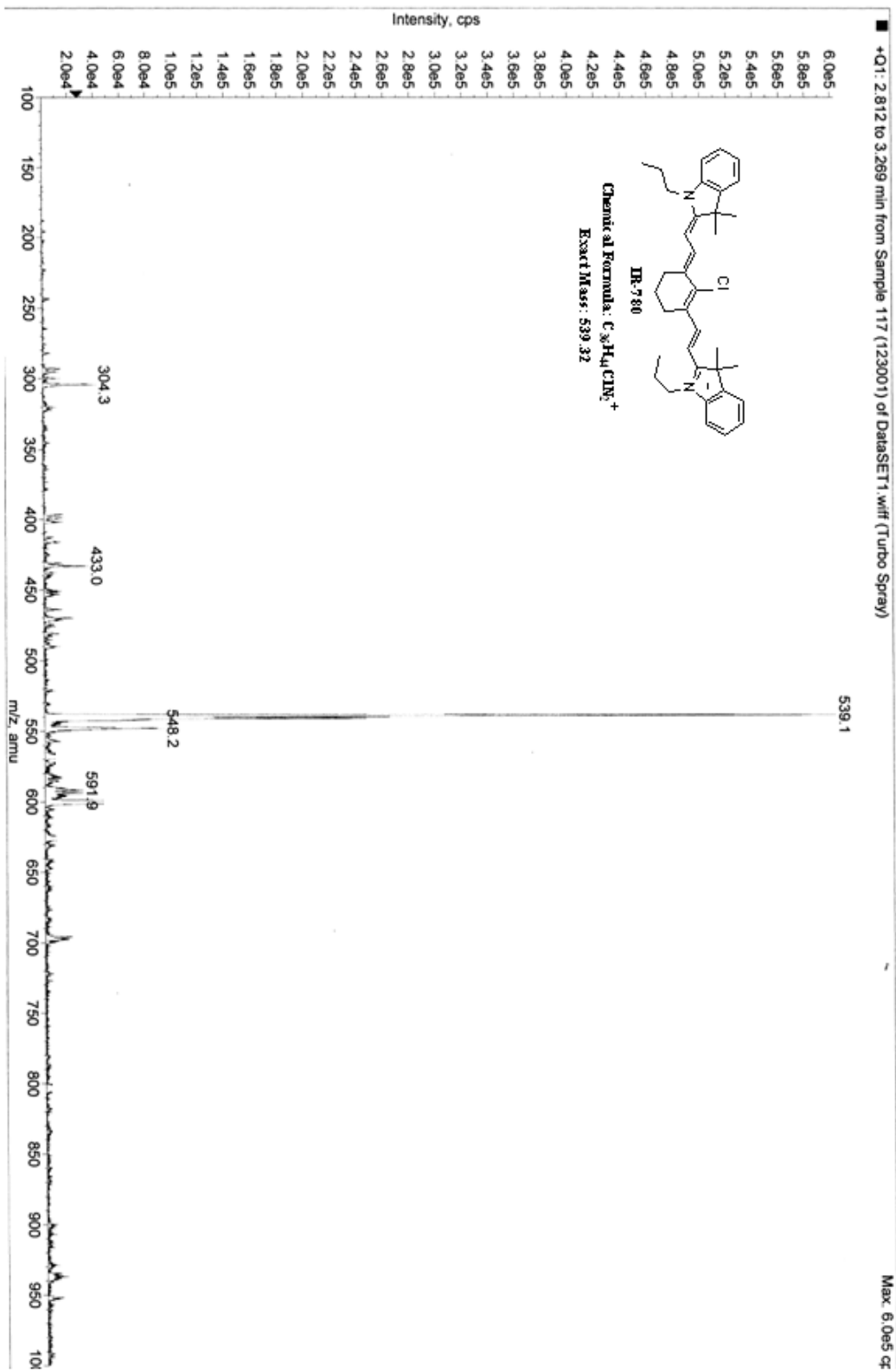
LB .300  
GB 0.0  
CX 20.00  
CY 5.00  
F1 177.100P  
F2 8.834P  
H2/CM 701.611  
PPM/CM 9.297  
SR -1405.95

D.3 <sup>13</sup>C-NMR spectrum of the sensor RPE in CDCl<sub>3</sub>

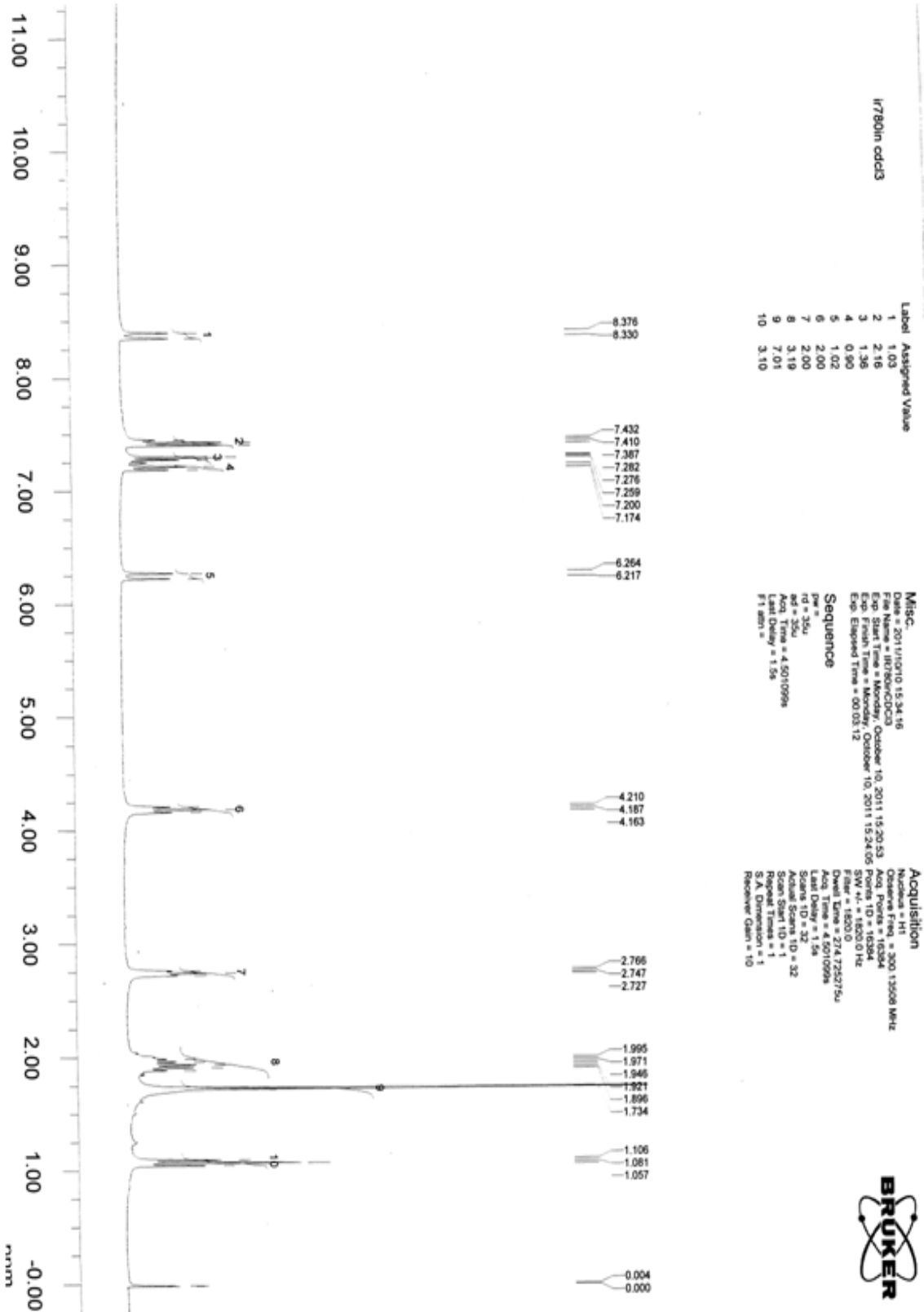
Acq. Date: Thursday, March 29, 2012  
Acq. Time: 09:48

University of Massachusetts - API150EX S/N 104904  
\*Install Testing: PEG Standard 1x10<sup>-4</sup> M @ 10ul/min

Workstation: API150A  
Operator: API-150A



D.4 ESI-Mass spectrum of IR-780 in  $CDCl_3$



D.5 <sup>1</sup>H NMR spectrum of IR-780 in CDCl<sub>3</sub>



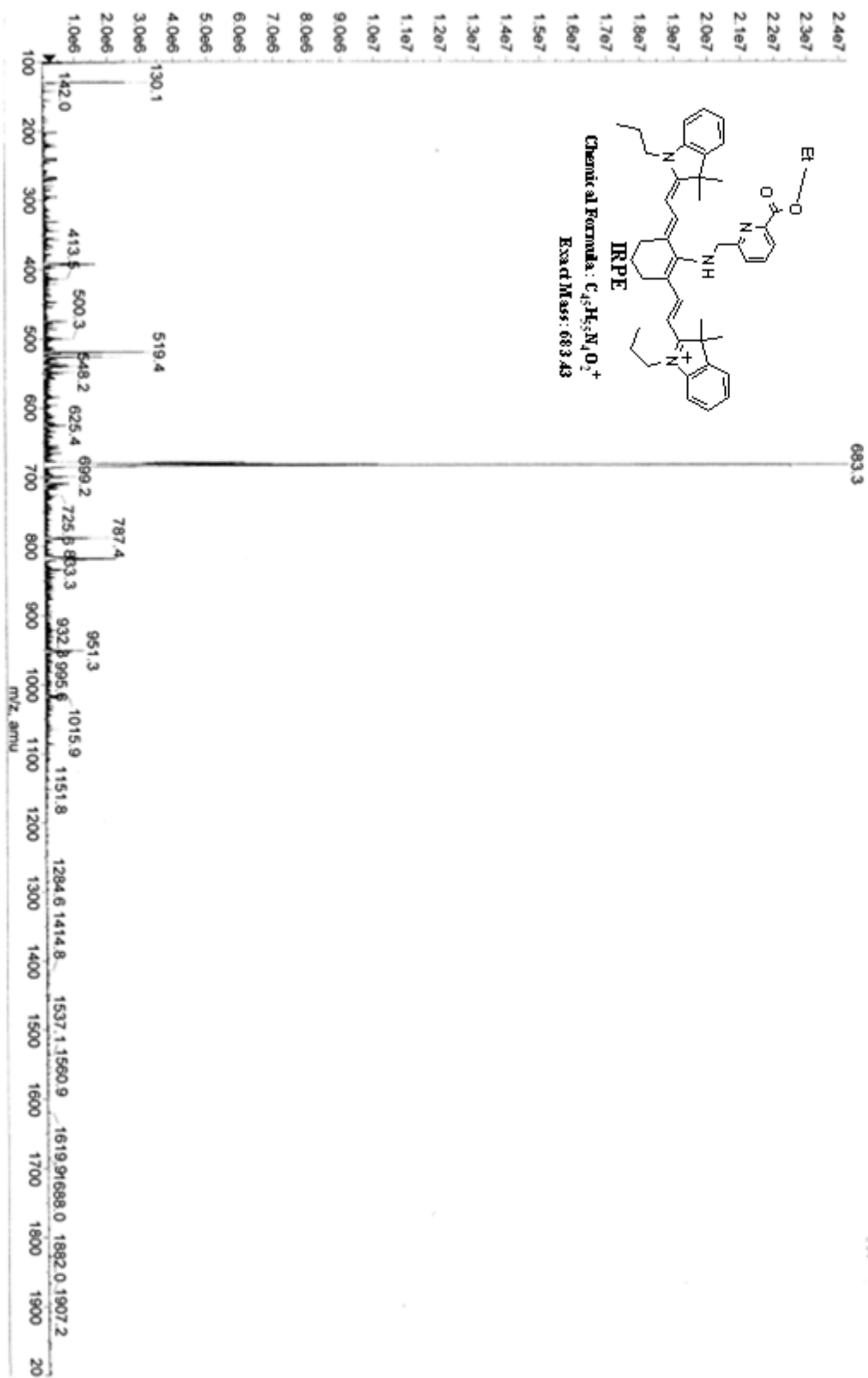
Date: Sunday, March 04, 2012  
Time: 18:03

University of Massachusetts - AP1150EX S/N 104904  
\*Install Testing: PPG Standard 1x10-4 M @ 10uL/min

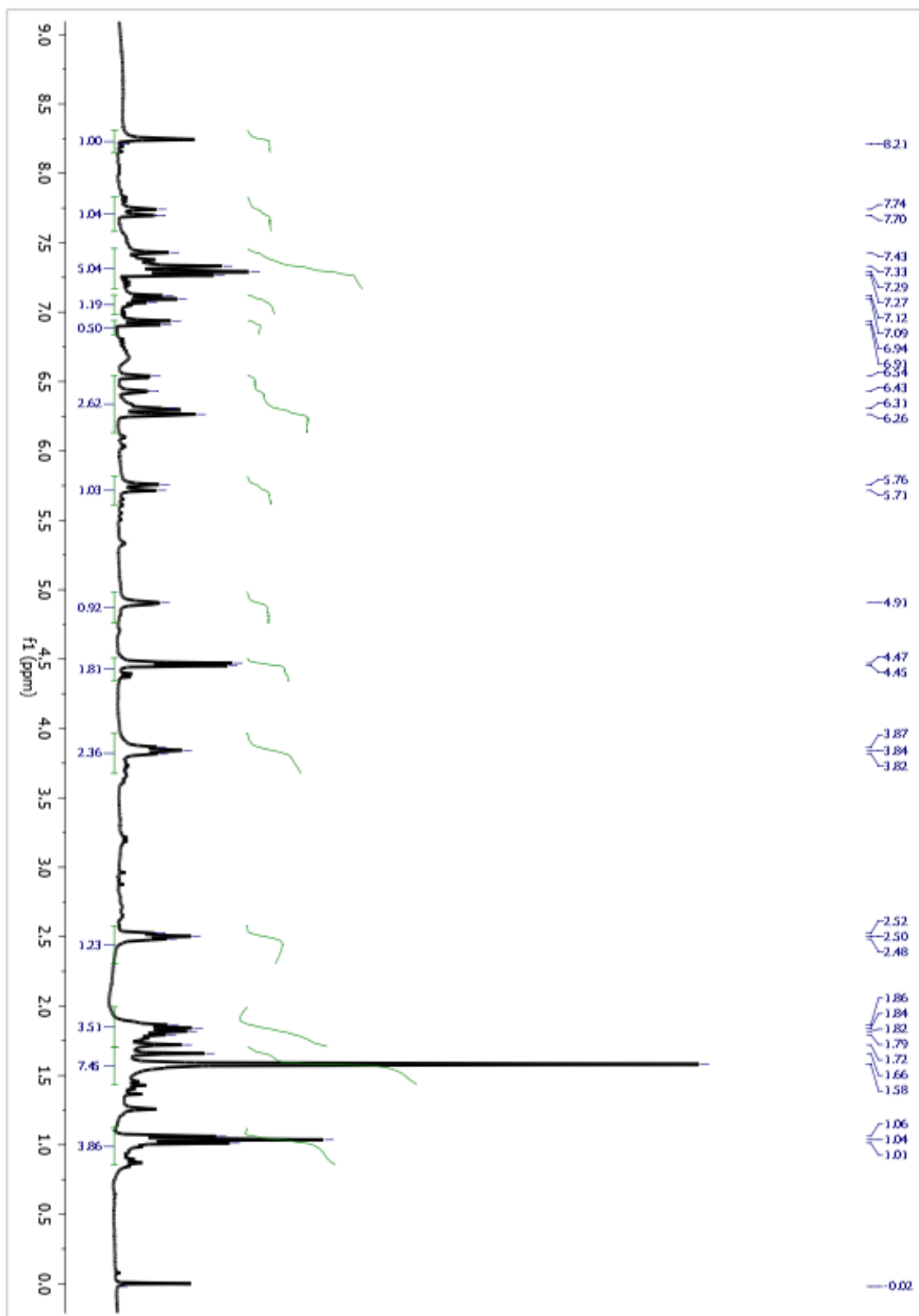
Workstation: AV1100A  
Operator: APF-150A

+Q1: 370 MCA scans from Sample 111 (3001) of Dataset1.wiff (Turbo Spray)

Max 2.4e7 c



D.6 ESI-Mass spectrum of the sensor IRPE

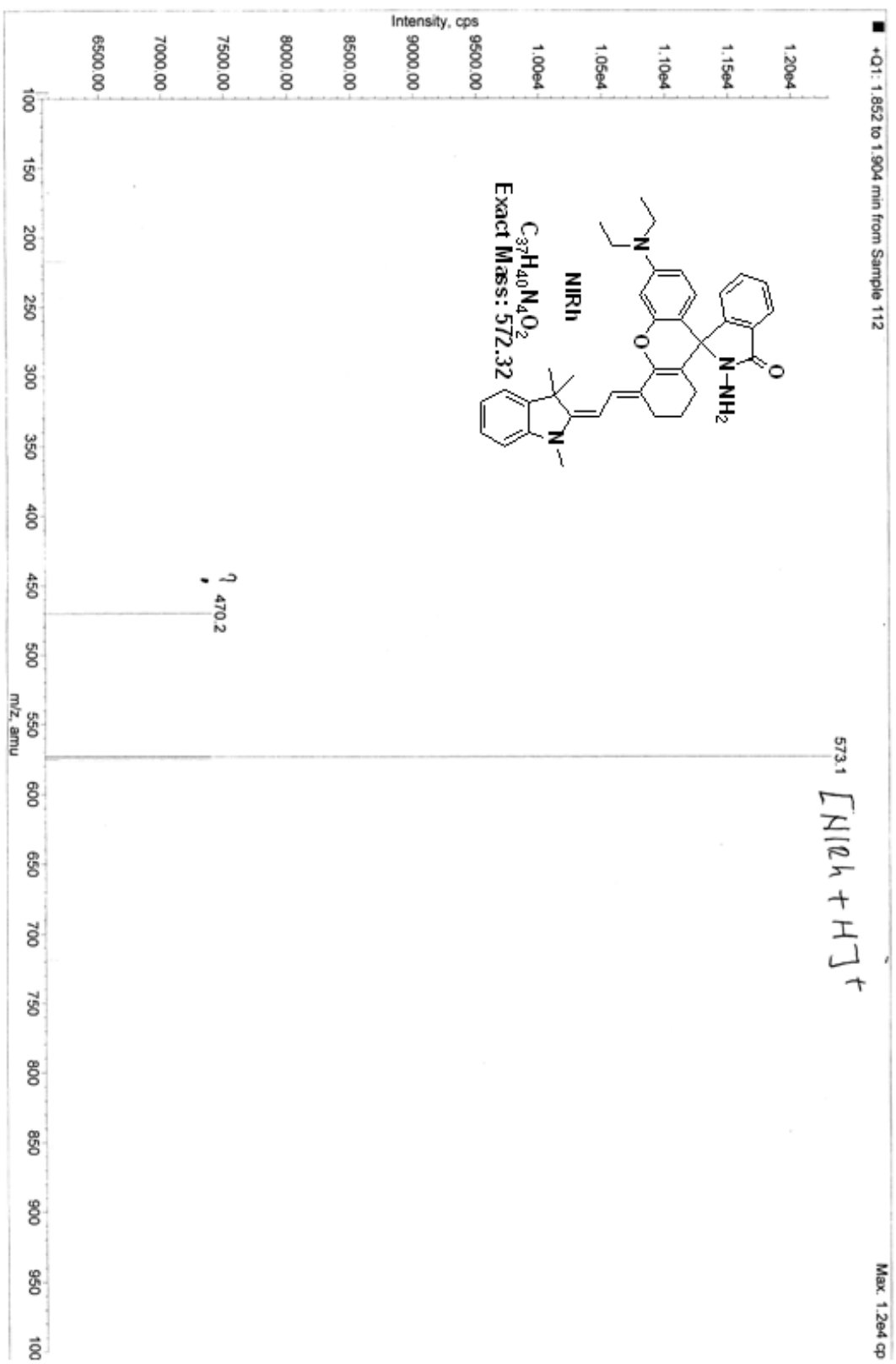


D.7  $^1\text{H}$  NMR spectrum of the sensor IRPE in  $\text{CDCl}_3$

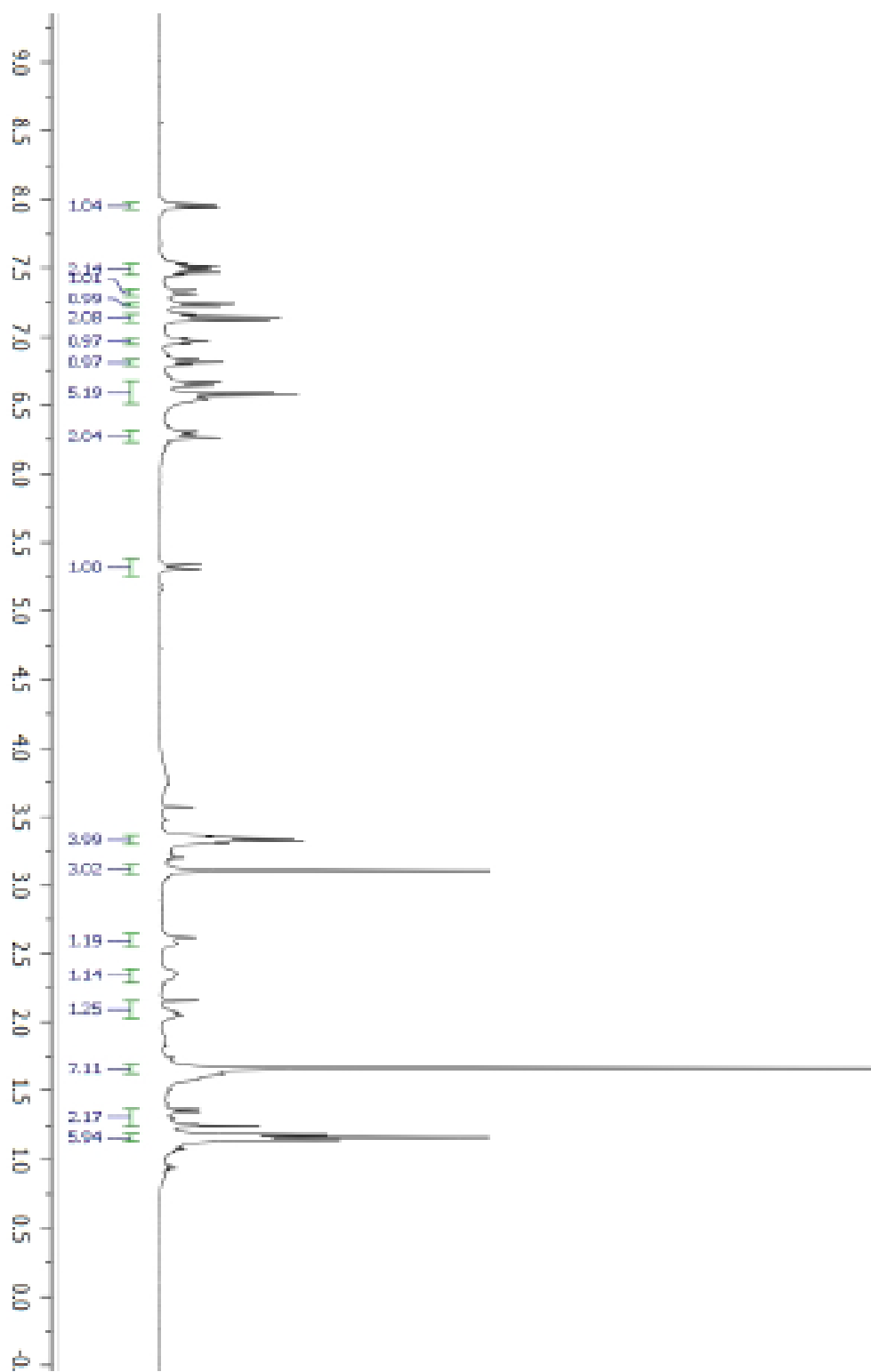
Acq. Date: Tuesday, July 16, 2013  
Acq. Time: 15:29

University of Massachusetts - API150EX S/N 104904  
\* Install Testing: PPG Standard 1X10-4 M @ 10uL/min

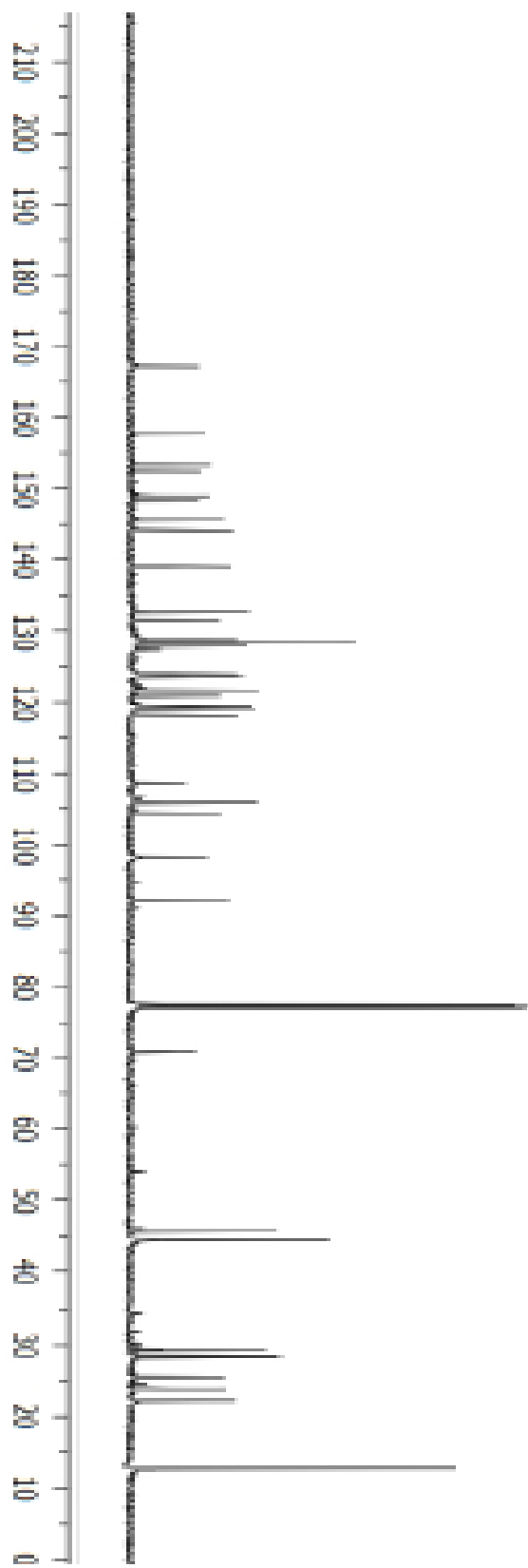
Workstation: API150A  
Operator: API-150A



D.8 ESI-Mass spectrum of NIRh



D.9  $^1\text{H}$  NMR spectrum of NIRh in  $\text{CDCl}_3$

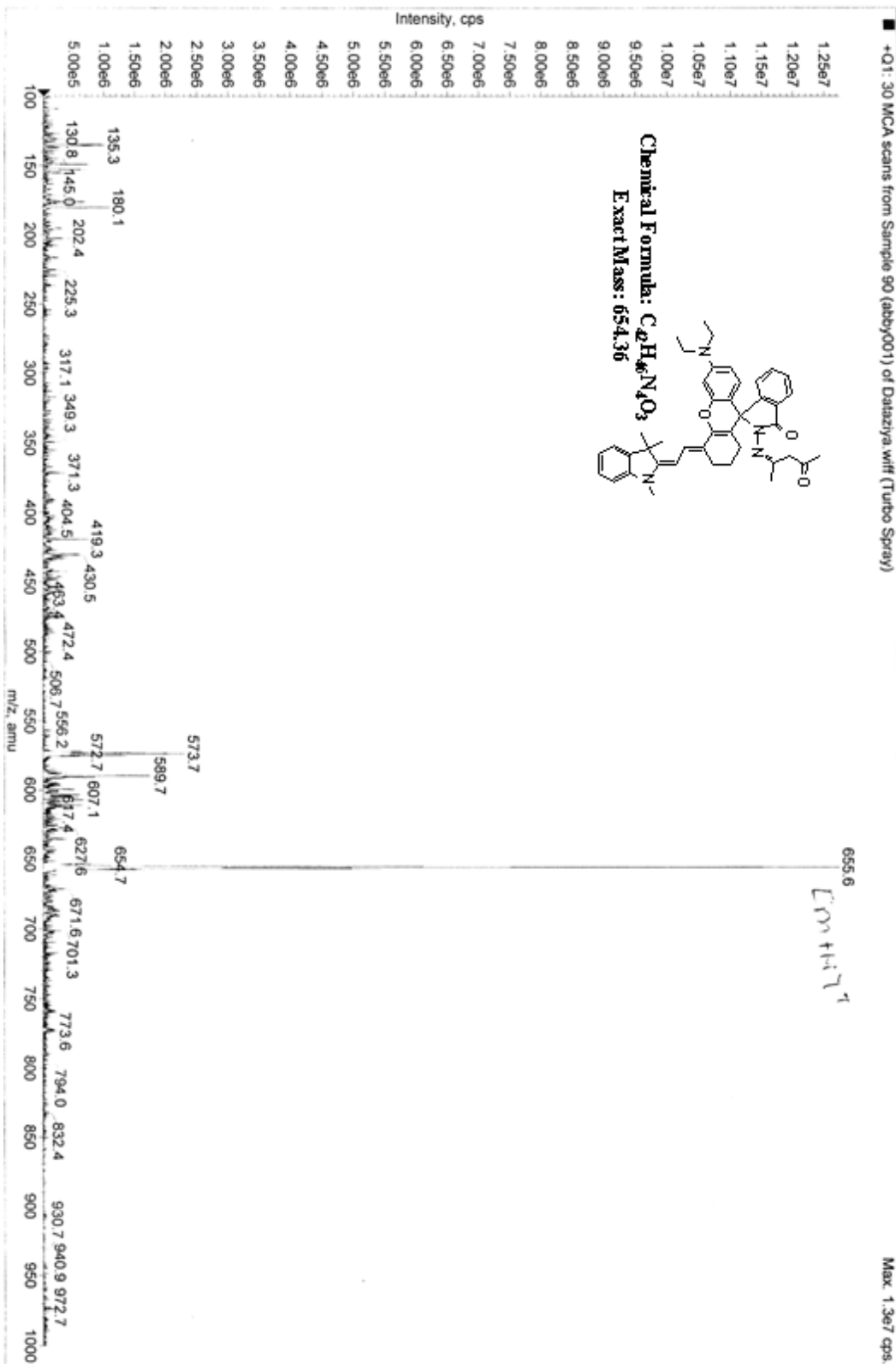


D.10  $^{13}\text{C}$  NMR spectrum of NIRh in  $\text{CDCl}_3$

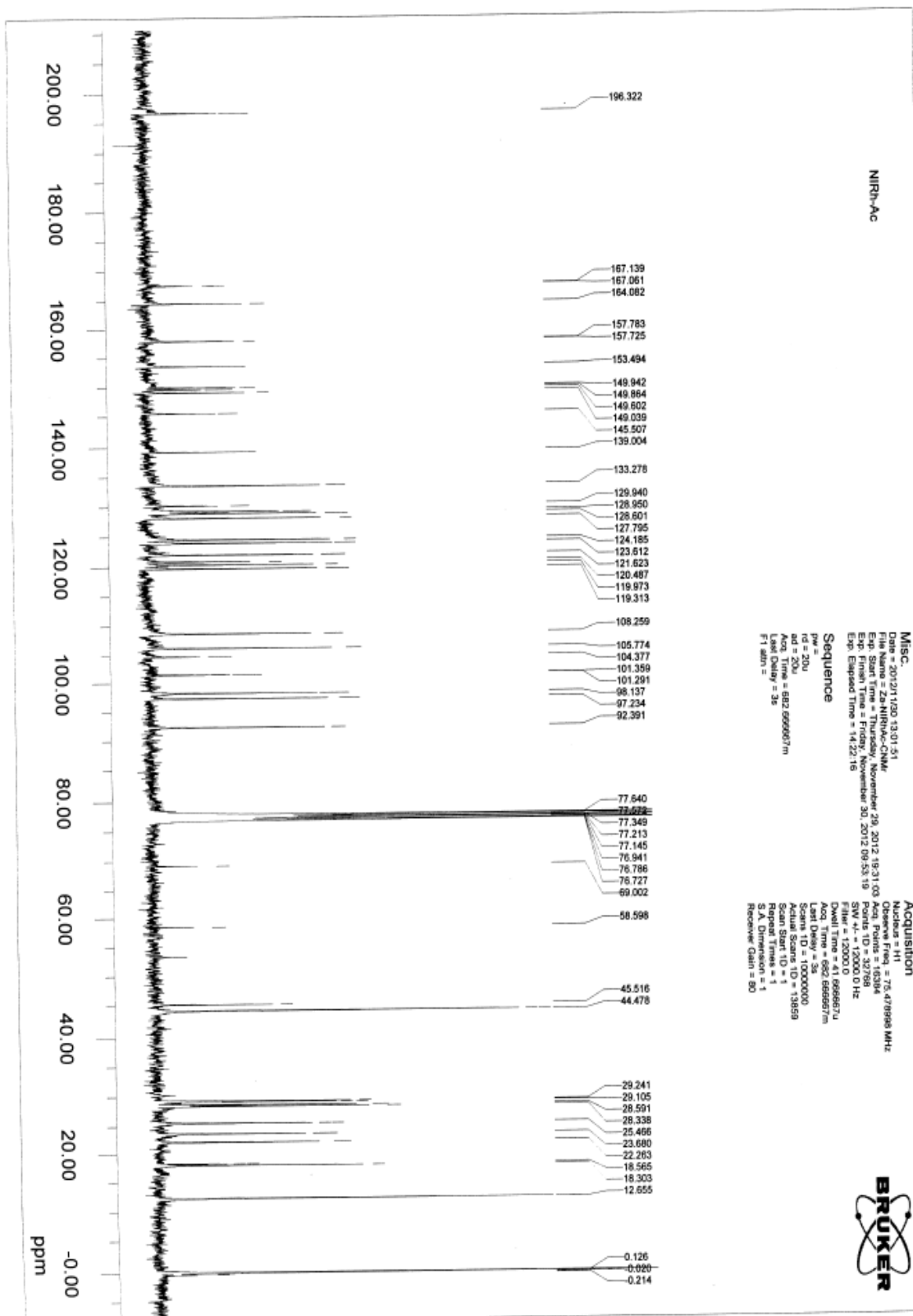
Acq. Date: Sunday, September 09, 2012  
Acq. Time: 16:32

University of Massachusetts - AP1150MCA S/N 012961142  
Post Install Testing: PPG Standard 1x10-4M @ 10uL/min  
Operator: AP1-150B

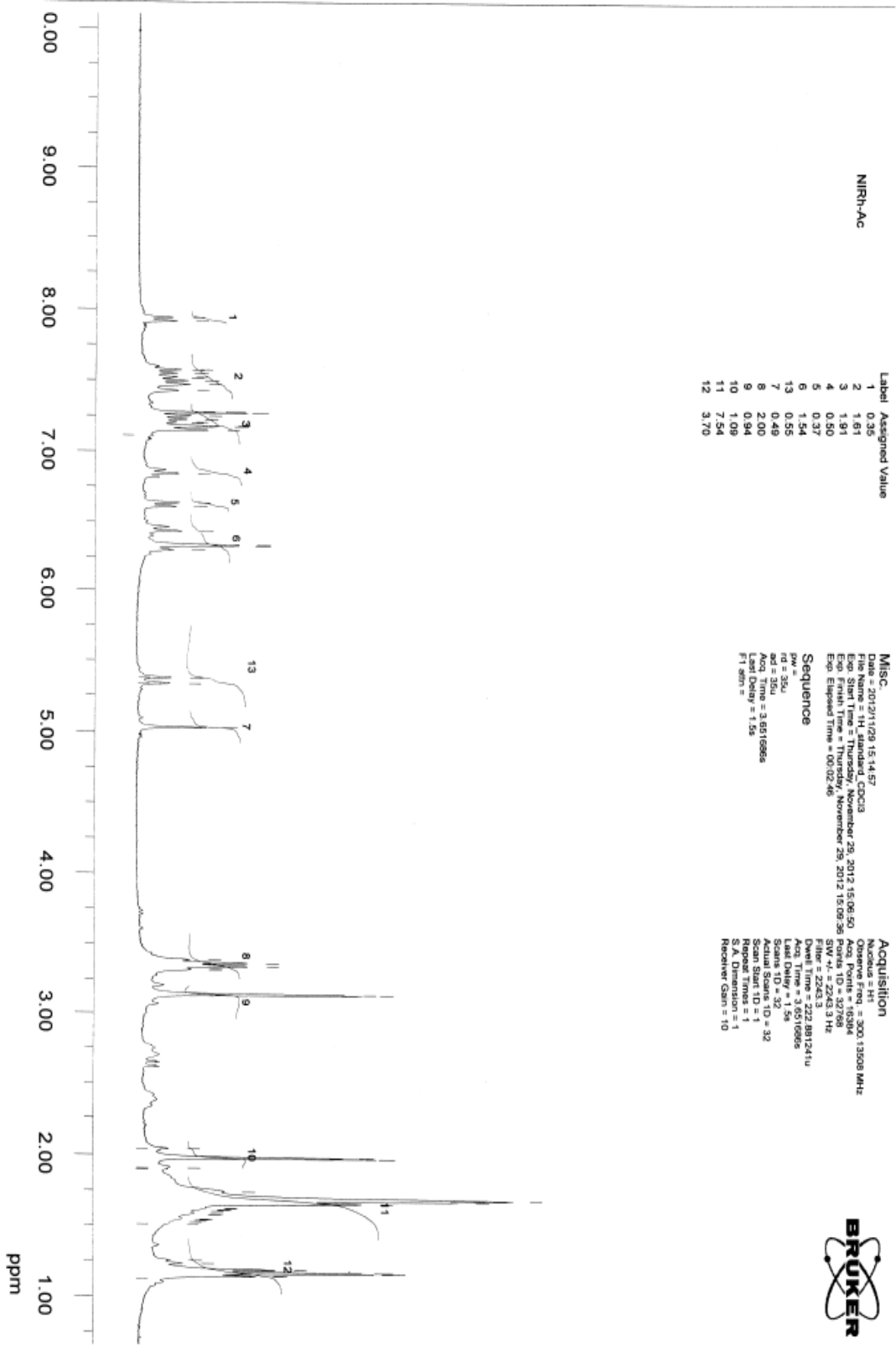
+Q1: 30 MCA scans from Sample 90 (abby001) of Datazyla.wiff (Turbo Spray)



D.11 ESI-Mass spectrum of the sensor NIRh-Ac



D.12 <sup>13</sup>C NMR spectrum of the sensor NIRh-Ac in CDCl<sub>3</sub>



D.13  $^1\text{H}$  NMR spectrum of the sensor NIRh-Ac in  $\text{CDCl}_3$



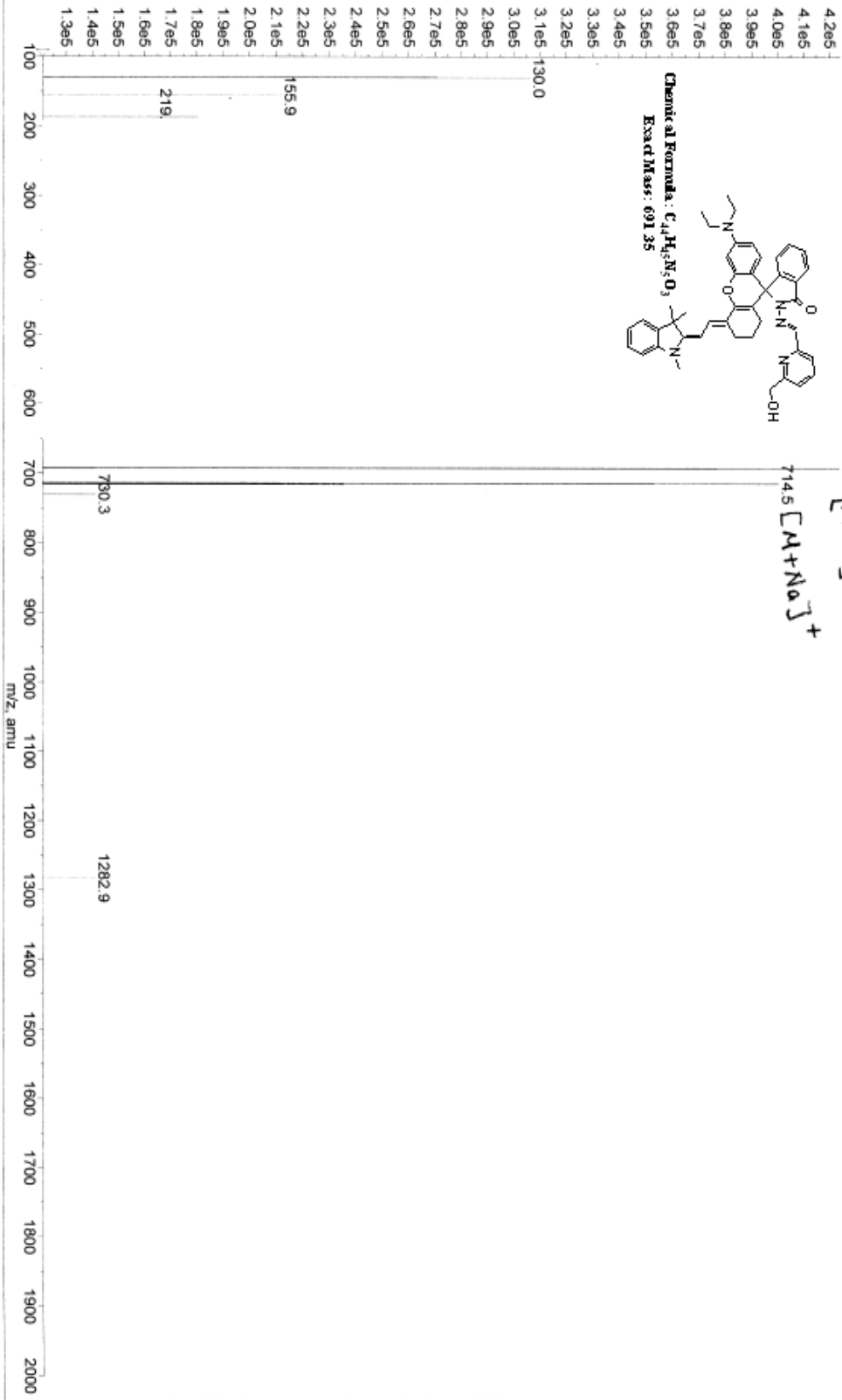
Date: Thursday, January 03, 2013  
Time: 11:43

University of Massachusetts - AP1150EX S/N 104904  
\*Incell Testing: PEO Standard 1X10-4 M @ 10uL/min

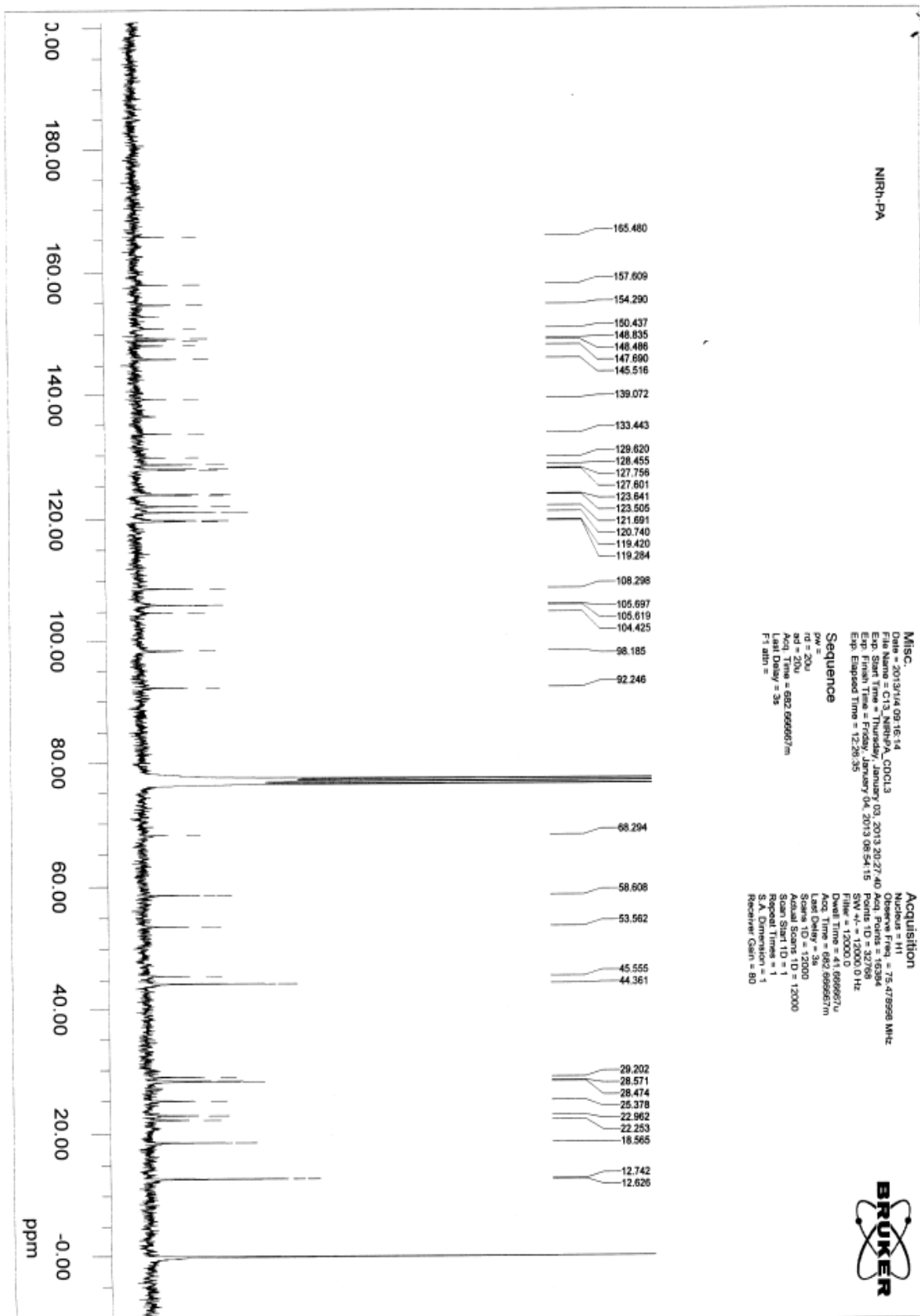
Workstation: AP1150A  
Operator: AP1-150A

+Q1: 52 MCA scans from Sample 29 (NIRhPA001) of Datamec w/ff (Turbo Spray)

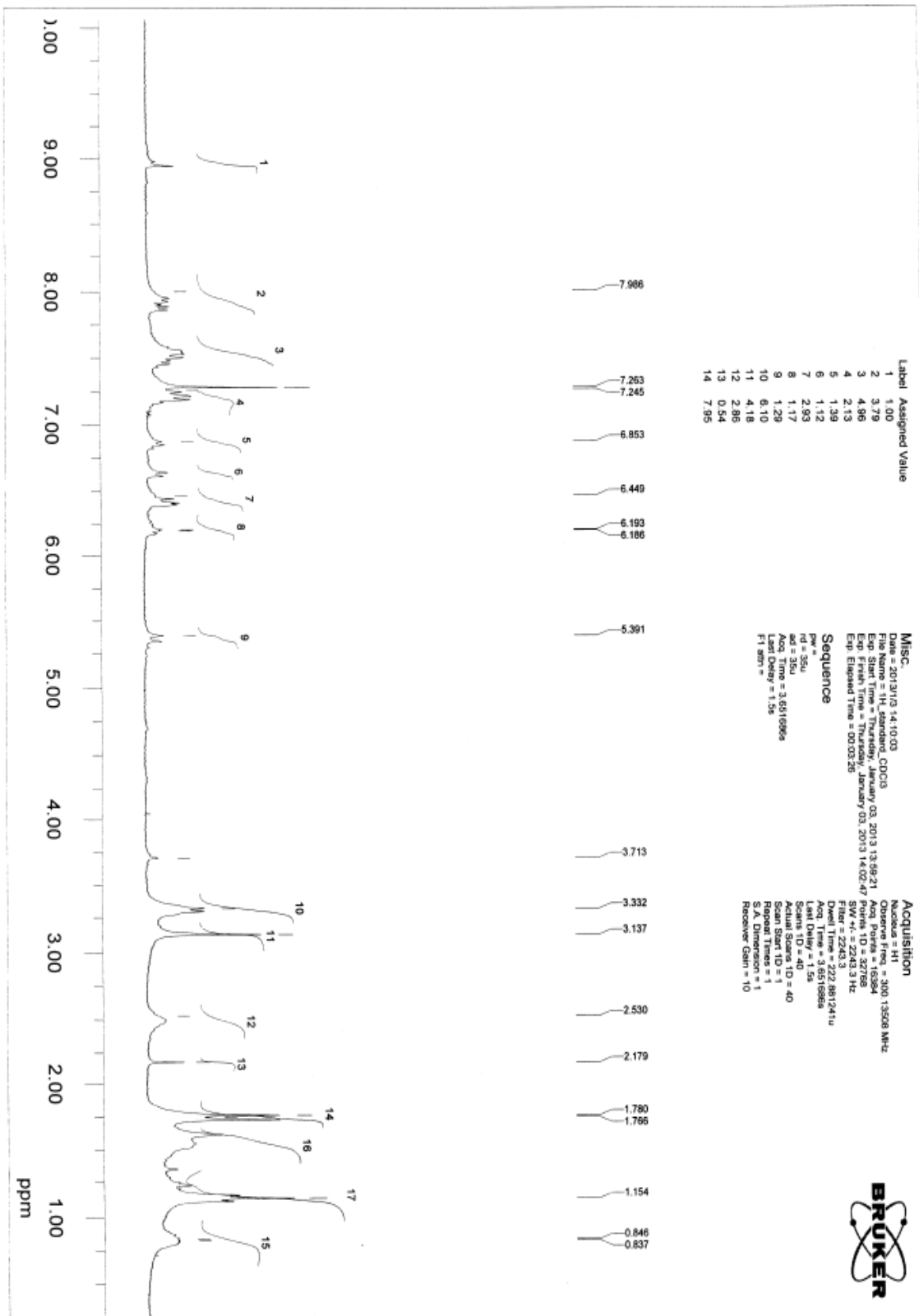
Max 4.2e5 cps.



D.14 ESI-Mass spectrum of the sensor NRPA



**D.15**  $^{13}\text{C}$  NMR spectrum of the sensor NRPA in  $\text{CDCl}_3$

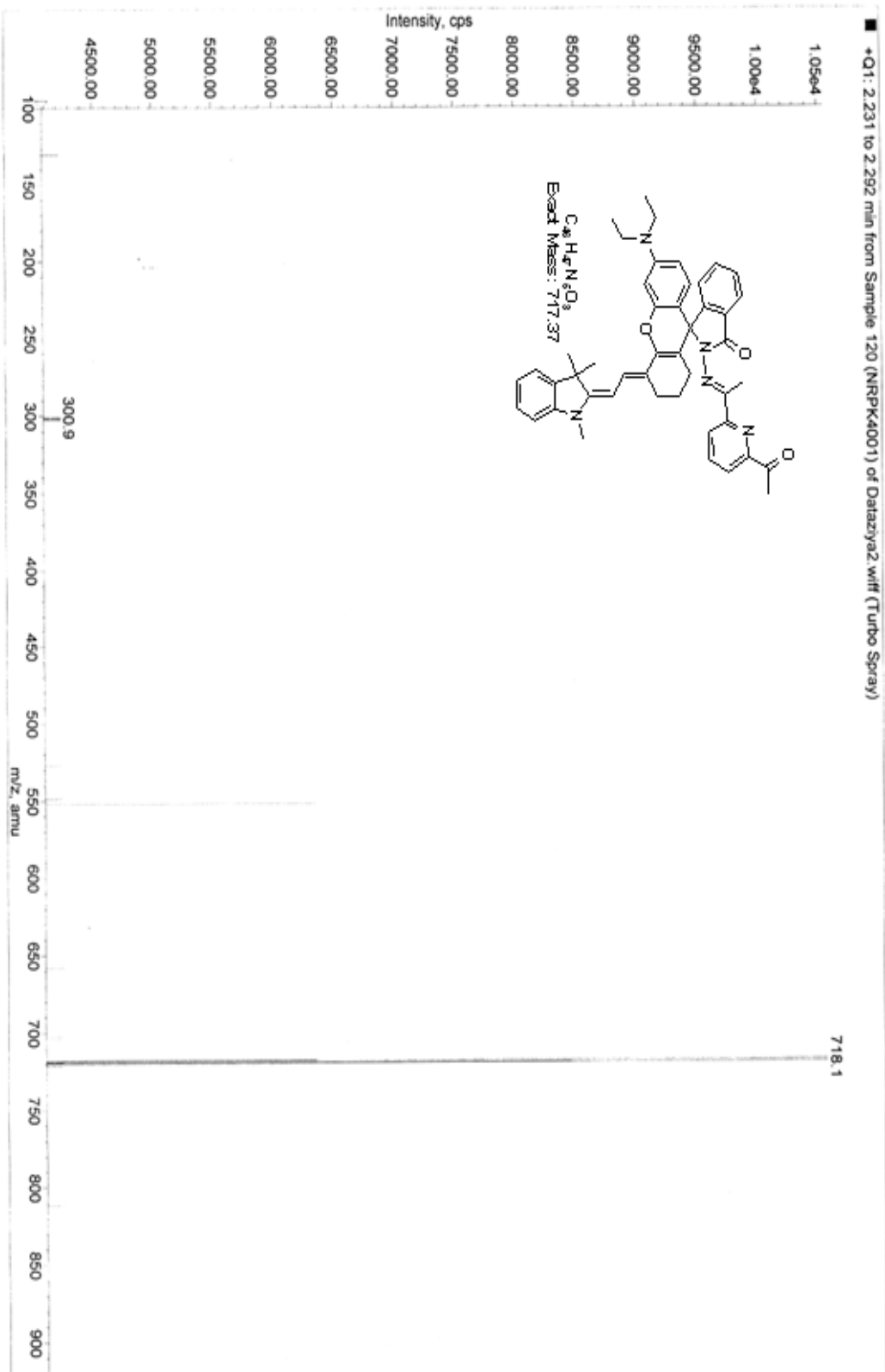


D.16 <sup>1</sup>H NMR spectrum of the sensor NRPA in CDCl<sub>3</sub>

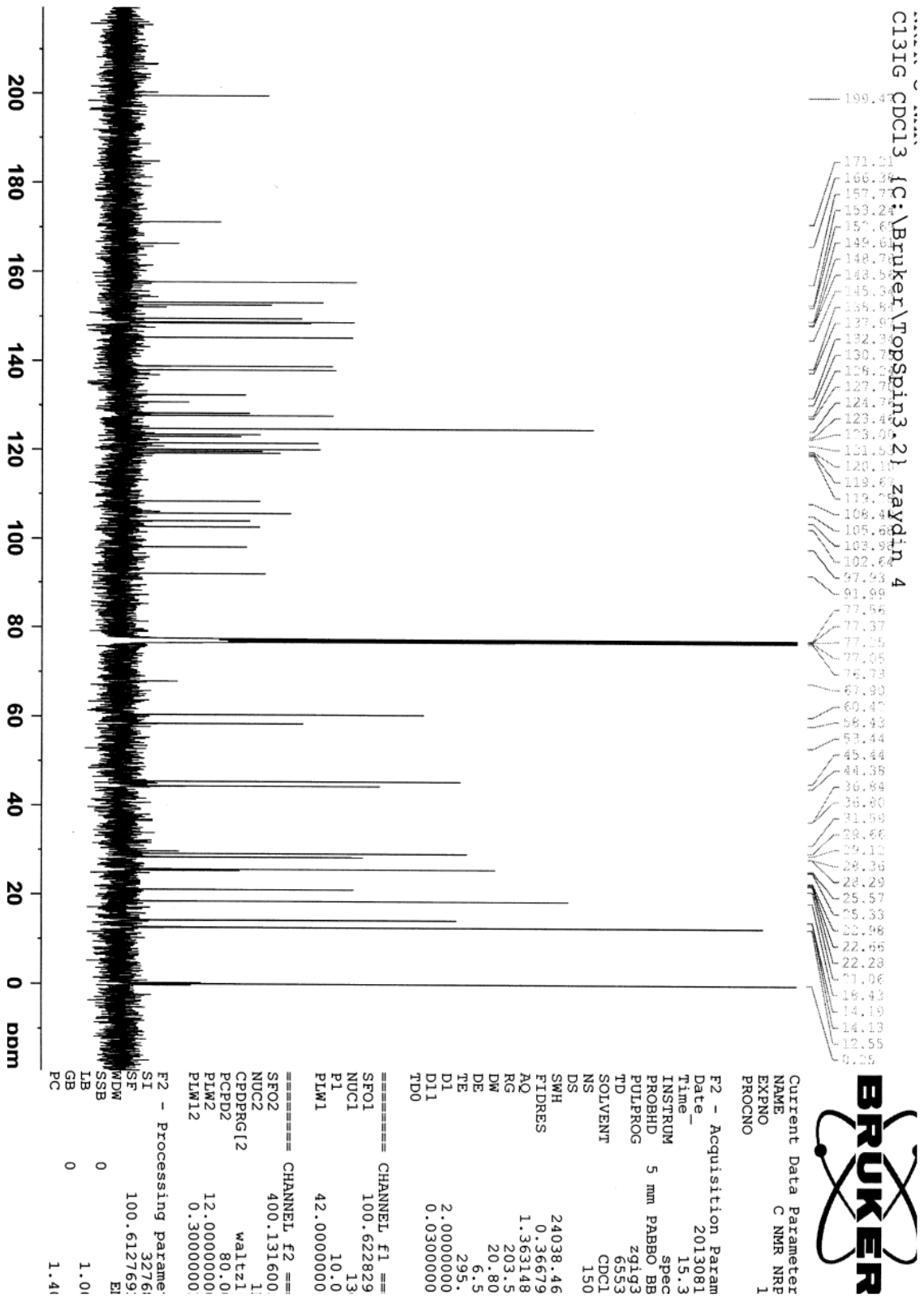
Acq. Date: Wednesday, August 07, 2013  
Acq. Time: 15:59

University of Massachusetts - API150EX S/N 104904  
Install Testing: PPG Standard 1x10-4 M @ 10uL/min

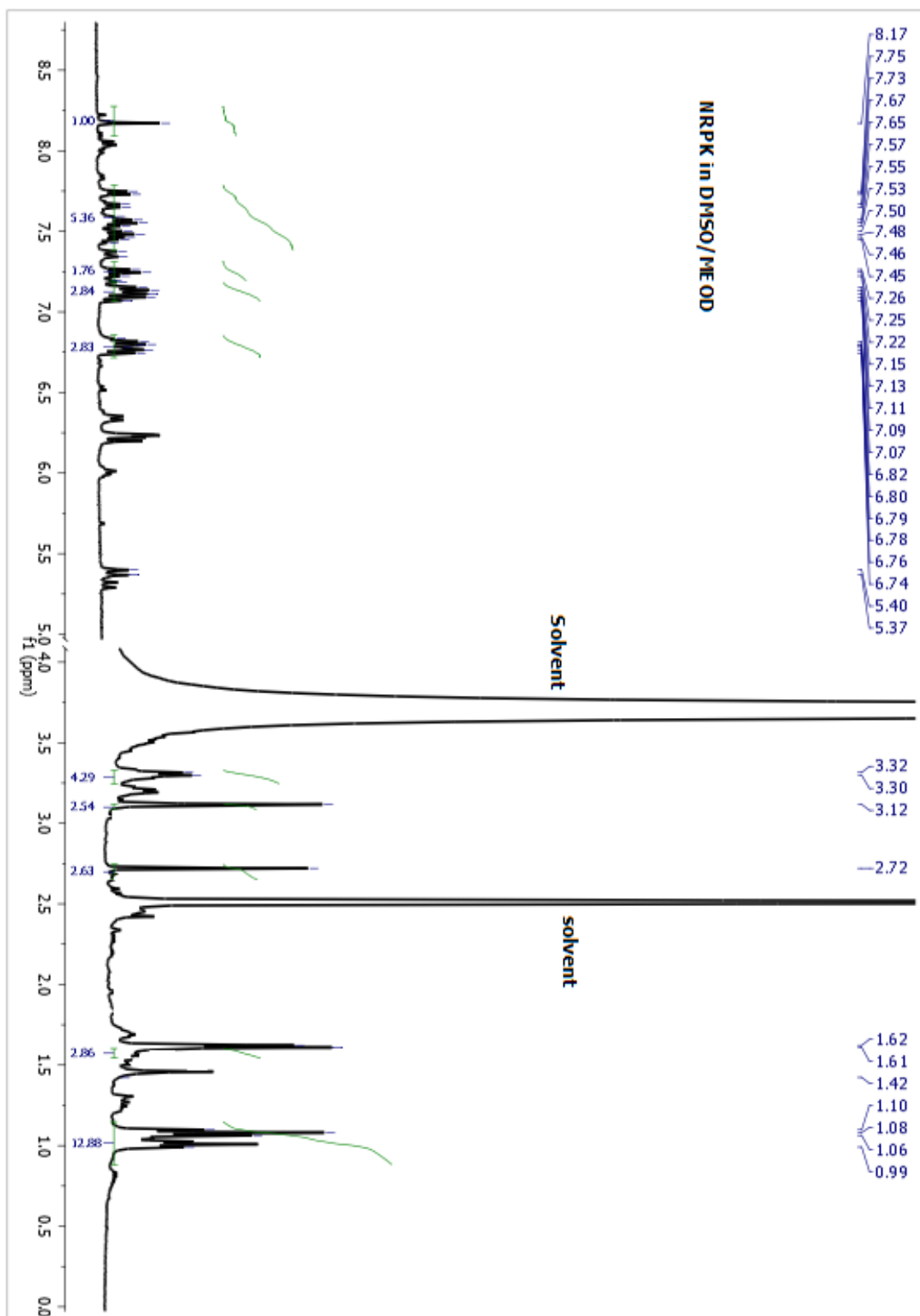
Workstation: API150A  
Operator: API-150A



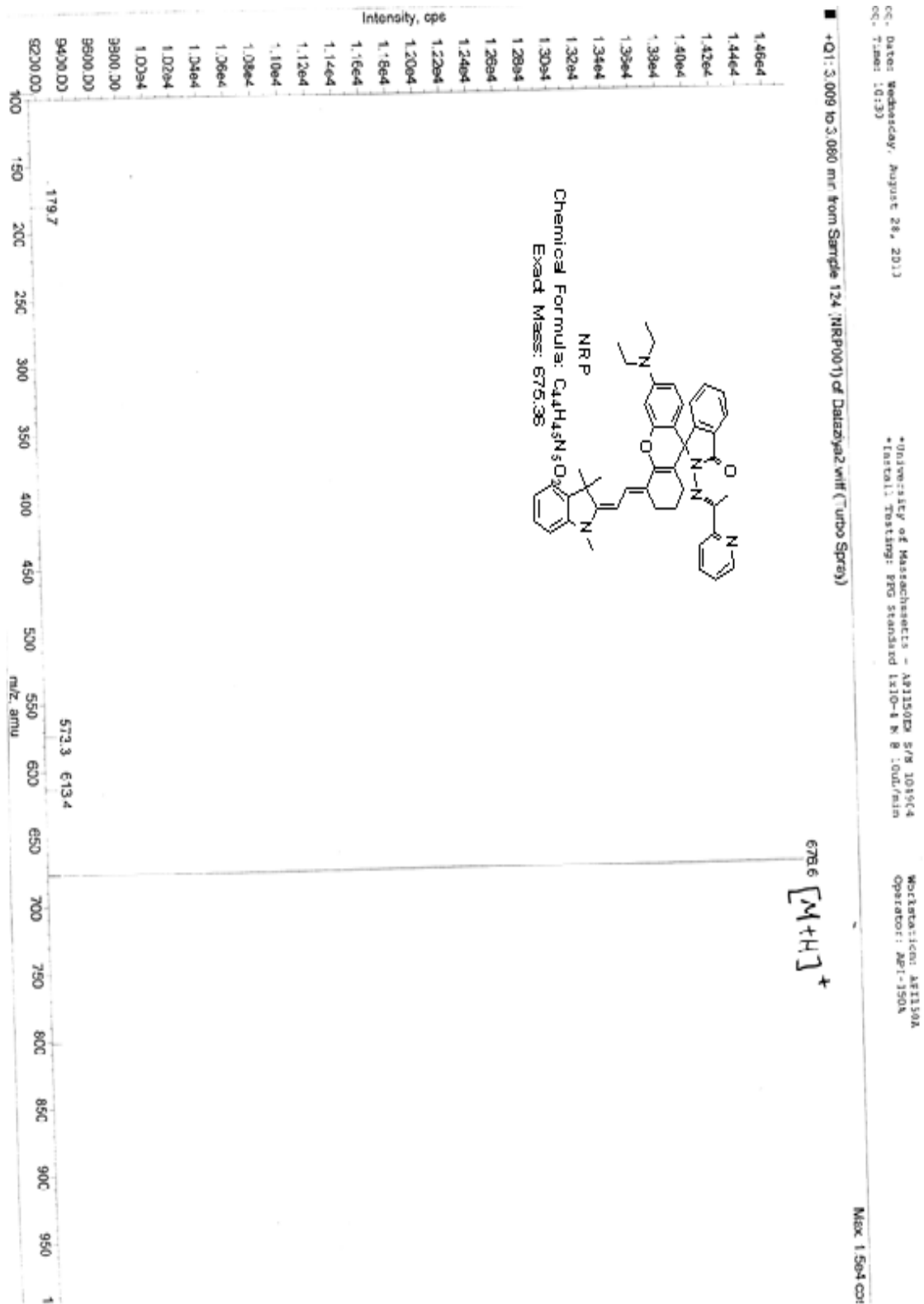
D.17 ESI-Mass spectrum of the sensor NRPK



D.18 <sup>13</sup>C NMR spectrum of the sensor NRPK in CDCl<sub>3</sub>



**D.19**  $^1\text{H}$  NMR spectrum of the sensor NRPK in  $\text{CDCl}_3$



D.20 ESI-Mass spectrum of the sensor NRP



Current Data Parameters  
NAME NRPY  
EXPNO 20  
PROCNO 1

F2 - Acquisition Parameters

Date\_ 20131014  
Time 14.20  
INSTRUM spect  
PROBHD 5 mm PABBO BB/  
PULPROG zgpg30  
TD 65536  
SOLVENT CDCl3  
NS 1024  
DS 4  
SWH 24038.461 Hz  
FIDRES 0.366798 Hz  
AQ 1.3631488 sec  
RG 203.51  
DM 20.800 usec  
DE 6.50 usec  
TE 311.0 K  
D1 2.00000000 sec  
D11 0.03000000 sec  
T00 1

CHANNEL #1

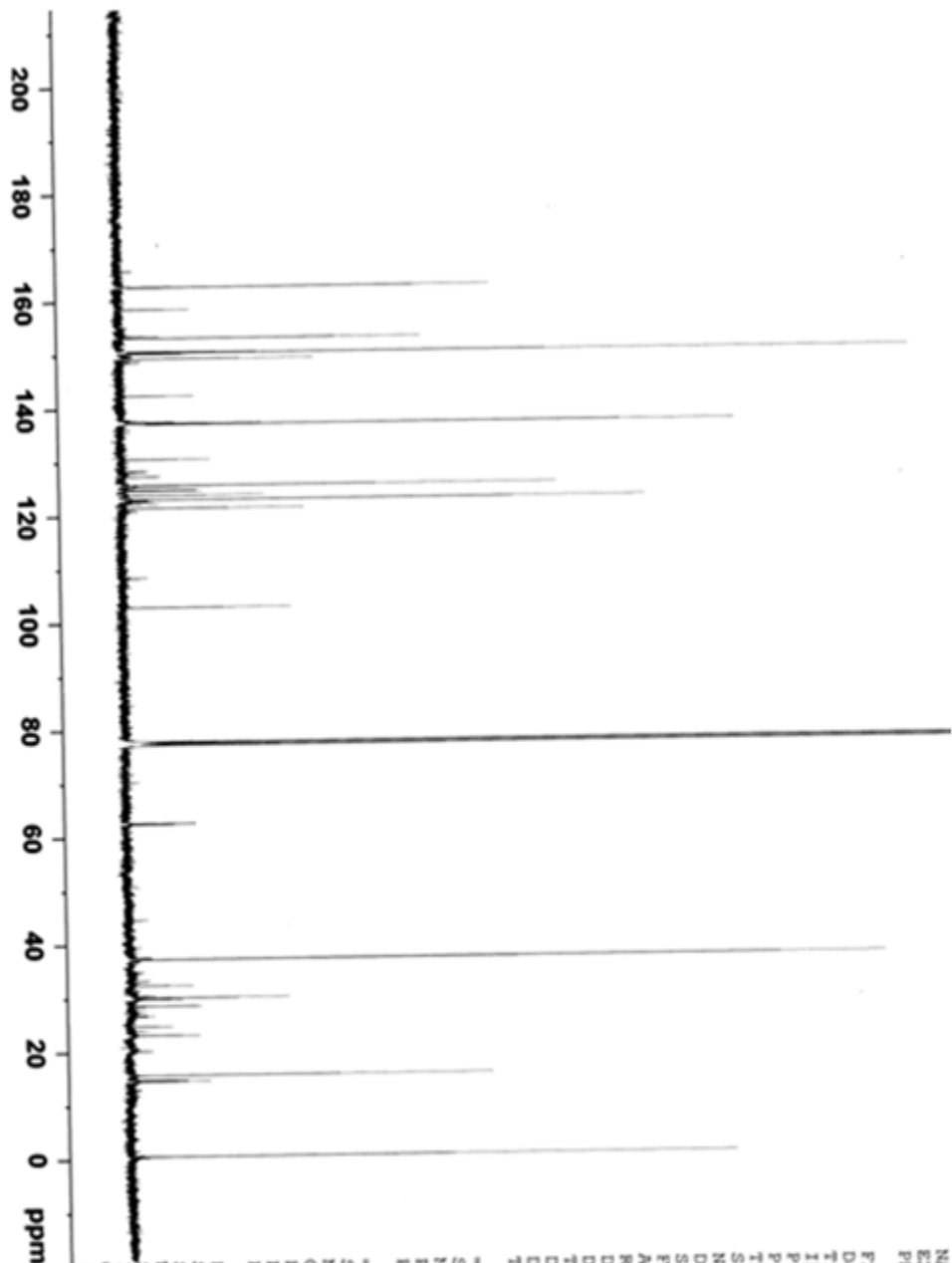
SFO1 100.6228298 MHz  
NUC1 13C  
P1 10.00 usec  
PLM1 42.00000000 W

CHANNEL #2

SFO2 400.1316005 MHz  
NUC2 1H  
CPOPRG12 waltz16  
PCPD2 80.00 usec  
PLM2 12.00000000 W  
PLM12 0.300000001 W

F2 - Processing parameters

SI 32768  
SF 100.6127701 MHz  
WDW EM  
SSB 0  
LB 1.00 Hz  
GB 0  
PC 1.40



D.21  $^{13}\text{C}$  NMR spectrum of the sensor NRP in  $\text{CDCl}_3$



<sup>1</sup>H NMR CDCl<sub>3</sub> (C:\data\Guo\ywei) zaydin 46

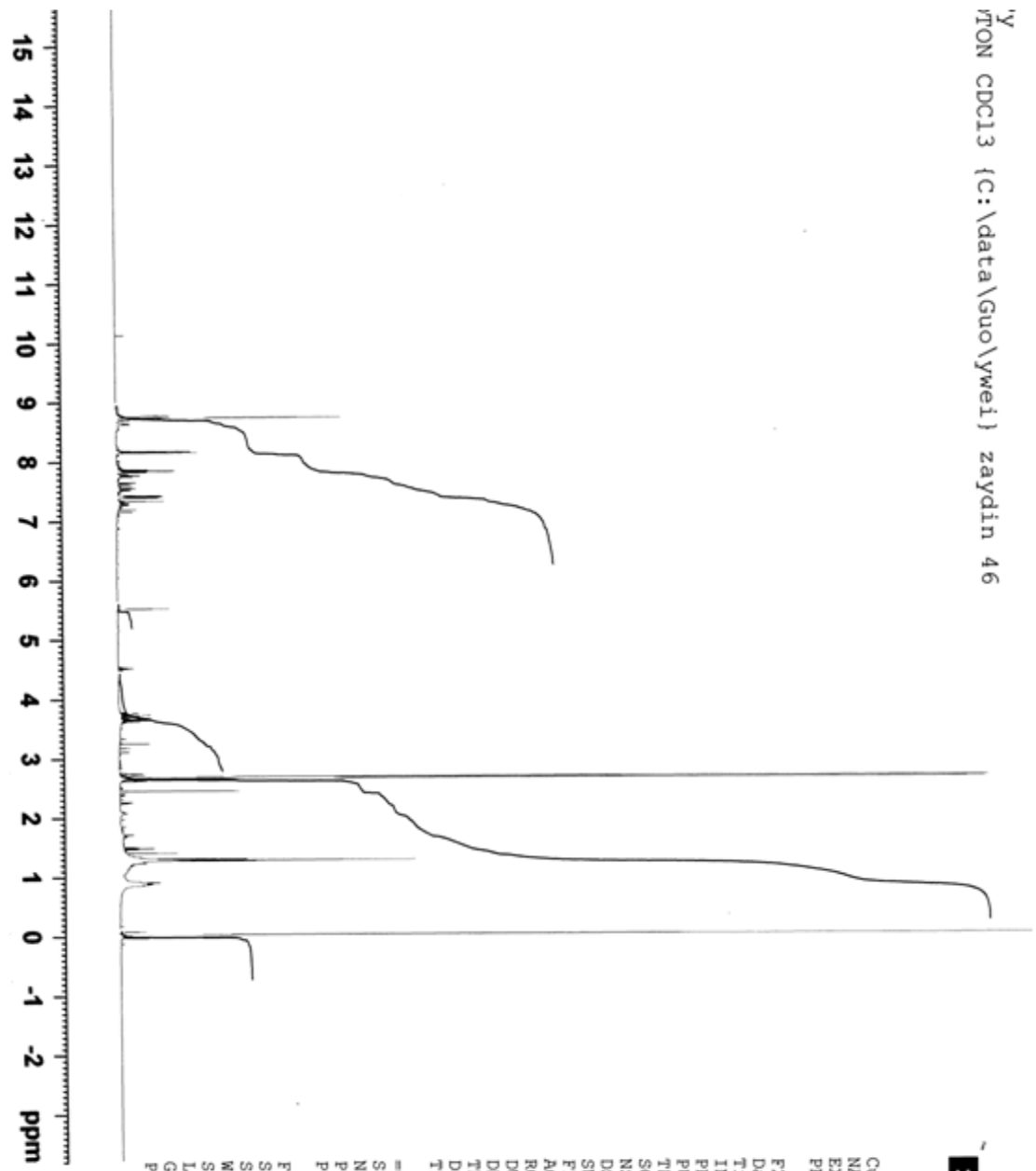


Current Data Parameters  
 NAME NRPY  
 EXPNO 10  
 PROCNO 1

F2 - Acquisition Parameters  
 Date\_ 20131014  
 Time 13.16  
 INSTRUM spect  
 PROBHD 5 mm PABBO BB/  
 PULPROG zg30  
 TD 65536  
 SOLVENT CDCl<sub>3</sub>  
 NS 16  
 DS 2  
 SWH 8012.820 Hz  
 FIDRES 0.122266 Hz  
 AQ 4.0894465 sec  
 RG 30.78  
 DW 62.400 usec  
 DE 6.50 usec  
 TE 305.4 K  
 D1 1.00000000 sec  
 TD0 1

CHANNEL f1  
 SFO1 400.1324710 MHz  
 NUCL1 1H  
 P1 14.00 usec  
 PLW1 12.00000000 W

F2 - Processing parameters  
 SI 65536  
 SF 400.1299884 MHz  
 MDM EM  
 SSB 0  
 LB 0.30 Hz  
 GB 0  
 PC 1.00



D.22 <sup>1</sup>H NMR spectrum of the sensor NRP in CDCl<sub>3</sub>

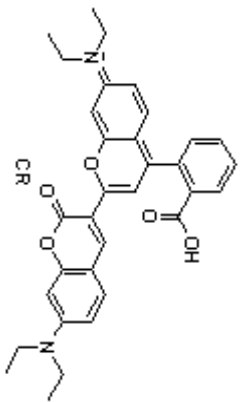
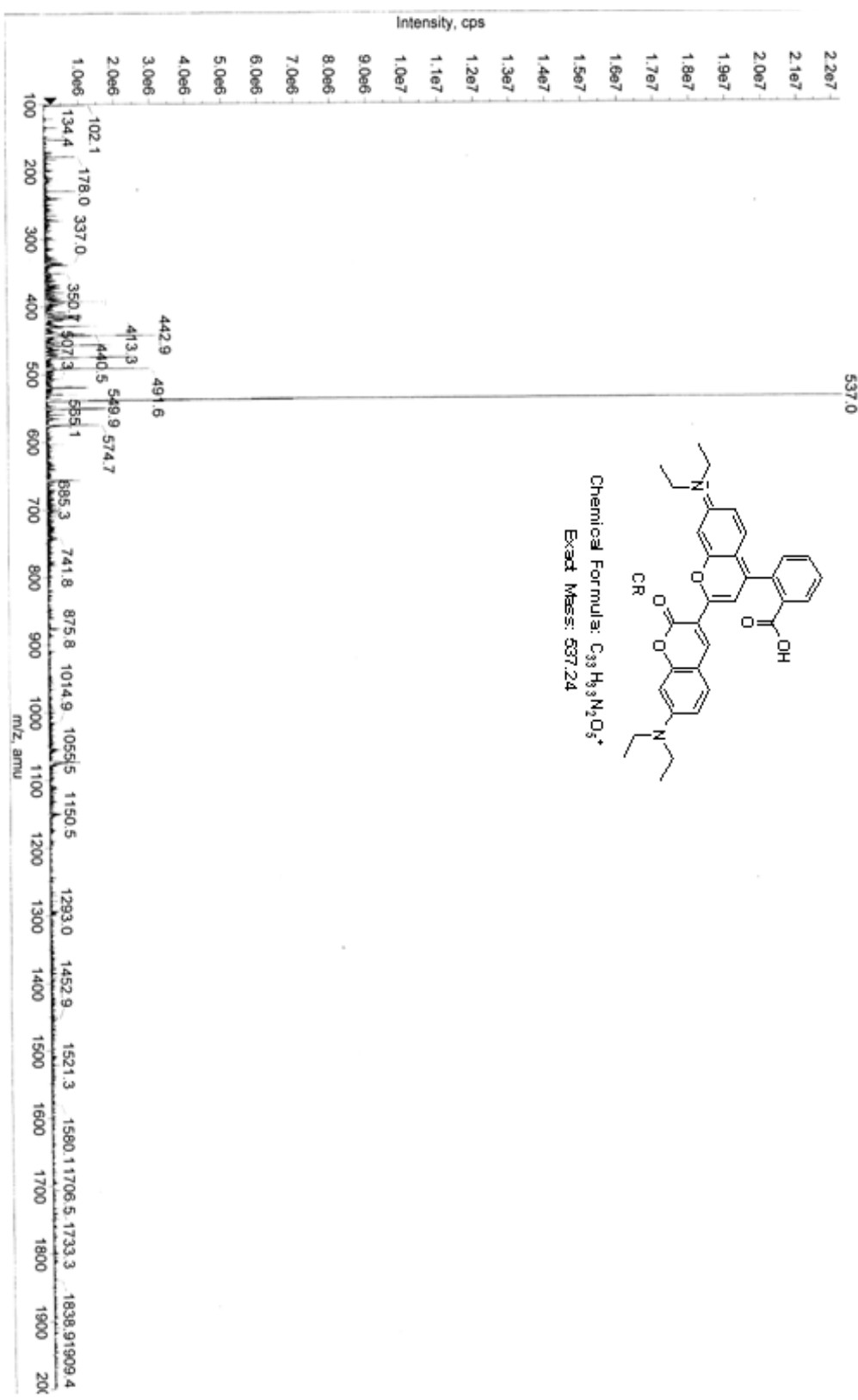
Acq. Date: Monday, September 09, 2013  
 Acq. Time: 13:27

University of Massachusetts - AP1150EX S/N 104904  
 \*Initial Testing: PPG Standard 1K10-4 M @ 10uL/min

Workstation: AP1150A  
 Operator: API-150A

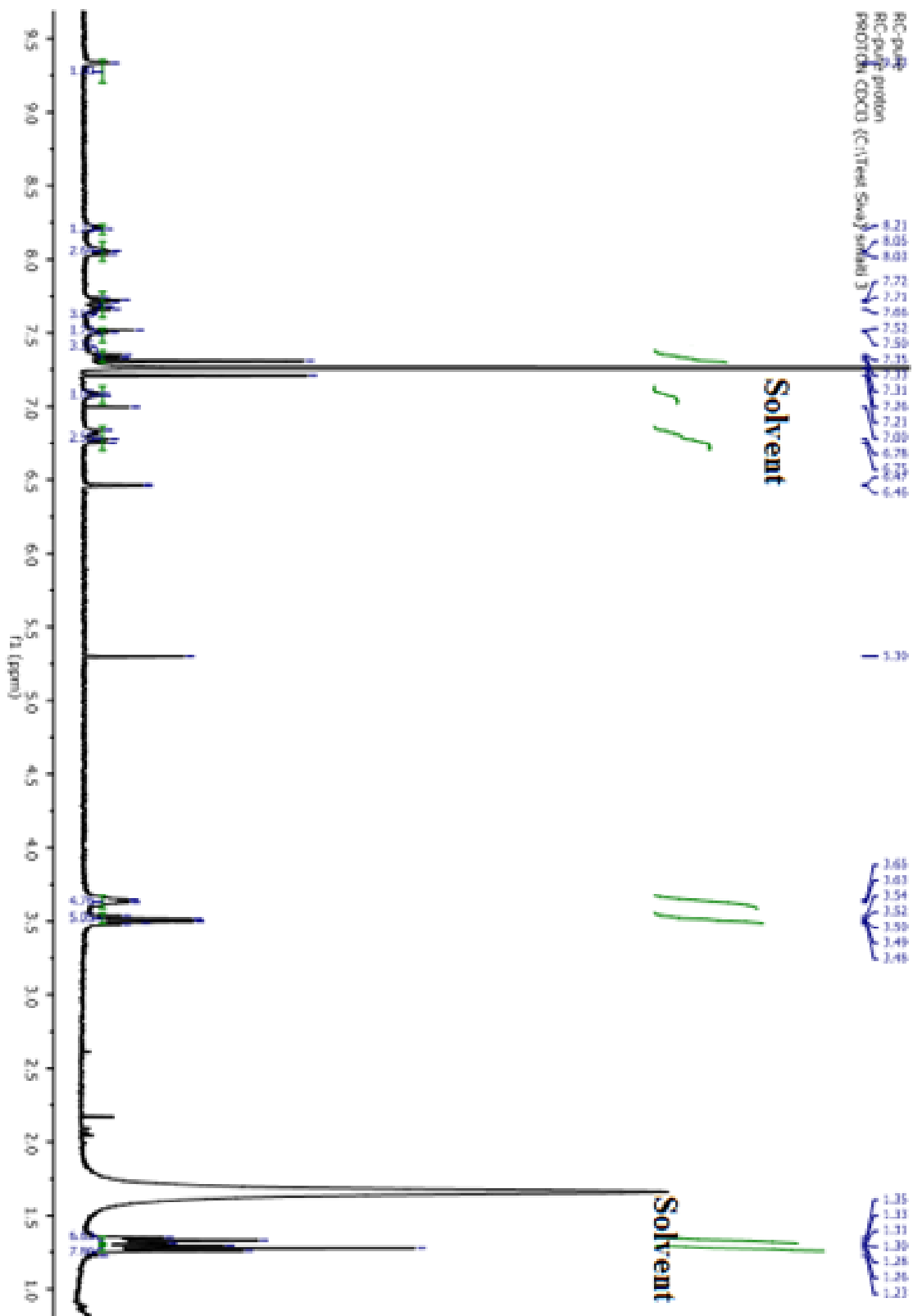
■ +Q1: 370 MCA scans from Sample 126 (ratioRPED01) of Dalazya2.wiff (Turbo Spray)

Max: 2.2e7 cps



Chemical Formula:  $C_{33}H_{33}N_2O_5^+$   
 Exact Mass: 537.24

D.23 ESI-Mass spectrum of CR

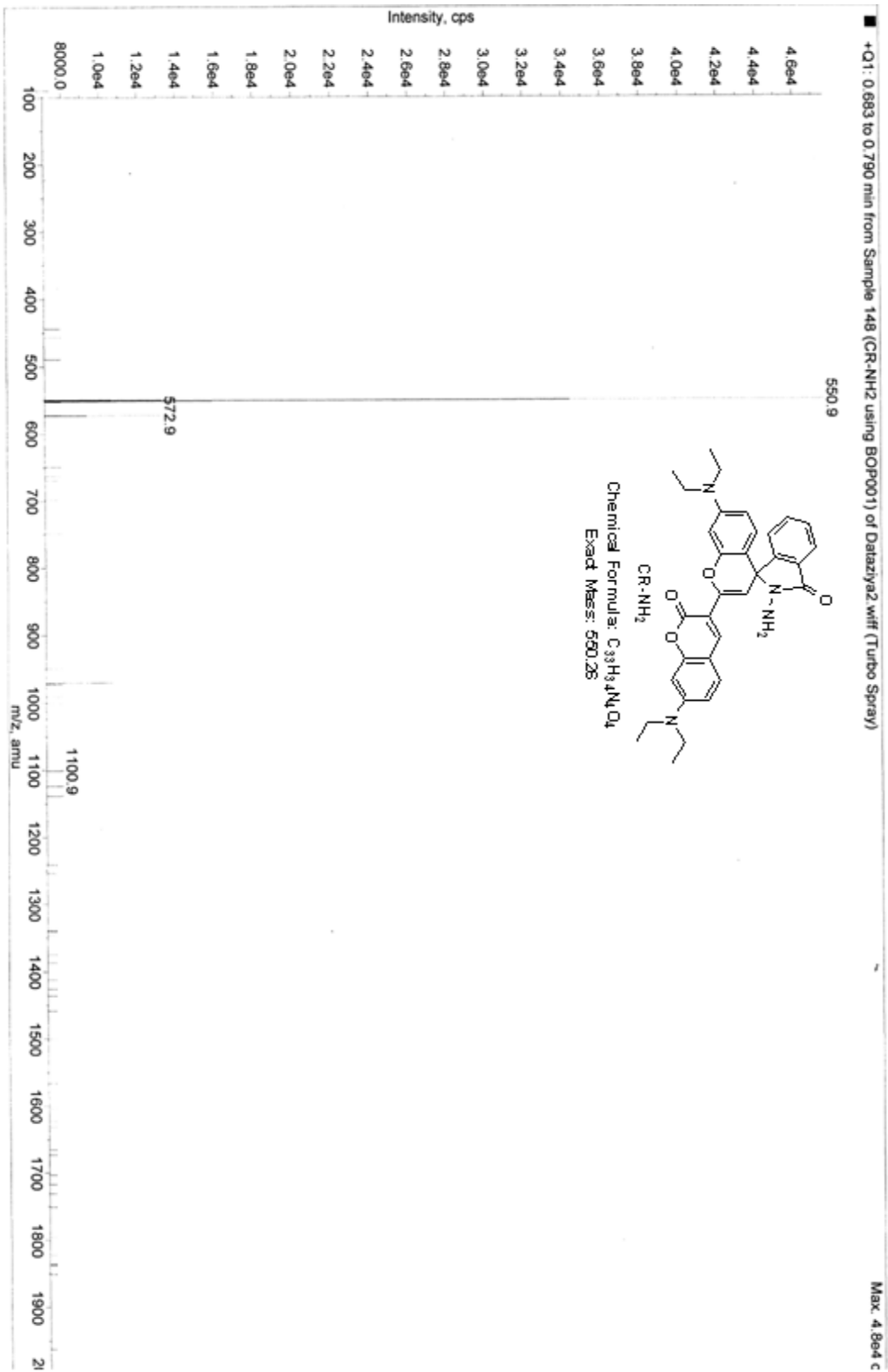


D.24 <sup>1</sup>H NMR spectrum of CR in DMSO/CDCl<sub>3</sub> (v/v, 1:1)

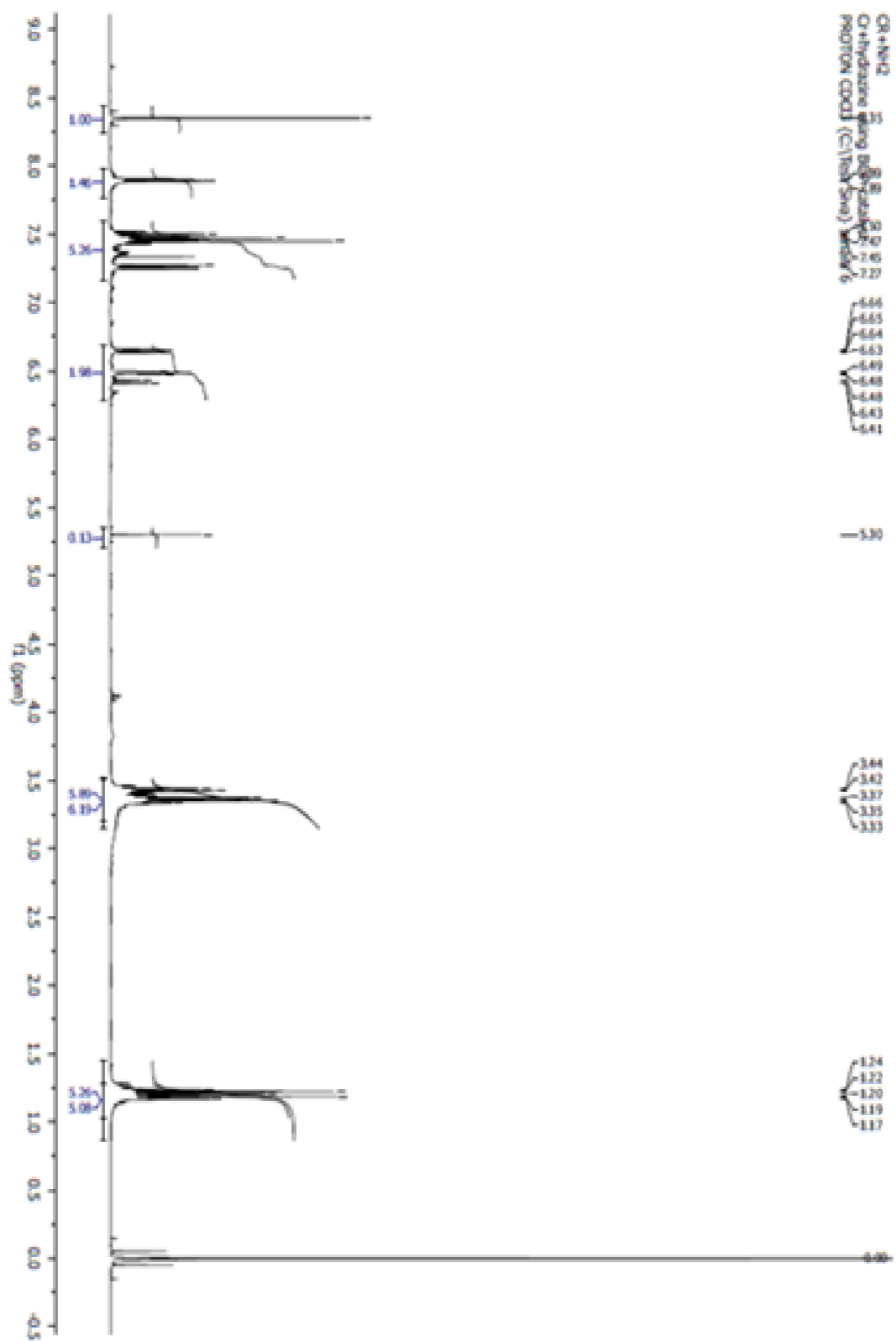
Acq. Date: Sunday, October 06, 2013  
Acq. Time: 13:17

•University of Massachusetts - API150EX S/N 104904  
•Install Testing: PPG Standard Ix10-8 M @ 10UL/min

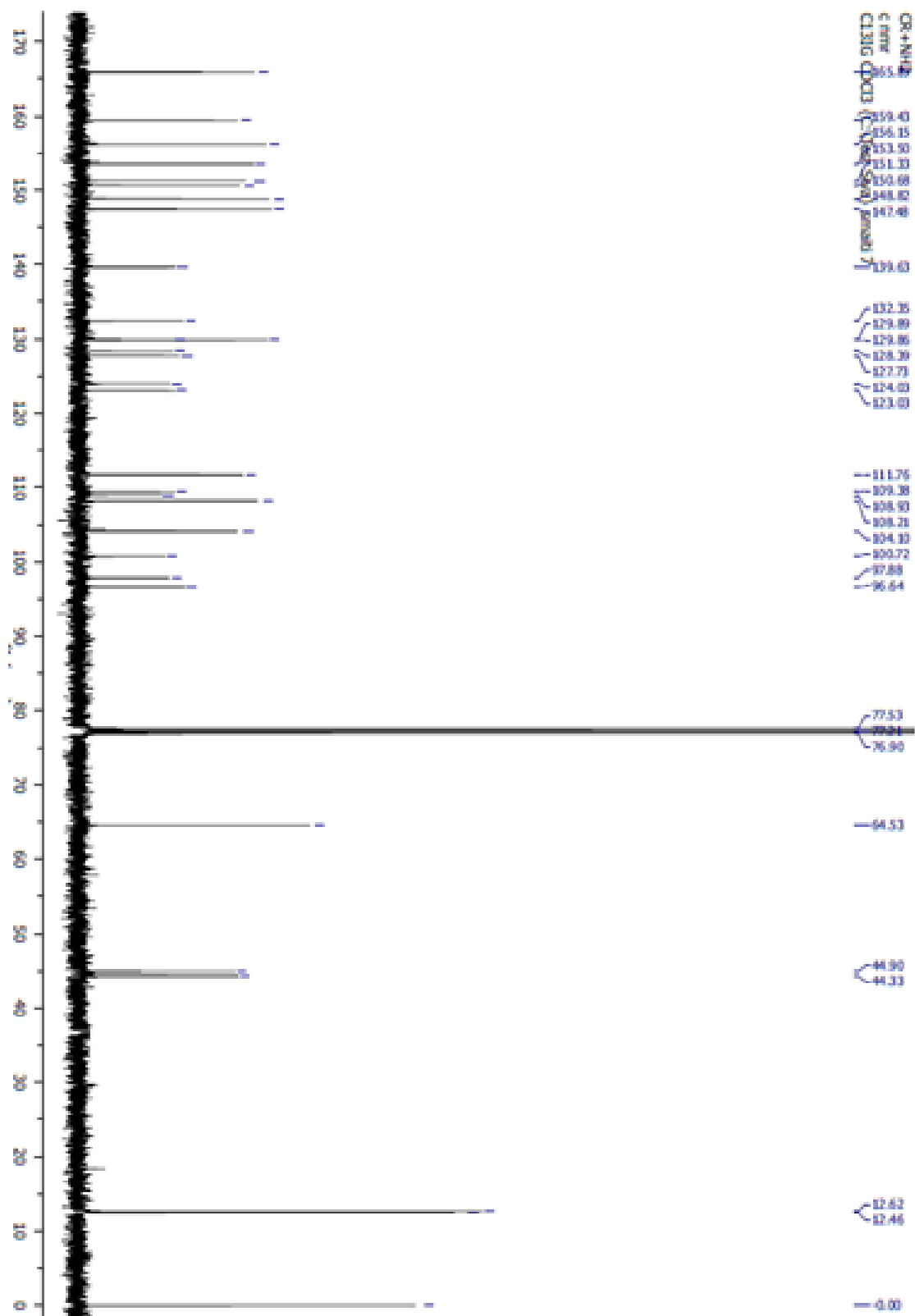
Workstation: API150A  
Operator: API-150A



D.25 ESI-Mass spectrum of CR-NH<sub>2</sub>



D.26 <sup>1</sup>H NMR spectrum of CR-NH<sub>2</sub> in CDCl<sub>3</sub>



D.27  $^{13}\text{C}$  NMR spectrum of CR-NH<sub>2</sub> in CDCl<sub>3</sub>

## BIBLIOGRAPHY

- Aisen P., Wessling-Resnick M., Leibold E. A., Iron metabolism, *Curr. Opin. Chem. Biol.*, **1999**, 3, 200-206.
- Altamura S., Muckenthaler M. U., Iron toxicity in diseases of aging: alzheimer's disease, parkinson's disease and atherosclerosis, *J. Alzheimer Dis.*, **2009**, 16, 879-895
- Amiot C. L., Xu S., Liang S., Pan L., Zhao J. X., Near-infrared fluorescent materials for sensing of biological targets, *Sensors*, **2008**, 8, 3082-3105
- Andrew N. C., Disorders of iron metabolism, *N. Engl. J. Med.*, **1999**, 341, 1986-1995
- Andrews N. C., Iron homeostasis: insights from genetics and animal models, *Nat. Rev. Genet.*, **2000**, 1, 208-217
- Arredondo M., Nunez M. T., Iron and copper metabolism, *Mol. Aspects Med.*, **2005**, 26, 313-327
- Atar D., Backx P. H., Appel M. M., Gao W. D., Marban E., Excitation-transcription coupling mediated by zinc influx through voltage-dependent calcium channels, *J. Biol. Chem.*, **1995**, 270, 2473-2477
- Au-Yeung H. Y., Chan J., Chantarojsiri T., Chang C. J., Molecular imaging of labile iron(II) pools in living cells with a turn-on fluorescent probe, *J. Am. Chem. Soc.*, **2013**, 135, 15165-15173
- Aydin Z., Wei Y., Guo M., A highly selective rhodamine based turn-on optical sensor for Fe<sup>3+</sup>, *Inorg. Chem. Commun.*, **2012**, 20, 93-96
- Basu S., Sachidanandan C., Zebrafish: A multifaceted tool for chemical biologists, *Chem. Rev.*, **2013**, 113, 7952-7980
- Beckera E. M., Huang M. L.-H., Whitnalla M., Rahmantoa Y. S., Sheftel A. D., Ponkac P., Mitochondrial iron trafficking and the integration of iron metabolism between the mitochondrion and cytosol, *Proc. Natl. Acad. Sci. USA*, **2010**, 107, 10775-10782
- Berchner-Pfannschmidt U., Petra F.T., Doege K., Trinidad B., Freitag P., Metzen E., de Groot H., Fandrey J., Chelation of cellular calcium modulates hypoxia-inducible gene expression through activation of hypoxia-inducible factor-1 $\alpha$ , *J. Biol. Chem.*, **2004**, 279, 44976-44986.
- Berezin M. Y., Achilefu S., Fluorescence lifetime measurements and biological imaging, *Chem. Rev.*, **2010**, 110, 2641-2684
- Bergonzi R., Fabbrizzi L., Licchelli M., Mangano C., Molecular switches of fluorescence operating through metal centred redox couples, *Coord. Chem. Rev.*, **1998**, 170, 31-46

- Bertini I., Gray H. B., Stiefel E. I., Valentine J. S., *Biological Inorganic Chemistry; Structure and Reactivity*, Sausalite, California, **2007**, pp. 60-61
- Biswas A., Drew M. G. B., Ghosh A., Nickel(II) and copper(II) complexes of unsymmetrical tetradentate reduced Schiff base ligands, *Polyhedron*, **2010**, 29, 1029-1034
- Bouteiller C., Clave G., Bernardin A., Chipon B., Massonneau M., Renard P., Romieu A., Novel water-soluble near-infrared cyanine dyes: synthesis, spectral properties, and use in the reparation of internally quenched fluorescent probes, *Bioconjugate Chem.*, **2007**, 18, 1303-1317
- Bradbury M. W. B., Transport of iron in the blood-brain-cerebrospinal fluid system, *J. Neurochem.*, **1997**, 69, 443-454
- Braun V., Killmann H., Bacterial solutions to the iron-supply problem, *Trends Biochem. Sci.*, **1999**, 24, 104-109
- Breuer W., Epstein S., Milligram P., Cabantchik Z.I., Transport of iron and other transition metals into cells as revealed by a fluorescent probe, *Am. J. Physiol.*, **1995**, 268, C1354-C1361
- Breuer W., Shvartsman M., Cabantchik Z. I., Intracellular labile iron, *Int. J. Biochem. Cell B.*, **2008**, 40, 350-354
- Bryson-Richardson R.J., Currie P.D., The genetics of vertebrate myogenesis., *Nat. Rev. Genet.*, **2008**, 9, 632-646
- Buss J. L., Arduini E., Shephard K.C., Ponka P., Lipophilicity of analogs of pyridoxal isonicotinoyl hydrazone (PIH) determines the efflux of iron complexes and toxicity in K562 cells, *Biochem. Pharmacol.*, **2003**, 65, 349-360
- Cabantchik Z. I., Labile iron in cells and body fluids: physiology, pathology, and pharmacology, *Front. Pharmacol.*, **2014**, 5, 45-54
- Chae M. Y., Czarnik A. W., Fluorometric chemodosimetry. Mercury(II) and silver(I) indication in water via enhanced fluorescence signaling, *J. Am Chem. Soc.*, **1992**, 114, 9704-9705
- Chartres J. D., Busby M., Riley M. L., Davis J. J., Bernhardt P. V., A turn-on fluorescent iron complex and its cellular uptake, *Inorg. Chem.*, **2011**, 50, 9178 - 9183
- Chen C. H., Hung P. J., Wan C. F., Wu A. W., A turn-on schiff-base fluorescence sensor for Fe<sup>3+</sup> ion, *Inorg. Chem. Commun.*, **2013**, 38, 74-77
- Chen J. L., Zhuo S. J., Wu Y. Q., Fang F., Li L., Zhu C. Q., High selective determination iron(II) by its enhancement effect on the fluorescence of pyrene-tetramethylpiperidinyI (TEMPO) as a spin fluorescence probe, *Spectrochim. Acta, Part A*, **2006**, 63, 438-443.
- Chen L. B., Chapter 7 fluorescent labeling of mitochondria, *Methods Cell Biol.*, **1988**, 29, 103-123



- Chen W. D., Gong W. T., Ye Z. Q., Lin Y., Ning G. L., FRET-based ratiometric fluorescent probes for selective Fe<sup>3+</sup> sensing and their applications in mitochondria, *Dalton Trans.*, **2013**, 42, 10093-10096
- Chen X., Jia J., Ma H., Wang S., Wang X., Characterization of rhodamine B hydroxylamide as a highly selective and sensitive fluorescence probe for copper(II), *Anal. Chim. Acta*, **2009**, 632, 9-14
- Chen X., Pradhan T., Wang F., Kim J. S., Yoon J., Fluorescent chemosensors based on spiroring-opening of xanthenes and related derivatives, *Chem. Rev.*, **2012**, 112, 1910-1956
- Cheng F., Tang N., Chen L., Synthesis, photophysical, and electrochemical properties of ruthenium(II) polypyridyl complexes containing open-chain crown ether, *Z. Anorg. Allg. Chem.*, **2008**, 634, 1608-1612
- Chung P. K., Liu S. R., Wang H. F., Wu S. P., A pyrene-based highly selective turn-on fluorescent chemosensor for iron(III) ions and its application in living cell imaging, *J. Fluoresc.*, **2013**, 23, 1139-1145
- Conway J.M., Norris K.M., Bodwell E.C., A new approach for the estimation of body composition: infrared interactance 1'2, *Am. J. Clin. Nutr.*, **1984**, 40, 1123-1130
- Cooper M.A., Label-free screening of bio-molecular interactions, *Anal. Bioanal. Chem.*, **2003**, 377, 834-842
- Cooper M.E., Gregory S., Adie E., Kalinka S., pH-sensitive cyanine dyes for biological applications, *J. Fluoresc.*, **2002**, 12, 425-429
- Coskun A., Akkaya E. U., Signal Ratio Amplification via Modulation of Resonance Energy Transfer: Proof of Principle in an Emission Ratiometric Hg(II) Sensor, *J. Am. Chem. Soc.*, **2006**, 128, 14474-14475
- Crichton R., Ed. *Inorganic biochemistry of iron metabolism*, 2nd ed.; John Wiley & Sons Ltd.: U.K., **2001**, pp. 160-180
- Crichton R., Ed. *Inorganic biochemistry of iron metabolism*, 2nd ed.; John Wiley & Sons Ltd.: U.K., **2001**, pp. 1-10
- Crichton R., Ed. *Inorganic biochemistry of iron metabolism*, 2nd ed.; John Wiley & Sons Ltd.: U.K., **2001**, pp. 17-48
- Crichton R., *Inorganic Biochemistry of Iron Metabolism; From Molecular Mechanisms to Clinical Consequences*, John Wiley and Sons, Baffins Lane, Chichester, **2001**, pp. 167-174
- Czarnik A. W., Chemical Communication in Water Using Fluorescent Chemosensors, *Acc. Chem. Res.*, **1994**, 27, 302-308
- Czerney P., Graneb G., Birckner E., Vollmer F., Rettig W., Molecular engineering of cyanine-type fluorescent and laser dyes, *J. Photochem. Photobiol. B*, **1995**, 89, 31-36

- Dautry-Varsat A., Ciechanover A., Lodish H. F., pH and the recycling of transferring during receptor-mediated endocytosis, *Proc. Natl. Acad. Sci. USA*, **1983**, 80, 2258-2262
- De Costa M. D. P. and Jayasinghe W. A. P. A., Detailed studies on complexation behaviour and mechanism of fluorescence quenching of naphthalene linked hydroxamic acid with transition metal ions by UV-visible and fluorescence spectra, *J. Photochem. Photobiol. A*, **2004**, 162, 591-598
- De Domenico I., M. Vaughn B., Li L., Bagley D., Musci G., Ward D. M., Kaplan J., Ferroportin-mediated mobilization of ferritin iron precedes ferritin degradation by the proteasome, *EMBO J.*, **2006**, 25, 5396-5404
- Desai S. D., Reed R. E., Babu S., Lorio E. A., ISG15 deregulates autophagy in genotoxin-treated ataxia telangiectasia cells, *J. Biol. Chem.*, **2013**, 288, 2388-2402
- Descalzo A.B., Rurack K., On the signalling pathways and Cu<sup>II</sup>-mediated anion indication of N-meso-substituted heptamethine cyanine dyes, *Chem. Eur. J.*, **2009**, 15, 3173-3185
- Diwan U., Kumar A., Kumar V., Upadhyay K. K., Solvent viscosity tuned highly selective NIR and ratiometric fluorescent sensing of Fe<sup>3+</sup> by a symmetric chalcone analogue, *Dalton Trans.*, **2013**, 42, 13889-13896
- Dodani S. C., He Q., Chang C. J., A Turn-On Fluorescent Sensor for Detecting Nickel in Living Cells, *J. Am. Chem. Soc.*, **2009**, 131, 18020-18021
- Domaille D. W., Que E. L., Chang C. J., Synthetic fluorescent sensors for studying the cell biology of metals, *Nat. Chem. Biol.*, **2008**, 4, 168-175
- Dujols V., Ford F., Czarnik A. W., Communication a long-wavelength fluorescent chemodosimeter selective for Cu(II) ion in water, *J. Am. Chem. Soc.*, **1997**, 119, 7386-7387
- En D., Guo Y., Chen B. T., Dong B., Peng M. J., Coumarin-derived Fe<sup>3+</sup>-selective fluorescent turn-off chemosensors: synthesis, properties, and applications in living cells, *RSC Adv.*, **2014**, 4, 248-253
- Epsztejn S., Glickstein H., Picard V., Slotki I., N., Breuer W., Beaumont C., Cabantchik Z. I., H-ferritin subunit overexpression in erythroid cells reduces the oxidative stress response and induces multidrug resistance properties, *Blood*, **1999**, 94, 3593-3603
- Epsztejn S., Kaklon O., Glickstein H., Breuer W., Cabantchik Z. I., Fluorescence analysis of the labile iron pool of mammalian cells, *Anal. Biochem.*, **1997**, 248, 31-40
- Espósito B. P., Epsztejn S., Breuer W., Cabantchik Z. I., A review of fluorescence methods for assessing labile iron in cells and biological fluids, *Anal. Biochem.*, **2002**, 304, 1-18
- Fabbrizzi L., Licchelli M., Mancin F., Pizzeghello M., Rabaioli G., Taglietti A., Tecilla P., Tonellato U., Fluorescence sensing of ionic analytes in water: from transition metal ions to vitamin B13, *Chem. Eur. J.*, **2002**, 8, 94-101

- Fabbrizzi L., Licchelli M., Pallavicini P., Sacchi D., Taglietti A., Sensing of transition metals through fluorescence quenching or enhancement. A review, *Analyst*, **1996**, 121, 1763-1768
- Fakih S., Podinovskaia M., Kong X., Schaible U. E., Collins H. L., Hider R. C., Monitoring intracellular labile iron pools: A novel fluorescent iron(III) sensor as a potential non-invasive diagnosis tool, *J. Pharm. Sci.*, **2009**, 98, 2212-2226
- Farrer N. J., Salassa L., Sadler P. J., Photoactivated chemotherapy (PACT): the potential of excited-state d-block metals in medicine, *Dalton Trans.*, **2009**, 48, 10690-10701
- Flanagan J. H., Khan S. H., Menchen S., Soper S. A., Hammer R.P., Functionalized tricarbocyanine dyes as near-infrared fluorescent probes for biomolecules, *Bioconjugate Chem.*, **1997**, 8, 751-756
- Fornasier R., Milani D., Scrimin P. Tonellato U., Functional micellar catalysis: Part 8: Catalysis of the hydrolysis of p-nitrophenyl picolinate by metal-chelating micelles containing copper(II) or zinc(II), *J. Chem. Soc. Perkin. Trans II*, **1986**, 233-237
- Garcia-Beltran O., Mena N., Yanez O., Caballero J., Vargas V., Nunez M. T., Cassels B. K., Design, synthesis, and cellular dynamics studies in membranes of a new coumarin-based "turn-off" fluorescent probe selective for Fe<sup>2+</sup>, *Eur. J. Med. Chem.*, **2013**, 67, 60-63
- Ghosh P., Bharadwaj P. K., Roy J., Ghosh S., Transition metal (II)/(III), Eu(III), and Tb(III) ions induced molecular photonic or gates using trianthryl cryptands of varying cavity dimension, *J. Am. Chem. Soc.*, **1997**, 119, 11903-11909
- Glickstein H., El R. B., Link G., Breuer W., Konijn A. M., Hershko C., Nick H. Cabantchik Z. I., Action of chelators in iron-loaded cardiac cells: Accessibility to intracellular labile iron and functional consequences, *Blood*, **2006**, 108, 3195-3203.
- Grabchev I., Chovelon J. M., Quian X., A polyamidoamine dendrimer with peripheral 1,8-naphthalimide groups capable of acting as a PET fluorescent sensor for metal cations, *New J. Chem.*, **2003**, 27, 337-340
- Greenberg G. R., Wintrobe M. M., A labile iron pool, *J. Biol. Chem.*, **1946**, 165, 397-398
- Gryniewicz G., Poenie M., and Tsien R. Y., A new generation of Ca<sup>2+</sup> indicators with greatly improved fluorescence properties, *J. Biol. Chem.*, **1985**, 260, 3440-3450
- Guo Z., Kim G. H. Shin., Yoon. I J., A cyanine-based fluorescent sensor for detecting endogenous zinc ions in live cells and organisms, *Biomaterials*, **2012**, 33, 7818-7827
- Halliwell B. and Gutteridge J. M. C., Biologically relevant metal ion-dependent hydroxyl radical generation-an update, *FEBS Lett.*, **1992**, 307, 108-112
- Hao E., Meng T., Zhang M., Pang W., Yunyou Z., Jiao L., Solvent dependent fluorescent properties of a 1,2,3-triazole linked 8-hydroxyquinoline chemosensor: tunable detection from Zinc(II) to Iron(III) in the CH<sub>3</sub>CN/H<sub>2</sub>O system, *J. Phys. Chem. A*, **2011**, 115, 8234-8241

- Harjani J. R., Liang C., Jessap P. G., A synthesis of acetamidines, *J. Org. Chem.*, **2011**, 76, 1683-1691
- Hasinoff B. B., The intracellular iron sensor calcein is catalytically oxidatively degraded by iron(II) in a hydrogen peroxide-dependent reaction, *J. Inorg. Biochem.*, **2003**, 95, 157-164.
- Hecht S., Vladimirov N., Frechet J. M. J., Encapsulation of Functional Moieties within Branched Star Polymers: Effect of Chain Length and Solvent on Site Isolation, *J. Am. Chem. Soc.*, **2001**, 123, 18-25
- Hirayama T., Okuda K., Nagasawa H., A highly selective turn-on fluorescent probe for iron(II) to visualize labile iron in living cells, *Chem. Sci.*, **2013**, 4, 1250-1256
- Hou G. G., Wang C. H., Sun J. F., Yang M. Z., Lin D., Li H.J., Rhodamine-based "turn-on" fluorescent probe with high selectivity for Fe(2+) imaging in living cells, *Biochem. Biophys. Res. Commun.*, **2013**, 439, 459-463.
- Hu S. L., She N. F., Yin G. D., Guo H. Z., Wu A. X. and Yang C. L., Synthesis, structural characterization, and fluorescent chemosensory properties of novel molecular clips based on diethoxycarbonyl glycoluril, *Tetrahedron Lett.*, **2007**, 48, 1591-1594
- Hua J., Wang Y. G., A highly selective and sensitive fluorescent chemosensor for Fe<sup>3+</sup> in physiological aqueous solution, *Chem. Lett.*, **2005**, 34, 98-99
- Iacopetta B. J., Morgan E. H., The kinetics of transferrin endocytosis and iron uptake from transferrin in rabbit reticulocytes, *J. Biol. Chem.*, **1983**, 258, 9108-9115
- Imlay J. A., Chin S. M., S. Linn, Toxic DNA damage by hydrogen peroxide through the fenton reaction in vivo and in vitro, *Science*, **1988**, 240, 640-642
- Inorganic Biochemistry of Iron Metabolism*, 2nd ed. (Ed.: R. Crichton), Wiley, Chichester, **2001**, pp. 1- 10
- Inorganic Biochemistry of Iron Metabolism*, 2nd ed. (Ed.: R. Crichton), Wiley, Chichester, **2001**, pp. 17- 48
- Ji S., Meng X., Ye W., Feng Y., Sheng H., Cai Y., Liu J., Zhu X. Guo Q., A rhodamine-based "turn-on" fluorescent probe for Fe<sup>3+</sup> in aqueous solution, *Dalton Trans.*, **2014**, 43, 1583-1588
- Jin T., Ichikawa K., and Koyama T. J., Fluorescent calix[4]arene as an intramolecular excimer-forming Na<sup>+</sup> sensor in nonaqueous solution, *Chem. Soc., Chem. Commun.*, **1992**, 499-501
- Johnson I., Fluorescent probes for living cells, *Histochem. J.*, **1998**, 30, 123-140
- Jung H. J., Singh N., Jang D. O, Highly Fe<sup>3+</sup> selective ratiometric fluorescent probe based on imine-linked benzimidazole, *Tetrahedron Lett.*, **2008**, 49, 2960-2964

- Jung H. J., Singh N., Lee D. Y. and Jang D. O., Single sensor for multiple analytes: chromogenic detection of  $I^-$  and fluorescent detection of  $Fe^{3+}$ , *Tetrahedron Lett.*, **2010**, 51, 3962-3965
- Kakhlon O., Cabantchik Z.I., The labile iron pool: characterization, measurement, and participation in cellular processes, *Free Radic. Biol. Med.*, **2002**, 33, 1037-1046
- Kar C., Samanta S., Mukherjee S., Datta B. K., Ramesh A., Das G., A simple and efficient fluorophoric probe for dual sensing of  $Fe^{3+}$  and  $F^-$ : application to bioimaging in native cellular iron pools and live cells, *New J. Chem.*, **2014**, 38, 2660--2669
- Karin M., Mintz B., Receptor-mediated endocytosis of transferrin in developmentally totipotent mouse teratocarcinoma stem cells. , *J. Biol. Chem.*, **1981**, 256, 3245-3252
- Kazmi F., Hensley T., Pope C., Funk R. S., Loewen G. J., Buckley D. B., Parkinson A., Lysosomal Sequestration (Trapping) of Lipophilic Amine (Cationic Amphiphilic) Drugs in Immortalized Human Hepatocytes (Fa2N-4 Cells), *Drug Metab. Dispos.*, **2013**, 41, 897-905
- Kell D. B., Iron behaving badly: inappropriate iron chelation as a major contributor to the aetiology of vascular and other progressive inflammatory and degenerative diseases, *BMC Medical Genomics*, **2009**, 2, 2
- Kennedy D. P., Kormos D. M, Burdette S. C., Ferribright: A Rationally designed fluorescent probe for redox active metals, *J. Am. Chem. Soc.*, **2009**, 131, 8578-8586
- Kidane T.Z., Sauble E., Linder M.C., In three cell types, release of iron from ferritin requires lysosomal activity, *Am. J. Physiol. Cell Physiol.* **2006**, 291, C445-C455.
- Kiessling M. K., Klemke C. D., Kaminski M. M., Galani I. E., Krammer P. H., Gulow K., Inhibition of constitutively activated nuclear factor- $\kappa$ B induces reactive oxygen species- and iron-dependent cell death in cutaneous t-cell lymphoma, *Cancer Res.*, **2009**, 69, 2365-2374
- Kim H.N., Lee M.H., Kim H.J., Kim J.S., Yoon J., A new trend in rhodamine-based chemosensors: application of spirolactam ring-opening to sensing ions, *Chem. Soc. Rev.*, **2008**, 37, 1465-1472
- Kim J. S., Quang T., Calixarene-Derived Fluorescent Probes, *Chem. Rev.*, **2007**, 107, 3780-3799
- Kiyose K., Aizawa S., Sasaki E., Kojima H., Hanaoka K., Terai T., Urano Y., Nagano T., Molecular design strategies for near-infrared ratiometric fluorescent probes based on the unique spectral properties of aminocyanines , *Chem. Eur. J.*, **2009**, 15, 9191-9200
- Kiyose K., Kojima H., Nagano T., Functional near-infrared fluorescent probes, *Chem. Asian J.* **2008**, 3, 506-515
- Klausner R. D., van Renswoude J., Ashwell G., Kempf C., Schechter A. M., Dean A., Bridges K. R., Receptor-mediated endocytosis of transferrin in K562 cells, *J. Biol. Chem.*, **1983**, 258, 4715-4724.

- Ko S.K., Chen X., Yoon J., Shin I., Zebrafish as a good vertebrate model for molecular imaging using fluorescent probes, *Chem. Soc. Rev.*, **2011**, 40, 2120-2130
- Ko S.K., Yang Y.K., Tae J., Shin I., In vivo monitoring of mercury ions using a rhodamine-based molecular probe, *J. Am. Chem. Soc.*, **2006**, 128, 14150-14155
- Koide Y., Urano Y., Hanaoka K., Terai T., Nagano T., Development of an si-rhodamine-based far-red to near-infrared fluorescence probe selective for hypochlorous acid and its applications for biological imaging, *J. Am. Chem. Soc.*, **2011**, 133, 5680-5682
- Kozlov A. V., Yegorov D. Y., Vladimirov Y. A., Azizova O. A., Intracellular free iron in liver tissue and liver homogenate: studies with electron paramagnetic resonance on the formation of paramagnetic complexes with desferal and nitric oxide, *Free Radic. Biol. Med.*, **1992**, 13, 9-16
- Kruszewski M., Labile iron pool: the main determinant of cellular response to oxidative stress, *Mutat. Res.*, **2003**, 531, 81-92
- Kwon Y., Jang Y. J., Lee Y. J., Kim K. M., Seo M. S., Nam W., J. Yoon, A highly selective fluorescent chemosensor for  $Pb^{2+}$ , *J. Am. Chem. Soc.*, **2005**, 127, 10107-10111
- Lee D. Y., Singh N., Jang D. O., Ratiometric and simultaneous estimation of  $Fe^{3+}$  and  $Cu^{2+}$  ions: 1,3,5-substituted triethylbenzene derivatives coupled with benzimidazole, *Tetrahedron Lett.*, **2011**, 52, 3886-3890
- Lee M. H., Giap T. V., Kim S. H., Lee Y. H., Kang C., Kim J. S., A novel strategy to selectively detect  $Fe(III)$  in aqueous media driven by hydrolysis of a rhodamine 6G schiff base, *Chem. Commun.*, **2010**, 46, 1407-1409
- Lee S. H., Kim S. H., Jung S. K., and Kim J. S., Fluorescence ratiometry of monomer/excimer emissions in a space-through PET system, *J. Org. Chem.* **2005**, 70, 9288-9295
- Leite A., Silva A.M.G., Cunha-Silva L., Castro de B., Gameiro P., Rangel M., Discrimination of fluorescence light-up effects induced by pH and metal ion chelation on a spirocyclic derivative of rhodamine B, *Dalton Trans.*, **2013**, 42, 6110-6118
- Leray I., Lefevre J. P., Delouij. F. S., Delaire J., and Valeur B., Synthesis and photophysical and cation-binding properties of mono- and tetranaphthyl calix[4]arenes as highly sensitive and selective fluorescent sensors for sodium, *Chem. Eur. J.* **2001**, 7, 4590-4598
- Li Z., Zhang L., Li X., Guo Y., Ni Z., Chen J., Wei L., Yu M., A fluorescent color/intensity changed chemosensor for  $Fe^{3+}$  by photo-induced electron transfer (PET) inhibition of fluoranthene derivative, *Dyes Pigm.*, **2012**, 94, 60-65
- Lim N. C., Pavlova S. V., Brückner C., Squaramide hydroxamate-based chemodosimeter responding to Iron(III) with a fluorescence intensity increase, *Inorg. Chem.*, **2009**, 48, 1173-1182

- Lin W., Long L., Yuan L., Cao Z., Feng J., A novel ratiometric fluorescent Fe<sup>3+</sup> sensor based on a phenanthroimidazole chromophore, *Anal. Chim. Acta*, **2009**, 634, 262-266
- Linder M.C., Mobilization of stored iron in mammals: a review, *Nutrients*, **2013**, 5, 4022-4050
- Lippard S. J. and Berg J. M., *Principles of Bioinorganic Chemistry*, University Science Books, Mill Valley, CA, **1994**
- Lister J.A., Robertson C.P., Lepage T., Johnson S.L., Raible D.W., Nacre encodes a zebrafish microphthalmia-related protein that regulates neural-crest-derived pigment cell fate, *Development*, **1999**, 126, 3757-3767
- Liu J. M., Zheng Q. Y., Yang J. L., Chen C. F., Huang Z. T., A new fluorescent chemosensor for Fe<sup>3+</sup> and Cu<sup>2+</sup> based on calix[4]arene, *Tetrahedron Lett.*, **2002**, 43, 9209-9212
- Liu S. R., Wu S. P., *Sensor Actuat. B-Chem.*, New water-soluble highly selective fluorescent chemosensor for Fe (III) ions and its application to living cell imaging, **2012**, 171-172, 1110-1116
- Liu Z., He W., Guo Z., Metal coordination in photoluminescent sensing, *Chem.Soc.Rev.*, **2013**, 42, 1568-1600
- Liu Z., Zhang C., Chen Y., Fang Q., Bai Y., He W., Guo Z., In vivo ratiometric Zn<sup>2+</sup> imaging in zebrafish larvae using a new visible light excitable fluorescent sensor, *Chem. Commun.*, **2014**, 50, 1253-1255
- Lohani C. R., Kim J. M. and Lee K. H., Facile synthesis of anthracene-appended amino acids as highly selective and sensitive fluorescent Fe<sup>3+</sup> ion sensors, *Bioorg. Med. Chem.Lett.*, **2009**, 19, 6069-6073
- Lohani C. R., Lee K.H., The effect of absorbance of Fe<sup>3+</sup> on the detection of Fe<sup>3+</sup> by fluorescent chemical sensors, *Sens. Actuators B*, **2010**, 143, 649-654
- London R. E., Methods for measurement of intracellular magnesium: NMR and fluorescence, *Annual Review of Physiology*, **1991**, 53, 241-258
- Lui J., Sun Y. Q., Wang P., Zhang J., Guo W., Construction of NIR and ratiometric fluorescent probe for Hg<sup>2+</sup> based on a rhodamine-inspired dye platform, *Analyst*, **2013**, 138, 2654-2660
- Lv H., Yang X. F., Zhang Y., Guo Y., Li Z., Li H., Native chemical ligation combined with spirocyclization of benzopyrylium yes for the ratiometric and selective fluorescence detection of cysteine and homocysteine, *Anal. Chem.*, **2014**, 86, 1800-1807
- Ma Y., Groot H. , Liu Z., Hider R. C., Petrat F., Chelation and determination of labile iron in primary hepatocytes by pyridinone fluorescent probes, *Biochem. J.*, **2006**, 395, 49-55

- Marenco M. J. C., Fowley C., Hyland B. W., Galindo-Riano D., Sahoo S. K. and Callan J. F., A new fluorescent sensor for the determination of Fe(III) in semi-aqueous solution, *J. Fluoresc.*, **2012**, 22, 795-798
- Marenco M. J. C., Fowley C., Hyland B. W., Hamilton G. R. C., Galindo-Riano D., Callan J. F., A new use for an old molecule: N-phenyl-2-(2-hydroxynaphthalen-1-ylmethylene)hydrazinecarbothioamide as a ratiometric 'Off-On' fluorescent probe for iron, *Tetrahedron Lett.*, **2012**, 53, 670-673
- Miwa M., The principle of icg fluorescence method, *Open Surg. Oncol. J.*, **2010**, 2, 26-28
- Mojzych M., Henary M., Synthesis of cyanine dyes, *Top. Heterocycl. Chem.*, **2008**, 14, 1-9
- Mokhir A., Kiel A., Herten D. P., Kraemer R., Fluorescent Sensor for Cu<sup>2+</sup> with a Tunable Emission Wavelength, *Inorg. Chem.*, **2005**, 44, 5661-5666
- Nolan E. M., Lippard S. J., Tools, and Tactics for the Optical Detection of Mercuric Ion, *Chem. Rev.*, **2008**, 108, 3443-3480
- Papanikolaou G., Pantopoulos K., Iron metabolism and toxicity, *Toxicol. Appl. Pharmacol.*, **2002**, 202, 199-211
- Paterson S., Armstrong N. J., Iacopetta B. J., McArdle H. J., Morgan E. H., Intravesicular pH and iron uptake by immature erythroid cells, *J. Cell. Physiol.*, **1984**, 120, 225-232
- Pearson R. G., Hard and soft acids and bases, *J. Am. Chem. Soc.*, **1963**, 85, 3533-3539.
- Peng R., Wang F. and Sha Y., Synthesis of 5-dialkyl(aryl)aminomethyl-8-hydroxyquinoline dansylates as selective fluorescent sensors for Fe<sup>3+</sup>, *Molecules*, **2007**, 12, 1191-1201
- Peng X., Song F., Lu E., Wang Y., Zhou W., Fan J., Gao Y., Heptamethine cyanine dyes with a large stokes shift and strong fluorescence: A paradigm for excited-state intramolecular charge transfer, *J. Am. Chem. Soc.*, **2005**, 127, 4170-4171
- Perez C. A., Guo M., Wei Y., Iron-binding and anti-fenton properties of baicalein and baicalin, *J. Inorg. Biochem.*, **2009**, 103, 326-332
- Petrat F., De Groot H., Sustmann R., Rauen U., The chelatable iron pool in living cells: a methodically defined quantity, *Biol. Chem.*, **2002**, 383, 489-502
- Petrat F., Rauen U., de Groot H., Determination of the chelatable iron pool of isolated rat hepatocytes by digital fluorescence microscopy using the fluorescent probe, phen green SK, *Hepatology*, **1999**, 29, 1171-1179
- Petrat F.I., de Groot H., Rauen U., Subcellular distribution of chelatable iron: a laser scanning microscopic study in isolated hepatocytes and liver endothelial cells, *Biochem. J.*, **2001**, 356, 61-69



- Ponka P., Tissue-specific regulation of iron metabolism and heme synthesis: distinct control mechanisms in erythroid cells, *Blood*, **1997**, 89, 1-25
- Praveen L., Reddy M. L. P., Varma R. L., Dansyl-styrylquinoline conjugate as divalent iron sensor, *Tetrahedron Lett.*, **2010**, 51, 6626-6629
- Qian F., Zhang C. Zang Y., He W., Gao X., Hu P., Guo Z., Visible light excitable Zn<sup>2+</sup> fluorescent sensor derived from an intramolecular charge transfer fluorophore and Its in vitro and in vivo application, *J. Am. Chem. Soc.*, **2009**, 131, 1460-1468
- Qian X. and Xiao Y., 4-Amino-1,8-dicyanonaphthalene derivatives as novel fluorophore and fluorescence switches: efficient synthesis and fluorescence enhancement induced by transition metal ions and protons, *Tetrahedron Lett.*, **2002**, 43, 2991-2994
- Que E. L., Domaille D. W., and Chang C. J., Metals in neurobiology: probing their chemistry and biology with molecular imaging, *Chem. Rev.*, **2008**, 108, 1517-1549
- Richardson D. R., Lane D. J. R., Becker E. M., Huang M., L., H., Whitnall M., Rahmanto Y. S., Sheftel A. D., Ponka P., Mitochondrial iron trafficking and the integration of iron metabolism between the mitochondrion and cytosol, *Proc. Natl. Acad. Sci. USA*, **2010**, 107, 10775-10782
- Roat-Malone, M. *Bioinorganic chemistry; a short course*, John Wiley and Sons, New Jersey, **2002**, pp.1-3
- Rossotti F. J. C., Rossotti H., (Series in Advanced Chemistry), McGraw-Hill Book Company, Inc., New York, Toronto, London, **1961**, pp. 97-98
- Rouault A. T., Iron metabolism in the CNS: implications for neurodegenerative diseases, *Nat. Rev. Neurosci.*, **2013**, 14, 551-564
- Rouault T. A., The role of iron regulatory proteins in mammalian iron homeostasis and disease, *Nat. Chem. Biol.*, **2006**, 8, 406-414
- Sahoo S. K., Sharma D., Bera R. K., Crisponi G., Callan J. F., Iron(III) selective molecular and supramolecular fluorescent probes, *Chem. Soc. Rev.*, **2012**, 41, 7195-7227
- Saleem M., Abdullah R., Ali A., Park B. J., Choi E. H, Hong I. S., Lee K. H., Facile synthesis, cytotoxicity and bioimaging of Fe<sup>3+</sup> selective fluorescent chemosensor, *Bioorg. Med. Chem.*, **2014**, 22, 2045-2051
- Samanta A., Vendrell M., Das R., Chang Y.T., Development of photostable near-infrared cyanine dyes, *Chem. Comm.*, **2010**, 46, 7406-7408
- Sankaran N. B., Banthia S., Das A., Samanta A., Fluorescence signaling of transition metal ions: a new approach, *New J. Chem.*, **2002**, 26, 1529-1531

- Santra M., Ryu D., Chatterjee A., Ko S. K., Shin I., Ahn K. H., A chemodosimeter approach to fluorescent sensing, imaging of inorganic, and methylmercury species, *Chem. Commun.*, **2009**, 2115-2117
- Sauvage J. P., *Transition Metals in Supramolecular Chemistry; Perspectives in supramolecular Chemistry Volume 5*, Wiley-VCH, **1999**, pp. 93-100
- Schmitt H., Lomoth R., Magnuson A., Park J., Fryxelius J., Kritikos M., Martensson J., Hammarstrom L., Sun L., Akermark B., Synthesis, redox properties, and EPR spectroscopy of manganese (III) complexes of the ligand N,N-Bis(2-hydroxybenzyl)-N'-2-hydroxybenzylidene-1,2-diaminoethane: formation of mononuclear, dinuclear, and even higher nuclearity complexes, *Chem. Eur. J.*, **2002**, 8, 3757-3768
- Sen S., Sarkar S., Chattopadhyay B., Moirangtham A., Basu A., Dhara K., Chattopadhyay P., A ratiometric fluorescent chemosensor for iron: discrimination of Fe<sup>2+</sup> and Fe<sup>3+</sup> and living cell application, *Analyst*, **2012**, 137, 3335-3342
- Senthilnithy R., De Costa M. D. P. and Gunawardhana H. D., Fluorescence quenching and bonding properties of some hydroxamic acid derivatives by iron(III) and manganese(II), *Luminescence*, **2009**, 24, 203-208
- Shaw G. C., Cope J. J., Li L, Corson K., Hersey C., Ackermann G. E., Gwynn B., Lambert A. J., Wingert R. A., Traver D., Trede N. S., Barut B. A., Zhou Y., Minet E., Donovan A., Brownlie A., Balzan R., Weiss M. J., Peters L. L., Kaplan J., Zon L. I., Paw B. H., Mitoferrin is essential for erythroid iron assimilation, *Nature*, **2006**, 440, 96-100
- Sheftel A. D., Zhang A. S., Brown C., Shirihai O. S., Ponka P., Direct interorganellar transfer of iron from endosome to mitochondrion, *Blood*, **2007**, 110, 125 - 132
- Shvartsman M., Kikkeri R., Shanzer A., Cabantchik Z. I., Non-transferrin-bound iron reaches mitochondria by a chelator-inaccessible mechanism: biological and clinical implications, *Am. J. Physiol.*, **2007**, 293, 1383-1394.
- Singh N., Kaur N. and Callan J. F., Incorporation of siderophore binding sites in a dipodal fluorescent sensor for Fe(III), *J. Fluoresc.*, **2009**, 19, 649-654
- Singh N., Kaur N., Dunn J., MacKay M. and Callan J. F., A new fluorescent chemosensor for iron(III) based on the  $\beta$ -aminobisulfonate receptor, *Tetrahedron Lett.*, **2009**, 50, 953-956
- Smanmoo S., Nasomphan W., Tangboriboonrat P., Highly selective fluorescent chemosensor for Fe<sup>3+</sup> imaging in living cells, *Inorg. Chem. Commun.*, **2011**, 14, 351-354
- Smith M. A., Harris P. L. R., Sayre L. M. Perry G., Iron accumulation in Alzheimer disease is a source of redox-generated free radicals, *Proc. Natl. Acad. Sci. USA*, **1997**, 94, 9866-9868
- Smith N. A., Sadler P. J., Photoactivatable metal complexes: from theory to applications in biotechnology and medicine, *Phil. Trans. R. Soc. A*, **2013**, 371, 20120519

- Song F., Peng X, Lu E., Wang Y., Zhou W., Fan J., Tuning the photoinduced electron transfer in near-infrared heptamethine cyanine dyes, *Tetrahedron Lett*, **2005**, 46, 4817-4820
- Song F., Peng X., Lu E., Zhang R., Chen X., Song B., Syntheses, spectral properties, and photostabilities of novel water-soluble near-infrared cyanine dyes, *J. Photochem Photobiol A: Chem*, **2004**, 168, 53-57
- Song F., Watanabe S., Floreancig P. E., Koide K., Electrospinning as a new technique to control the crystal morphology and molecular orientation of polyoxymethylene nanofibers, *J. Am. Chem. Soc.*, **2008**, 130, 16460-16461
- Sterzel W., Bedford P., Eisenbrand G., Automated determination of DNA using the fluorochrome Hoechst 33258, *Anal. Biochem.*, **1985**, 147, 462-467
- Strekowski L., Lipowska M., Patonay G., Substitution reactions of a nucleofugal group in heptamethine cyanine dyes. Synthesis of an isothiocyanato derivative for labeling of proteins with a near-infrared chromophore, *J. Org. Chem.* **1992**, 57, 4578-4580
- Sugasawa K., Masutani C., and Hanaoka F., Cell-free repair of UV-damaged simian virus 40 chromosomes in human cell extracts. I. Development of a cell-free system detecting excision repair of UV-irradiated SV40 chromosomes, *J. Biological Chem.*, **1993**, 268, 9098-9104
- Sung K., Fu H. K. and Hong S. H., A Fe(3+)/Hg(2+)-selective anthracene-based fluorescent PET sensor with tridentate ionophore of amide/beta-amino alcohol, *J. Fluoresc.*, **2007**, 17, 383-389
- Taki M., Wolford J. L. O'Halloran T. V., Emission ratiometric imaging of intracellular zinc: design of a benzoxazole fluorescent sensor and its application in two-photon microscopy, *J. Am. Chem. Soc.*, **2004**, 126, 712-713
- Tan S. S., Kim S. J., Kool E. T., Differentiating between fluorescence-quenching metal ions with polyfluorophore sensors built on a DNA backbone, *J. Am. Chem. Soc.*, **2011**, 133, 2664-2671
- Tang B., Yu F., Li P., Tong L., Duan X., Xie T., Wang X., A near-infrared neutral pH fluorescent probe for monitoring minor pH changes: imaging in living HepG2 and HL-7702 cells, *J. Am. Chem. Soc.*, **2009**, 131, 3016-3023
- Tang L., Li F., Liu M., Nandhakumar R., A new rhodamine B derivative as a colorimetric chemosensor for recognition of copper(II) ion, *Bull. Korean Chem.Soc.*, **2010**, 31, 3212-3216
- Toyokuni S., Iron-induced carcinogenesis: the role of redox regulation, *Free Radic Biol. Med.*, **1996**, 20, 553-566
- Trump W. J. V., McHenry M.J., Lateral line morphology and sensitivity in zebrafish larvae (*Danio rerio*)., *J. Exp. Biol.*, **2008**, 2105-2115

- Truty J., Malpe R., Linder M.C., Iron prevents ferritin turnover in hepatic cells, *J. Biol. Chem.*, **2001**, 276, 48775-48780
- Tumambac G. E., Rosencrance C. M., Wolf C., Selective metal ion recognition using a fluorescent 1,8-diquinolynaphthalene-derived sensor in aqueous solution, *Tetrahedron*, **2004**, 60, 11293-11297
- Valeur B., *Molecular Fluorescence-Principles and Applications*; Wiley-VCH, Weinheim, **2002**
- Van Renswoude J., Bridges K. R., Harford J. B., Klausner R. D., Receptor-mediated endocytosis of transferrin and the uptake of Fe in K562 cells: Identification of a nonlysosomal acidic compartment, *Proc. Natl. Acad. Sci. USA*, **1982**, 79, 6186-6190
- Wallace K. N., Pack M., Unique and conserved aspects of gut development in zebrafish, *Dev. Biol.*, **2003**, 255, 12-29.
- Wallander M. L., Leibold E. A., Eisenstein R. S., Molecular control of vertebrate iron homeostasis by iron regulatory proteins, *Biochim. Biophys. Acta*, **2006**, 1763, 668-689
- Wang B., Hai J., Liu Z., Wang Q., Yang Z., Sun S., Selective detection of iron(III) by rhodamine-modified Fe<sub>3</sub>O<sub>4</sub> nanoparticles, *Angew. Chem. Int. Ed.*, **2010**, 49, 4576-4579
- Wang H., Wang D., Wang Q., Li X., C. A. Schalley, Nickel(II) and iron(III) selective off-on-type fluorescence probes based on perylene tetracarboxylic diimide, *Org. Biomol. Chem.*, **2010**, 8, 1017-1026
- Wang S., Meng X., Zhu M., A naked-eye rhodamine-based fluorescent probe for Fe(III) and its application in living cells, *Tetrahedron Lett.*, **2011**, 52, 2840-2843
- Wang T., Zhao Q. J., Hu H. G., Yu S. C., Liu X., Liu L., Wu Q. Y., Spirolactonized si-rhodamine: a novel NIR fluorophore utilized as a platform to construct si-rhodamine-based probes, *Chem. Commun.*, **2012**, 48, 8781-8783
- Weerasinghe A. J., Schmiesing C., Sinn E., Highly sensitive and selective reversible sensor for the detection of Cr<sup>3+</sup>, *Tetrahedron letters*, **2009**, 50, 6407-6410
- Wei Y., Aydin Z., Yi Z., Liu Z., Guo M., A turn-on fluorescent sensor for imaging labile Fe<sup>3+</sup> in live neuronal cells at subcellular resolution, *ChemBioChem*, **2012**, 13, 1569-1573
- Wei Y., Guo M., Hydrogen peroxide triggered prochelator activation, subsequent metal chelation, and attenuation of the fenton reaction, *Angew. Chem. Int. Ed.*, **2007**, 46, 4722-4725
- Wei Y., Qin G., Wang W., Bian W., Shuang S. and Dong C., Development of fluorescent Fe(III) sensor based on chalcone, *J. Lumin.*, **2011**, 131, 1672-1676
- Wei Y., Zhang Y., Liu Z., Guo M., A novel profluorescent probe for detecting oxidative stress induced by metal and H<sub>2</sub>O<sub>2</sub> in living cells. , *Chem. Comm.*, **2010**, 46, 4722-4726

- Whitnall M., Rahmanto Y. S., Sutak R., Xu X., Becker E. M., Michael M. R., Ponka P., Richardson D. R., The MCK mouse heart model of friedreich's ataxia: alterations in iron-regulated proteins and cardiac hypertrophy are limited by iron chelation, *Proc. Nat. Acad. Sci.*, **2008**, 105, 9757-9762
- Wolf C., Mei X. and Rokadia H. K., Selective detection of Fe(III) ions in aqueous solution with a 1,8-diacridylnaphthalene-derived fluorosensor, *Tetrahedron Lett.*, **2004**, 45, 7867-7871
- Xi P., Dou J., Huang L., Xu M., Chen F., Wu Y., Bai D., Li W., Zeng Z., A selective turn-on fluorescent sensor for Cu(II) and its application in imaging in living cells, *Sens. Actuators, B*, **2010**, 148, 337-341
- Xiang Y., Tong A., Jin P., Ju Y., New fluorescent rhodamine hydrazone chemosensor for Cu(II) with high selectivity and sensitivity, *Org. Lett.*, **2006**, 8, 2863-2866
- Xiang Y., Tong A., A new rhodamine-based chemosensor exhibiting selective Fe<sup>III</sup>-amplified fluorescence, *Org. Lett.*, **2006**, 8, 1549-1552
- Xu J., Jia Z., Knutson M. D., Leeuwenburgh C., Impaired iron status in aging research, *Int. J. Mol.Sci.*, **2012**, 13, 2368-2386.
- Yamashiro D. J., Tycko B., Fluss S. R., Maxfield F. R., Segregation of transferrin to a mildly acidic (pH 6.5) para-Golgi compartment in the recycling pathway., *Cell*, **1984**, 37, 789-800
- Yang H., Zhou Z., Huang K., Yu M., Li F., Yi T., Huang C., Multisignaling optical-electrochemical sensor for Hg<sup>2+</sup> based on a rhodamine derivative with a ferrocene unit, *Org. Lett.* **2007**, 9, 4729-4732
- Yang R. H., Chan W. H., Lee A. W. M., Xia P. F., Zhang H. K., Li K., A Ratiometric Fluorescent Sensor for Ag<sup>I</sup> with High Selectivity and Sensitivity, *J. Am. Chem. Soc.*, **2003**, 125, 2884-2885
- Yang Y.K., Ko S.K, Shin I., Tae J., Synthesis of a highly metal-selective rhodamine-based probe and its use for the in vivo monitoring of mercury, *Nat. Protoc.*, **2007**, 2, 1740-1745
- Yang Z., She M., Yin B., Cui J., Zhang Y., Sun W., Li J., Shi Z., Three rhodamine-based "off-on" chemosensors with high selectivity and sensitivity for Fe<sup>3+</sup> imaging in living cells, *J. Org. Chem.*, **2012**, 77, 1143-1147
- Yao J., Dou W., Qin W. and Liu W., A new coumarin-based chemosensor for Fe<sup>3+</sup> in water, *Inorg. Chem. Commun.*, **2009**, 12, 116-118.
- Yong Y. K., Yook K. J., Tae J., A rhodamine-based fluorescent and colorimetric chemodosimeter for the rapid detection of Hg<sup>2+</sup> ions in aqueous media, *J. Am. Chem. Soc.*, **2005**, 127, 16760-6761
- Yu M., Shi M., Chen Z., Li F., Li X., Gao Y., Xu J., Yang H., Zhuo Z., Yi T., Huang C., Highly sensitive and fast responsive fluorescence turn-on chemodosimeter for Cu<sup>2+</sup> and its application in live cell imaging, *Chem. Eur. J.*, **2008**, 14, 6892-6900

- Yuan L., Lin W., Yang Y., Chen, H., A unique class of near-infrared functional fluorescent dyes with carboxylic-acid-modulated fluorescence on/off switching: rational design, synthesis, optical properties, theoretical calculations, and applications for fluorescence imaging in living animals, *J. Am. Chem. Soc.*, **2012**, 134, 1200–1211
- Zalewski P. D., Forbes I. J. and Betts W. H., Correlation of apoptosis with change in intracellular labile Zn(II) using zinquin [(2-methyl-8-p-toluenesulphonamido-6-quinolyloxy)acetic acid], a new specific fluorescent probe for Zn(II), *Biochem. J.*, **1993**, 296, 403-408
- Zhang L., Wang J., Fan J., Guo K., Peng X., A highly selective, fluorescent chemosensor for bioimaging of Fe<sup>3+</sup>, *Bioorg. Med. Chem. Lett.*, **2011**, 21, 5413-5416
- Zhang M., Gao Y., Li M., Yu M., Li F., Li L., Zhu M., Zhang J., Yi T., Huang C., A selective turn-on fluorescent sensor for Fe<sup>III</sup> and application to bioimaging, *Tetrahedron Letters*, **2007**, 48, 3709-
- Zhang X., Shiraishi Y., Hirai T., A new rhodamine-based fluorescent chemosensor for transition metal cations synthesized by one-step facile condensation, *Tetrahedron Lett.*, **2007**, 48, 5455-5459
- Zhang X., Shiraishi Y., Hirai T., Cu(II)-Selective green fluorescence of a rhodamine–diacetic acid conjugate, *Org. Lett.*, **2007**, 9, 5039-5042
- Zhang X., Shiraishi Y., Hirai T., Fe(III)- and Hg(II)-selective dual channel fluorescence of a rhodamine-azacrown ether conjugate, *Tetrahedron Lett.*, **2008**, 49, 4178-4181
- Zhang Y. Z., Olwu Z., Mao F., Haugland W. L., Novel fluorescent acidic organelle-selective dyes and mitochondrion-selective dyes that are well retained during cell fixation and permeabilization, *Mol. Biol. Cell*, **1994**, 5, 113a (abstract 653)
- Zhao Y., Lin Z., He C., Wu H., Duan C., A “turn-on” fluorescent sensor for selective Hg(II) detection in aqueous media based on metal-induced dye formation, *Inorg. Chem.*, **2006**, 45, 10013-10015
- Zheng H., X. Zhang J., Cai X., Bian Q. N., Yan M., Wu G. H., Lai X. W., Jiang Y. B., Ratiometric fluorescent chemosensor for Hg<sup>2+</sup> based on heptamethine cyanine containing a thymine moiety, *Org. Lett.*, **2012**, 14, 1986-1989
- Zheng H., Yan M., Fan X., Sun D., Yang S., Yang L., Li J., Jiang Y., A heptamethine cyanine-based colorimetric and ratiometric fluorescent chemosensor for the selective detection of Ag<sup>+</sup> in an aqueous medium, *Chem. Commun.*, **2012**, 48, 2243-2245